CHARACTERISATION OF HEAVY MINERAL SANDS AND SOILS BY RADIOMETRY AND ITS USE IN MINERAL BENEFICIATION AND AGRICULTURE

Dawid de Villiers

Dissertation presented for the degree of Doctor of Philosophy, Stellenbosch University

Promotors: Dr. J.A. Stander (Physics)
Prof A. Rozendaal (Earth Science)

March 2011

DECLARATION

By submitting this dissertation electronically, I declare that the entirety of the work contained therein is my own, original work, that I am the owner of the copyright thereof (unless to the extent explicitly otherwise stated) and that I have not previously in its entirety or in part submitted it for obtaining any qualification.

Date : 2011/02/20

ABSTRACT

Radioactivity is well known and well understood, but its usefulness in industrial applications to optimise processes or increase economic viability is not yet fully utilised by many industries. This study focuses on the measurement of natural radioactivity and its application in heavy mineral separation and vineyard soil classification.

The gamma radiometry set-up consisted of a high purity germanium detector, a Marinelli beaker as sample container and associated electronics. It was calibrated for laboratory-based measurements by minimising the background radiation with the use of lead castle and energy and resolution calibrations. Furthermore, detection parameters were optimised; these included the counting time, the selection of gamma rays used for analysis of a sample, the peak area calculation for the detector dead time and the detector efficiency. Given that the samples had different densities and volumes, the detector efficiency had to be corrected for volume and density effects. After implementation of the corrections and optimisations the detection system was tested and found able to accurately measure radioactivity concentrations. The systematic measurement errors for ^{238}U were 5.1 % in the case of the heavy mineral sands and 34.3 % for the vineyard soils, 4.5 % for the ^{232}Th concentrations and 4.7 % for ^{40}K concentrations. Statistical errors were kept below 2 %.

The application of radiometry has not been done before at any South African heavy mineral separation plant. For this reason radiometry is suggested as an easier, faster and cheaper alternative to X-ray fluorescence (XRF) for effective implementation of grade control for zircon to improve the cost benefit of the heavy mineral separation process. Zircon is an example of a heavy mineral that is worldwide in demand with a consumption of more than a million tonnes per year. It is used in a wide range of industrial applications and products that include tiles, sanitary ware and plasma displays. South Africa is the second largest producer of zircon in the world and also has the second largest reserve of available zircon, making this mineral a viable source of income for several years to come. Radioactivity, in the form of uranium and thorium, and other impurities such as iron oxide and titanium oxide are found in the crystal lattice of zircon. For it to be a sellable product, the sum of the uranium and thorium concentrations must be less than 500 parts per million for prime or first grade zircon and less than 1000 parts per million for second grade zircon. At present the concentrations of uranium and thorium in zircon concentrates are measured

on a whole rock basis by XRF during and at the end of the processing cycle before the final products are ready to be shipped. This is not an ideal situation as the grab samples are taken periodically and are not necessarily representative of the stream or final assignment and has resulted in significant losses by the producer. The solution is to accurately measure the uranium and thorium concentrations fast or immediately, preferably the measurements must be made online and in real time so that processing decisions can be implemented quickly to optimise the final product.

Heavy mineral sand samples were obtained from the various separation processes in a Mineral Separation Plant and their ^{238}U and ^{232}Th concentrations determined. The results indicated that the samples' uranium to thorium ratios together with their total concentrations can be used to differentiate between the samples (i.e. separation processes). The measurement results were compared with those obtained with XRF. The correlations with radiometry were excellent for the uranium (r^2 = 0.992), thorium (r^2 = 0.998) and total concentrations (r^2 = 0.998). Radiometric measurements were also conducted by decreasing the counting time from 3600 s to 1 s to investigate its effect on the accuracy of the results. Correlations between the different times and 3600 s ranged from excellent to good. The obtained results are then used to recommend that radiometry is used in a Mineral Separation Plant to verify that the zircon and zirkwa meet the specifications, to optimise the entrance feed and the other separation processes and to monitor the tailings streams. Finally the practical aspects of the implementation of radiometry are discussed.

As a second application was radiometry applied in an agricultural pilot study to demonstrate the applicability of radiometry as a possible useful tool in soil classification. The creation of a vineyard is a long term and expensive investment and its yield and quality will be influenced by many factors such as the type of soil, viticultural preparations and climate. Information on the different soil types in a vineyard is therefore indispensable for the optimisation of land use with respect to vine cultivar, wine quality and production.

Soil samples were obtained from Kanonkop, Simonsig and Spier vineyards and their ^{238}U, ^{232}Th and ^{40}K concentrations determined, assuming that fertilisers would have no effect on the results. The difference in ^{40}K concentrations were related to the clay fraction of the soil and demonstrated that the Kanonkop and Simonsig soils are fine-grained and clay-rich compared to the sandy coarse-grained soils of Spier. The uranium and thorium

concentrations were indicators of whether the mineralogy of the soil is the same as the underlying bedrock as well as soil maturity. The measurement results were compared with those obtained with XRF. The correlation with radiometry were poor for the uranium concentrations (r^2 = 0.314), as many of the samples concentrations were below the XRF detection limit. The correlations were excellent for both thorium (r^2 = 0.985) and potassium (r^2 = 0.999). As a positive result from the findings of the study was an in-situ measurement performed by Newman et al. for the radiometric mapping of a Simonsig vineyard for soil classification.

OPSOMMING

Radioaktiwiteit is wel bekend en word goed verstaan, tog is die gebruik daarvan in industriele toepassings om prosesses te optimiseer of winsgrense te verhoog nog nie deur baie industrië ten volle benut nie. Hierdie studie fokus op die meting van natuurlike radioaktiwiteit en die toepassing daarvan in swaar mineraal skeiding en wingerd grond klassifikasie.

Die gamma radiometrie opstelling het bestaan uit ‘n hoë suiwerheid germanium detektor, 'n Marinelli beker as monster houer en verwante elektronika. Dit was gekalibreer vir laboratorium gebaseerde metings deur die vermindering van die agtergrondstraling met die gebruik van lood kasteel en energie en resolusie kalibrasies. Verder was deteksie parameters geoptimaliseer, dit sluit in die teltyd, die keuse van gammastrale wat gebruik word vir die ontleding van 'n monster, die piek area berekening, die korreksie vir die detektor se dooie tyd en die detektor doeltreffendheid. Gegee dat die monsters van mekaar verskil het in terme van dighteid en volume was dit nodig om die detektor doeltreffendheid te korrigeer vir volume en digtheid effekte. Na die implementering van die korreksies en optimalisasie was die detektor stelsel getoets en was gevind dat radioaktiwiteit konsentrasies akkuraat gelewer kan lewer. Die sistematiese meet foute vir ^{238}U was 5.1 % vir die mineraal sand en 34.3 % vir wingerd grond, 4.5 % vir ^{232}Th konsentrasies en 4.7 % vir ^{40}K konsentrasies. Statistiese foute was onder 2 % gehou.

Die toepassing van radiometrie was nog nie voorheen by enige Suid-Afrikaanse swaar mineraal skeidings aanleg gedoen nie. Vir die rede is radiometrie voorgestel as ‘n makliker, vinniger en goedkoper alternatief teenoor XSF vir effektiewe implementering van graad beheer vir zirkon om die koste voordeel van die swaar mineral skeiding proses te verbeter. Zirkon is ‘n voorbeeld van ‘n swaar mineraal wat wêreldwyd in aanvraag is met ‘n verbruik van meer as ‘n miljoen ton per jaar. Dit word in ‘n wye reeks van industriele toepassings en produkte gebruik onder andere teëls, sanitêre ware en plasma skerms. Suid Afrika is die tweede grootste vervaardiger van zirkon in die wêreld en het ook die tweede grootste reserwe van besikbare zirkon. Dit veroorsaak dat die mineraal ‘n lewensvatbare brom van inkomste is vir nog etlike jare. Radioaktiwiteit, in die vorm van uraan en thorium, word tesame met ander onsuiwerhede soos ysteroksied en titaanoksied in zirkon se kristal rooster gevind. Om ‘n verkoopbare produk te wees moet die som van die uraan en thorium konsentrasies minder wees as 500 dele per miljoen vir prima en

eerste graad zirkon en minder wees as 1000 dele per miljoen vir tweede graadse zirkon. Huidiglik word die uraan en thorium konsentrasies in die zirkon konsentraat gemeet op ‘n heel gesteente basis met X-straal fluoroskopie (XSF) gedurende en op die einde van die prosesering siklus net voor die finale produk reg is om versend te word. Dit is nie die ideale situasie nie, want die monsters word periodies geneem en is nie noodwendig verteenwoordigend van die stroom of die finale produk nie en het al tot beduidende verliese deur die vervaardiger gelei. Die oplossing is om die uraan en thorium konsentrasies vinnig of onmiddelik te meet, verkieslik moet die metings inlyn en intyds gedoen word om verwerkings besluite vinnig geimplementeer kan word om die finale produk te optimaliseer.

Swaar mineraal sand monsters was verkry van die verskeie skeidingsprosesse in ‘n Mineraal Skeidings Aanleg en hul ^{238}U en ^{232}Th konsentrasies bepaal. Die resultate het aangetoon dat die monsters se uraan en thorium verhoudings saam met hul totale konsentrasies gebruik kan word om te onderskei tussen die monsters (oftewel die skeiding prosesse). Die meting resultate was vergelyk met dié verkry met XSF. Die korrelasies met radiometrie was uitstekend vir die uraan (r^2 = 0.992), thorium (r^2 = 0.998) en totale konsentrasies (r^2 = 0.998). Radiometriese metings was ook uigevoer deur die teltyd te verminder van 3600 s tot 1 s om die uitwerking daarvan op die akkuraatheid van die resultate te ondersoek. Korrelasies tussen die verskillende tye en 3600 s het gewissel van uitstekend tot goed. Die bevindinge was dan gebruik om aan te beveel dat radiometrie in a Mineraal Skeidings Aanleg gebruik kan word om te verifeer dat daar aan die zirkon en zirkwa spesifikasies voldoen word, om die begin voer en ander skeidings prosesse te optimaliseer en ook die uitskot strome te monitor. Laastens is die praktiese aspekte van die implementering van radiometrie bespreek.

Vir die tweede toepassing was radiometrie toepgepas in ‘n loods studie in die landbou om die toepaslikheid van radiometrie as ‘n moontlike nuttige instrument in grond klassifikasie te demonstreer. Die skepping van ‘n wingerd is ‘n lang termyn en duur belegging waarvan die opbrengs en kwaliteit beinvloed sal word deur vele faktore, onder andere die tipe grond, wynbou voorbereidings en die klimaat. Inligiting oor die verskillende grond tipes in ‘n wingerd is daarom onmisbaar vir die optimalisering van land gebruik in betrekking tot die wingerdstok kultivar, wyn kwaliteit en produksie. Radiometrie is toegepas om te demonstreer die toepaslikheid daaran as ‘n moontlike nuttige instrument in grond klassifikasie.

Grondmonsters was verkry vanaf Kanonkop, Simonsig en Spier wingerde en hul ^{238}U, ^{232}Th en ^{40}K konsentrasies bepaal met die aanname dat kunsmis nie ‘n uitwerking op die resultate sou hê nie. Die verskil in ^{40}K konsentrasies was verwant aan die kleifraksie van die grond en het getoon dat die Kanonkop en Simonsig gronde is fyn korrelrig en kleiryk is in vergelyking met die sanderige growwe korrel grond van Spier. Die uraan en thorium konsentrasies het gedui op die samestelling van die grond en ook aangedui watter grond dieselfde is as die onderliggende rots. Die meting resultate was vergelyk met dié verkry met XSF. Die korrelasie met die radiometrie was sleg vir die uraan konsentrasies (r^2 = 0.314) aangesien baie van die monster konsentrasies laer was as die XSF deteksie limiet. Die korrelasies was uitstekend vir beide thorium (r^2 = 0.985) en kalium (r^2 = 0.999). As ‘n positiewe resultaat van die studie se bevindinge was ‘n in-situ meting gedoen deur Newman et al. om ‘n Simonsig wingerd radiomeries te karteer vir grond klassifasie.

ACKNOWLEDGEMENTS

So many friends and colleagues of the Earth Science and Physics Departments and iThemba LABS aided me in the research for this dissertation and the writing hereof. Thanks to every one of you! A special mentioning to the following people:

Prof. Abraham Rozendaal, who shared the wonders of Geology with me, with whom I could share ideas concerning this project and above all who inspired and motivated me and in the last steps of the writing process helped me with insightful direction and support.

Dr. Anton Stander for his mentorship and helpful questions and insights on the content of this dissertation.

Esme Spicer, who did (and sometimes repeated) the XRF analyses on the samples.

Dr. Kobus Lawrie and Dr. Richard Newman from iThemba LABS with whom I started the Environmental Radioactivity Laboratory.

Chris Cole, who introduced me to the practicalities of Applied Nuclear Physics and with whom I could discuss radioactivity into the late hours of the night.

My parents, whose constant love and support carried me through my years as a student. Especially during this period where they saw me yet again, like in my younger days, play in the sand and having fun.

My brother, Frikkie, who made all the technical drawings seen in this dissertation and who encouraged me every now and again.

Then to the one person who came into my life halfway through this project, who encouraged me, stood by me in the good and bad times and constantly believe in me: Ange, thank you for being you!

TABLE OF CONTENTS

LIST OF TABLES

LIST OF FIGURES

“In every piece of land, in every curving beach, in every grain of sand there is a story of the earth”
(Rachel Carson)

CHAPTER 1 INTRODUCTION

Radioactivity is well known and well understood, but its usefulness in industrial applications to optimise processes or increase economic viability is not yet fully utilised by many industries. This study focuses on the measurement of natural radioactivity found in all sands and soils, particularly in the heavy mineral sand zircon and in soils from different vineyards.

The geological processes that formed zircon also caused the inclusion of the uranium and thorium radioisotopes (and as a result also their daughter products) into its crystal structure. The amounts of these radioisotopes are not significant enough to have any commercial value, however, zircon is an economically important mineral for South Africa and the presence of the uranium and thorium can be utilised in zircon beneficiation. This will be the first application of radiometry.

Soils are part of the terroir characteristics of an area and are formed through different weathering processes of the earth's crust and other materials. The measurement of the radioisotopes found in vineyard soils may be used as an alternative method for soil classification in viticulture and related industries. This will be the second application of radiometry.

1.1 OBJECTIVES

The first objective is common to both applications. In order to apply laboratory-based radiometry in the measurement of heavy mineral sands and vineyard soils, the system must be able to measure sand and soil samples with a high degree of accuracy and precision. The objective is to set-up and calibrate the radiometry detection system as to obtain a total error of less than 10 %, in all measurements, the norm in many laboratories around the world.

Radiometry has not yet been applied in any South African heavy mineral plant. The objective for the heavy mineral sand application is therefore the demonstration that radiometry may be an alternative technique for grade control of heavy mineral sands that can improve the cost benefit of the heavy mineral separation process. Characterisation of

the feeds and products of a heavy mineral separation plant will be performed by the determination of their respective ^{238}U and ^{232}Th concentrations.

The objective for the vineyard soil application is to demonstrate the applicability of radiometry as a possible useful tool in soil classification, by defining some terroir characteristics based on the measured ^{238}U, ^{232}Th and ^{40}K concentrations of soil and rock samples obtained from three Pinotage producing vineyards.

1.2 DISSERTATION STRUCTURE

The remainder of Chapter 1 describes, in brief, the histories of radioactivity and radiometry as a tool to measure natural radioactivity and present an overview of the heavy mineral zircon. The final section outlines the motivations for the heavy mineral and agriculture applications.

Chapter 2 reviews the theory behind this study. The first section includes the occurrence of radioisotopes, the different decay modes, decay chains and the derived definitions used throughout this study. The interaction mechanisms of gamma rays and their detection with the use of a semiconductor detector are briefly discussed in the second section. In the last section an overview of the X-ray fluoroscopy (XRF) technique, which was used for comparison to radiometry, is given.

The measurement methodologies of radiometry and XRF are discussed in Chapter 3. In the first section the experimental set-ups of radiometry and XRF, as well as, the measurement methodologies followed to determine the uranium, thorium and potassium concentrations in the respective samples, are discussed. It is followed by a section that describes the sampling process and sample preparations for both XRF and radiometry.

In Chapter 4, the set-up and calibration of the radiometric method for the application as a laboratory-based method are discussed. It starts with the Marinelli beaker and how the ever-present background signal is minimised. Secondly the detection parameters that could influence the results are analysed and optimised. These parameters include the calculation of the counting time, the selection of gamma rays, peak area calculation and the detector efficiency. Furthermore, radon loss is analysed and the resulting error in the

uranium concentration is estimated. The section ends with an analysis of the accuracy and precision of the detection system after all the corrections and optimisations were implemented. Finally the errors that are associated with each measurement are discussed.

Chapter 5 describes the application of radiometry in the measurement of heavy mineral sands. The first section gives an overview of the geological setting of the heavy mineral deposit. In the next section the measured radioisotope concentrations of the various feeds and products of the heavy mineral separation process are presented and discussed. It is followed by a section that investigates the effect of reducing the counting time and another that presents the results of the XRF comparison exercise. In the next section the implementation of radiometry at the separation plant is discussed. In the final section the conclusions on the use of radiometry as a heavy mineral sand application are reviewed.

In Chapter 6 the application of radiometry in the measurement of vineyard soils is described. In the first two sections an overview of the term terroir and the geological setting of Kanonkop, Simonsig and Spier are given. Thereafter the measured radioisotope concentrations of the soil and rock samples are presented and discussed. The results of the comparison exercise with XRF are also presented as well as the important findings of three ex-situ and in-situ radiometric studies of Simonsig. Finally the conclusions on the use of radiometry as a vineyard soil application are discussed.

In Chapter 7 a summary of the study together with the conclusions and suggestions for future work are given.

1.3 RADIOACTIVITY, AS OLD AS THE WORLD

The existence of radioactivity is now a common fact, but on the scale of mankind's history its discovery is very recent as it is a mere 100 years old.

In November 1895, Wilhelm Conrad Rőntgen (McGraw-Hill, 1982) studied the emissions generated by discharging electrical currents in evacuated glass tubes. After charging a cathode ray tube, he was surprised by the glow of a barium platinum-cyanide treated sheet of paper, which was used as a screen on the other side of the room. He knew that this fluorescence was not from the cathode rays he was investigating, but from some unknown

origin and so he called it "X-rays". This revolutionary discovery let to the search for more kinds of unknown rays that might exist.

During 1896, Antoine Henri Becquerel (Genet, 1995) conducted an experiment to show the thermoluminescent nature of uranium salts. He wrapped potassium uranyl sulphate tightly in black paper, placed it on a photographic plate and exposed it to sunlight. After development, the plate showed dark spots in the region where the salt was placed. He decided to repeat the experiment at a later stage and stored the photographic plate together with the uranium salt in a drawer. Days later, Becquerel developed the photographic plate before commencing a new experiment and to his surprise the same dark spots appeared on the plate. He interpreted this result with the assumption that a new type of penetrating ray, which is spontaneously released by the uranyl, exists. Later other experiments with uranium substances showed the same behaviour and he concluded that it was the uranium itself that produced these effects by the emission of, what he called, “uranic rays”.

The importance of this discovery dwindled but in 1898, two scientists Marie Sklodowska-Curie and Gerhardt C. Schmidt, independently found that thorium compounds also emitted rays similar to that from uranium. A few months later Marie and Pierre Curie discovered two new elements (radium and polonium) that exhibit the same characteristics. They concluded that these uranic rays were an atomic event that is distinctive to the element and not related to the physical or the chemical state of the element. They introduced the term "radioactivity" for this new phenomenon. In the years to follow, not only were two new types of emission radiation found: alpha rays (later to be identified as helium atoms) and beta rays (later to be identified as electrons), but many more naturally occurring radioactive elements were discovered from investigations of soils and rocks. Amongst these were potassium and rubidium, which were previously considered stable elements. Based on this evidence that the phenomenon was not only applicable to uranium compounds but to a whole range of elements, the uranic rays were thus renamed to gamma rays.

In 1900 Becquerel returned to the scene with his experiments that showed that radioactive elements could still emit rays of undiminished intensity, for years without any energy being supplied. Soon after, the Curies published their observation that radium is always at a higher temperature than its surroundings. Their measurements showed a heating effect of 100 calories per hour per gram of radium. This evidence of a large store of energy in a

small amount of matter caused a stir in the physics realm (later seen in the works of Albert Einstein) and also in earth sciences.

Lord Kelvin aired the view that the earth's internal heat resources were obtained from the sun during the formation process of the solar system and therefore diminishing. This hypothesis was shattered after R.J. Strutt discovered radium in a large variety of common rocks. Together with the Curies' measurements of the amount of heat generated by radium, it showed that due to the energy released by radioactive decay, it is possible for the earth to have its own constant source of heat. This forever changed the way geologists viewed the formation and age of the earth (Durrance, 1986). Natural radioactivity became a new way of discovering the world.

Today natural radioactivity is again the focus point as its existence now proves useful in many physics, geology and mineral processing applications.

1.4 RADIOMETRY

Radiometry is the measurement of radiation. This radiation can be any one of the different types e.g. alpha particles, gamma rays or X-rays. Different techniques exist by which this radiation is measured, either in a laboratory or in the field. Examples are gamma spectroscopy, X-ray fluorescence and neutron activation. These techniques are further divided into two groups: active and passive depending on the origin of the radiation source. Active techniques involve the use of a manmade radiation source to measure the net effect of the radiation on the material that is investigated. Passive techniques rely on the natural radioactivity emitted by the material for the investigation. In this study radiometry is defined as the measurement of gamma rays emitted by the natural radioactive elements ^{40}K, ^{232}Th and ^{238}U found in all sands and soils.

A gamma energy spectrum is characteristic of the radioisotopes present in a sample. The intensities of the different gamma rays relate directly to the amount of that particular radioisotope found in the sample. This concentration depends on its mineral composition and origin. Different types of minerals and sediments can therefore be characterised based on its radioisotope concentrations.

Over the past decades the above-mentioned knowledge has been utilised in various applications. Examples include: geophysical well logging, geological mapping (IAEA, 1976a), exploration for uranium (IAEA 1976b) or other minerals (Tsoulfandis, 1983) and the subsequent recovery of mineral resources (Clayton, 1983), and environmental monitoring (Klusoň, 2001). For the latter is gamma radiometry using natural radioactivity the general choice in the determination of the radiological impact on humans from building materials (Amrani and Tahtat, 2001), (Khan and Khan, 2001), regions of land (e.g. Um-Greifat area in eastern desert of Egypt (Nada, 2003) or the granitic plutons in Eskisehir, Turkey (Örgün et al., 2005) or mine dumps (Lindsay et al., 2004).

Passive gamma radiometry is not commonly used in the field of mineral processing but applications do exist. These applications are: the determination of the aluminium content in iron ore (Killeen, 1997) based on the association with koalinitic material (that correlates with the thorium content in Australian ore) and the determination of the manganese content in iron (Killeen, 1997) (correlated with the potassium content). It is also used in the ore preparation phase to distinguish between waste rock and mineral rock (Chanturiya, 2001) or estimate the grade of uranium ore (Killeen, 1997). Phosphorus and tin/tungsten deposits have also been assayed using their association with uranium (Killeen, 1997). The determination of the ash content in coal (an economic and application-specific indicator), normally done with active techniques, is now also being performed using the passive gamma ray technique (Álvarez and Vivero, 2002) during the plant feed preparation phase and shipping phase. This study intends to extend this application list to include the mineral processing of heavy mineral sands.

The Nuclear Geophysics Division (NGD) of the University of Groningen started in 1980 to study sand transport and sediment characteristics using natural radioactivity. One of these studies was to determine whether heavy minerals are found along the Dutch coast (De Meijer et al., 1988) and if so then also to investigate the feasibility of mapping the region radiometrically. The latter would gather information on the physical processes that influence sand transport along the coast. Exposure rates were determined and it was observed that in the presence of heavy minerals the exposure rates are higher . This then lead to the observation that there are radiometric differences between glacial and fluviatile sands. This aided their understanding of the sands origins and transport. Further research included other locations as well e.g. beaches of the island of Texel. Differences in the radioactivity level were again observed (Greenfield et al., 1989), which indicated that the

method of radiometric mapping is sensitive enough to study sand transport processes (De Meijer et al., 1988). Comparisons between the results of different locations also indicated that the heavy mineral composition of the sands had differences (De Meijer et al., 1990). This led to the idea of a radiometric fingerprint, which is a characteristic set of ^{238}U, ^{232}Th and ^{40}K concentrations that belong to a specific sediment type.

In all these studies were the locations mapped by gathering samples and measuring them individually on a high purity germanium detector in a laboratory set-up. To map large areas more efficiently NGD developed in co-operation with the British Geological Survey (Jones, 2001) a detector which could be towed on underwater surfaces. This MEDUSA (multi-element detector system for underwater sediment activity detection) detector was first used in 1994 to map a part of the seafloor north of the Dutch island Ameland. Other locations (e.g. Baltic coast) soon followed which aided the investigation in the determination of sediment composition with the use of radiometric fingerprinting (De Meijer and Donoghue, 1995). This in-situ measurement method proved its usefulness in a study of the dispersal and transport of dredge soil from the Rotterdam harbour to a new disposal site (Venema and De Meijer, 2000). By monitoring the situation regularly with the MEDUSA system an optimal site location was determined. Continual improvement to this radiometric methodology and its applications is also seen from recent surveys (Van Wijngaarden et al., 2002).

Amidst the above-mentioned research another type of application, that of mineral processing, came to the surface. In 1996 a geological study to describe a heavy mineral deposit at the Geelwal Karoo, was undertaken by Macdonald (Macdonald, 1996). For this small stretch of the west coast of South Africa he showed that the variations in zircon content are related to the variations in the uranium concentrations. Besides an indication of origin it meant that the uranium concentration is in principle a telltale of the amount of zircon or purity of zircon in the sand. This was taken further by De Meijer and Rozendaal (De Meijer et al., 1997a), (De Meijer et al., 1997b). They demonstrated that there exists a large variation in the radiometric properties of the South African sediments and that the possibility existed to determine the mineral composition with radiometry.

1.5 ZIRCON

1.5.1 Overview

Zirconium is the 18th most abundant element on Earth. In nature it is found mostly as zircon ($ZrSiO_4$) but also as baddeleyite (ZrO_2). Zircon has a tetragonal crystal structure, poorly developed cleavage directions and a density of 4.7 g/cm^3. The density will categorise it as a heavy mineral. These are per definition minerals with densities larger than 2.9 g/cm^3. It is a very tough and resistant mineral with a hardness factor of 7.5-8.0 on the Mohs scale (in comparison it is harder than quartz (7) but softer than diamond (10)). It also has an extremely low chemical reactivity, very high refractive index of 1.80-1.98 and a melting point over 2500 °C. It has been classified as the toughest mineral on earth (Mange and Mauer, 1991). Its mineral chemistry is relatively simple ($ZrSiO_4$) but substitution of zirconium by hafnium, thorium, uranium, rare earth elements and a diversity of trace elements is a common feature. Metamict zircons may host significant concentrations of uranium and thorium resulting in the radioactive destruction of the crystal lattice.

Zircon occurs as small, square, prismatic crystals or grains as an accessory mineral in a wide variety of sedimentary, metamorphic and granitic and syenitic igneous rocks. In the rock formation it is not generally suitable for commercial mining. However, weathering and subsequent transportation by fluvial and Aeolian processes produces a natural separation of heavy and light minerals and the formation of large alluvial placer deposits found mostly alongside fluvial and coastal areas. These placers contain enhanced levels of zircon and other heavy minerals such as rutile, ilmenite, monazite, garnet, kyanite and staurolite.

1.5.2 Commercial uses

Zircon is worldwide in demand with a consumption of more than a million tonnes per year (USGS, 2007). It is used in a wide range of industrial applications and products that include amongst others: as a pigment in colours and glazes in tableware, tiles, sanitary ware (which in addition also improve the lustre, hardness and smoothness of these products) as well as an opacifier for ceramic products, for furnaces where zircon bricks are used to hold molten metals and glass, for facings on foundry casts and to coat surfaces of moulds, corrosion resistant agent in piping for chemical processes, a constituent of various specialty alloys, heat exchangers, nuclear fuel shielding (as it has a low absorption cross

section for neutrons), fibre optics, and also used in the glass substrates of liquid crystal and plasma displays. The main commercial uses of zircon is summarised in Table 1 (TZ Minerals Int., 2003a) and its relative consumption by different regions in the world is summarised in
Table 2 (TZ Minerals Int., 2003b).

Table 1 ***Summary of the main commercial uses of zircon.***

Commercial Use	**Proportion of Total (%)**
Ceramics	49
Foundry sands and mould washes	17
Refractories	16
Feedstock for production of zirconia and other zirconium compounds	9
Cathode ray tubes, liquid crystal and plasma displays	8
Other	1

Table 2 ***Summary of the relative consumption of zircon by region.***

Region	**Relative consumption (%)**
Europe	36
China	20
North America	14
Asia-Pacific	14
Japan	7
Rest of the world	9

1.5.3 Impurities in crystal lattice

Although zircon is very sought after, its market value is influenced by the amount of impurities, in the form of elements other than zirconium, silicon and oxygen, found in its crystal lattice.

Zircon has a stoichiometric composition of 67.2 wt % ZrO_2 and 32.8 wt % SiO_2. The structure of zircon contains two cation sites: the distorted 8-coordinated Zr-site and the 4-coordinated Si-site. Both Zr and Si are tetravalent and have ionic radii of 0.26 Å and 0.84 Å, respectively. This structure has structural voids that are potential sites for impurities provided that these sites can accommodate interstitial ions without excessive structural strain. These impurities are introduced in the crystal lattice through the processes of simple or coupled substitution. In these substitutions a large number of elements such as Fe, Al, rare-earth elements Sc, Y, P, U, Th replace the Zr and Si during the crystallisation of the zircon from a silicic magma while keeping the overall charge constant. Examples are ("=" means substitutes for):

Simple substitution mechanisms:

- Hf^{4+}, U^{4+}, Th^{4+}, Ti^{4+}, Sn^{4+} = Zr^{4+}
- $(OH)_4 = SiO_4$

Coupled substitution mechanisms:

At one structural site:

- $(Y, REE)^{3+} + (Nb, Ta)^{5+} = 2\ Zr^{4+}$

At two structural sites:

- $(Y, REE)^{3+} + P^{5+} = Zr^{4+} + Si^{4+}$
- $Sc^{3+} + P^{5+} = Zr^{4+} + Si^{4+}$
- $M^{n+} + n(OH)^- + (4-n)H_2O = Zr^{4+} + (SiO_4)^{4-}$

(where *M* is a metal cation and *n* is an integer)

At an interstitial site:

- $(Mg, Fe)^{2+}_{(int)} + 3\ (Y,REE)^{3+} + P^{5+} = 3\ Zr^{4+} + Si^{4+}$
- $(Al, Fe)^{3+}_{(int)} + 4\ (Y,REE)^{3+} + P^{5+} = 4\ Zr^{4+} + Si^{4+}$

The combined concentrations of these impurities can range from trace amounts to percentage levels. In this manner the quality of the zircon is compromised. For example, the typical composition of premium grade commercial zircon sand used for ceramic opacifier applications is 66 % ZrO_2, 32 % SiO_2, 0.1 % TiO_2, 0.35 % Al_2O_3 and 0.05 % Fe_2O_3. More iron will tend to give the zircon a red to orange colour, which negatively influence the opacity properties.

Uranium and thorium can be hosted within the zircon crystal lattice. The removal of uranium and thorium is therefore not easily accomplished without the destruction of the crystal lattice. Since the concentrations of these elements can range from tens to thousands of parts per million they introduce another problem, that of radiation.

Due to international environmental impact regulations and public dose limits, the level of radioactivity from a radiation source (in this case zircon sand) must be within certain limits. Thus the lower the concentration of uranium and thorium in the zircon, the higher is its demand and hence the higher the selling price. Typically the prime zircon product provided by the Exxaro Namakwa Sands mine along the west coast of South Africa contains less than 500 ppm U+Th. Their lower quality zirkwa product contains less than 1000 ppm U+Th.

1.6 MOTIVATION

1.6.1 Motivation for Heavy Mineral application

In South Africa the mining industry is the largest industry sector, followed by manufacturing, oil and gas, chemicals, agriculture and tourism (Dept. of Minerals and Energy, 2009). In 2007 South Africa's total primary mineral sales amounted to R 223.9 billion (Dept. of Minerals and Energy, 2008) of which R 4.76 billion (2.1 %) was contributed by zircon sales.

South Africa is the second largest producer of zircon in the world, with a total of 395 kT per year for 2009 (USGS, 2009). That is just over 32 % of the total world production of 1.23 Mt (USGS, 2009), which for the past several decades increased steadily (Figure 1). Australia produced 510 kT and China 140 kT over the same period. South Africa also has the second largest reserve of available zircon (14 Mt), making zircon a viable source of income for several years to come. The world reserve and production values are tabulated in Table 3.

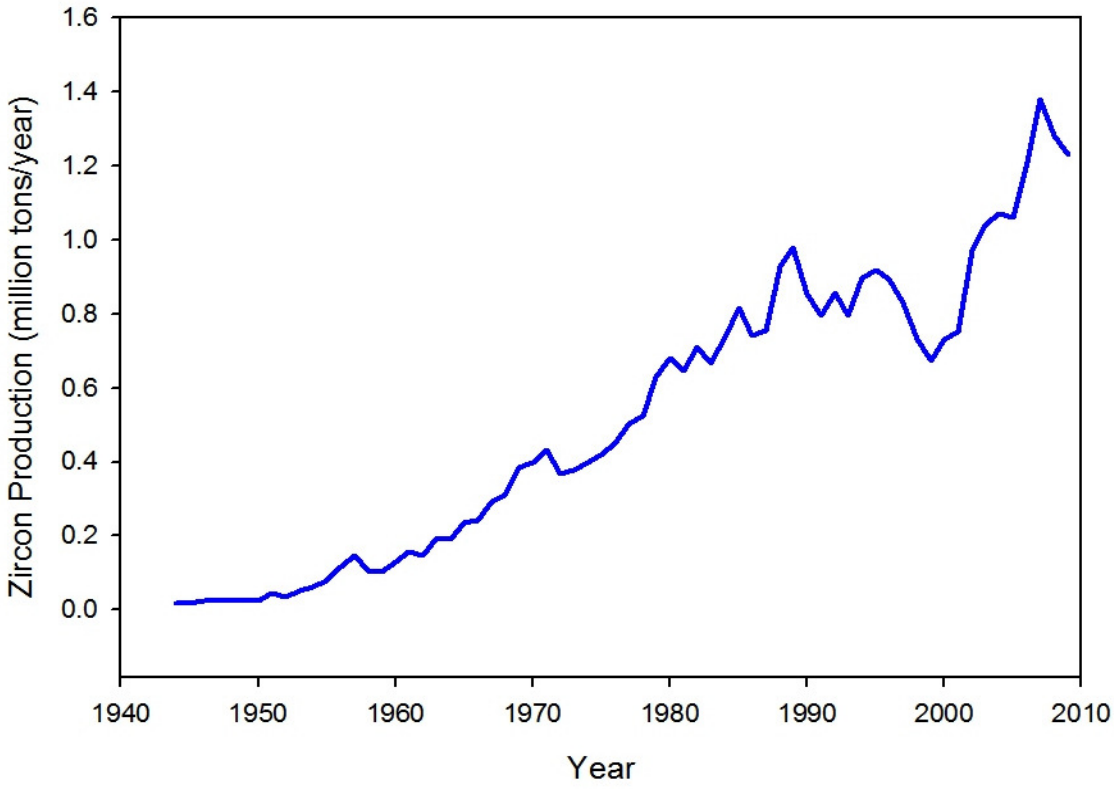

Figure 1. ***The total world production of zircon, from 1944 to 2009.***

Table 3 ***World production and reserves of zircon for and at 2009*****.**

Country	Production (kT) for 2008	Production (kT) for 2009	Reserves (Mt)
South Africa	400	395	14
Australia	550	510	25
Brazil	27	27	2.2
China	140	140	0.5
India	30	30	3.4
Indonesia	42	42	Data not available
Ukraine	35	35	4.0
United States	Data not available	Data not available	3.4
Other countries	58	48	3.5
World Total (rounded)	**1280**	**1230**	**56**

The demand-supply balance for the zircon market is marginally negative, with supply lagging behind the demand (Dept. of Minerals and Energy, 2009). To worsen the situation a United States forecast suggests that the consumption of zircon will grow by an average of 3.8 % per year through 2015, while the increase in production will perhaps not be so much (USGS, 2009). This supply gap will positively influence exploration for zircon and improvement of the beneficiation process. The timing of this study is therefore critical and the results could contribute to the improved recovery of zircons and supply to the market.

The international market accepts only zircon products that adhere to the strict requirement of a very low amount of impurities. Besides the amounts of the main impurities Fe_2O_3 and TiO_2 plays the amount of radioactivity (this is the total uranium and thorium concentration) also a role in the classification of zircon products. Prime grade and first grade products all have a limit of less than 500 parts per million uranium plus thorium. (A summary of these types of zircon products and their specifications is tabulated in Table 4 (Strydom, 2009)). This is an international safety regulation which was placed on all zircon products that will be used in applications where members of the public can be exposed to radioactivity or radiation.

Table 4 ***Specifications for prime grade and first grade zircon products.***

Product	Fe_2O_3 % max	TiO_2 % max	ZrO_2 % min	U + Th ppm max
Zircon Opacifier Grade	0.06	0.10	65.0	475
Zircon Prime Grade	0.10	0.15	65.0	500
Zircon Uncalcinated Grade	0.10	0.15	65.0	500
Zircon Standard Grade	0.25	0.30	65.0	500
Zircon Intermediate Grade	0.15	0.30	65.0	500
Zircon Refractory Grade	0.15	0.65	65.0	500
Zircon Foundry Grade	0.35	0.80	60.0	500

However, Exxaro Namakwa Sands, a South African mining company also produces another product called zirkwa. The product specifications are somewhat relaxed due to the specific application of this type of zircon. The specifications for this second grade product

are given in Table 5 together with the specifications for their prime product (Van Zyl, 2009). Of importance is the total uranium plus thorium content that must be below 1000 parts per million.

Table 5 ***Specifications of the prime grade zircon and zirkwa (second grade) of Exxaro Namakwa Sands.***

Product	Fe_2O_3 % max	TiO_2 % max	Al_2O_3 % max	$ZrO_2 + HfO_2$ % min	U + Th ppm max
Zircon Prime Grade	0.06	0.12	0.35	66.0	500
Zirkwa (Second Grade)	0.20	0.70	Not given	64.0	1000

All of the mentioned zircon products have the same thing in common: if they fall within specification they can be sold (e.g. all the prime and first grade zircon products sell currently for more or less $ 800 per ton while the zirkwa sells for approximately 25 % less). Any other zircon product that falls outside the mentioned specifications is not accepted by the market and therefore worthless.

This is the typical dilemma. A mining company, like Exxaro Namakwa Sands, cannot sell all the zircon it produces since some of the product falls outside the mentioned specifications. This is highlighted in a study done by Philander (Philander, 2001) where analyses by means of LA-ICP-MS were done on a random selection of single zircon grains of the Exxaro Namakwa Sands mine. The results for the amount of Fe_2O_3 against the total radioactivity concentration are shown in Figure 2.

This figure depicts the grains that, based on their specification qualify for the two marketable grades of zircon product (isolated by the black frames) in relation to the specifications of all the other grains. The prime zircon product is 50 % of the total and 70 % of the total can be classified as zirkwa. There still remains a portion of the population of the total zircon resource that is rejected based on the uranium plus thorium content despite meeting the specifications for the other penalty elements.

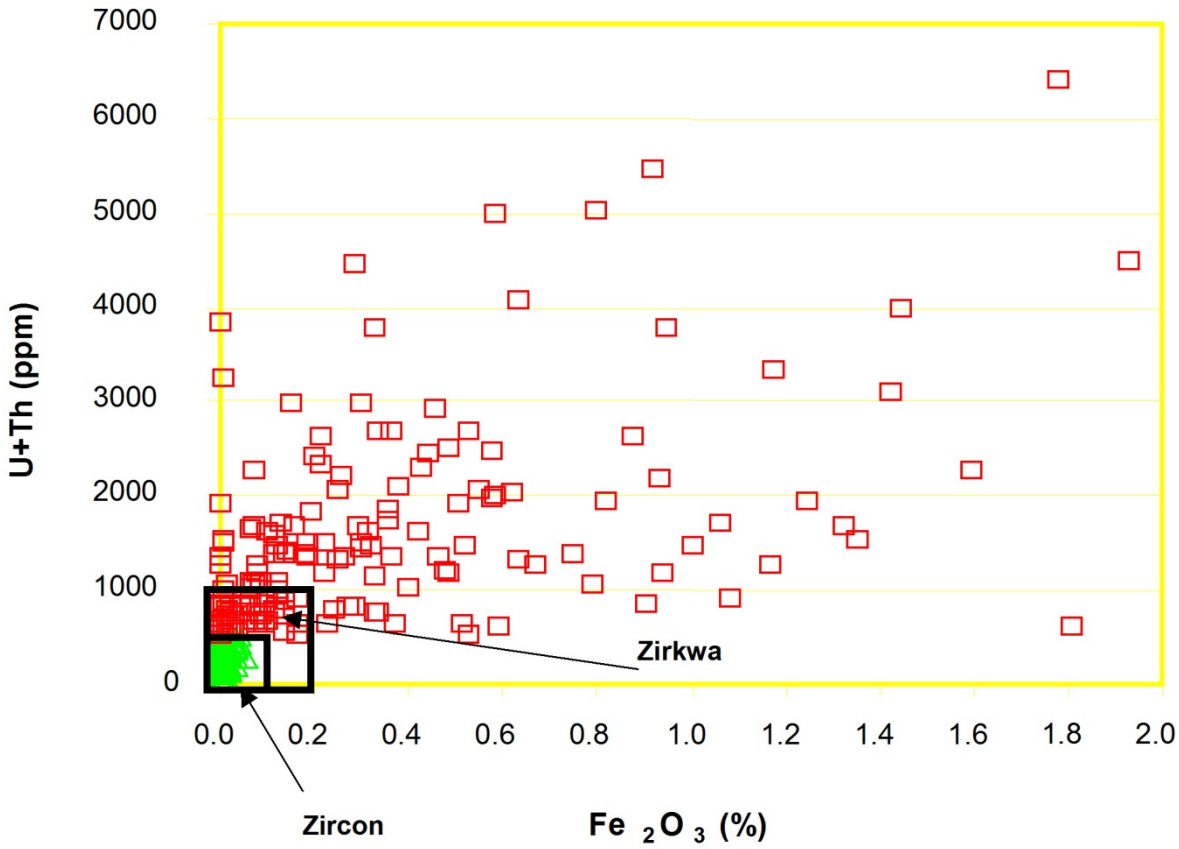

Figure 2. ***The Fe_2O_3 and U+Th specifications of a random sample of zircon grains from the Exxaro Namakwa Sands mine.***

Because of the strict international regulations and quality control by customer demand, grade is based on the total concentration of uranium and thorium for zircon. At present the concentration of uranium and thorium in zircon concentrates is measured on a whole rock basis by XRF during and at the end of the processing cycle before the final product is ready to be shipped.

This is not an ideal situation as these grab samples are taken periodically and are not necessarily representative of the stream or final assignment. The frequent poor correlation between a spot check by the customer at the harbour and the product ex Namakwa sands has resulted in significant losses by the producer. It is obvious that good grade control is imperative for any resource based operation and a continuous sampling method would be the ideal. In addition, the turnaround time for XRF analyses results is more than 24 hours and is not ideal for controlling a continuous process.

The solution is to accurately measure the uranium and thorium concentration fast or immediately. Preferably the measurements must be made online and in real time. This can be done during the various stages of the mineral separation process. It will allow for the identification of potential reject products throughout the entire beneficiation process. By doing this, products that fall outside specified limits can be rerouted back to a specific separation process or discarded immediately. In this way resources can be fully utilized and a product is generated that will comply with international regulations.

The application of radiometry has not been done before at any South African heavy mineral separation plant. For this reason this study suggests radiometry as an easier and cheaper alternative to effectively implement grade control for zircons. Although XRF measures the uranium and thorium concentration directly, the gamma ray intensities can also quantify the concentration of the amount of these elements in the sample. The end result of radiometry could be similar to that of XRF. As gamma rays are emitted continuously, radiometry could also be used as an online application. Although this study focuses on the experimental offline radiometry technique in order to prove that it is a valid alternative, the general benefits of radiometry apply for both. As such is a radiometry detector system not nearly as costly as a XRF system. For the offline measurement the sample preparation is easy and a larger more representative sample taken from the original product can be analysed. For the online measurement no sample preparation is needed as detectors can be set-up at various points along the processing path. This include before, during and after separation stages. In this way large volumes of product can be analysed. Since the concentration levels are recorded in real time, monitoring of the system is much easier. Processing decisions can then be implemented quickly to optimise the final product.

1.6.2 Motivation for Agriculture application

Land use profoundly influences the productivity of a piece of land and the condition of the land for future utilisation. It also impacts positively or negatively on the economy of a country. Eighty percent of South Africa's land surface area is used for agriculture (CSIR, 2000). However, only about 13% can be used for growing crops, and then just 22% of this area can be classified as high-potential land (Wikipedia, 2010).

Wine farms form part of this high-potential land. About 4500 grape producers have 103 300 hectares of land under cultivation, making South Africa the 20th largest wine growing area in the world. This area produces a wine harvest that ranks South Africa seventh in the world (Nations Encyclopedia, 2010). In financial terms this means that the wine industry contributes in the order of 2.2% to the South African gross domestic product (SAInfo, 2010). The export of grapes forms about 3% of South Africa's total earnings from agricultural exports (Wikipedia, 2010). Given that vine estates have limited area for expansion, the optimal use of the land is crucial in order to keep up the production and the revenue.

Land use, for a viticulturist, means the creation and maintaining of vineyards. A successful vineyard is a long term and expensive investment and its yield and quality will be influenced by many factors. Amongst these factors are the type of soil, viticultural preparations and the climate of the region. Understandably plays soil an important part in the growth and production of vines. The soil type may be related to the geology of the area or it could have been transported from elsewhere. Reworking of the soil or the use of fertilisers could have changed the characteristics of the soil so much that it is chemically different from its original state or the state of a previous season. It is therefore important to characterise vineyard soils based on properties such as pH of the soil, trace element concentrations, grain size and clay content (Van der Merwe, 2001) as to optimise land use with respect to vine cultivar, wine quality and production.

Soil type and soil characteristics are conventionally determined with chemical and elemental analysis methods, for example XRF. While these methods are time consuming and expensive it does provide information on all the elements found in the particular soil. Amongst these elements are uranium, thorium and potassium. They are of interest as they have radioisotopes that are also found in the soil. The measurement thereof is relatively easy with radiometry. Depending on the type of information that is needed can radiometry be applied in a laboratory or in-situ. The latter also has the advantage that large areas can be mapped fairly quickly when the detector setup is attached to a vehicle. For this reason radiometry is suggested as a possible tool for soil classification.

Of course for radiometry to be considered an alternative tool for soil classification various investigations need to be done to prove its worth. As a pilot study it was the aim to investigate whether it would be possible to link the radiometric character of a soil to the soil

type found at three different wine estates. Specifically the relation between the ^{40}K concentration and the clay content of the soil will be considered. The possibility of linking geology and soil type may assist in the further understanding of the influence of terroir on different regions. For this reason the relation between the uranium and thorium concentrations and the geologies of the three sites are also regarded. Furthermore, the radiometry results of the three radioisotopes will be compared to those obtained with XRF in order to obtain a correlation between the two methods.

Since the start of this study correlations between the natural radioisotope concentrations in vineyard soils and vine-growth potential were investigated (Modisane, 2005) as well as the feasibility of using radiometry as an alternative for determining the physico-chemical parameters in vineyard soil (Mlwilo, 2010) (these studies will be discussed in Chapter 6). These studies and the results of this one will bring the usefulness of radiometry as a tool to aid decision making on land use in viticulture one step closer to being a reality. It may also lead to its application in other agricultural sectors for their benefit.

CHAPTER 2 THEORY

In this chapter radiometry is discussed in terms of radioactivity and gamma ray detection. Radioactivity is explained by investigating the structure of matter and different radioactive decay modes. By introducing definitions, such as activity, the concept of radioactive decay for a single radioisotope is introduced and expanded to include many radioactive products. The three special cases of parent-daughter activity are also explained. The section rounds off with a brief overview of radioactivity found in nature. The next section is a discussion on gamma ray detection and starts with the three gamma ray interaction mechanisms with matter. These are then linked to the linear and mass attenuation coefficients. The general properties of radiation detectors, highlighting resolution, efficiency and dead time are explained. It is followed by an overview of a semiconductor detector and the spectral features of a gamma ray spectrum. The minimum detectable activity, a parameter of the gamma ray spectrum is also mentioned. In the last section the physical principles of X-ray fluorescence (XRF) and its analysis method are described.

2.1 RADIOACTIVITY

2.1.1 Structure of Matter

The building blocks of matter are atoms. According to the Rutherford-Bohr model of an atom it consists of protons, neutrons and electrons. The protons together with the neutral neutrons form the positively charged nucleus with the negatively charged electrons surrounding it. An element's chemical properties are determined by the number of electrons. In an electrically neutral atom the electrons are equal to the number of protons per atom, called the atomic number, Z. The mass number or A is the number of protons plus neutrons in an atom ($A = Z + N$).

The atomic number of a specific element is fixed but the mass number can vary. This means that there are substances that have the same chemical properties, but differ in the number of neutrons. These are referred to as isotopes. There are more than 2000 known isotopes, some naturally occurring and the vast majority produced in accelerator laboratories and nuclear reactors. Of this total only 266 are stable isotopes. The rest is unstable or radioactive and referred to as radioisotopes.

The stability of the nucleus is determined by three types of forces: the strong force, electromagnetic force and the weak force. The strong force is an attractive force that acts between protons and neutrons and has a very short range. The electromagnetic force is either attractive or repulsive and has a long range. The weak force also has a short range and acts between leptons and baryons.

Plotting neutron number against atomic number of all the isotopes emphasise the symmetry in the protons and neutrons displayed by stable isotopes. For most (159) of the stable isotopes N and Z are both even numbers while only four stable isotopes have both N and Z uneven values. This is the result of the pairing force that exists between pairs of protons or neutrons with opposite spins. It also hold true that for $Z \leq 20$, $N \approx Z$ and for Z above 20, $Z < N$. In the first case is the nucleus small and as a result are the protons and neutrons close to each other. This configuration ensures that the strong force dominates the electromagnetic force. In the second case is the effect of the increased electrostatic repulsion of the protons compensated for by adding more neutrons than protons thus maintaining stability by the increased nuclear force between the neutrons.

The unstable radioisotopes lie on the outer boundary of the two sides of the band of stable isotopes. They have either too many protons for the number of neutrons or too many neutrons for the number of protons. Heavy nuclei, with more than 83 protons, are always unstable irrespective of their proton to neutron ratio. In all these cases the long-ranged Coulomb repulsion (electromagnetic force) that acts between the protons dominates the strong force. All unstable isotopes will spontaneously disintegrate or decay to form a stable isotope or a radioisotope with a proton to neutron configuration that is closer to stability. This process of reaching stability is radioactivity and the energy or particles emitted during this process is called radiation. The radiation can be gamma rays, neutrons, alpha particles, beta plus particles, beta minus particles and neutrinos.

2.1.2 Radioactive Decay Modes

A radioisotope can undergo radioactive decay by means of several radioactive decay modes. In some cases several of these decay modes may occur one after another, while in others the radioisotope has the possibility to decay in one of two different ways. For this reason every radioisotope has a decay scheme that describes the processes that are

applicable to that specific radioisotope. For example, ^{40}K can either decay by electron capture or beta minus decay. Its decay scheme is depicted in Figure 3.

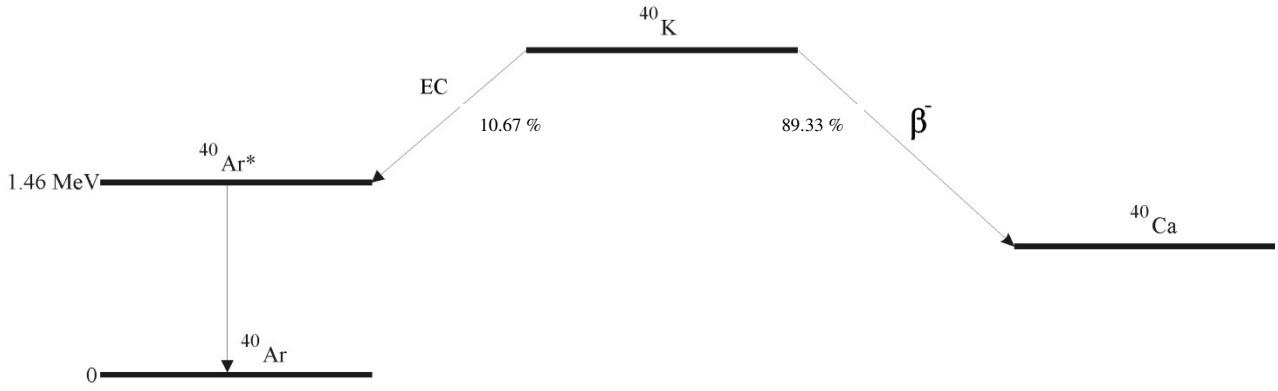

Figure 3. ***The decay scheme of ^{40}K.***
The decay scheme depicts the two different decay modes (beta minus decay and electron capture) by which ^{40}K can decay. The excited ^{40}Ar* decays to the ground state of ^{40}Ar by the emission of the 1.46 MeV characteristic gamma ray.

Given that the nucleus consists of protons and neutrons implies that radioactive decay can either increase or decrease the proton to neutron ratio. The different decay modes whereby radioisotopes reach stability are alpha decay, beta minus decay, beta plus decay, gamma ray emission and spontaneous fission.

Alpha decay

Alpha decay is the most probable decay mode for heavy radioisotopes (mass number greater than 150) that is proton-rich i.e. nuclei having a high proton to neutron ratio. Symbolically it can be represented by

$$ {}^{A}_{Z}X \rightarrow {}^{A-4}_{Z-2}Y + {}^{4}_{2}\alpha + Q, \qquad 2.1 $$

where *X* and *Y* are the parent (initial) and daughter (final) radioisotopes and *Q* the decay energy. The nucleus ejects an alpha particle (2 protons and 2 neutrons). The decrease by 4 in the mass number results in a lighter nucleus with an atomic number of 2 less than the original radioisotope. The daughter radioisotope is often unstable or left in an excited energy state. In these cases it may decay further or reach the ground state by emission of a gamma ray. Since energy and mass are conserved in the decay process, the decay energy is equal to the differences in masses of the initial and final radioisotopes. It is

shared between the daughter radioisotope and the alpha particle. As a consequence is alpha decay only possible if the decay energy is positive.

Beta decay and electron capture

Radioisotopes of mass number smaller than 150 decay predominantly by beta decay. In beta decay the nucleus corrects the excess of neutrons or protons by converting a neutron into a proton or vice versa with the weak force. Three types of transitions are possible.

Radioisotopes having an excess of neutrons undergo beta minus decay with the emission of an electron. This type of decay is visualised as a conversion of a neutron into a proton and a negative beta particle,

$$n \rightarrow p + \beta^- + \bar{\nu}\,, \qquad 2.2$$

with $\bar{\nu}$ an antineutrino. In this decay the mass number remains the same, while the atomic number increases by 1,

$$^{A}_{Z}X \rightarrow {}^{A}_{Z+1}Y + \beta^- + \bar{\nu} + Q\,. \qquad 2.3$$

The decay energy is the maximum energy that the beta particle and the antineutrino may possess and is shared between them. Since the energy contribution to each is not fixed the beta particle can have a broad spectrum of energies, unlike the discrete energies of the alpha particles.

In contrast to beta minus decay, occurs beta plus decay with radioisotopes having an excess of protons. A positron (i.e. a positive beta particle) is emitted after the conversion of a proton into a neutron,

$$p \rightarrow n + \beta^+ + \nu\,, \qquad 2.4$$

with ν a neutrino. Similar to beta minus decay remains the mass number unchanged, but the atomic number decreases with 1,

$$^{A}_{Z}X \rightarrow {}^{A}_{Z-1}Y + \beta^+ + \nu + Q\,. \qquad 2.5$$

As in beta minus decay is a neutrino emitted concurrently with the positron and shares the decay energy. Thus positrons may also possess a broad spectrum of energies from zero to the maximum.

In the event that beta plus decay is not energetically possible, the nucleus captures one of its own orbital electrons and a proton is converted into a neutron and a neutrino,

$$p + e \rightarrow n + \nu, \qquad 2.6$$

thereby decreasing the atomic number by 1 while the mass number remains unchanged. Due to the formation of a vacancy in one of the inner electron shells, characteristic X-rays are produced during electron de-excitation between atomic energy levels. The released energy can also be transferred to one of the outer shell electrons, resulting in the ejection of the electron from the atom (called Auger electrons).

Gamma ray emission

After certain decay processes a nucleus can still be in an excited state. To become stable it decays to a lower state by the release of a gamma ray. The energy of the gamma ray is the difference between the two nuclear states and is characteristic to the particular radioisotope. Gamma ray emission changes neither the atomic number nor the mass number.

Spontaneous fission

The last type of decay process is that of spontaneous fission. Fission occurs in nuclei of mass number 230 or more. After the absorption of a neutron the fissionable nucleus splits into two fragments while a few neutrons and gamma rays are also emitted.

2.1.3 Radioactive Decay

In the simplest case of radioactive decay a radioisotope can transform from unstable to stable using one of the mentioned decay modes,

$$\mathrm{A} \xrightarrow{\lambda} \mathrm{B(stable)},$$

with λ the decay constant for radioisotope A to decay to isotope B. The decay constant of a nuclide is defined as the probability that a particular nucleus will decay during one second.

Consider a sample of *N* radioactive nuclei with a decay constant of λ. The number of decays, *dN*, in a time interval *dt* is known as the activity, *A(t)*. It is expressed by

$$A(t) = -\frac{dN}{dt} = \lambda N \,. \qquad 2.7$$

Assuming that the decay constant is independent of *t,* Equation 2.7 can be solved by integration. If there were *N(0)* radioactive nuclei at *t = 0,* while *N* radioactive nuclei remain at time *t = t,* the number of nuclei at any time *t* is expressed by

$$N(t) = N(0)e^{-\lambda t} \,. \qquad 2.8$$

Substituting Equation 2.8 in Equation 2.7, the activity can be written as

$$A(t) = \lambda N(0)e^{-\lambda t} = A(0)e^{-\lambda t}, \qquad 2.9$$

with the unit of Becquerel (Bq).

To normalise activity values for different masses of sample, the activity is divided by the mass of the sample. This is defined as the specific activity and is expressed by

$$S_A = \frac{A(t)}{m}, \qquad 2.10$$

with the unit of Bq/kg. Since the definition of concentration, *C*, (with the units of parts-per-million (ppm)) is more often used in industry, specific activity values were converted to those of concentration by the following relations (Appendix A):

1 ppm U = 12.35 Bg/ kg ^{238}U, 2.11

1 ppm Th = 4.10 Bq/ kg ^{232}Th , 2.12

1 ppm K in KCl = 0.0302 Bq/ kg ^{40}K and

1 ppm K in K_2O = 0.0251 Bq/ kg ^{40}K 2.13

2.1.4 Decay Constant and Half-life

From Equation 2.9 the activity decreases exponentially in time. The average time required for a radioactive sample to decay to one half of its original activity is defined as the half-life, $T_{1/2}$. The relation between half-life and the previously mentioned (section 2.1.3) decay constant is

$$T_{1/2} = \frac{\ln 2}{\lambda}. \qquad 2.14$$

2.1.5 Radioactive Series Decay

Section 2.1.3 described the easiest case of radioactive decay. However, in many cases the daughter product is also radioactive and has to decay to form a stable isotope,

$$\mathrm{A} \xrightarrow{\lambda_A} \mathrm{B} \xrightarrow{\lambda_B} \mathrm{C(stable)}.$$

If the decay constants for the two decays are λ_A and λ_B, the number of radioactive nuclei, N_A and N_B, at any time are

$$-\frac{dN_A}{dt} = \lambda_A N_A, \qquad 2.15$$

$$\frac{dN_B}{dt} = \lambda_A N_A - \lambda_B N_B . \qquad 2.16$$

In Equation 2.16 the first term represents the rate at which B increases due to the decay of A, while the second term represents the decay rate of B. With $N_A=N(0)_A$ and $N_B(0) = 0$ at $t = 0$ the solutions for Equations 2.15 and 2.16 are

$$N_A = N(0)_A e^{-\lambda_A t} \qquad 2.17$$

and

$$N_B = \frac{\lambda_A}{\lambda_B - \lambda_A} N_A(0)(e^{-\lambda_A t} - e^{-\lambda_B t}). \qquad 2.18$$

The activity of A is similar to Equation 2.9 while the activity of the daughter product B is

$$A_B = \lambda_B N_B = \frac{\lambda_B}{\lambda_B - \lambda_A} A_A(1 - e^{-(\lambda_B - \lambda_A)t}) . \qquad 2.19$$

Very often the daughter undergoes many decay events (granddaughters) before stability is reached,

$$\mathrm{A} \xrightarrow{\lambda_A} \mathrm{B} \xrightarrow{\lambda_B} \mathrm{C} \xrightarrow{\lambda_C} \mathrm{D} \xrightarrow{\lambda_D} \ldots ,$$

and is called a decay series. Equations 2.9 and 2.19 that refer to one and two decay products can therefore be expanded to include any number of decay products.

Consider a decay chain that starts with a parent A that has $N_A(0)$ nuclei at $t = 0$ and its decay products B to N are all zero. The number of nuclei of radioisotope N at any time t will then be expressed by the integral of

$$\frac{dN_N}{dt} = \lambda_M N_M - \lambda_N N_N \qquad 2.20$$

where N_M describes all the preceding decay products and is calculated from a series of Equations similar to Equation 2.20. Bateman showed that the solution for Equation 2.20 is (Bateman, 1910)

$$N_N = N_A(0)[h_A e^{-\lambda_A t} + h_B e^{-\lambda_B t} + ... + h_N e^{-\lambda_N t}], \quad 2.21$$

with the constants h_A to h_N expressed by

$$h_A = \frac{\lambda_A}{\lambda_N - \lambda_A}\frac{\lambda_B}{\lambda_B - \lambda_A}\cdots\frac{\lambda_M}{\lambda_M - \lambda_A},$$

$$h_B = \frac{\lambda_A}{\lambda_A - \lambda_B}\frac{\lambda_B}{\lambda_N - \lambda_B}\cdots\frac{\lambda_M}{\lambda_M - \lambda_B}, \quad 2.22$$

$$h_N = \frac{\lambda_A}{\lambda_A - \lambda_N}\frac{\lambda_B}{\lambda_B - \lambda_N}\cdots\frac{\lambda_M}{\lambda_M - \lambda_N}.$$

2.1.6 Equilibrium in Parent-Daughter Activities

The derived equations from the previous sections indicate that the activity of the parent to that of its daughter(s) depends on the relative magnitudes of their decay constants.

Based on Equation 2.18 the daughter activity will increase till it reaches a maximum activity at time t_{max}. Equation 2.18 then simplifies to

$$\lambda_A N_A(0) e^{-\lambda_A t_{\max}} = \lambda_A N_A = \lambda_B N_B \ . \quad 2.23$$

At this time the activity of daughter is equal to that of the parent and is called ideal equilibrium. This situation is indicated in all the subfigures of Figure 4.

Before this time, $0 < t < t_{max}$, the activity of the parent exceeds that of the daughter. From t_{max} onwards the activity of the daughter continuously exceeds that of the parent. The activity of the parent to that of its daughter(s) after t_{max} depends on the relative magnitudes of λ_A and λ_B. The following three special cases are of interest. In all of them it is assumed that at $t = 0$ the daughter activity is zero and that no activity of the parent is removed before or during the decay process (or measurement).

The first case is when the daughter is longer lived than the parent, that is $\lambda_B < \lambda_A$. The activity ratio of the daughter to the parent increases continuously over time and can be written from Equation 2.19 as

$$\frac{A_B}{A_A} = \frac{\lambda_B}{\lambda_A - \lambda_B}(e^{(\lambda_A - \lambda_B)t} - 1) \ . \qquad 2.24$$

An example is depicted in Figure 4 (a).

The opposite case where the daughter is shorter lived than the parent, i.e. $\lambda_B > \lambda_A$. is depicted in Figure 4(b). Initially the ratio of activities increases but after some time (that exceeds both the parent and the daughter's half-lives) the parent daughter activity ratio is constant and the respective activities decrease at the same rate. This ratio is expressed by

$$\frac{A_B}{A_A} = \frac{\lambda_B}{\lambda_B - \lambda_A}. \qquad 2.25$$

When the ratio is reached it is called a state of transient equilibrium.

The last special case is when the half-life of the daughter is very short compared to that of the parent that is $\lambda_B >> \lambda_A$. In this case the daughter will, after a time *t,* acquire the same activity as the parent if they are in a closed system. From Equation 2.24 the activity ratio reduces to 1, i.e.

$$\frac{A_B}{A_A} = \frac{\lambda_B}{\lambda_B - \lambda_A} \approx \frac{\lambda_B}{\lambda_B} = 1. \qquad 2.26$$

This condition is called a state of secular equilibrium and is illustrated in Figure 4 (c). Once secular equilibrium is established between a parent and daughter, the activity of daughter will decrease at the same rate as the parent. The time to reach secular equilibrium is dependent on the half-life of the daughter. If one assumes the daughter activity is zero to begin with, it will take between approximately 7-10 half-lives of the daughter before they can be considered to be more or less in secular equilibrium.

The usefulness of secular equilibrium is that the activity of a parent can be determined from a measurement of the activity of the daughter. Examples are the ^{238}U and ^{232}Th as parent radioisotopes. Both have very long half-lives (4.47×10^9 y and 1.41×10^{10} y respectively) while the half-lives of all the daughter products are far shorter (e.g. 26.8 min for ^{214}Pb and 6.13 h for ^{228}Ac).

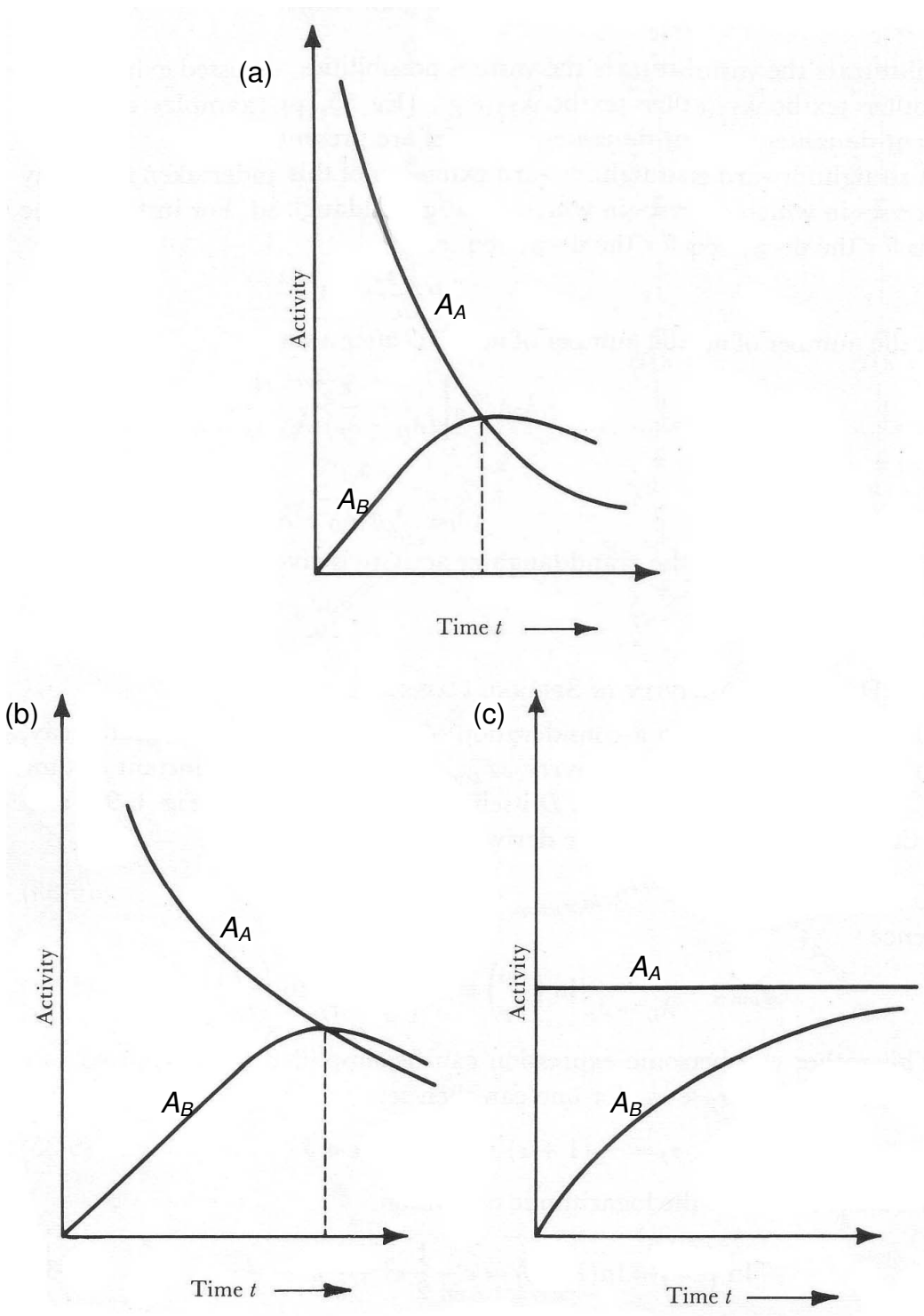

Figure 4. ***An illustration of the special cases of equilibrium.***
The dashed line indicates the time t_{max} when ideal equilibrium occurs, (a) illustrates the case where $\lambda_B < \lambda_A$, (b) transient equilibrium and (c) secular equilibrium.

2.1.7 Radioactivity in Nature

Radioactivity is found everywhere in nature and is categorised as artificial or naturally occurring. Naturally occurring radioactivity is either produced from cosmic ray interactions or found in the earth's crust.

Artificial radioactivity

Artificial radioisotopes do not belong in the environment and are found due to human activities for instance nuclear power plant accidents or nuclear weapons testing. An example is the fission product ^{137}Cs. Other radioisotopes such as ^{30}P are made through man-made nuclear reactions.

Cosmogenically produced radioactivity

Radioisotopes are also continuously produced in the atmosphere. High-energy charged particles and neutrons from the sun and outer space enter the earth's atmosphere and collide with atoms. In this way radioisotopes such as ^{3}H, ^{7}Be and ^{14}C are formed, together with a cascade of reaction products.

Terrestrial radioactivity

The crust and mantle of the earth are the sources of the terrestrial radioactivity found in sands and soils. It includes the primordial radioisotopes (which are radioisotopes with sufficiently long half-lives to have survived since the formation of the earth) and the daughter radioisotopes which formed following their decay. Some of these radioisotopes occur singly such as ^{40}K, ^{87}Rb and ^{115}In, while others form part of a decay series.

Originally there were four naturally occurring decay series with mass numbers $4n$, $4n$+1, $4n$+2 and $4n$+3 respectively, where n is an integer ranging from 50 to 59. The factor of 4 is explained by alpha decay that always decreases the mass number by four. The $4n$ series is known as the thorium series with ^{232}Th as parent (100 % abundance). A block representation of this series is depicted in Figure 5. The parent, ^{237}Np, of the neptunium series ($4n$+1) is no longer found on earth due to its short half-live of 2.14×10^{6} y. Only one member of the series namely ^{209}Bi has a half-life long enough to still be found in nature. The uranium ($4n$+2) series starts with ^{238}U as parent (99.27 % abundance), depicted as a

block representation in Figure 6. Lastly the 4*n*+3 or actinium series has ^{235}U as parent (0.72 % abundance). Some long-lived terrestrial radioisotopes together with their half-lives, decay modes and abundances (the proportion of an element that consists of the particular radioisotope) are tabulated in Table 6.

Table 6 ***Examples of long-lived natural radioisotopes (Firestone, 1996) with their half-life, abundance, decay mode and their final decay products.***

Radioisotope	Half-life (y)	Abundance (%)	Decay Mode	Final Decay Product
^{40}K	1.28×10^{9}	0.0117	β^-,EC	^{40}Ca, ^{40}Ar*
^{87}Rb	4.88×10^{10}	27.8	β^-	^{87}Sr
^{115}In	4.40×10^{14}	95.7	β^-	^{115}Sn
^{144}Nd	2.38×10^{15}	23.8	α	^{140}Ce
^{148}Sm	7.00×10^{15}	11.2	α	^{144}Nd
^{187}Re	4.12×10^{10}	62.6	β^-	^{187}Os
^{232}Th	1.41×10^{10}	100	α	^{208}Pb
^{235}U	7.04×10^{8}	0.720	α	^{207}Pb
^{238}U	4.47×10^{9}	99.3	α	^{206}Pb

The activity ranges of ^{238}U, ^{232}Th and ^{40}K in soil are reported as 10 - 50 Bq/kg, 7 - 50 Bq/kg and 300 - 1000 Bq/kg respectively (IAEA, 2000). However, soils originate from many different types of rock formations and the activities can therefore vary considerably as tabulated in Table 7 (Van Rooyen, 2000; Oyedele, 2006; Ngachin et al., 2008; Jabbar et al, 2009; Singh et al., 2009). Heavy mineral sand concentrates have ^{238}U and ^{232}Th activities that are higher than the tabulated values.

Table 7 ***Activity ranges of ^{238}U, ^{232}Th and ^{40}K in soil.***

Place	^{238}U (Bq/kg)	^{232}Th (Bq/kg)	^{40}K (Bq/kg)	Author
World	10 - 50	7 – 50	100 - 700	IAEA (2000)
South Africa	40 - 200	37 – 250	300 – 1000	Van Rooyen (2000)
Windhoek, Namibia	15 – 38	17.5 – 62.1	169 – 785	Oyedele (2006)
Rechna, Pakistan	49	62	671	Jabbar et al. (2009)
North India	28 – 81	61 - 140	363 – 1002	Singh et al. (2009)

2.1.8 Radioisotopes used in this study

In this study only gamma ray emitters are useful. They are ^{214}Bi and ^{214}Pb in the ^{238}U series and in the ^{232}Th series they are ^{208}Tl and ^{228}Ac. Tallium-208 is one of two products that can be formed when its parent, ^{212}Pb, decays. It has a 38 % probability of formation while the other radioisotope ^{212}Po has a probability of 62 % to be formed. The parents of the other three gamma emitters decay 100 % to their respective daughters. Potassium-40 decays with a probability of 10.67 % by electron capture to an excited state of ^{40}Ar. During the de-excitation to the ground state a 1.46 MeV characteristic gamma ray is emitted. The decay scheme of ^{40}K is depicted in Figure 3. The gamma rays selected for analysis are discussed in section 4.2.3.

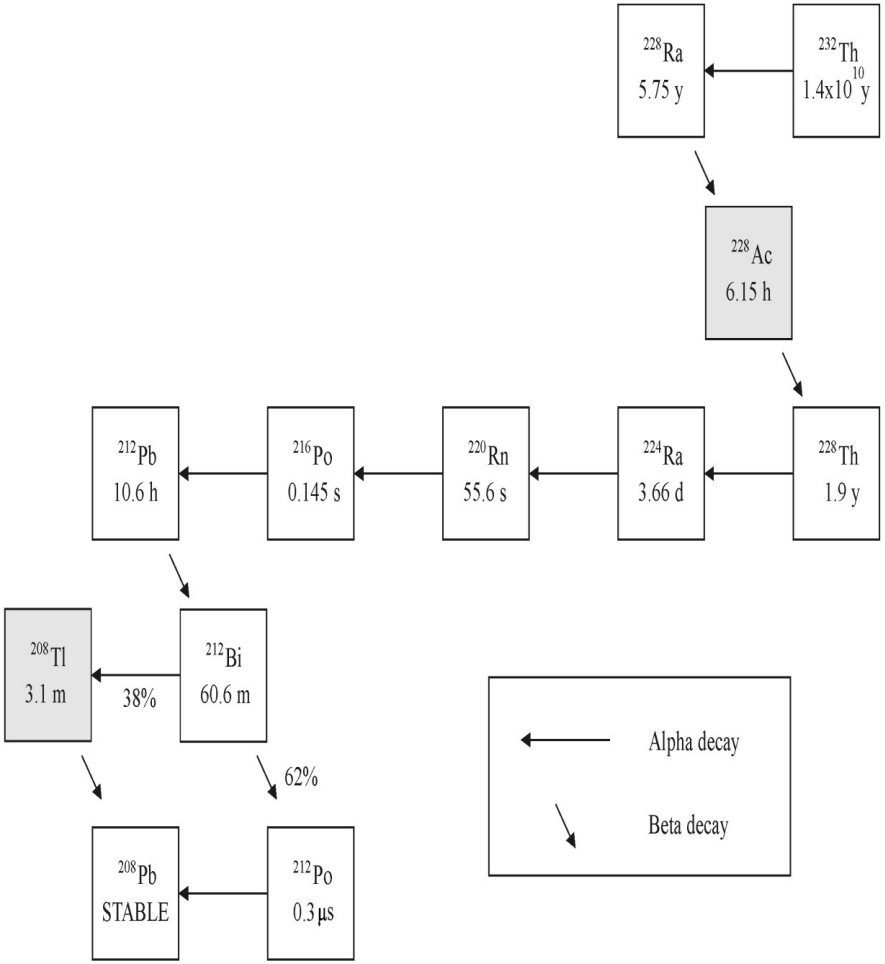

Figure 5. ***Block representation of the ^{232}Th decay series. Grey boxes indicate the radioisotopes that are used in this work as they also emit gamma rays.***

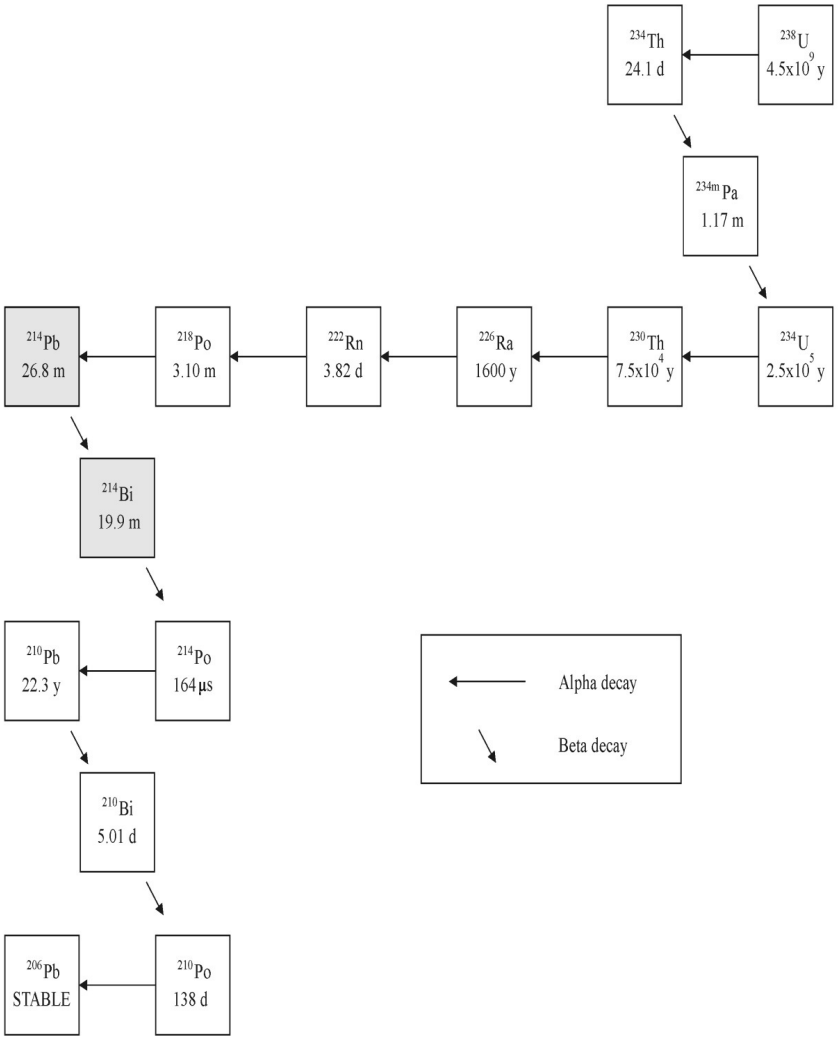

Figure 6. ***Block representation of the ^{238}U decay series. Grey boxes indicate the radioisotopes that are used in this work as they also emit gamma rays.***

2.2 GAMMA RAY DETECTION

2.2.1 Gamma Ray Interactions with Matter

Gamma rays interact with matter through interactions with the atomic electrons or the nucleus or the electric field surrounding the electrons or nucleus. The effects are either complete absorption or elastic scattering or inelastic scattering. For radiation measurements, in the energy range from 0.01 to 10 MeV, only three major processes play a role: the photoelectric effect, Compton scattering and pair production. In all these processes the gamma ray's energy is completely or partially transferred to electron energy. The result is either the disappearance of the gamma ray or one that is scattered through an angle. These processes are discussed in the following sections. The regions where the three processes are individually dominant are depicted in Figure 7.

Photoelectric Effect

The photoelectric effect is the process whereby the atom completely absorbs the gamma ray and all its energy is transferred to a bound atomic electron. The electron is ejected with a kinetic energy of

$$T = E_\gamma - E_B \qquad 2.27$$

where E_γ is the energy of the incident gamma ray and E_B the binding energy of the emitted electron. It is observed that for gamma rays with energy of more than a few hundred keV, the ejected electron carries off the majority of the original gamma ray energy. For this reason the photoelectric effect is the dominant interaction mechanism for photon energies below 0.1 MeV.

The probability for the photoelectric effect per atom can be described by the atomic cross section τ_a expressed by

$$\tau_a \approx const \frac{Z^n}{(E_\gamma)^3}. \qquad 2.28$$

In this expression the exponent n increases from 4.0 to 4.6 as E_γ increases from 0.1 MeV to 3 MeV. This dependence on Z also shows that the photoelectric effect increases with the atomic number of the absorber material.

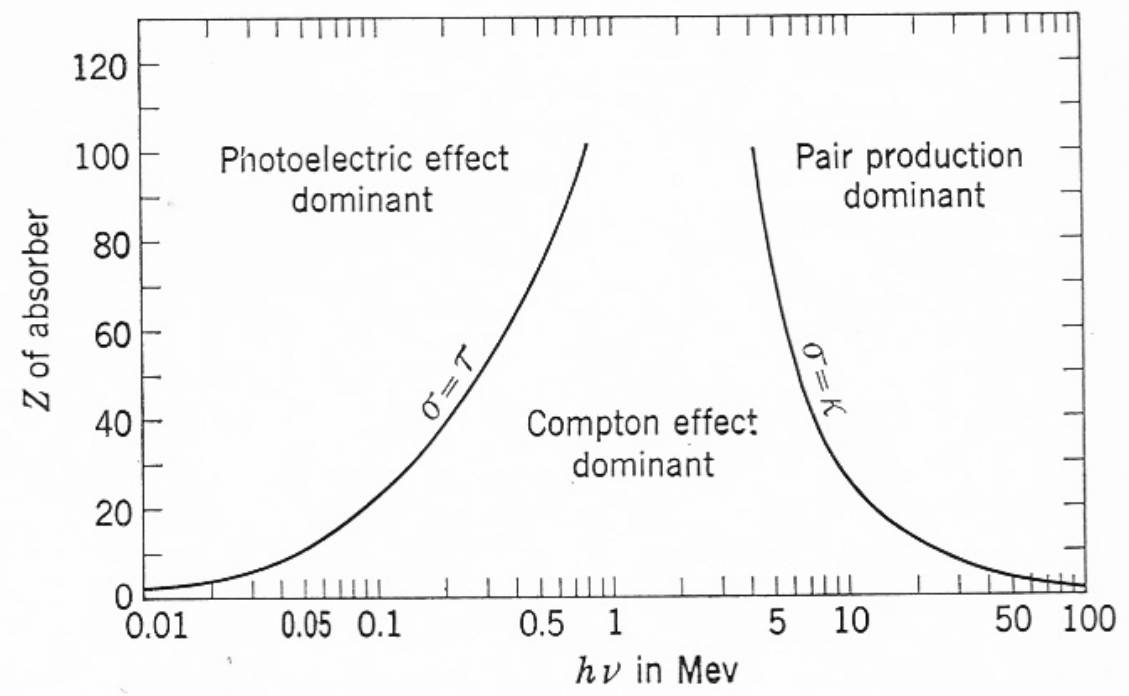

Figure 7. ***The regions where the three interaction processes are individually dominant.***
The curves that separate the regions depict photon energies and absorber materials at which adjacent mechanisms are equally probable.

Compton Scattering

Compton scattering is the dominant process for photons in the energy range of 0.5 to 5 MeV. In this process the gamma ray undergoes elastic scattering from an unbound atomic electron in the absorber material. The result is a less energetic photon and an electron with kinetic energy equal to

$$T = h\nu - h\nu' = h\nu - \frac{h\nu}{1+(\frac{h\nu}{m_0c^2})(1-\cos\theta)}. \qquad 2.29$$

In this expression $h\nu$ is the energy of the original gamma ray and $h\nu'$ the energy of the scattered gamma ray. The m_0c^2 term is the rest mass energy of the electron. The scattering angle between the gamma ray and the electron is presented by θ. Depending on the angle the kinetic energy can range from zero (for $\theta = 0$) to a large fraction (for $\theta = \pi$) of the original gamma ray energy. For the differential scattering cross section $d\sigma_e/d\Omega$

the angular distribution of the scattered gamma rays is described by the Klein-Nishina formula,

$$\frac{d\sigma_e}{d\Omega} = r_0^2 \left[\frac{1}{1+\frac{h\nu}{m_0c^2}(1-\cos\theta)} \right]^3 \left[\frac{1+\cos^2\theta}{2} \right] \left[1+\frac{\left(\frac{h\nu}{m_0c^2}\right)^2 (1-\cos\theta)^2}{(1+\cos^2\theta)\left\{1+\frac{h\nu}{m_0c^2}(1-\cos\theta)\right\}} \right], \qquad 2.30$$

with r_0 the classical electron radius. Integrating Equation 2.31 over all scattering angles φ,

$$\sigma_e = 2\pi \int_{\vartheta=0}^{\pi} \frac{d\sigma_e}{d\Omega_\vartheta} \sin\vartheta d\vartheta \qquad 2.31$$

result in a cross section for scattering from a single electron. Since the number of electrons in the absorber material determines scattering, the probability of Compton scattering per atom increases linearly with Z,

$$\sigma_a = Z\sigma_e. \qquad 2.32$$

Pair Production

If the energy of the gamma ray exceeds 1.02 MeV the process of pair production becomes energetically possible. In this process the gamma ray interacts with the Coulomb field of the nucleus and transfers all of its energy in the creation of a positron and electron pair. All energy above the 1.02 MeV (that is needed to create the pair) is shared between the positron and electron as kinetic energy. After interactions within the absorber material the positron will annihilate with an electron and two 511 keV gamma rays are formed. Due to the energy threshold for pair production, this process is dominant for energies above 5 MeV.

The probability for pair production per atom is dependent on the square of the absorber material's atomic number. It can be described by the atomic cross section σ_κ expressed by

$$\sigma_\kappa \approx const.Z^2\bar{P}, \qquad 2.33$$

with P a function of Z and the photon energy.

Linear and Mass Attenuation Coefficients

Through the previously mentioned interaction processes a gamma ray can either be absorbed or scattered in a single event. The probability for a gamma ray to propagate through a material without any of these interactions taking place is the product of the probabilities of survival for every type of interaction. To quantify these probabilities, the total linear attenuation coefficients, which are a measure of the number of photons that have interactions, are used. It is dependent on the cross-section for the particular process, the number of atoms in the medium and the energy of the gamma ray. For the photoelectric effect, Compton scattering and pair production the linear attenuation coefficients are respectively expressed by:

$$\tau = \tau_a N\,, \tag{2.34}$$

$$\sigma = \sigma_a N \text{ and} \tag{2.35}$$

$$\kappa = \sigma_\kappa N \tag{2.36}$$

with N the number of atoms per cubic centimetre, τ_a , σ_e and σ_κ the interaction cross sections defined in Equations 2.28, 2.32 and 2.33 respectively. The total linear attenuation coefficient is expressed by the sum of all three interaction cross sections,

$$\mu = \tau + \sigma + \kappa. \tag{2.37}$$

The linear attenuation coefficient changes in proportion to the density of the absorber material. By dividing by the material density a density independent mass attenuation coefficient is obtained. Hubble (Hubble, 1999) and Berger (Berger and Hubbell, 1999) compiled lists of mass attenuation coefficients as a function of energy for all elements. From these lists, the mass attenuation coefficients for a material that consists of more than one element can be calculated.

For a multi-element material it is assumed that the attenuation processes depend on the total cross section presented by all the atoms in the material. Consequently the total mass attenuation coefficient is expressed as the sum of the mass attenuation coefficients of the individual elements,

$$\mu_m^{total} = \sum w_i \mu_{mi} = \sum \frac{w_i \mu_i}{\rho_i}. \tag{2.38}$$

Here w_i is the weight fractions of the elements that make up the material. For example, the mass attenuation coefficients for zircon ($ZrSiO_4$) with a total atomic mass of 183 are expressed by

$$\mu_{ZrSiO_4}^{total} = \frac{91}{183}\mu_{Zr} + \frac{28}{183}\mu_{Si} + \frac{64}{183}\mu_{O}. \quad 2.39$$

Furthermore, it can be shown that there is an exponential relationship between the initial number of gamma rays, $I_{0,}$ and the number of gamma rays that were not attenuated by the material, I, by

$$I = I_0 e^{-\mu x}, \quad 2.40$$

with x the thickness of the absorber material. With the total attenuation coefficient defined as in Equation 2.37, Equation 2.40 refers to the probability for gamma rays to move through a material without undergoing any of the mentioned interaction mechanisms.

2.2.2 Gamma Ray Detection

General properties of radiation detectors

A gamma ray detector performs two functions. The first is to act as a medium in which gamma rays can interact. The second is to detect the corresponding electrical signals that are produced.

A gamma ray must first undergo an interaction with the detector material by means of the photoelectric effect, Compton scattering or pair production before it is detected. The interaction time is so small that the transfer of energy can be considered to be instantaneous. The result is an amount of electric charge within the detector volume. Through the application of an electric field within the detector the positive and negative charges flow in opposite directions and form an electrical signal. Depending on the detector mode of operation the output signals can either be an average current from many interactions or the current from each individual interaction. The latter is generally preferred in many applications. In this case the output will consists of individual pulses each the result of a single gamma ray interaction. The amplitude of the pulses is directly proportional to the charge generated by the corresponding gamma ray. The rate at which these interactions occur in the detector is also reflected in the rate at which the pulses are generated. The

individual pulses form a pulse amplitude distribution (also called the gamma ray spectrum) from which information about the incident gamma rays or detector operation can be extracted (Knoll, 1979).

Three detector properties that influence this gamma ray spectrum will be discussed hereafter, that is resolution, efficiency and dead time.

Resolution

One of the functions of a radiation detector is to measure the energy distribution of the incident radiation. The accuracy of these energy measurements is determined by the detector resolution. Resolution is the width of a single energy peak at specific incident energy. It is a dimensionless number and is defined by the full width at half maximum (FWHM) divided by the location of the peak centroid H_0 (Knoll, 1979) as illustrated in Figure 8,

$$R = \frac{FWHM}{H_0}. \qquad 2.41$$

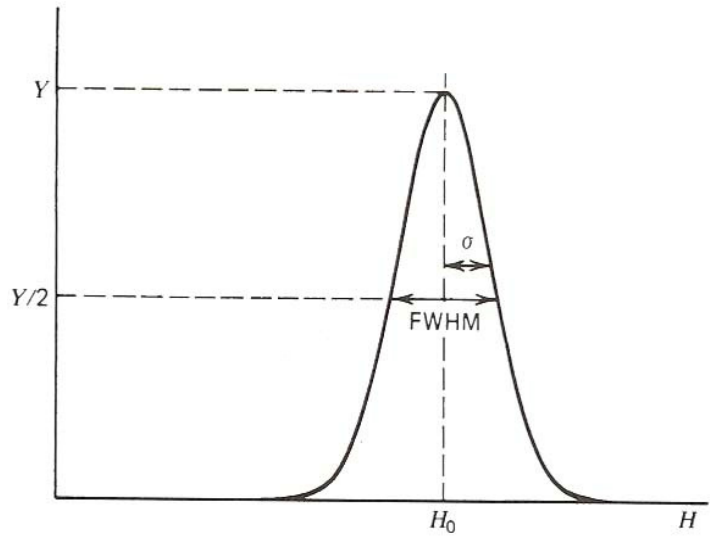

Figure 8. ***An illustration depicting the definition of resolution***

The FWHM is the width of the signal distribution at a position that is half of the maximum peak value. Besides the type of detector crystal, the width depends on potential sources of the fluctuation in the response of the detector. These are sources of random noise in the counting system, drift in the detector operating conditions and statistical variation in the measured signal. The reason for the latter fluctuation is that the collected charge is not a

continuous parameter but consists of a discrete number of charge carriers. During the creation of these charge carriers all the possible interaction processes occur and thus show statistical fluctuations from event to event. If the number of fluctuations is reduced, the resolution will become smaller. In turn the detector will be able to differentiate between radiation energies that lie close to one another.

Efficiency

The efficiency of the detector determines how many of the incident radiations will be recorded as electrical signals. It is divided into two groups absolute or intrinsic. Absolute efficiency depends on the detector properties and the distance between the detector and the source. It is defined by (Knoll, 1979)

$$\varepsilon_{abs} = \frac{\text{number of pulses recorded}}{\text{number of radiation quanta emitted by source}}. \qquad 2.42$$

Intrinsic efficiency depends mainly on the radiation energy, the detector material and the detector thickness. It is defined by

$$\varepsilon_{\text{int}} = \frac{\text{number of pulses recorded}}{\text{number of radiation quanta incident on detector}}. \qquad 2.43$$

The relation between the two efficiencies is

$$\varepsilon_{\text{int}} = \frac{4\pi}{\Omega} \cdot \varepsilon_{abs} \qquad 2.44$$

with Ω the solid angle of the detector seen from the source position. Efficiencies are also classified according to the nature of the event. If all the events recorded in the detector is of importance then the total efficiency is used. More often one is interested to count those interactions that deposit their full energy. This is referred to as the photopeak efficiency.

Dead time

All counting systems need a minimum amount of time to separate two events so that they will be measured as two separate electronic signals. When a subsequent event arrives while the detection system is still processing the first, the second event will not be registered. An estimate of these dead time losses can be modelled in two ways. According to a so called nonparalyzable model the arrival of a subsequent event does not influence the dead time of the system. The observed count rate, *m,* true count rate, *n*, and the dead time of the system, *τ*, is then related by (Knoll, 1979)

$$n = \frac{m}{1 - m\tau}. \qquad 2.45$$

In the case of the paralyzable model a subsequent event lengthens the dead time. The observed count rate is related by (Knoll, 1979)

$$m = ne^{-n\tau}. \qquad 2.46$$

Semiconductor Detectors

A semiconductor detector consists of a crystalline detection material, e.g. germanium and two electrodes with a high voltage applied between them. In the coaxial geometry the outer surface of the detector serves as the one electrode and the inner core as the other. The crystalline material has a periodic lattice that creates energy bands in which electrons are allowed to exist. There are two bands of interest, the valence band and the conduction band with a bandgap in between. The valence band is the lower band and represents the bound outer shell electrons that exist in specific lattice sites within the material. The higher lying conduction band represents free electrons that can migrate through the material (Knoll 1979).

In a semiconductor detector a gamma ray interacts with the semiconductor material and the deposited energy produces free electrons and holes in the valence band. The holes and the free electrons behave as positive and negative charges and by applying an electric field they are collected at the electrodes. The amount of charge collected is proportional to the deposited energy. In a semiconductor such as germanium the average energy needed to produce an electron-hole pair is very small (~ 3eV) (Knoll, 1979). This means that more charge carriers are produced in a single interaction compared to other detector types. The result is a smaller statistical fluctuation in the number of electrons, therefore a much better resolution than for example a scintillation detector such as NaI(Tl).

The good resolution of a germanium detector is set off against two disadvantages. One is the lower effective atomic number than NaI(Tl). Since the probability of gamma ray interactions depends strongly on the atomic number of the absorber material, the detection efficiency of a germanium detector is considerably lower than that of a NaI(Tl) detector. For example, in this work the germanium detector is only 45.4 % relative to a 3” x 3” NaI detector.

The other disadvantage is that the band gap of germanium is very small (0.7 eV) and operating it at room temperature would result in a large thermally induced leakage current (Knoll 1979). This current (that is formed without a gamma ray interaction) can degrade the energy resolution. For this reason a germanium detector is cooled with liquid nitrogen to 85-105 °K inside a specially-designed cryostat. This makes a germanium detector more difficult to use as a portable field instrument.

One of the objectives of this study is to determine the uranium, thorium and potassium concentrations with very good accuracy. The decision of the type of detector was therefore based on good resolution, to distinguish between the close lying uranium and thorium photopeaks. Since the measurements would be laboratory-based the nitrogen cooling was not a problem. Also, detector efficiency was increased with a close geometry setup i.e. Marinelli beaker together with longer counting times.

Gamma Ray Spectrum

The spectral features

The various features in a gamma ray spectrum reflect the different interaction mechanisms of gamma radiation with the detector material. For instance, the sharp peaks (called photopeaks or full-energy peaks) correspond to gamma rays that deposit its full energy via the photoelectric effect. Compton scattering of gamma rays give rise to the Compton continuum, which are a continuum of energies that range from zero to the incident energy. The maximum angle of scattering corresponds to the Compton edge.

A single escape peak corresponds with the escape of one of the annihilation gamma rays produced in pair production. If both gamma rays escape the detector a double escape peak is observed. Besides the normal photopeaks summation peaks can also be formed. These peaks are a result of two coincident gamma rays that are measured by the counting system as one. Its energy is the sum of the two coincident gamma rays. These features are depicted in Figure 9 (Knoll 1979).

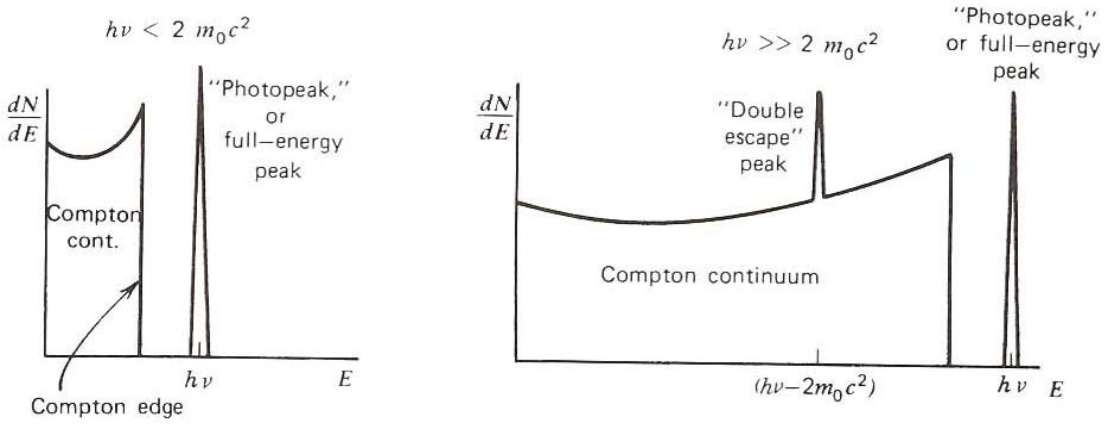

Figure 9. ***The spectrum features from a typical source: photopeak, Compton continuum, Compton edge and a double escape peak.***

Gamma rays interact also with the material surrounding the detector. These gamma rays correspond with a backscatter peak or annihilation peak that is superimposed on the source spectrum. X-ray peaks due to bremstrahlung can also contribute to the spectrum. These contributions are depicted in Figure 10 (Knoll 1979).

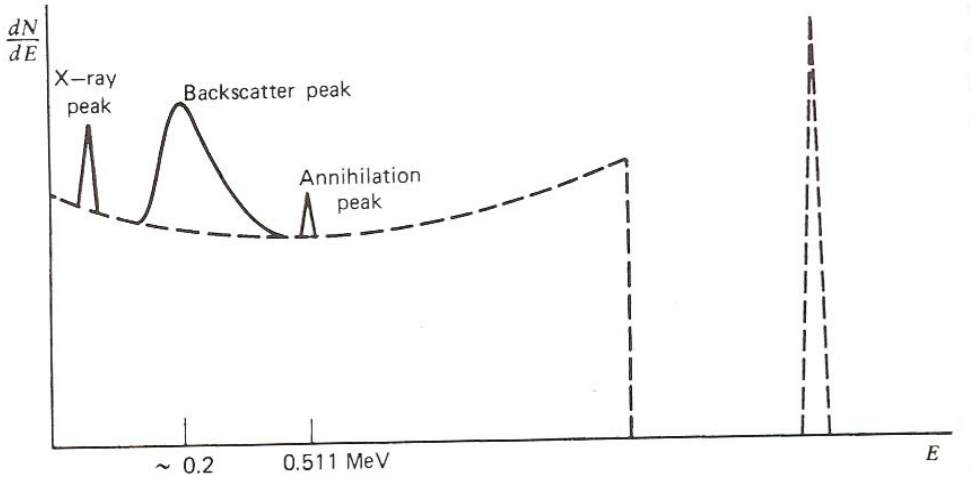

Figure 10. ***The spectrum features due to the surroundings: X-ray peak, backscatter peak and annihilation peak.***

An ever present background spectrum underlies the source spectrum. This spectrum differs for the type and size of the detector and the amount of shielding around it. The contributions to the background spectrum are from the ^{40}K and other natural radioisotopes found in building materials around the detector. The background signal is reduced by placing shielding around the detector. High purity lead is used to minimise the contributions of the trace amounts of uranium and thorium found in the lead. In addition the

beta particles of ^{210}Pb at energies of 16.5 keV and 63 keV and its daughter ^{210}Bi at 1.16 MeV are superimposed on the Compton continuum (Brodzinski et al., 1995). Beta particles and gamma rays that are the result of cosmic radiation interactions with the shielding also form part of the background signal. This unwanted signal and the process to minimise it are discussed in section 4.1.3.

Minimum Detectable Activity

The measurement of a sample is influenced by the relative contribution of the background signal. If it is small compared to the concentration of the sample, the analysis would be straight-forward as the peaks of interest will stand out clearly. However, if the sample gives rise to signals that are comparable to the background, it may not be so easy to analyse correctly. A statistical variation in the background can easily be confused with a low concentration value. To know beforehand if a measurement will result in a useful answer the minimum detectable activity (MDA) can be determined by (Strom and Stansbury, 1992)

$$MDA = \frac{2.71 + 3.29\sqrt{\frac{R_b}{T_s} + \frac{R_b}{T_B}}}{T_s \times \varepsilon \times I} \qquad 2.47$$

for every gamma ray of interest. Here R_b is the background count rate, T_S the sample counting time, T_B the background counting time, ε the detector efficiency at the energy of interest and I the photon intensity of the gamma ray. This expression, as it is stated, is discussed in Appendix C since it is not often used in literature.

2.3 THE X-RAY FLUORESCENCE (XRF) TECHNIQUE

The XRF technique is extensively used in laboratories for the determination of trace element concentrations in all kinds of samples, as it is a non-destructive method with a high degree of accuracy and a detection limit in the low parts-per-million range (Sbarato and Sánchez, 2001). In this study the uranium and thorium concentrations in the samples as obtained by radiometry were compared with the concentrations as obtained by XRF. Both these techniques use uncharged radiation, although different in origin (X-rays from electron transitions in the atom and gamma rays from the nucleus) to identify and estimate concentrations of elements. The theory of interactions is similar and will not be repeated here. Instead, as XRF was used as a comparative technique, a brief overview of the physical principles and its analysis method are described.

2.3.1 Physical Principles of XRF

Radiometry uses the gamma rays that are spontaneously emitted by a radioactive sample. In contrast, to use the XRF technique the sample must first be irradiated with X-rays to produce secondary X-rays. These characteristic X-rays are the ones measured and analysed.

When the energy of the incident X-rays are higher than the binding energy of an inner shell electron, the electron is ejected from the shell. Subsequently an outer electron fills this vacancy. As the binding energy of the outer shell electron is less than that of the inner shell electron the difference in energy is emitted as an X-ray (an illustration of this process is depicted in Figure 11). The presence of these characteristic X-rays together with their observed intensity are a unique measure of the presence and the quantities of the elements found in a sample.

In 1913 Mosley showed that by measuring the wavelengths of the emitted characteristic X-rays, the elements in a sample can be deduced. This relation between the wavelength and the atomic number Z is expressed by

$$\frac{1}{\lambda} = k_1(Z - k_2) \qquad 2.48$$

Here k_1 and k_2 are constants that depend on the specific X-ray. For example, for all K_α lines (a K shell vacancy being filled with an L shell electron) Equation 2.48 can be rewritten as

$$\frac{1}{\lambda} = 2.48 \times 10^{15}(Z - 1)^2. \qquad 2.49$$

2.3.2. XRF Analysis

X-ray wavelengths are measured by an experimental set-up that together with the associated electronics and software consists of an X-ray tube, analysing crystal and a detector. A sample of unknown elemental composition is prepared by either crushing it to a powder and pressed into a briquette or fused into a glass bead. Thereafter it is bombarded with X-rays or electrons. A small fraction of the resulting secondary X-rays is selected by means of a collimator and sent to a flat diffraction grated analysing crystal. The atoms in the planes within the crystal cause the X-rays to scatter and a diffraction pattern is formed.

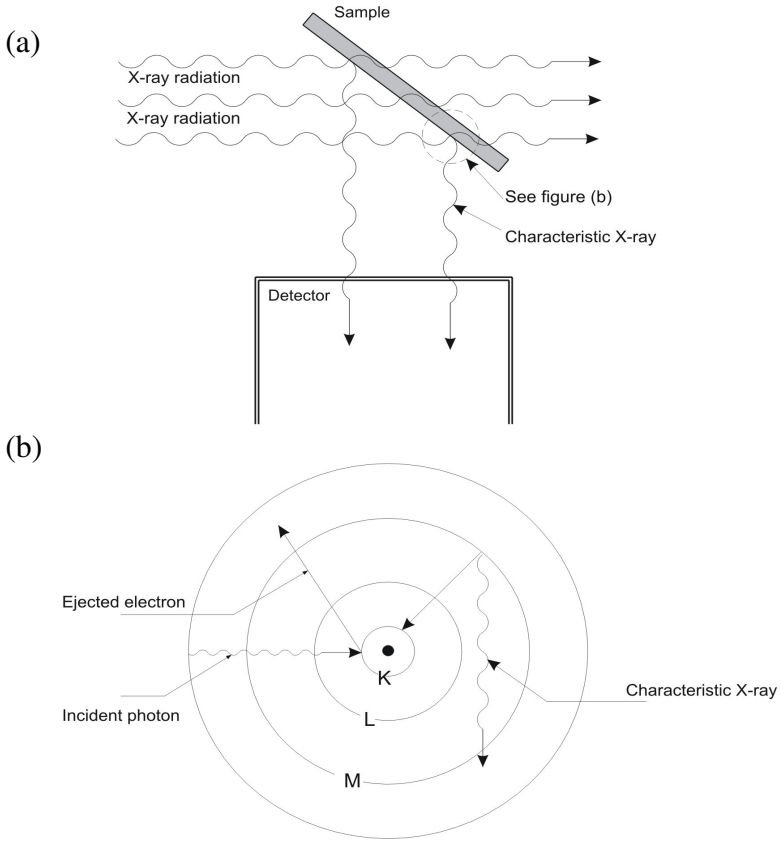

Figure 11. ***A re-presentation of the XRF process.***
In (a) incident X-rays produce characteristic X-rays from a sample. Figure (b) shows on an atomic scale how the incident X-ray photon interacts with the atomic electrons resulting in a characteristic K_β X-ray.

The maxima of this pattern corresponds to the X-ray wavelengths that satisfy Bragg's Law, that is

$$n\lambda = 2d\sin\theta. \qquad 2.50$$

Here n is an integer, λ the wavelength of the incident X-ray, d the distance between atomic layers in the crystal and θ the angle of incidence. The detector is moved around the crystal to locate the maxima and hence the wavelengths are determined. Using Equation 2.50 the elements from which the X-rays originate are derived.

The concentration of an element can also be calculated from the XRF results. Firstly the intensity of the element's X-ray emissions from the sample is determined. Secondly the particular element's X-ray emission intensity is determined from a sample of known

concentration. Finally the unknown concentration is calculated by comparing the intensities of the two samples by the following equation

$$C_i = C_{std} \times \frac{I_i}{I_{std}} \times \frac{M_i}{M_{std}}, \qquad 2.51$$

Here C is the concentration of the element, I the net peak intensity and M the composition correction.

CHAPTER 3 METHODOLOGY

In this chapter the measurement methodologies of radiometry and XRF are explained. The first section describes the different electronic components and the Marinelli beaker (as sample container) that form the radiometry detection system. Thereafter the experimental setup of XRF and its measurement methodology are discussed. In the final section the sampling for both the heavy mineral sands and vineyard soils are discussed. It includes where samples were taken and how they were prepared for measurement with the radiometry and the XRF techniques.

3.1 EXPERIMENTAL SET-UP AND METHODOLOGY

3.1.1 Radiometry Experimental Set-up

The radiometry analyses were performed at the iThemba LABS Environmental Radioactivity Laboratory. A Marinelli beaker was used as the sample container while the detector set-up used for the gamma-spectroscopy consisted of a coaxial p-type high purity germanium (HPGe) detector (Canberra Model GC4520 with a 700 µm Al window) housed in a 10 cm thick lead castle with an inner electrolytic copper lining of 2 mm. The HPGe crystal has a diameter of 62.5 mm and a length of 59.9 mm. At 1332.5 keV it has an efficiency of 45.4 % relative to a 3” x 3” NaI(Tl) detector. The resolution at this energy was 2.13 keV.

The detector was coupled to an Oxford 16-k multi-channel analyser (MCA) with a built-in successive-approximation type analogue to digital converter (ADC). The conversion gain on the ADC was set at 8192 channels. The system included a Silena Model 7716 high voltage supply and an Ortec Model 572 spectroscopy amplifier set to a pulse shaping time (rise time and fall time) of 6 µs. The gamma ray signals were stored and analysed using the associated MCA software package OxWinMCA. The electronic equipment used for this experimental set-up is depicted in Figure 12.

The radiometric methods that can be used for the online measurement at the mine or for in-situ measurements in the vineyard use another type of detector, which has different

specifications. Nonetheless, the outcome of this study will include recommendations and the assurance that it will be useful for industry.

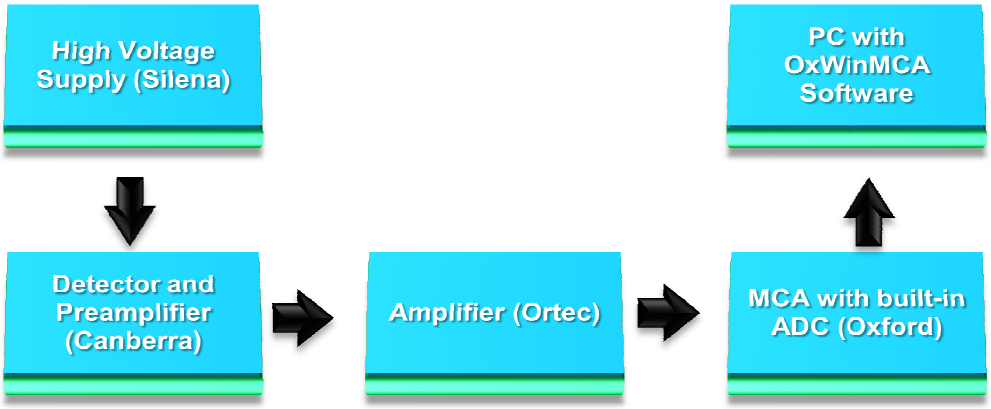

Figure 12. ***The electronic components of the experimental set-up used for the measurement of the U, Th and K concentrations in the samples forming part of this study.***

3.1.2 Radiometry Methodology

The heavy mineral sands and vineyard soils were counted with the gamma spectroscopy system for 3600 s and 10800 s respectively, according to the calculation in section 4.2.2. Photopeak selection and peak area calculations were performed as described in section 4.2.3. The $\varepsilon_0(E)$ efficiency values were taken from Table 18 and corrected for each sample with the use of the procedures described in section 4.2.4. Thereafter the ^{238}U, ^{232}Th and ^{40}K concentrations were calculated with a Microsoft Excel spreadsheet for each of the samples.

3.1.3 XRF Experimental Set-up

Chemical analyses of mineral sand, soil and whole rock were done with XRF Spectrometry by the Department of Earth Sciences, Stellenbosch University. The instrument used was a Philips 1404 Wavelength Dispersive spectrometer. The spectrometer is fitted with a Rhodium tube, which is the primary source of X-ray radiation to the sample. The unfiltered Rh-K_α or Rh-K_β excitation allowed determination of elements with characteristic K-or L-lines in the energy range 3 - 12 keV. Other components of the experimental set-up are six

analysing crystals (LIF200, LIF220, LIF420, PE, TLAP and PX1), a combination of a gas-flow proportional counter (for X-rays with low energy) and a scintillation detector (for the higher X-ray energies). The gas-flow proportional counter used a mixture of 90 % Argon and 10 % Methane. The software used for data acquisition, spectrum analysis, interpretation and quantitative analysis is SuperQ from Philips. The detection limits of the system were 1 ± 4 ppm for uranium and 1 ± 3 ppm for thorium.

3.1.4 XRF Methodology

The concentrations of the elements in the samples were derived by comparing the X-ray intensities for each element to the intensities of standards with known elemental compositions. These standards are tabulated in Table 7 together with their uranium and thorium concentrations. Many of the concentrations of the heavy mineral sands and vineyard soils were outside the range of the concentrations of the standards. In these cases extrapolation to the acquired value was performed. Matrix effects in the samples were corrected for by applying theoretical alpha factors (calibration factors used to broaden the concentration range of the instrument) and measured line overlap factors to the raw X-ray intensities that were measured.

The XRF measurement errors were derived from the comparison of the published uranium and thorium concentrations in the granite standard (NIM-G) and the measured values. The published concentration for uranium was 15 ppm, while 19 ppm was measured. For thorium the published value was 52 ppm, while 53 ppm was measured. This relates to measurement errors of 27 % and 1.9 % for uranium and thorium respectively. For the determination of the measurement error in the potassium, a sub sample of the KCl standard, used in the calibration of the radiometry (refer to section 4.2.4.3) was analysed. The measurement error was determined as 8.3 %. The systematic error due to the extrapolation to unknown concentrations was not determined, but it’s possible effect, mostly an underestimation of the value at higher concentrations, were observed in concentration comparisons with radiometry.

Table 7 ***The standards that were used in the XRF calibration procedures for both major and trace element analyses (Spicer, 2003).***

Place of purchase	Type of standard (reference name)	U (ppm)	Th (ppm)
United States Geological Survey, Reston	Andesite (AGV-1)	1.92	6.5
	Basalt (BHVO-1)	0.42	1.08
Geological Survey of Japan	Granodiorite (JG-1)	3.3	13.5
	Granodiorite (JB-1)	1.6	9
Canadian Certified Reference Materials Project	Syenite (SY-2)	284	379
	Syenite (SY-3)	650	1003
Council for Mineral Technology, South Africa	Dunite (NIM-D)	-	0.8
	Granite (NIM-G)	15	52
	Norite (NIM-N)	0.6	0.6
	Pyroxenite (NIM-P)	0.4	1.0
	Syenite (NIM-S)	0.6	1.0
Centre de Recherches Petrographiques et Geochimiques	Granite (GA)	5	17
	Granite (GH)	18	87

3.1 SAMPLING

3.1.1 Sampling Processes for the Heavy Mineral Sands

Thirty-three mineral sand samples were collected from the Mineral Separation Plant of Exxaro Namakwa Sands. The samples represented the complete separation processes, from input sand to output products, which were conducted on three separate days. The places where samples were taken are indicated in Figure 13 as green blocks and described as

- IRMS Feed,
- IRMS Magnetic Rejects,
- IRMS Non Magnetics,
- Minerals from Hot Acid Leach (samples taken here are referred to as Hot Acid Leach),
- Wet Gravity Tailings,
- Heavy Minerals Concentrate (samples taken here are referred to as SDO),
- 506 Feed,
- Rutile rejects,
- 511 Feed,
- Zircon Product,
- Zirkwa Product and
- Zircon Rejects.

The samples were homogenised and sieved to remove any debris. A sub-sample from each of the samples was crushed and milled to produce a powder with a grain size of smaller than 30 µm. An amount of 8 g of the powder was thoroughly mixed with 3 drops of Mowiol wax binder and pressed into a pellet with a pill press to 15 ton pressure. The pellet was dried for 30 minutes in an oven at 100 ºC, whereafter it was analysed for trace elements using XRF.

The rest of the sample was transferred to a Marinelli beaker and closed with a lid (no sealant were used). After mass and volume determinations (Table 8), the Marinelli beakers were left for more than 26 days for the sample to re-establish secular equilibrium in the uranium series to be counted on the radiometry gamma-spectroscopy set-up.

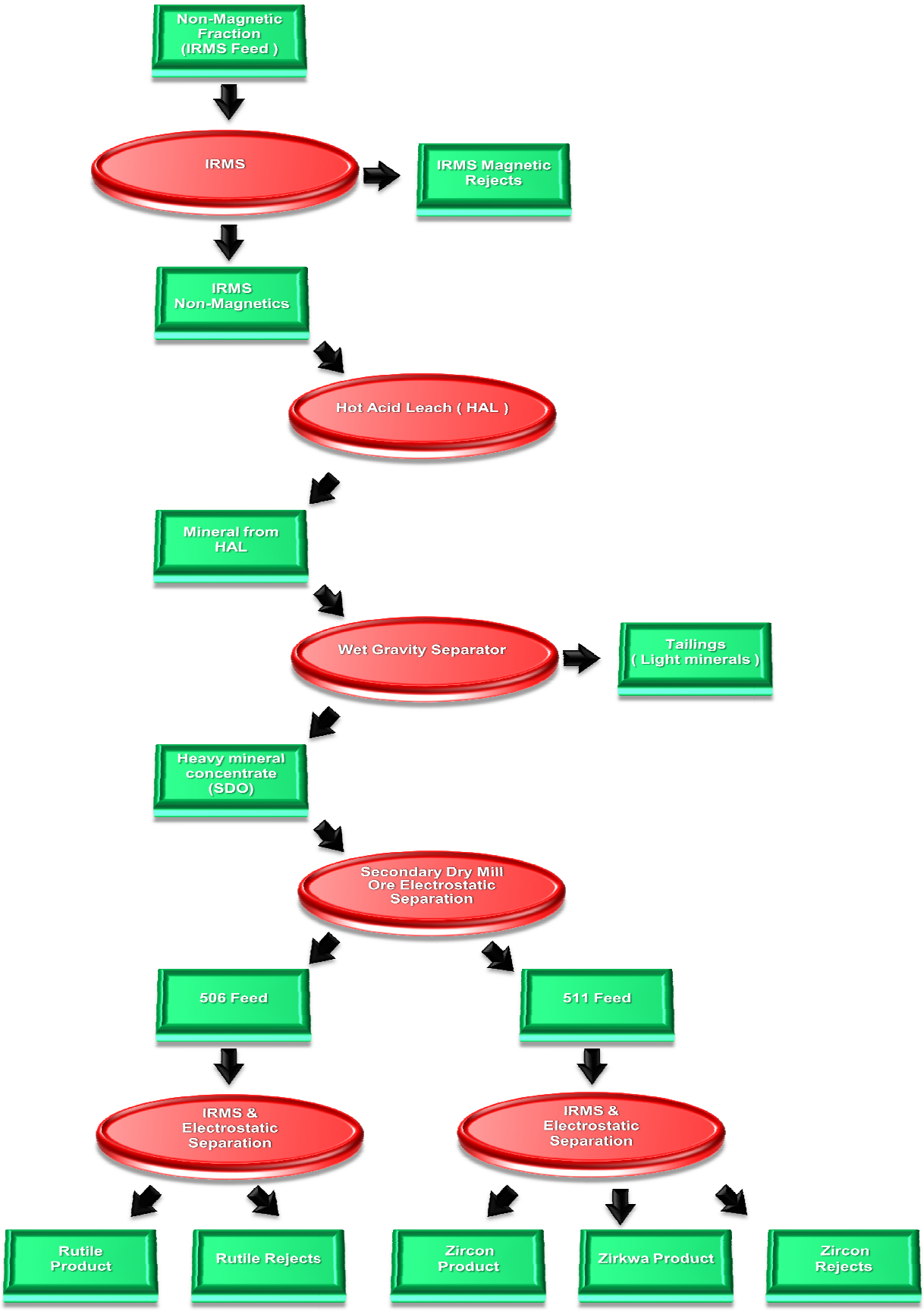

Figure 13. ***The sample locations, indicated by green blocks, within the Mineral Separation Plant at Exxaro Namakwa Sands.***

Table 8 ***Volumes and densities of the heavy mineral sand samples.***

Sample ID		Volume (ml)	Density (g/cm^3)
IRMS-Feed	1	1000	2.72
	2	1000	2.74
	3	1000	2.60
IRMS-Magnetic Rejects	1	1000	2.49
	2	1000	2.64
	3	1000	2.67
IRMS-Non Magnetic	1	1000	2.66
Hot Acid Leach Recycle	1	1000	3.05
	2	1000	2.88
	3	1000	2.81
Wet Gravity Tailings	1	1000	2.42
	2	900	2.03
	3	600	2.18
SDO	1	1000	3.04
	2	1000	2.93
	3	1000	2.84
	4	1000	2.90
506-Feed	1	1000	2.70
	2	1000	2.68
	3	1000	2.76
Rutile Rejects	1	1000	2.73
	2	1000	2.95
	3	1000	2.63
	4	1000	2.66
511-Feed	1	1000	3.05
	2	1000	2.96
Zircon Product	1	1000	3.08
	2	1000	3.04
	3	1000	3.05
Zirkwa Product	1	1000	2.92
	2	1000	3.05
Zircon Reject	1	1000	2.99
	2	1000	2.81

3.1.2 Sampling Processes for the Vineyard Soils

A total of forty two soil and rock samples were collected from Kanonkop, Simonsig and Spier vine estates. At each location, a 20 m × 30 m site was identified which represented a

part of the vineyard that was actively used in Pinotage production. Five sampling points were marked out (the sampling arrangement is illustrated in Figure 14) where samples were taken from the surface and at a depth of one meter. In the case of the Bottom Block of Kanonkop soil samples were taken from only the surface. On the Spier and Simonsig sites it was possible to take granite samples from the outcrop in the vicinity of the sampling area as well.

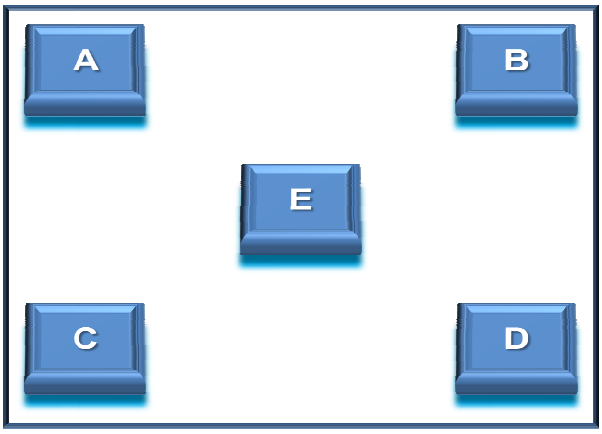

Figure 14. ***The sampling arrangement of a typical 20m x 30m block at each location. Samples were taken from the surface, at a depth of 1 metre and from outcrop.***

Afterwards the samples were washed, oven-dried, homogenised and sieved to remove any debris. A sub-sample of each of the samples was crushed and milled to produce a powder with a grain size of smaller than 30 µm. An amount of 8 g of the powder was thoroughly mixed with 3 drops of Mowiol wax binder and pressed into a pellet with a pill press to 15 ton pressure. The pellet was dried for 30 minutes in an oven at 100 ºC, where after it was analysed for trace elements using XRF. The trace elements and their concentrations, as found in one of the Kanonkop samples are tabulated in Table 9 as an example.

Next the concentrations of the major elements (according to XRF definition, but better described as compounds) were derived. Firstly the H_2O content was determined by placing 1 g of the milled sample in an oven at 110 ºC for 60 minutes. Thereafter the sample was placed in an oven heated to 1000ºC to determine the Loss of Ignition (LOI). In this technique the volatile substances in the sample is allowed to escape or oxygen is added to the sample, until its mass ceases to change. The Loss of Ignition is made of contributions from the volatile compounds H_2O^+, OH^-, CO_2, F, Cl, S and in parts K and Na (if heated for too long). As a last step the sample was mixed with 10 g of Claisse flux and fused into a glass bead with a M4 Claisse fluxer for 23 minutes. The glass bead was

analysed for major elements using XRF. The major elements and their concentrations as found in one of the Kanonkop samples are tabulated in Table 10 as an example.

Table 9 ***The trace elements, determined by XRF, found in one of the Kanonkop samples.***

Element	Concentration (ppm)	Element	Concentration (ppm)
Mo	7.1	Th	25
Nb	17	Pb	20
Zr	452	Ga	18
Y	33	Zn	23
Sr	28	Cu	-3
U	6.5	Ni	19
Rb	121		

Table 10 ***The major elements, determined by XRF, found in one of the Kanonkop samples.***

Element	Concentration (ppm)	Element	Concentration (ppm)
SiO_2	73	MgO	0.40
TiO_2	0.67	CaO	0.11
Al_2O_3	13	Na_2O	0.00
Cr_2O_3	0.03	K_2O	1.4
Fe_2O_3	4.2	P_2O_5	0.08
MnO	0.04	H_2O^-	0.9
NiO	0.00	Loss of Ignition	6.0

The rest of the sample was transferred to a Marinelli beaker. After mass and volume determinations (Table 11), the Marinelli beakers were closed with a lid (no sealant were used) and left for more than 26 days for the sample to re-establish secular equilibrium in the uranium series to be counted on the radiometry gamma-spectroscopy set-up and radioisotope concentrations determined.

Table 11 ***Volumes and densities of the vineyard soil samples.***

Sample ID		Volume (ml)	Density (g/cm^3)
Kanonkop Bottom Block – Surface	1A	330	1.42
	1B	520	1.06
	1C	280	1.30
	1D	500	1.28
	1E	600	1.17
Kanonkop Top Block - 1m	2A	400	1.13
	2B	600	1.02
	2C	500	1.25
	2D	500	1.16
	2E	320	1.55
Kanonkop Top Block – Surface	3A	320	1.31
	3B	620	1.32
	3C	480	1.46
	3D	800	1.70
	3E	280	1.25
Kanonkop Top Block – Crushed	4 (1)	700	1.21
Rock	4 (2)	700	1.21
Spier – 1m	5-1m	740	1.65
Spier – Surface	5A	900	1.64
	5B	400	2.29
	5C	620	2.07
	5D	760	1.71
	5E	480	2.02
Spier - Crushed Rock	6	500	1.52
Simonsig Kriekbult – 1m	7-1m	400	1.18
	7-2m	240	1.08
Simonsig Kriekbult – Surface	8A	430	1.62
	8B	380	1.56
	8C	300	1.53
	8D	280	1.59
	8E	460	1.63
Simonsig – Surface	9A	175	1.23
	9B	370	1.09
	9C	170	1.18
	9D	750	1.00
	9E	200	1.48
Simonsig – 1m	9-1m(1)	220	1.52
	9-1m(2)	220	1.52
Simonsig Dam - Crushed Rock	10(1)	700	1.38
	10(2)	700	1.38
Simonsig - Crushed Rock	11(1)	400	1.46
	11(2)	400	1.46

CHAPTER 4 SET-UP AND CALIBRATION OF RADIOMETRY

Radiometry is suggested as an alternative to XRF, and for it to be a feasible substitute it must be validated against XRF in terms of accuracy and precision. For this validation radiometry was set-up and calibrated within the laboratory context to be applied in the measurement of heavy mineral sand and vineyard soils.

In this chapter the set-up and calibration procedures for radiometry are explained. It starts off with the Marinelli beaker that is chosen as sample container. The background signal, as well as the effort to shield this unwanted signal, is examined. As a result the minimum detectable activity of the detection system is calculated. In the next section the energy and resolution calibrations are described. Thereafter the detection parameters that could influence the results are analysed and optimised. The parameters include the calculation of the counting time to ensure good statistics, the selection of gamma rays used for analysis of a sample, the peak area calculation, the correction for the detection system dead time and the detector efficiency. Since the various samples were different in terms of their density and volume it is necessary to apply corrections to the detector efficiency. These corrections are reviewed and used in the calculation of the detector efficiency. Furthermore, radon loss is analysed and the resulting error in the uranium concentration is estimated. The section ends with an analysis of the accuracy and precision of the detection system after all the corrections and optimisations are implemented. Finally the errors associated with each measurement are discussed.

4.1 RADIOMETRY SET-UP

The different electronic components of the radiometry detection system were described already and will not be repeated here.

4.1.1 Marinelli Beaker Geometry

The concentrations of natural radioisotopes in environmental samples can be less than 15 parts per million. In order to reach a statistical error of less than 1 % in the counting statistics, long counting times or large volumes of sample are to be used (Debertin and Ren, 1989). A sample placed on top of the detector has the disadvantage that the counting efficiency is low because the sample is a distance away from the detector crystal. This

problem can be reduced by counting samples in a near 4π geometry to cover the detector volume from all directions. In this way the counting efficiency is increased while reasonable counting times are achieved. The best suited sample container that has the advantages of 4π geometry is a Marinelli beaker.

A Marinelli beaker, which is cylindrical in shape with an annular bottom that slides over the outer housing of the detector crystal, was used as the sample container. It had a volume of 1 litre and a wall thickness of 2.0 mm. The Marinelli beaker was 13.3 cm in height and had a top diameter of 13.9 cm, the inner cavity that fits over the detector was 8.40 cm wide and 7.79 cm in height. Furthermore, it had a volume of 1 litre, a wall thickness of 2.0 mm and the beaker and lid were made from polyethylene and polypropylene respectively. A typical Marinelli beaker is illustrated in Figure 15.

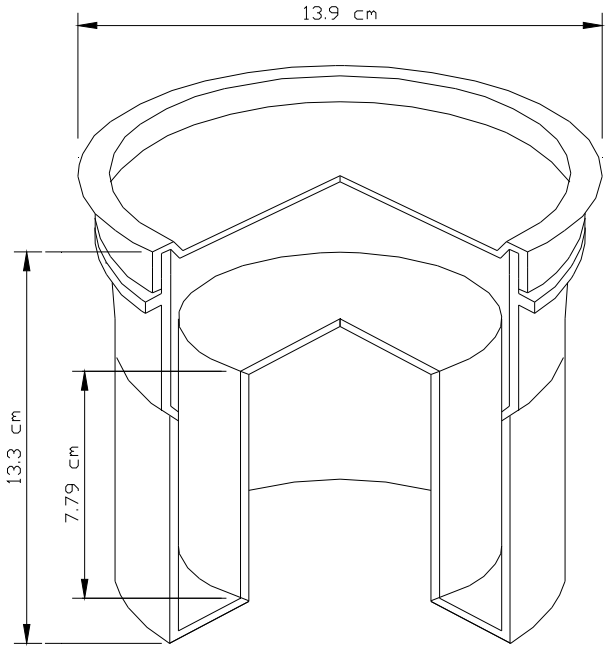

Figure 15. ***An illustration of a typical 1-litre Marinelli beaker, which was used as the sample container.***

4.1.2 Background Signal and Shielding

The existence of natural radioactivity in the environment as well as cosmic radiation gives rise to signals that contribute to the background spectrum (Verplancke, 1992). The contribution of the background to the observed spectrum depends on the detector type

and size. The relative size of the background signal also determines the minimum detectable activity (section 4.1.4). With the appropriate choice of shielding this signal can be reduced. Keeping in mind that contamination within the shielding material also contributes to the background, the materials used must be pure or at least with a low inherent activity. Lead and copper are two materials often used as shielding. For example, a 10 cm lead shield will reduce the background by two orders of magnitude (Nunez-Lagos and Vitro, 1996). The reason is that its high density and large atomic number enhances photoelectric absorption of gamma rays. Copper is a good absorber of the X-rays emitted by the lead after the gamma-ray interactions.

A rectangular lead castle formed the shield that accommodates the high purity germanium detector. The lead castle wall was low-activity lead of 100 mm thickness, formed by two rows of interlocking lead bricks. On top four lead plates (thickness ~100 mm) formed a lid that can slide open. The bottom also consisted of four lead plates (thickness ~100mm) with a small hole to fit the collar of the detector. The castle was supported and held together by a welded steel frame. Beneath the frame and the detector dewar is a steel plate to absorb radiation from the concrete floor and for levelling. In order to attenuate low energy X-rays, the cavity was lined with 2 mm electrolytic copper obtained from Goodfellow Metals Ltd (Cambridge, England). With the detector located at the centre of the cavity it could easily accommodate the 1.0 litre Marinelli beaker. This configuration (further on referred to as Lead Castle 2) was used in the measurement of the heavy mineral sand samples. An illustration of Lead Castle 2 is depicted in Figure 16.

The lead castle used in the measurement of the vineyard soil samples was the initial effort for shielding and therefore different from the previously mentioned one. The 100 mm thick wall also consisted of two rows of interlocking low-activity lead bricks. A steel frame and steel plate (with a hole to fit around the detector collar) formed the bottom onto which the bricks were placed. In addition, two lead plates of 20 mm thickness and width of 150 mm were placed on top of the castle to act as a removable lid. This configuration is further on referred to as Lead Castle 1.

The background count rate was obtained by measuring a 1 litre Marinelli beaker filled with water placed on the detector for a counting time of 5 days.

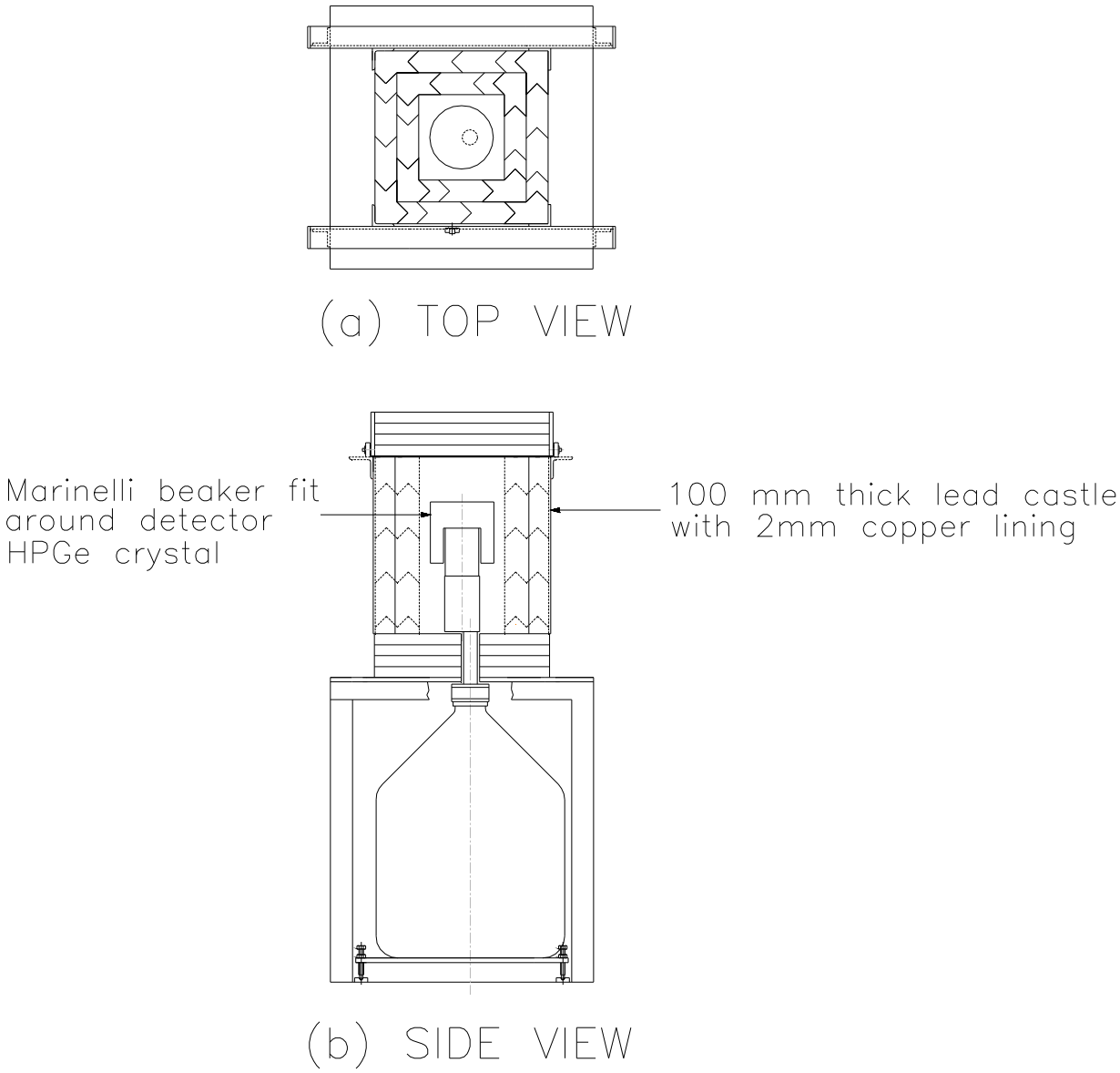

Figure 16. ***An illustration of the Lead Castle 2 set-up.***
It consists of the lead castle, supporting frame and steel plate onto which the dewar is placed. Also depicted is the lead castle cavity with a Marinelli beaker fitted over the detector.

The background count rate was regularly monitored during the counting of samples and no evidence of any significant variations was found. Of the total background spectrum only the photopeaks that correspond to the ones used in the analysis were of interest. The count rates of the background in these photopeaks are tabulated in Table 12.

Table 12 ***The net count rates of the photopeaks in the background spectrum that were used in the calculation of the ^{238}U, ^{232}Th and ^{40}K concentrations.***

Energy (keV)	Net Count Rate Lead Castle 2 (cnts.10^{-3}s)	Net Count Rate Lead Castle 1 (cnts.10^{-3}s)
338.32	1.12	1.26
351.92	1.86	2.17
463.01	0.1	1.81
583.19	0.91	9.27
609.31	1.89	12.5
727.33	0.82	1.67
794.95	0.42	2.81
860.56	0.17	2.55
911.21	1.40	14.6
934.06	0.32	1.79
1120.3	0.44	9.35
1238.1	0.15	4.67
1460.8	4.21	129
1729.6	0.01	1.96
1764.5	0.65	12.7
2204.2	0.18	4.38
2614.5	2.80	39.7

A typical example of the background spectrum of Lead Castle 2 is depicted in Figure 17. The photopeaks seen in the spectrum are from the natural radioactivity found in the lead and surrounding materials. In Figure 18 the Lead Castle 2 background spectrum is compared to the one of Lead Castle 1 and the background spectrum in the absence of any shielding. The effect of the shielding is clearly seen in this comparison, and also illustrates that Lead Castle 2 was an improvement over Lead Castle 1.

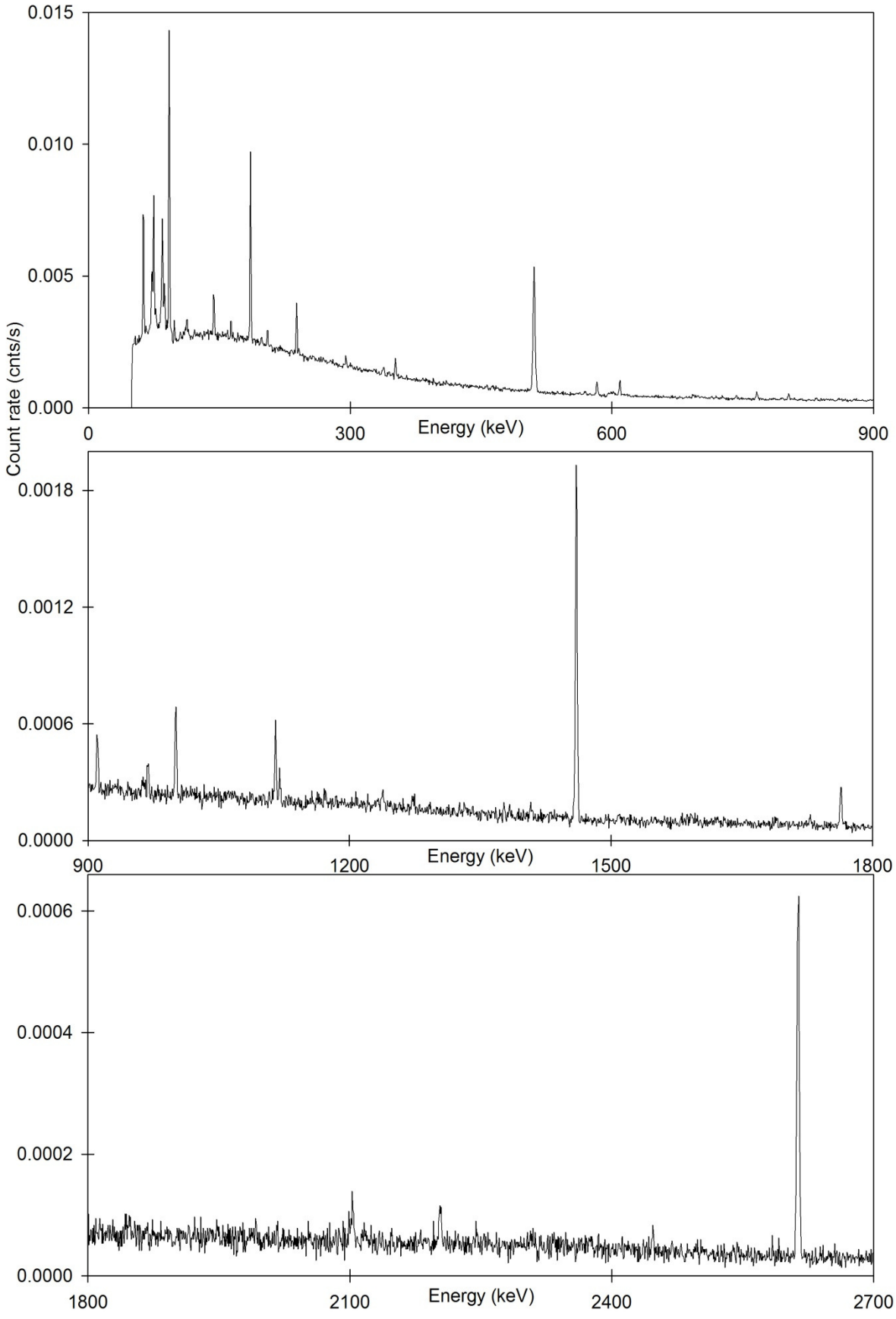

Figure 17. ***The background spectrum of Lead Castle 2 for the energy range 0 - 2700 keV.***

The photopeaks are from the uranium and thorium series decay products and ^{40}K found in the shielding and surroundings.

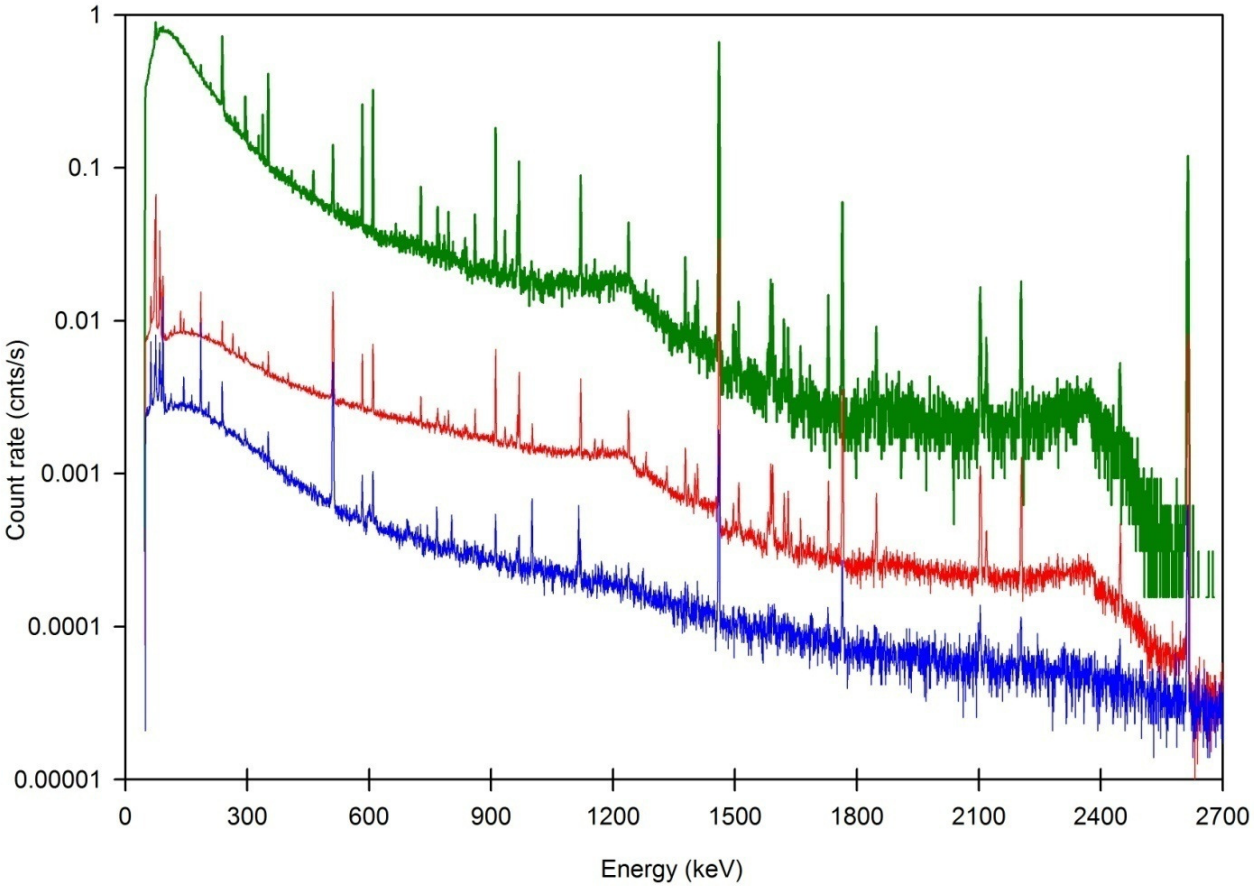

Figure 18. ***Graphical comparison of the different observed background spectra: no shielding Top, Lead Castle 1 Middle and Lead Castle 2 Bottom.***
The difference due to the effect of the shielding is clearly illustrated.

4.1.3 Minimum Detectable Activity

The minimum detectable activity (MDA) for each of the photopeaks was calculated (Table 13) for both the Lead Castle 1 and Lead Castle 2 configurations. The values were obtained for a sample counting time of 3600 s and efficiency derived for a 1 litre zircon sample. Although none of the analysed samples had activities below the MDA values, they do prove that Lead Castle 2 is a better configuration than Lead Castle 1 and well suited to measure low activity samples.

Table 13 ***The MDA values for the photopeaks used in the analysis using both lead castle set-ups.***

Energy (keV)	MDA Lead Castle 2 (Bq)	MDA Lead Castle 1 (Bq)
338.32	0.81	1.7
351.92	0.35	3.4
463.01	1.7	2.2
583.19	0.63	10
609.31	0.46	12
727.33	1.9	3.9
794.95	2.9	2.1
860.56	2.6	2.8
911.21	0.76	13
934.06	2.7	1.7
1120.3	1.2	8.8
1238.1	2.7	3.9
1460.8	5.1	118
1729.6	5.8	2.9
1764.5	1.8	13
2204.2	4.9	3.4
2614.5	1.9	39

4.2 CALIBRATION AND ANALYIS OF DETECTION SYSTEM

In order to calculate concentrations, the detection system must first be calibrated and the detection parameters that could influence the results analysed. In this section these factors are discussed. It includes the energy calibration for determination of the corresponding gamma ray energies for the various signal pulses. Another calibration was that of resolution in order for the software to determine the correct peak widths. Detection parameters that were analysed and then optimised or corrected for were: the counting time, selection of photopeaks, the peak area calculation, dead time and the detector efficiency. Relating to the detector efficiency the effects of coincidence summing, volume of the sample, self-absorption and density on the obtained results are discussed.

Accordingly corrections for the effects that are applicable are incorporated in the calculation of the efficiency. The error in the uranium concentration due to radon loss via diffusion from the Marinelli beaker was also estimated. Lastly the accuracy and the precision of the detection system were analysed.

4.2.1 Energy and Resolution Calibration

To execute the energy and resolution calibration of the counting system, a liquid reference sample in Marinelli geometry was used. It was chosen such that the gamma ray photopeaks of the included radioisotopes were evenly spread across the energy range of interest. The 1 litre source (obtained from the CSIR South Africa, reference date 14/01/2002) is a 0.1 Molar hydrochloric acid solution spiked with accurately known concentrations of ^{152}Eu (6.550 ± 0.197 kBq/l), ^{137}Cs (0.661 ± 0.013 kBq/l) and ^{60}Co (1.907 ± 0.381 kBq/l).

The reference sample was counted for 7200 seconds to obtain a statistical error of less than 2 % in the lowest intensity photopeak. After acquisition regions of interest (ROIs) were set around the prominent peaks of ^{152}Eu (Figure 19) using the *Peak Search* function within the OxfordMCA software. To ensure that the full photopeak is included in a ROI, the width of the ROIs was chosen to be 5 times the peak's FHWM. The energy calibration was done using the *Energy by ROI centroids* calibration procedure found within the software. The software fitted the best-fit quadratic function,

$$\text{keV} = -1.506 + (6.469\times10^{-1}\times\text{Channel}) + 9.321\times10^{-8}\times(\text{Channel})^2, \qquad 4.1$$

to calibrate the MCA channel numbers in terms of energy.

Using the *Detector Resolution* calibration procedure, in the OxfordMCA software, the software fitted a best-fit quadratic function,

$$\text{Resolution} = 1.058 + (9.732\times10^{-4}\times\text{Energy}) - 1.256\times10^{-7}\times(\text{Energy}^2), \qquad 4.2$$

through the same photopeaks for resolution calibration.

The energy calibration was verified by using the the *Peak Search* function to locate the photopeaks of ^{137}Cs and ^{60}Co. Centroid values were calculated as 661.2 keV, 1173.2 keV

and 1332.5 keV, which accurately correspond with the known values. The resolutions of these peaks were calculated as 1.65 keV, 2.03 keV and 2.13 keV respectively.

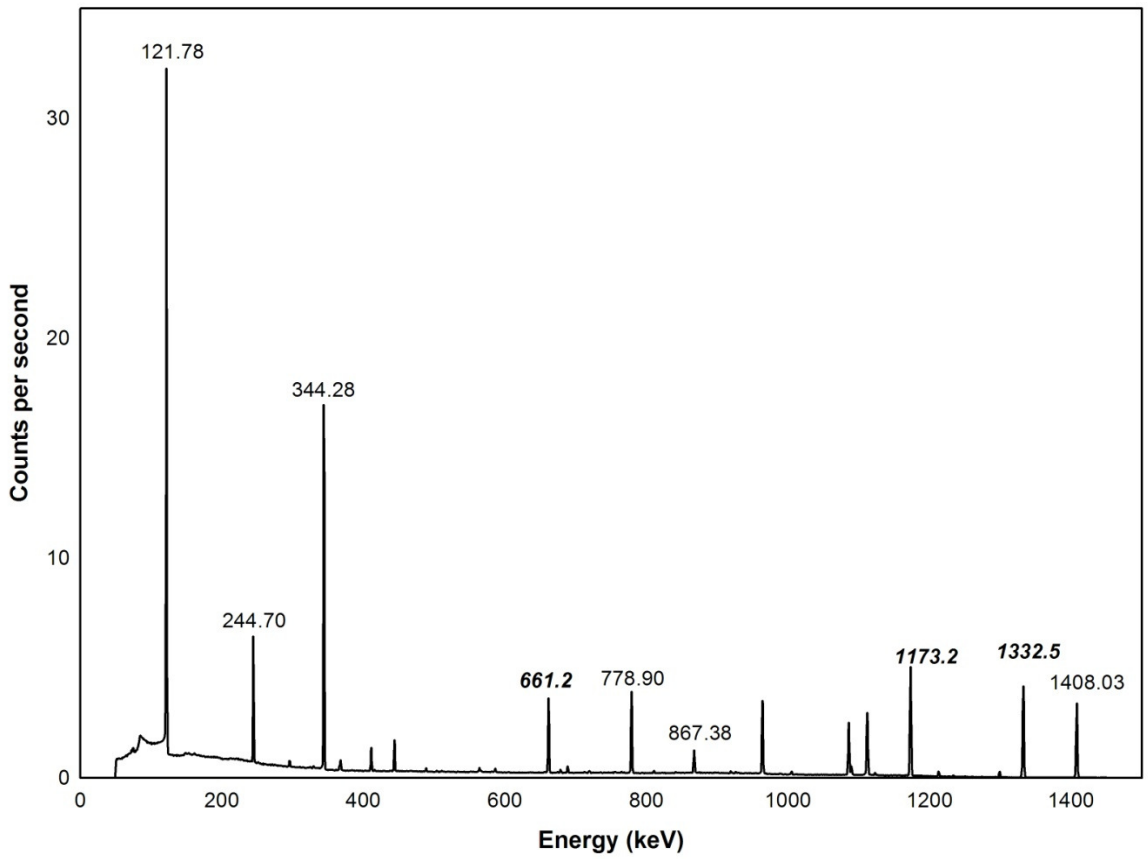

Figure 19. ***The spectrum of the liquid reference sample containing ^{152}Eu, ^{60}Co and ^{137}Cs.***

The photopeaks of ^{152}Eu (in normal font) were used for the energy and resolution calibration. The accuracy of the energy calibration was verified with the 661.2 keV photopeak of ^{137}Cs and the 1173.2 keV and 1332.5 keV photopeaks of ^{60}Co.

4.2.2 Calculation of Counting Time

Samples were counted in close Marinelli beaker geometry with the criteria that the net peak areas of the photopeaks have a statistical error of less than 2 %. For this requirement the equation given by Knoll (1979) for optimisation of the statistical error in counting experiments, with the 2 % criterion,

$$\sigma_{N_i} = \sqrt{\frac{G_i}{T_{Gi}} + \frac{B_i}{T_B}} = 0.02 \times N_i, \qquad 4.3$$

was applied to each sample. From Equation 4.3 the counting times (T_{Gi}) for the individual selected photopeaks were calculated as

$$T_{Gi} = \frac{T_B G_i}{T_B (0.02 N_i)^2 - B_i}, \qquad 4.4$$

with B_i the background count rate obtained from a five day (T_B) measurement with an Marinelli beaker filled with water. The net count (N_i) was calculated by

$$N_i = G_i - B_i, \qquad 4.5$$

It was assumed that the gross count rate (G_i) will not change over the sample measurement time, so it was determined by counting each sample for 10 minutes. From the counting times, T_{Gi}, the highest counting time was rounded up to the nearest hour (to further improve the counting statistics) and used as the sample's counting time T_S.

4.2.3 Photopeaks in Gamma Spectra

Selected Gamma Rays

The uranium and thorium decay series emit gamma rays at more than 100 energies each (Firestone, 1996). Of these, sixteen energies were selected for use in routine analysis of samples. The selection was based on three criteria: photopeak energy above 200 keV, photon intensity and peak separation. To ensure that X-rays originating in the shielding is not mistakenly identified as gamma rays, all gamma rays below 200 keV were omitted. The gamma rays with the highest photon intensities were selected to reduce counting times. Photon intensity is the fraction of all the decays that lead to the emission of a specific photon. The higher the number, the more pronounced the photopeak in the spectrum. In some cases high intensity gamma rays are emitted at nearly the same energy as lower intensity gamma rays from another decay series. An example is the 238.63 keV gamma ray from ^{212}Pb (thorium series) and the 241.98 keV gamma ray from ^{214}Pb (uranium series). As this type of interference complicates peak area calculation, these gamma rays were not selected. Instead gamma rays with lower intensities that were easier to separate from neighbouring photopeaks were chosen. The selected gamma rays are tabulated in Table 14.

In the case where a sample contains both potassium and thorium an exception to the above criterion is made. Actinium-228 emits a gamma ray at 1459.2 keV with an intensity

of 0.798 % (Firestone, 1996), which interferes with ^{40}K only gamma ray at 1460.8 keV. As the detector cannot distinguish between these two energies, a correction to the ^{40}K concentration is made. This correction is calculated as 0.798 % times the sample's thorium concentration and subtracted from ^{40}K concentration determined from the 1460.8 keV peak.

Table 14 ***The uranium, thorium and potassium concentration in samples were calculated from the area of the photopeaks at the following gamma ray energies (Firestone, 1996).***

Series	Energy (keV)	Intensity (%)
Uranium		
	351.92	35.79
	609.31	44.79
	934.06	3.03
	1120.29	14.80
	1238.11	5.86
	1729.60	2.88
	1764.49	15.36
	2204.21	4.86
Thorium		
	338.32	11.25
	463.01	4.44
	583.19	30.36
	727.33	6.58
	794.95	4.34
	860.56	4.47
	911.21	26.60
	1459.14	0.80
	2614.53	35.64
Potassium	1460.8	10.67

Peak Area Calculation

The number of counts under each photopeak i.e. peak area, is essential in the calculation of the concentration. To ensure that the peak area calculation is consistent each time a sample is measured, a standard set of ROIs were used. This set was obtained by counting each of the reference samples and setting a ROI around the appropriate photopeaks. The width of the ROIs was set to 5 times the peak's FWHM, which was calculated by the OxWinMCA software.

From these ROIs the OxWinMCA software calculates the net area of a photopeak (N) in a sample using the expression,

$$N = S - K, \tag{4.6}$$

where S is the gross counts in the peak ROI and K is the continuum calculated by

$$K = \left(\frac{P}{2n}\right)(C_1 + C_2). \tag{4.7}$$

In this equation P is the number of channels in the peak ROI, n the number of continuum channels on each side and C_1 and C_2 are the sum of counts in the continuum region to the left and right of the peak respectively. These ROIs were used in a similar way on the background spectrum to calculate the net area (B) of the contribution of the background signal to a photopeak at that energy. The observed peak area, A_o, is calculated as

$$A_o = N - B\frac{T_S}{T_B}, \tag{4.8}$$

with T_S the counting time of the sample and T_B the counting time of the background.

Correction for System Dead Time

System dead time was calculated by the OxWinMCA software. It was generally low (1-5 %) with a few exceptions that were at most 18 %. The software calculated the total counts using the live time, so manual correction for dead time was not necessary.

4.2.4 Calculation of the Detector Efficiency

The detector efficiency values are amongst others dependent on the type of reference sample from which it was derived. As all the analysed samples differ in volume and density

from the reference sample, corrections for these differences must be made. In this section these corrections and the resulting calculation of the detector efficiency are discussed.

Literature Review of the Different Efficiency Corrections

Coincidence Summing Correction

Coincidence summing can be a complex effect and depends on the type of decay scheme, the efficiency of the detector and the source-to-detector geometry (Park and Jeon, 1995). It occurs with radioisotopes which are detected that emit more than one photon within the dead time of the detector system. These photons will then be detected as a single pulse. In this case the detector output pulse will correspond to the sum of the energies of the individual gamma rays. This results in a loss in the photopeaks of the corresponding gamma rays. If this effect is not corrected it can lead to errors greater than the accuracy required (Debertin and Helmer, 1988). From experiments conducted De Felice et al. (2002) states that this error can be between 5-10 % for volume sources and between 20-50 % for close source-detector geometries.

Coincidence summing is often a problem in efficiency calibrations that are performed with a mixture of radioisotopes which emit multiple gamma rays. For this reason many authors (e.g. (Korun and Martinčič, 1993; Sima and Arnold, 2000; Abbas, 2001; Garcia-Talavera, 2001; De Felice et al., 2002 and Dryák et al., 2002 have discussed the correction needed. Often mathematical expressions are used to directly calculate the correction factors based on the photon emission probabilities, photon path length through the detector volume and detector efficiencies. Although a very tedious exercise, when used with specific detector parameters the results of these expressions show very good agreement with experiment e.g. Abbas (2001). The alternative is to obtain results through Monte Carlo simulations e.g. Sima (2000). With this method, corrections for different radioisotopes can easily be done and detector parameters quickly changed. Garcia-Talavera (2001) was one of the first authors to derive corrections for the natural decay series based on a Monte Carlo simulation from a multi-radioisotope mixture. She concluded that corrections are essential for the radioisotopes ^{214}Bi (uranium series), ^{228}Ac and ^{208}Tl (thorium series).

Absorption, Density and Sample Volume Corrections

Using a Marinelli beaker close to the detector crystal, the measurement of the peak area counts is subject to self-absorption. Self-absorption is when the gamma rays emitted by a sample are reabsorbed in the sample material. The photopeak area will be less; hence a lower efficiency value is obtained. It is increasingly problematic with high density material, as self-absorption is highly dependent on both the sample's atomic number and density (Vargas et al., 2002). As an example, the absorption in zircon can be as much as 23 times that of water (Sima, 1996). For this reason a self-absorption correction factor is used for every sample that is different in density from the reference sample.

These correction factors are difficult to calculate, so several authors (Sanchez et al. (1991), (Haase et al. (1993) and Vargas et al.(2002)) used Monte Carlo methods to determine it for their specific detector set-ups. Other authors for example Ay□ik (1992); Park and Jeon (1995); Boshkova and Minev (2001) and Hasan et al. (2002) determined these factors experimentally for different volumes and densities. The downside of this method is that a large number of samples of different densities must be prepared.

However, if the composition of the sample is known, analytical models can be used to approximate these correction factors. This is indeed the case for this study and hence these methods are discussed next.

Debertin and Ren (1989) approximate the detector by a point at the detector centre on the axis of the cylindrical Marinelli beaker. For an arbitrary infinitesimal volume element *dV* within the Marinelli beaker, a photon from within the sample that is emitted in the direction of the detector will have an efficiency that is expressed by

$$\varepsilon_a(E) = c(E)\frac{\exp[-\mu(E)z_a]}{z^2}. \qquad 4.9$$

Here *c(E)* is a proportionality constant, z_a the thickness of sample from the point of photon emission, *z* the distance between the point detector and the point of photon emission and *μ(E)* the linear attenuation coefficient of the sample. By integrating over the sample volume *V*, the total efficiency is expressed by

$$\varepsilon(E) = \frac{c(E)}{V}\int_V \frac{\exp[-\mu(E)z_a]}{z^2}dV = \frac{c(E)}{V}I(\mu), \qquad 4.10$$

with

$$I(\mu) = \int_V \frac{\exp[-\mu(E) z_a]}{z^2} dV. \qquad 4.11$$

Using the indices *r* for reference sample and *s* for the sample, the efficiency for the sample is expressed by

$$\varepsilon_s(E) = \varepsilon_r(E) \frac{I(\mu_s)}{I(\mu_r)} = \varepsilon_r(E) f_a, \qquad 4.12$$

where f_a (the ratio of the integrals) is the self-absorption correction factor due to the difference in density between the samples. Despite the fact that this is a simplified approach, the authors state that good accuracy is expected.

Dryák et al. (1989) used a different approach. He suggests a correction, K_2 to the measured peak area A_m. He assumes the Marinelli beaker to be a spherical shell source and uses the model of absorption in a foil of thickness *t.* The corrected peak area, A_c is then expressed by,

$$A_c = A_m K_2 = A_m \frac{\mu t}{1 - e^{-\mu t}}, \qquad 4.13$$

with *t* the thickness of the sample and μ the linear attenuation coefficient of the sample. Using a constant value of t = 1.6 cm (from the dimensions of the Marinelli beakers he used), he shows good agreement with his experimental data.

Sima (1991) disagrees that t = 1.6 cm is a constant value. He states that the photon path length in a Marinelli beaker has a wider distribution than in a shell source. This means that there is a variation in the thickness, depending on the dimensions of the Marinelli beaker. He improves on the model of Dryák by deriving an equation for *t* based on the evaluation of the mean photon path length through the sample,

$$t = \frac{1}{p}\left[f(r_e, h_1) + f(r_e, h_0) - f(r_i, h_2) - f(r_i, h_0) \right] \qquad 4.14$$

with

$$p = 1 + \frac{h_0}{\sqrt{h_0^2 + r_i^2}} \qquad 4.15$$

and

$$f(r,h) = r \arctan\left(\frac{h}{r}\right) + \frac{h}{2} \ln\left[\left(\frac{r}{h}\right)^2 + 1\right]. \qquad 4.16$$

In equations 4.14 to 4.16 the outer and inner radius of the sample are given by r_e and r_i respectively. The heights h_0, h_1 and h_2 are related to the inner (h_i) and outer height (h_o) of the Marinelli beaker.

4.2.4.2 Efficiency Corrections

Coincidence Summing

Corrections for coincidence summing are unnecessary when the radioisotopes in the reference sample and in the analysed samples are the same. The rationale being that the same measure of coincidence summing occurs in both samples and hence the effect cancels out. In this study uranium, thorium and potassium reference samples were used and so no corrections were necessary.

Sample Volume Correction

Many of the samples differed in volume to the references samples. These differences were corrected for by determining the effective thickness, *t*, of each of the samples according to Equations 4.14 – 4.16. As this thickness is dependent on the height to which the beaker is filled (volume) the inner and outer heights h_i and h_o were determined by measurement.

Volumes were determined by adding 100 ml of water (measured with a 100 ml volumetric flask) into a Marinelli beaker until 1 litre was obtained. At each 100 ml step the water level was marked (there is a standard 1 litre marking on the Marinelli beaker for reference) and afterwards the height was measured with callipers.

These measured height and radii values together with the calculated *t* values are tabulated in Table 15. These values are also graphically represented in a cross-section presentation of the Marinelli beaker in Figure 20. The graph of effective thickness as a function of the volume is illustrated in Figure 21.

Table 15 ***The measured height and radii values and the calculated effective thickness value (t) of the Marinelli beaker for different volumes.***

Volume (ml)	Outer radius (r_e) (cm)	Inner radius (r_i) (cm)	Inner height (h_i) (cm)	Outer height (h_e) (cm)	Effective thickness *(t)* (cm)
100	6.580	4.334	1.746	1.746	0.6033
200	6.580	4.334	3.158	3.158	0.9544
300	6.580	4.334	4.668	4.668	1.245
400	6.580	4.334	6.100	6.100	1.466
500	6.580	4.334	7.616	7.616	1.661
600	6.943	4.334	7.786	8.290	2.110
700	6.943	4.334	7.786	9.110	2.388
800	6.943	4.334	7.786	9.754	2.570
900	6.943	4.334	7.786	10.420	2.733
1000	6.943	4.334	7.786	11.276	2.911

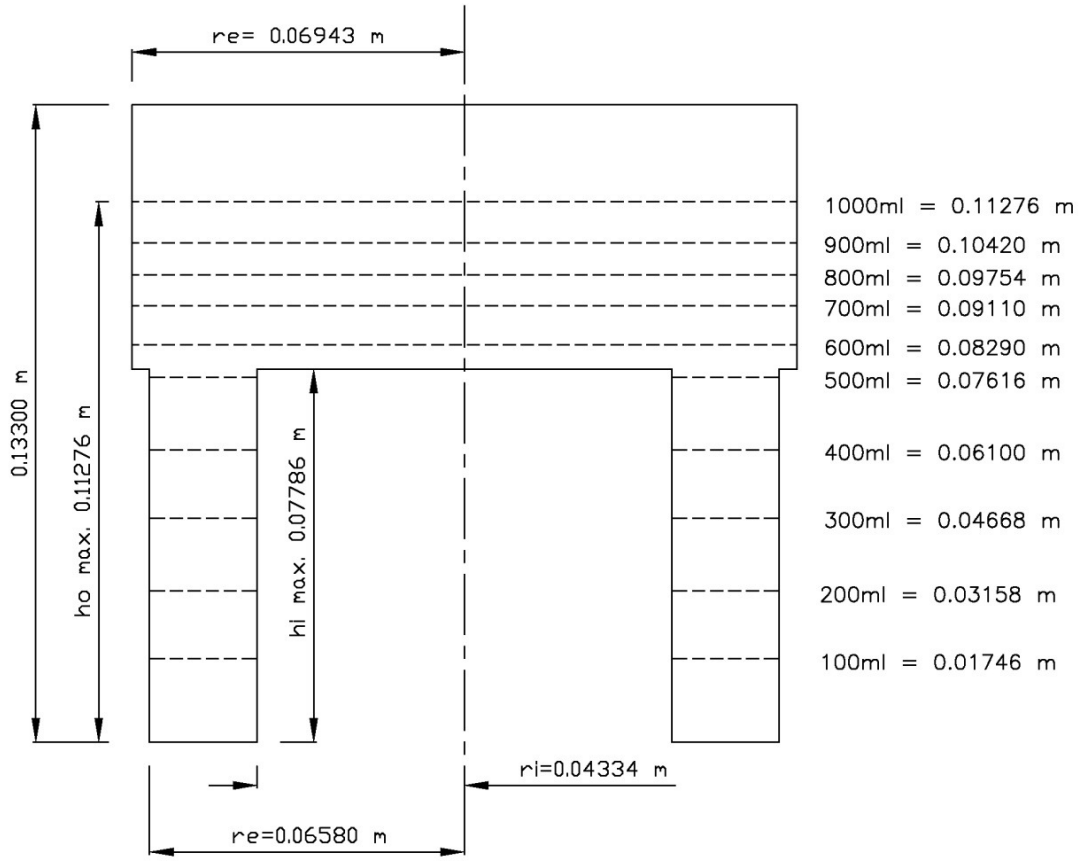

Figure 20. ***A cross-section presentation of a Marinelli beaker indicating the different volumes and the corresponding filling heights and radii (same line).***
These values were used in the calculation of the effective thickness, t.

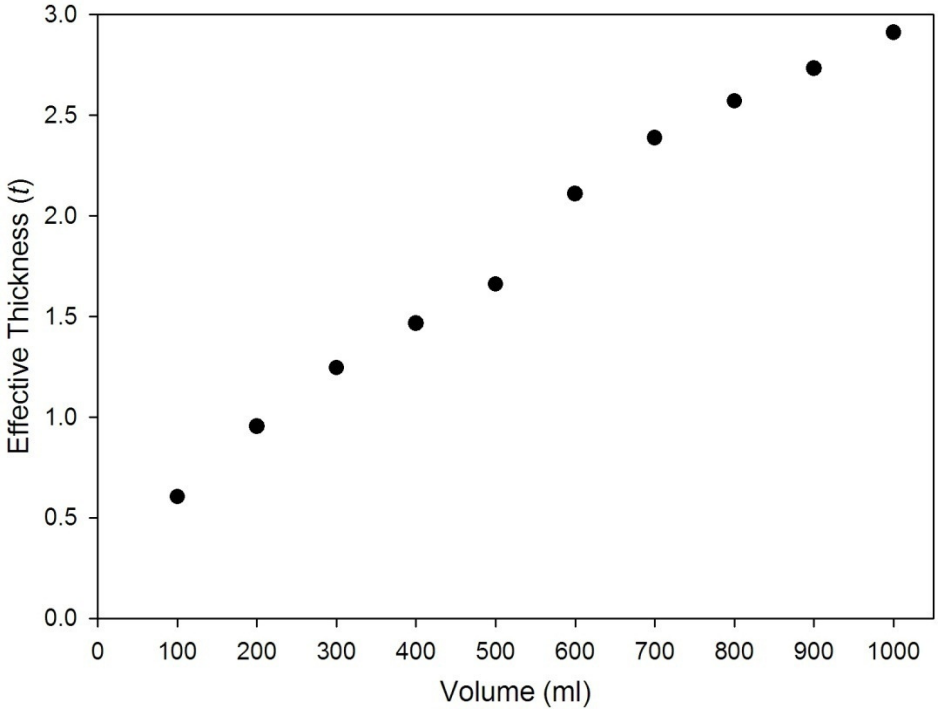

Figure 21. ***The effective thickness (t) as a function of volume for the Marinelli beaker used in this work.***

Self-absorption and Density Corrections

The self-absorption correction factors, $F_a(\mu)$, for every sample were calculated using the studies of Sima (1991) and Dryák et al. (1989) and are defined as

$$F_a(\mu) = \frac{1-\exp(-\mu t)}{\mu t}, \qquad 4.17$$

with t the effective thickness for the Marinelli beaker geometry and μ the linear attenuation coefficient of the sample at the different photopeak energies. The latter is the product of the sample density (mass to volume ratio) and its mass attenuation coefficients. The mass attenuation coefficients were calculated by determination of the elemental composition of the sample by XRF and adding the mass attenuation coefficients of each of the elements from the tables of Hubble (1999) and Berger and Hubbell (1987) according to Equation 2.40. A comparison between the mass attenuation coefficients for the reference samples and a zircon sample is depicted in Figure 22.

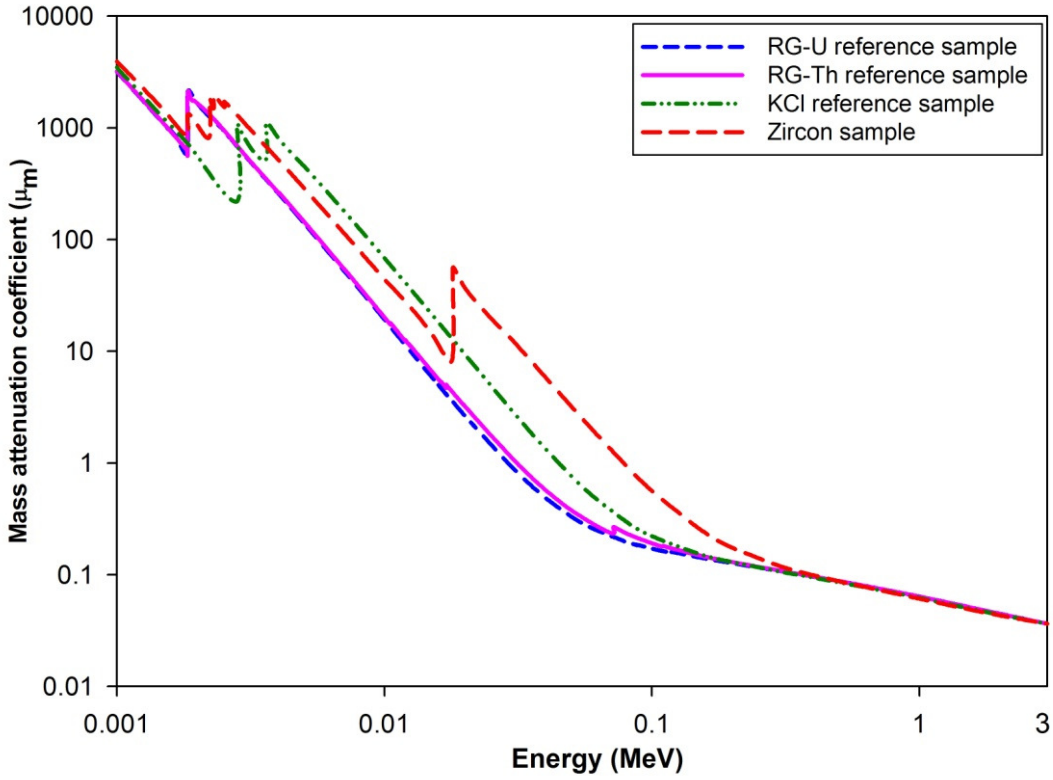

Figure 22. ***A comparison of the mass attenuation coefficients for the reference samples RG-U, RG-Th, KCl and one of the zircon samples, as a function of the photon energy.***
The mass attenuation coefficients were calculated by adding the mass attenuation coefficients (Hubbell, 1999) and (Berger and Hubbell, 1987) for every element found in the sample according to Equation 2.40.

Calculation of the Efficiency Values

Reference Samples

Two reference samples (RGU-1 and RGTh-1) with accurately known concentrations were obtained from the International Atomic Energy Agency (IAEA, 1987). They were used for the determination of the photopeak efficiency of the detector for all the prominent gamma energies of the uranium and thorium decay series. To determine the photopeak efficiency of the 1461 keV photopeak of ^{40}K, potassium chloride obtained from SAARCHEM South Africa, was used.

RGU-1 is a dilution of uranium ore in a silica powder with a uranium content of 400 ± 1.1 µg/g (IAEA, 1987). Given that the sample has a mass of 487.37 g (volume of 400.0 ml) the

specific activity was calculated to be 4940 ± 14 Bq/kg (Appendix D). The chemical composition, as described in the IAEA report, of this standard is tabulated in Table 16. RGTh-1 is a blend of britholite ore (2.765 %) and silica powder with a thorium content of 800 ± 8 µg/g (IAEA, 1987). With a mass of 515.73 g (volume of 400.0 ml) its specific activity was calculated as 3250 ± 33 Bq/kg (Appendix D). Table 17 summarises the chemical composition of this standard. The SAARCHEM potassium chloride sample was a pure KCl salt. With a mass of 494.72g (volume 400 ml) the calculated specific activity was 16252 Bq/kg.

Table 16 ***The chemical composition of RGU-1.***

Constituent	Mass %	Constituent	Mass %
SiO_2	46.4	Mg	0.01
U	0.04	Pb	0.008
Al	0.1	K	0.002
Fe	0.03	Ti	0.008
Ca	0.03	Si	0.002
Na	0.02	Th	< 1 µg/g
C	0.01		

Table 17 ***The chemical composition of RGTh-1.***

Constituent	Mass %	Constituent	Mass %
SiO_2	97.6	SrO	0.0194
CaO	0.700	MnO	0.0138
Re_2O_3+Y_2O_3	0.926	ZnO	0.0138
P_2O_3	0.246	NiO	0.00553
Fe_2O_3	0.160	TiO_2	0.0166
ThO_2	0.0910	Na_2O	0.0111
F	0.0359	K_2O	0.0113
MgO	0.0332	C	0.00829
Al_2O_3	0.0221	U_2O_8	0.000713

Efficiency Calculation

The reference samples RG-U, RG-Th and KCl were placed in Marinelli beakers, weighed and volume determined. To attain secular equilibrium it was left for 30 days after which the samples were counted for 7200 seconds to obtain a statistical error of less than 1 % in the lowest intensity photopeak. Peak areas for the selected gamma rays were obtained and efficiency values, $\varepsilon_{ref}(E)$, for the photopeaks were calculated using

$$\varepsilon_{ref}(E) = \frac{A_o}{T_S \cdot I \cdot C}, \qquad 4.18$$

with A_o the observed peak counts, T_S the counting time, I the photon intensity of the gamma ray of energy E and C the known concentration of the reference sample.

Hereafter the self-absorption correction factors $F_a(\mu_{ref})$ for the reference sample were calculated using Equation 4.17. Using these values the efficiency values, $\varepsilon_0(E)$, that are independent of volume, density or absorption, were calculated according to the equation of Sima and Dovlete (1997)

$$\varepsilon_0(E) = \frac{1}{F_a(\mu_{ref})}\varepsilon_{ref}(E) = \frac{\mu_{ref} t_{400ml}}{1-\exp(-\mu_{ref} t_{400ml})}\varepsilon_{ref}(E). \qquad 4.19$$

These efficiency values are tabulated in Table 18 and depicted in Figure 23. Since only the chosen photopeaks were needed there was no need for interpolation of the values and hence no function fitted through the values.

Not all of the efficiency curve values line up with one another. It is an indication that coincidence summing could have an effect on the photopeaks. This was judged by comparing the concentrations obtained for the individual photopeaks of uranium in two randomly chosen samples, Kanonkop Top Block Surface B and Zircon Rejects 2. The results (Table 19) indicated that the photopeaks of 934 keV, 1238 keV and 1729 keV have concentrations that are significantly higher or lower than the other photopeaks (Figures 24 and 25). Removing these photopeaks from the analysis resulted in average concentrations that were 0.7% (Kanonkop sample) and 0.4% (Zircon Reject sample) higher than previously.

Table 18 ***The efficiency values, $\varepsilon_0(E)$,which are independent of volume, density and absorption for the photopeaks used in the determination of concentration.***

Energy (keV)	$\varepsilon_0(E)$ values
338.32	0.0340
351.92	0.0360
463.01	0.0257
583.19	0.0211
609.31	0.0209
727.33	0.0214
794.95	0.0168
860.56	0.0176
911.21	0.0166
934.06	0.0150
1120.29	0.0133
1238.11	0.0124
1461	0.0124
1729.6	0.0126
1764.49	0.0104
2204.21	0.00869
2614.53	0.00643

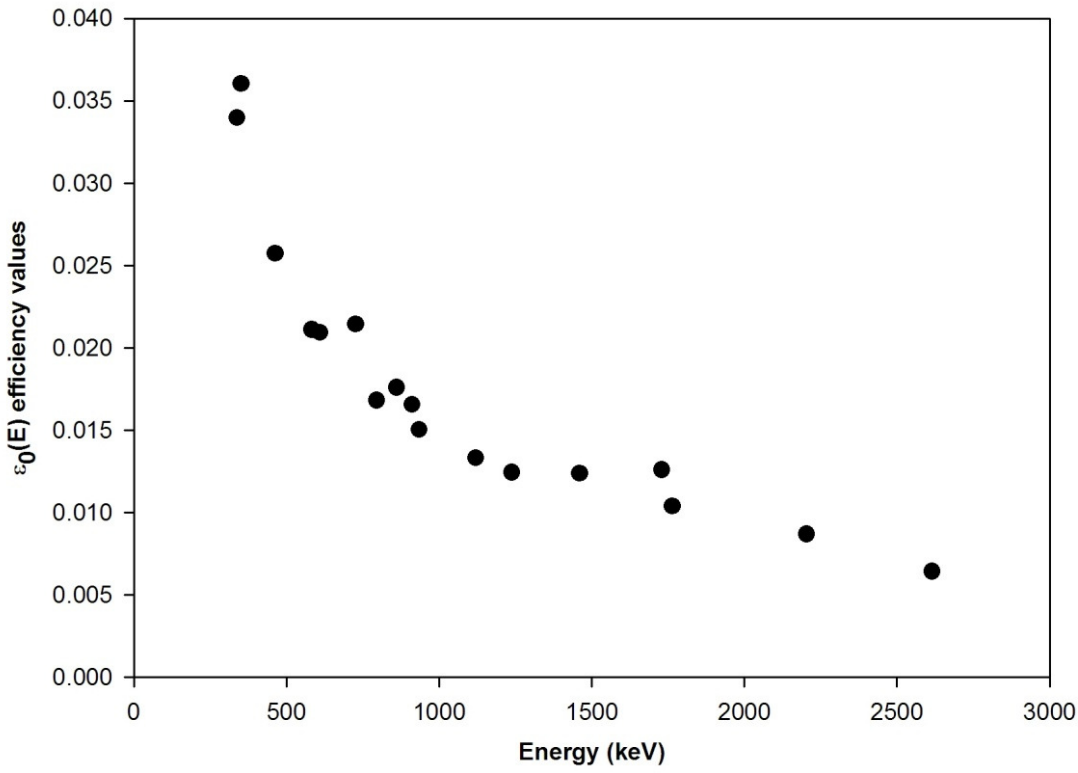

Figure 23. ***The efficiency values $\varepsilon_0(E)$, used in the determination of concentration.***

Table 19 ***Concentrations (ppm) for the individual photopeaks of uranium for Kanonkop Top Block B Surface and Zircon Rejects 2 (only statistical errors are shown).***

Energy (keV)	Kanonkop Top Block B Surface		Zircon Rejects 2	
	Concentration (ppm)	Statistical Error (ppm)	Concentration (ppm)	Statistical Error (ppm)
351.92	4.5	0.06	389	1
609.31	4.6	0.07	389	1
934.06	6.5	0.4	400	3
1120.29	5.0	0.2	386	2
1238.11	3.0	0.2	354	3
1729.6	1.7	0.3	337	2
1764.49	4.4	0.2	388	2
2204.21	4.1	0.4	382	3

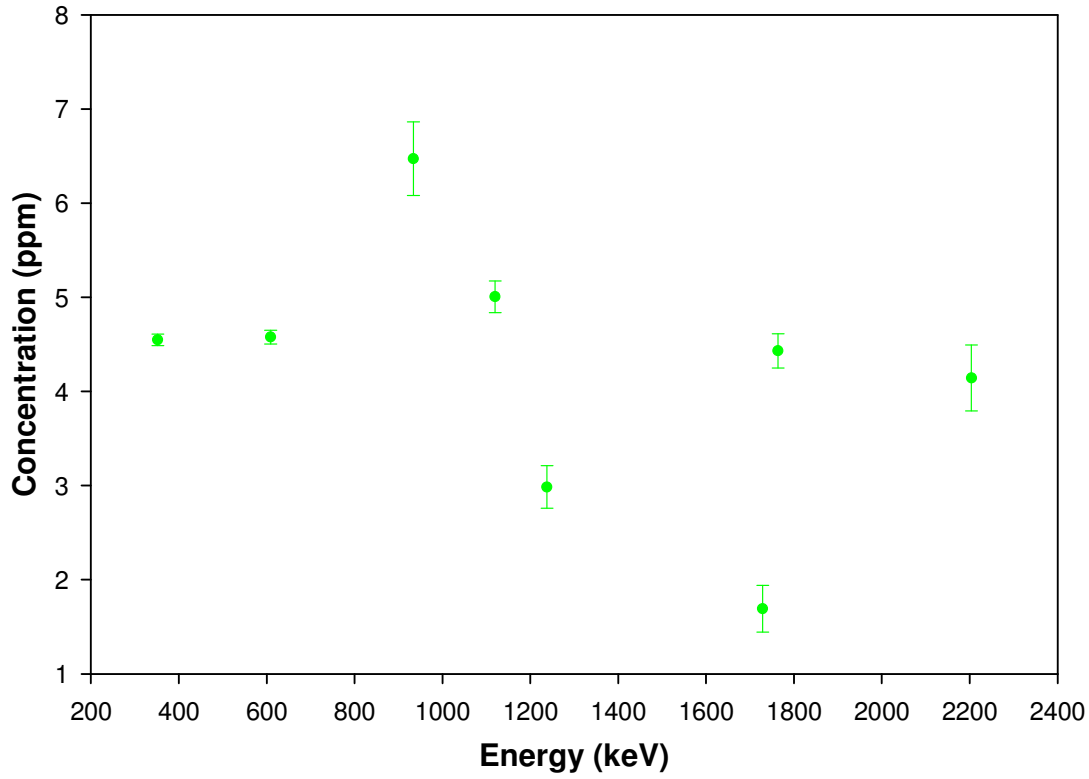

Figure 24. ***The concentrations (ppm) for the individual photopeaks of uranium for Kanonkop Top Block B Surface.***

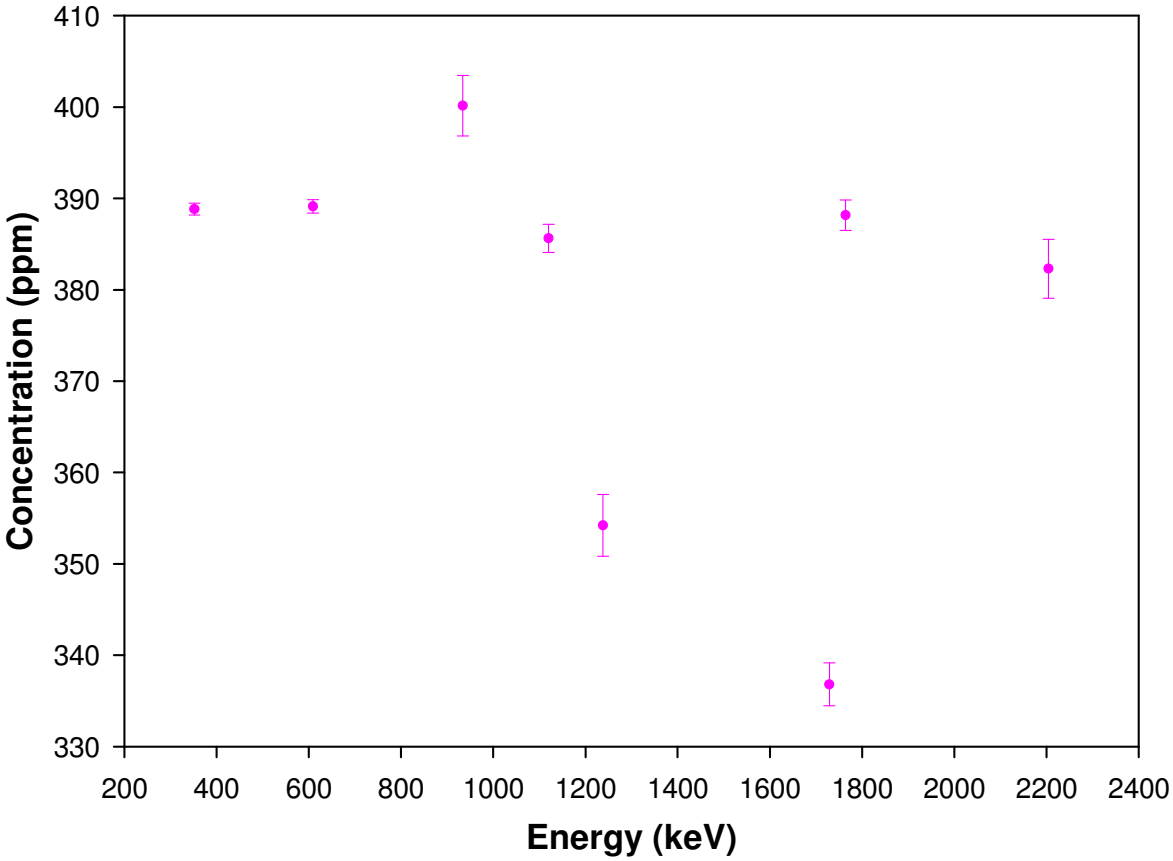

Figure 25. ***The concentrations (ppm) for the individual photopeaks of uranium for Zircon Rejects 2.***

Next the self-absorption correction factors, $F_a(\mu_{sample})$, for each sample was calculated according to Equation 4.17. These correction factors were multiplied with the $\varepsilon_0(E)$ efficiency values to obtain the volume, density and absorption corrected efficiency values:

$$\varepsilon_{sample}(E) = F_a(\mu_{sample}) \times \varepsilon_0(E). \qquad 4.20$$

The importance of the $F_a(\mu_{sample})$ factors is illustrated in Figure 26 and Figure 27. In Figure 26 these factors are depicted as a function of energy for different volumes of a zircon sample (ρ = 2.99 g/cm^3). From this figure it can be deduced that the error in the efficiency can be as much as 30 %, depending on the volume and energy, if these corrections are not used. Figure 27 depicts the correction factors as a function of energy for 400 ml for three samples that differ in elemental composition and density (ρ = 2.99 g/cm^3, 1.63 g/cm^3 and 1.21 g/cm^3). Again it can be used to determine the error when not correcting for the differences in density.

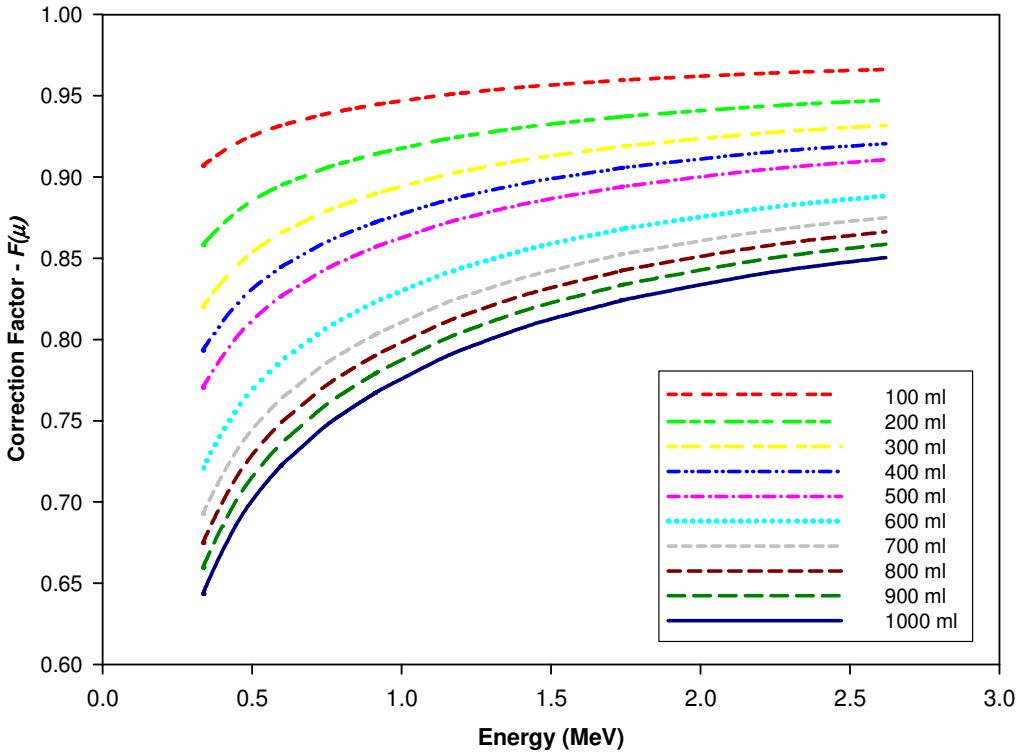

Figure 26. ***The self-absorption correction factor $F_a(\mu)$ as a function of energy for a zircon sample with a density of 2.99 g/cm^3 for different volumes.***

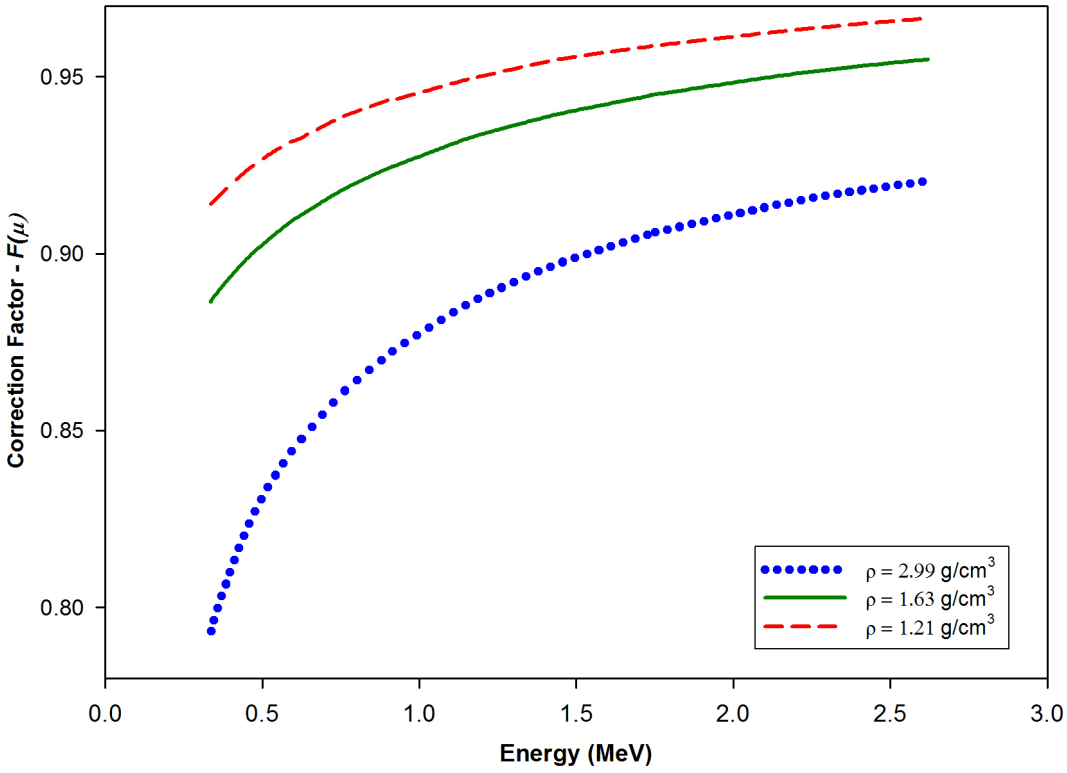

Figure 27. ***The self-absorption correction factor $F_a(\mu)$ for a 400 ml sample as a function of the energy for three samples with different elemental compositions and densities: ρ = 2.99 g/cm^3, 1.63 g/cm^3 and 1.21 g/cm^3.***

Equation 4.20 was experimentally verified to ensure that it is correct. This was done by measuring different volumes of the KCl reference sample and calculating the corresponding $\varepsilon_{sample}(E)$ values. Since the concentration was known, the efficiency according to Equation 4.18 could also be determined and compared. Excellent agreement was found between the two sets of values (Figure 28).

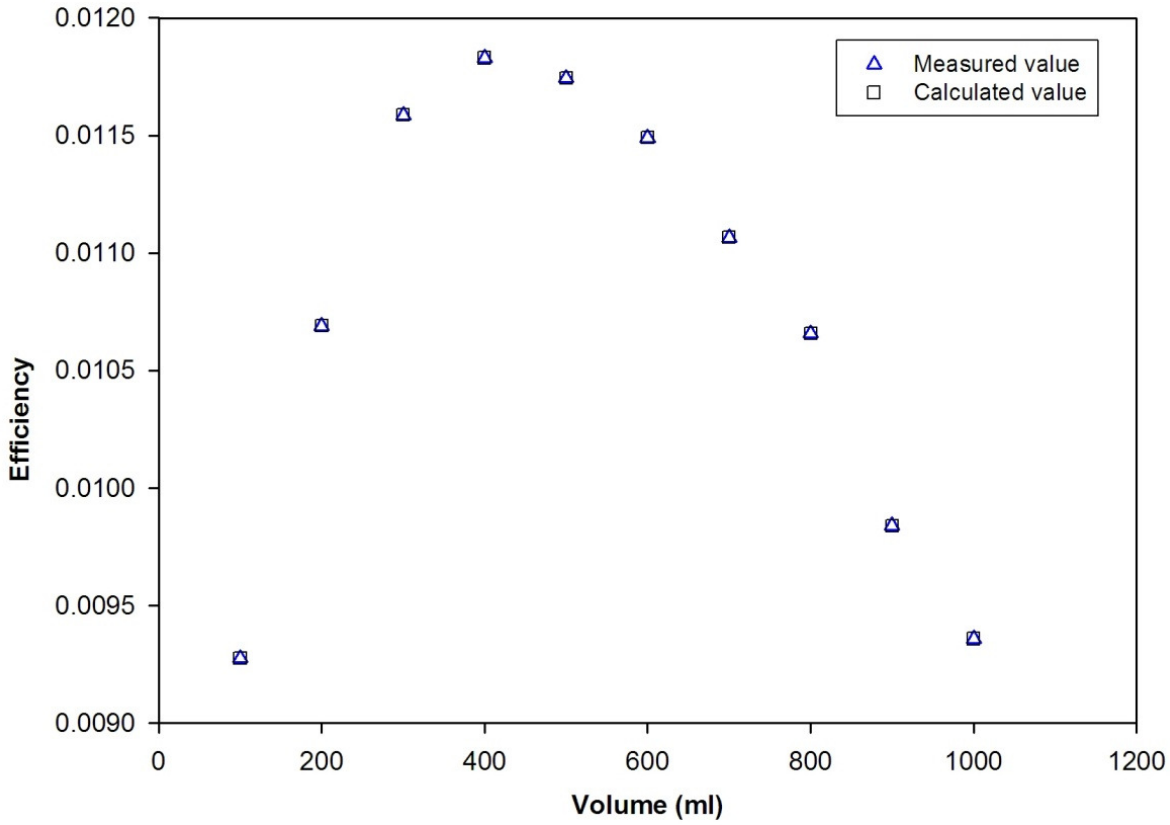

Figure 28. ***Comparison between the measured efficiency values of KCl at different volumes determined by Equation 4.18 to those determined by Equation 4.20.***

The method of correction factor calculation was also compared to the method of Debertin and Ren (1989). They did not involve a ε_0 value and from Equation 4.12 it was deduced that their self-absorption correction factor, f_a, and $F_a(\mu)$ from the present work is related by

$$f_a = \frac{F_a(\mu)_{sample}}{F_a(\mu)_{reference}}. \qquad 4.21$$

Using their sample density and Marinelli beaker geometry, the $F_a(\mu)$ self-absorption correction factors were calculated. Comparison showed excellent agreement with a

maximum difference of 0.3 % for the 450 ml and 0.08 % for the 1 litre geometry. This comparison is depicted in Figure 29.

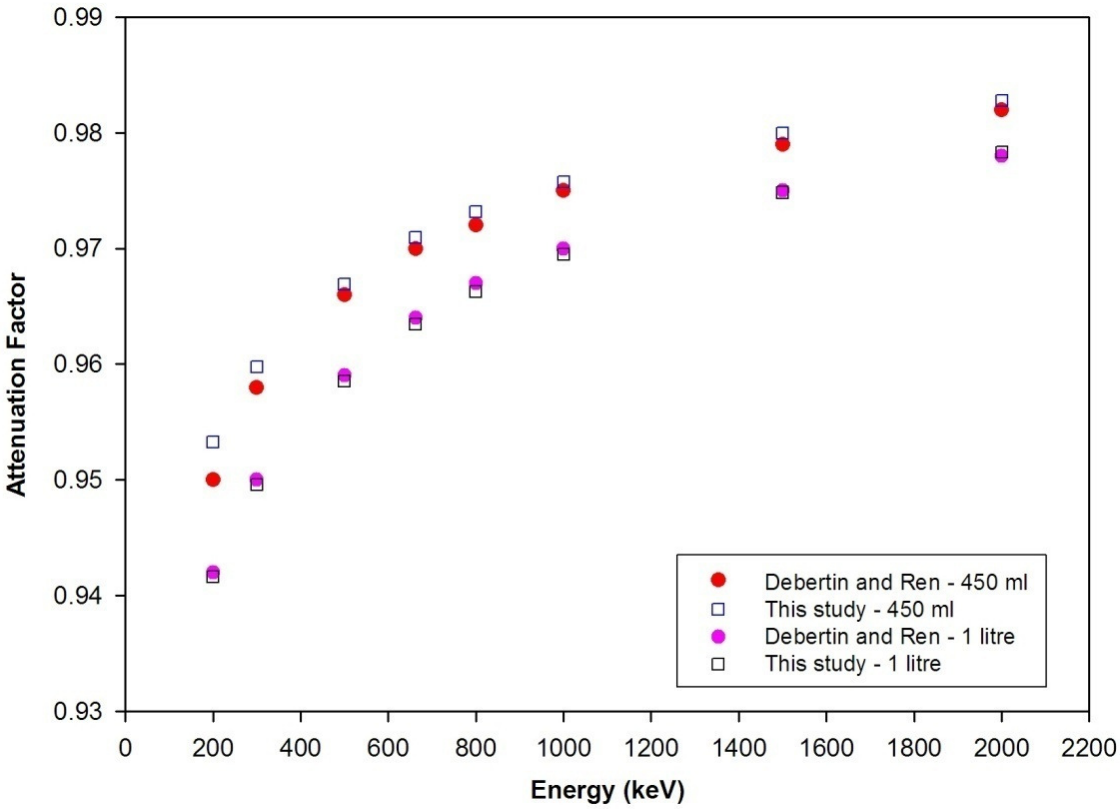

Figure 29. C*omparison between the self-absorption correction factors f_a of Debertin and Jen (1989) and ($F_a(\mu)_{sample}$ / $F_a(\mu)_{reference}$) obtained from the present work for the 450 ml and 1 litre Marinelli beaker geometry.*

4.2.5 Error due to Radon Loss

The determination of the uranium content in a sample by means of a daughter product will only be valid if the sample is in secular equilibrium. If radon, a gaseous precursor to the gamma emitting radioisotopes, escape from the Marinelli beaker disequilibrium occurs resulting in an underestimation of the uranium concentration. This is a possibility as the lids of the Marinelli beakers are not very tight fitting. Secular equilibrium was verified by determining the uranium concentration from the 1001 keV gamma ray (branching ratio of 0.837 % (Firestone, 1996)) of ^{234m}Pa (Yücel et al., 1998) for one sample of each group. The 1001 keV concentrations were then compared to their respective weighted average concentrations (Table 20).

Table 20 ***The uranium concentrations obtained with the 1001 keV gamma ray compared to the weighted average concentrations obtained with gamma lines used in this study (only statistical errors are shown).***

Sample	1001 keV *C*oncentration (ppm)	Weighted average Concentration (ppm)
506 Feed 2	122 ± 3	122 ± 0.2
511 Feed 1	311 ± 5	308 ± 0.3
IRMS Feed 2	193 ± 4	192 ± 0.3
IRMS Non Magnetic 1	218 ± 4	215 ± 0.3
IRMS Magnetic Rejects 2	114 ± 3	120 ± 0.2
SDO 4	289 ± 5	283 ± 0.4
Wet Gravity Tailings 2	40.2 ± 2	39.7 ± 0.2
Rutile Rejects 2	193 ± 4	192 ± 0.4
Zircon Product 1	251 ± 4	249 ± 0.3
Zirkwa Product	366 ± 5	362 ± 0.4
Zircon Rejects 2	389 ± 6	386 ± 0.4
Kanonkop Top Block Surface D	4.8 ± 0.9	6.8 ± 0.1
Kanonkop Top Block Surface B	7.0 ± 0.8	4.5 ± 0.04
Simonsig Surface C	-4.7 ± 0.2	2.4 ± 0.1
Simonsig Kriekbult Surface A	3.5 ± 0.6	2.3 ± 0.03
Spier Surface B	1.3 ± 0.4	1.5 ± 0.1
Spier Crushed Rock	1.7 ± 0.4	4.3 ± 0.04

Unfortunately was this gamma ray not part of the original analysis routine. This meant that the counting times of the soil samples were in most cases too short to produce a photopeak that is distinguishable from the noise and background. This led to erroneous results for most of the soil samples where the 1001 keV concentrations were lower than the weighted average concentrations (incidentally also the case for the IRMS Magnetic Rejects) or even negative (Simonsig Surface C). Only in two samples were useable results obtained; Simonsig Kriekbult Surface A and Kanonkop Top Block Surface B. The 1001 keV concentrations were 34 % and 36 % different from the weighted average values. This

cannot be verified by the XRF results as in the former case the concentration was below the detection limit and in the latter case the XRF result is lower. In the study of Joseph (2007) he hermitically sealed the vineyard soil samples and found a 13 % discrepancy between an immediate measurement and equilibrium. Human (2005) made similar measurements using gold-bearing rock and showed that the radon in-growth is more pronounced with a 50 % difference between the immediate and equilibrium value. However, none of these authors delivered proof that the samples were indeed hermitically sealed. Nonetheless, the 34 - 36 % loss of radon (i.e. error in uranium concentration) may therefore be very plausible when it comes to the vineyard soil samples as the samples were not sealed as in the case of Joseph (2007). A maximum error of 36 % is assumed for the vineyard samples due to the loss of radon.

The mineral sand samples have different results. The 1001 keV concentrations differ with 0.29 % - 1.92 % from the weighted average concentrations (not taking the statistical errors into account). The attainment of secular equilibrium is therefore not a big problem for the heavy mineral sand samples. A maximum error of 1.92 % is assumed for the mineral sand samples due to radon loss.

The uranium reference sample was transferred to another Marinelli beaker, simulating a total loss of radon, and counted immediately. The concentration was 1.5 % different from the equilibrium value and hence it was assumed that a 1.5 % error was introduced in the efficiency calculation.

4.2.6 Accuracy and Precision

4.2.6.1 Accuracy of the Detection System

The accuracy of radiometry, after all the calibrations, corrections and methods of analysis were implemented, was investigated by analysing a zircon sample supplied by Richards Bay Minerals (Van der Walt, 2001). The results were compared with the ones obtained by two other laboratories, that of Necsa and California Lab (Van der Walt, 2001).

The concentration for uranium was calculated as 70 ± 4 ppm and the thorium concentration 405 ± 18 ppm. These values have excellent agreement with the results obtained by the other two laboratories (Table 21). Necsa determined the concentrations as

70 ppm for uranium and 407 ppm for thorium. The California Lab obtained concentrations of 77 ppm and 410 ppm for uranium and thorium respectively. Unfortunately in both cases no errors were provided, so the typical 10 % error was assumed.

Table 21 ***The U and Th concentrations determined for a zircon sample using the methodology of this study compared to results from Necsa and California Lab.***

Source	Uranium concentration (ppm)	Thorium concentration (ppm)
Present work	70 ± 4	405 ± 18
Necsa	70 ± 7	407 ± 41
California Lab	77 ± 8	410 ± 41

4.2.6.2 Precision of the Detection System

The precision (i.e. how close repeated measurements are to one another) of the set-up was investigated by measuring three randomly chosen samples 10 times. Comparing with the weighted average and its standard deviation, the individual measurements show good agreement with each other. One set of measurements (for uranium and thorium concentrations) is depicted in Figure 30.

(a)

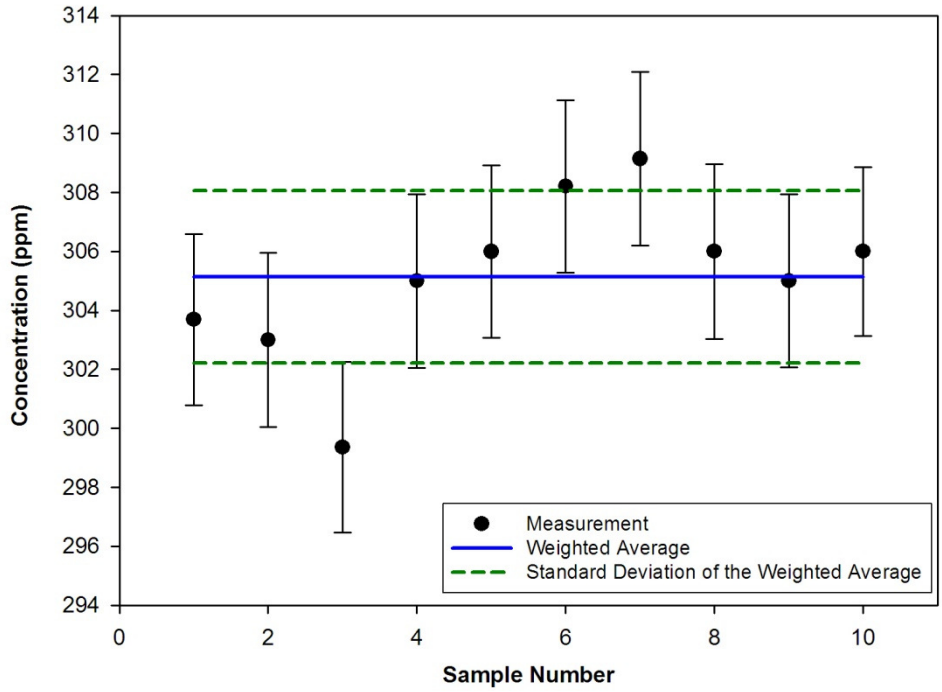

(b)

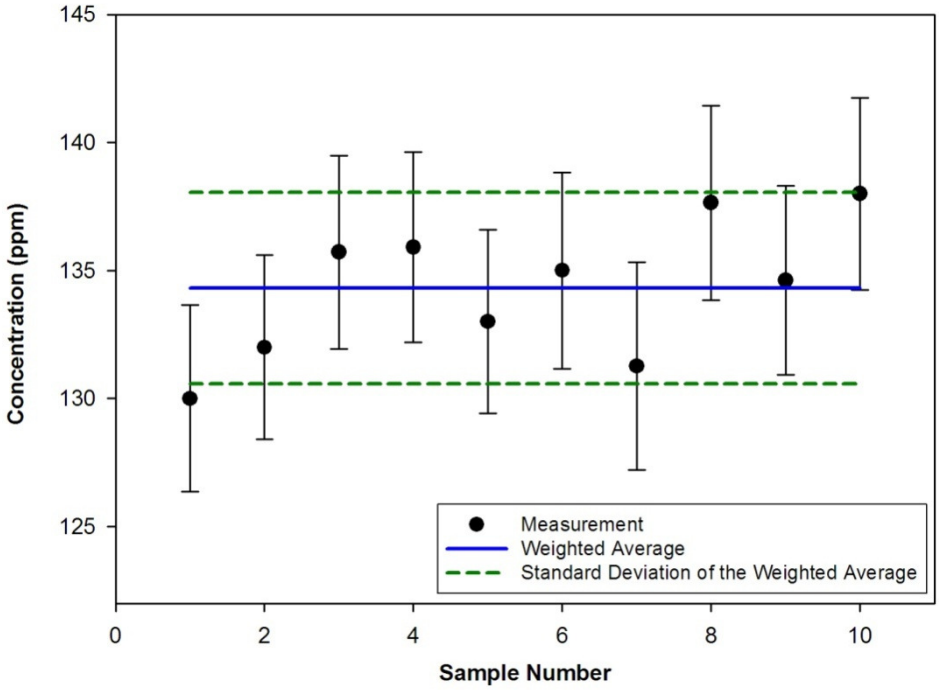

Figure 30. ***An example of the results when a sample is measured 10 times. Graph (a) depicts the uranium concentration and (b) the thorium concentration. The individual measurements show good agreement with the weighted average (blue line) and its standard deviation (green lines).***

4.3 MEASUREMENT ERRORS

The calculation of a concentration has an error associated with it. This error, hereafter called total error, consists of a statistical and systematic error. The statistical error is dependent on the counting statistics. Although a maximum statistical error of 2% was set for each photopeak the statistical error in the concentration was less than 1% for many of the samples. This is due to longer counting times that benefited the higher intensity photopeaks and increased their weight in the final concentration calculation.

The systematic error can be divided into two contributions: firstly, the errors associated with the efficiency determination and secondly the errors made during the measurement of a sample. The errors in the determination of the efficiency consisted of the following. The statistical error in the photopeak area was 0.80 % for the uranium reference sample and 0.9 % for both the thorium and potassium reference samples. Although this is a statistical error, it was included here as part of the once-off error associated with the determination. Mass measurements were done on a Sartorius scale (BP2100s model) which stood in an air-conditioned room. The movement of air in the room resulted in an error in the determination of the mass of an empty or filled Marinelli beaker. By repeating measurements ten times a maximum fluctuation in the mass of 0.7 % for an empty and 0.5 % for a filled Marinelli beaker were observed. Markings, to indicate volume, were made on the Marinelli beaker by filling the beaker with certain volumes of water (section 4.2.4.2). Repeated measurements indicated an error of 2.0 %. Sample volume determinations also had an error of 2.0 %. The errors in the specific activity of the reference samples were taken from the IAEA report as 0.28 %, 1.00 % (IAEA, 1987) and 0.50 % for the uranium, thorium and potassium standards respectively. In the case of the uranium reference sample an error of 1.5 % contributed to radon loss was also included.

The errors in the measurement of the samples were the same for the mass and volume determinations. The errors due to radon loss were 1.92 % and 36 % for mineral sand samples and soil samples respectively. Mass attenuation coefficients for each sample group (e.g. Spier soil samples or zircon product samples) were calculated from average major element compositions obtained from XRF. These averages were at most 1 % different from the actual values. Furthermore, radiometry measures ^{238}U, which is 99.27 % of all uranium, whereas XRF measures natural uranium. This underestimation of 0.73 %,

which is contributed to the ^{235}U that is not measured, is included as an error. A summary of the different errors are tabulated in Table 22.

Combining all the systematic errors according to Equation B.14, the total systematic errors were calculated as 5.1 % for ^{238}U in the case of the mineral sand samples and 36.3 % in the case of the vineyard soil samples, 4.5 % for ^{232}Th and 4.7 % for ^{40}K. With a statistical error in the order of 1-2 %, according to the counting time used, the maximum total error in a measurement of a heavy mineral sand sample was 5.4 % and was in accordance with the objective of obtaining a total error of less than 10 %. This was also the case for the thorium and potassium in the vineyard soil samples but not for the uranium. The total error of 36.4 % was higher than the objective. (Statistical and systematic errors are normally not added this way (Newman, 1996), as the systematic errors are in most cases estimated by non-statistical methods. For these cases a rectangular error distribution can be assumed (Castrup, 2004) and the procedure followed (Newman, 1996) to estimate the standard deviation of the systematic errors. Then can it be added in quadrature to the statistical error. However by repeating the estimations of a systematic error and consequently determining the average value constitutes as a statistical method of estimation (Glosup and Axelrod, 1996). This implies that the systematic error can be added to the statistical error in quadrature without any correction.)

Table 22 ***A summary of the different errors in the measurement of ^{238}U, ^{232}Th and ^{40}K that contribute to the total systematic error (refer to section 4.3 for more detail).***

Source of Error	Error	^{238}U (%)	^{232}Th (%)	^{40}K (%)
Efficiency calibration	Counts in Photopeak	0.80	0.90	0.90
	Mass of empty Marinelli beaker	0.70	0.70	0.70
	Mass of sample	0.50	0.50	0.50
	Volume determination (water)	2.00	2.00	2.00
	Volume determination (reference)	2.00	2.00	2.00
	Concentration of standard	0.28	1.00	0.50
	Radon loss	1.50	-	-
Measurements	Mass of empty Marinelli beaker	0.70	0.70	0.70
	Mass of sample	0.50	0.50	0.50
	Volume determination (water)	2.00	2.00	2.00
	Volume determination (sample)	2.00	2.00	2.00
	Radon loss	1.92 or 36	0.00	0.00
	Mass attenuation coefficient	1.00	1.00	1.00
	Uranium correction	0.73	-	-
	TOTAL	**4.1 Or 36.3**	**4.5**	**4.7**

CHAPTER 5 THE HEAVY MINERAL SANDS APPLICATION

In this chapter radiometry is applied in mineral beneficiation to demonstrate that it can be an alternative method for grade control of heavy mineral sands. The chapter starts with brief discussions on the stratigraphy, genesis and mineralogy of the West Coast Heavy Mineral Deposits and the heavy mineral separation process. In the following section the ^{238}U and ^{232}Th concentrations of the various separation products and feeds are presented and discussed. Next the concentrations are compared and a general correlation between the radiometry and XRF obtained. The effect of reducing the counting time was also investigated and results presented. Finally the use of radiometry and the practical implementation thereof in the heavy mineral separation processes are discussed.

5.1 GEOLOGICAL SETTING

Heavy minerals are sourced from a diversity of lithologies from igneous and metamorphic terranes and include the mineral fraction with a density of > 2.9 g/cm^3 per definition. The placer deposits that host these heavy minerals are derived from surface weathering of these rocks and transport of the light and heavy mineral fraction by fluvial and Aeolian processes. Repeated upgrading of the sedimentary material by means of wave and wind action, results in the removal of the light minerals and an increase in the heavy mineral fraction. Concentrations of up to 12 % total heavy minerals (THM) may constitute an economic deposit provided the minerals zircon, rutile and ilmenite are present in abundance. These heavy mineral placer deposits are concentrated along the west coast of South Africa and hosted by young , < 10Ma unconsolidated sands.

5.1.1 Stratigraphy of the West Coast Heavy Mineral Deposits

The occurrence of heavy mineral placer deposits along the west coast has been known since the discovery of alluvial diamonds in the years following 1900. In 1975 the South African Geological Survey defined seven narrow beach/coastal dune deposits in that region. However, it was only in 1986 that Anglo American Prospecting Services confirmed the existence of a large mineralisation site, which became known as the Graauwduinen-West orebody (Esterhuyse, 1996). Heavy minerals found included the economic valuable minerals ilmenite, rutile, leucoxene, zircon and monazite and non-valuable minerals

garnet, pyroxene and amphibole. Later an inland extension was identified and named the Graauwduinen-East orebody. Collectively these ore bodies are known as the Graauwduinen deposit (Figure 31).

Figure 31. ***A map of the South African west coast depicting the locations of the heavy mineral deposits, Geelwal Karoo and Graauwduinen owned by Exxaro Namakwa Sands.***

Based on drilling data and field observations the Graauwduinen deposit consists of a succession of Quarternary enriched sediments overlying Pre-Cambrium rocks belonging to the Namaqualand Metamorphic Complex. The sand was deposited by fluvial (river) processes and upgraded by marine and Aeolian processes. The most characteristic feature of the deposit is the presence of two paleo-strandlines at 20 and 35 m above mean

sea level (amsl), displaying an extremely high concentration of heavy minerals and situated at the base of the succession. These units formed during relative sea-level stand stills at the respective elevations. The basal marine units are each overlain by a sequence of Aeolian sediments which accreted onto the western margin of the regressing sea after the stand stills at 20 and 30 m above mean sea level. (Estherhuyse, 1996).

5.1.2 Genesis and Mineralogy of the West Coast Heavy Mineral Deposits

Provenance studies on titane-bearing minerals suggest they source from metamorphic rocks, probably from the high grade metamorphic terrains in the Garies-Bitterfontein region. The zircon, which is present in higher proportions than most other heavy mineral sand deposits, is believed to have been derived from the NMC and basal Table Mountain Group which outcrops along the Van Rhynsdorp escarpment.

The sediments containing the heavy minerals were transported into a J-shaped paleo-bay by drainage systems belonging to the ephemeral Sout/Garoep/Olifants Rivers. Eustatic movements and transgressive/regressive events redistributed the minerals. During these periods sea-level regression and sea-level standstills, long shore currents and wind/wave action concentrated the minerals by removing the lighter, less dense fractions. This resulted in the formation of high grade, black strandlines along the beaches (Estherhuyse, 1996).

Another source of heavy minerals is found at the Geelwal Karoo region (Figure 31). Here the present beach strandline with its steep back-wall provides the ideal site for the concentration of heavy mineral sands. This is seen at several other localities where heavy minerals are concentrated in semi-consolidated sands of palaeo and recent strandlines and are overlain by dune fields. In some areas these heavy minerals constitute up to 90 % of the total sand (Philander et al., 1999). A photo of an example of a placer is depicted in Figure 32.

Mineralogy of the heavy mineral sand deposits consists of a dominant light mineral fraction of quartz and minor potash feldspar with admixed shell fragments. The heavy minerals consist of non-economic garnet, clinopyroxene, magnetite, amphibole, tourmaline, spinel, kyanite, epidote and choromite and an economic fraction. The latter is dominated by ilmenite (60 %), a suite of other Fe-Ti-oxides including leucoxene and significant amounts

of zircon and rutile. Table 23 gives a summary of the percentage heavy minerals found at the different deposit sites.

Figure 32. ***An example of a heavy mineral placer along the West Coast of South Africa.***

Table 23 ***The total heavy mineral concentration (THM) and the percentage of the major heavy minerals of the different Exxaro Namakwa Sands Ltd deposits (Estherhuyse, 1996).***

Deposit	THM % of deposit	Ilmenite % THM	Rutile % THM	Zircon % THM
Geelwal Karoo	67	22	1	5
Geelwal Palaeostrand	78	10	< 1	<1
Graauwduinen Strandlines	> 60	25	< 1	< 1
Graauwduinen Aeolian	18	41	1	12

5.2 HEAVY MINERAL SEPARATION PROCESS

The Exxaro Namakwa Sands mineral beneficiation process consists of several stages to firstly separate the light from the heavy minerals and the valuable and gangue minerals.

5.2.1 Concentration Plants

The mineral sand feed, approximately 17 million tons (Rozendaal and Philander, 2007) comes from an open pit where the top soil (red Aeolian sands) is gathered using scrapers and bulldozers. To ensure a relatively constant grade of ore the mining is done progressively across a deposit from top to bottom. A screening process follows where the ore is broken into particles of less than 2 mm in size. The particles are sieved according to three sizes, below 0.05 mm, 0.05 – 0.3 mm and greater than 0.3 mm. Heavy minerals typically fall in the second size range (0.05 - 0.3 mm) and are transported by conveyors and loaders to the primary concentration plant. The other two groups of particles are not used and removed to a tailings facility.

At the primary concentration plant a Wet Gravity concentration process is used to upgrade the heavy mineral concentration to around 90 % (Rozendaal and Philander, 2007). This concentrate is pumped to a secondary concentrator plant.

At the secondary concentration plant a Wet High Intensity Magnetic Separator (WHIMS) process is used to separate the feed into magnetic (ilmenite) and a non-magnetic (zircon and rutile) fractions. These two fractions are separately transported to the mineral separation plant.

5.2.2 Mineral Separation Plant

At the mineral separation plant the two feed streams are processed further. The ilmenite (magnetic fraction) is purified by an electrostatic process to separate the conductive ilmenite from the non-conducting minerals (e.g. garnet). The reject materials are discarded as tailings while the ilmenite is placed in storage containers and transported to the smelter. The amount of ilmenite produced per year is approximately 350 000 tons (Rozendaal and Philander, 2007).

The non-magnetic fraction (zircon and rutile) is purified from slightly magnetic material by Induced Roll Magnetic Separators (IRMS). In this process an IRMS reject fraction and an IRMS non-magnetic fraction are created. The reject fraction is discarded as tailings while the other fraction undergoes a Hepworth Hot Acid Leach process to remove iron oxide from the grain surfaces. The resulting product forms the feed for the Wet Gravity concentrator. The concentrator consists of several spirals that, through gravitation, separate the more dense heavy minerals from the lighter minerals (e.g. quartz and leucoxene). The light minerals are discarded as tailings while the heavy minerals form the feed for the Secondary Dry Mill ore (SDO). Here an electrostatic process separates the conductive rutile (known as the 506 feed) from the non-conductive zircon (known as the 511 feed). Both streams are purified by a final IRMS and an electrostatic process resulting in rejects (again discarded as tailings) and rutile and zircon products. The latter has two grades known as zircon and zirkwa based on their specifications. The products are fed to railroad trucks for transport to storage silos at the smelter site. The amounts of zircon and rutile produced are approximately 120 000 tons and 25 000 tons per year respectively (Rozendaal and Philander, 2007).

Block representations of the mentioned separation processes are depicted in Figure 33 and Figure 34, while Figure 35 illustrates the start of the separation process (ore body) and end products (rutile, zircon and ilmenite) through close-up photos of the different sands.

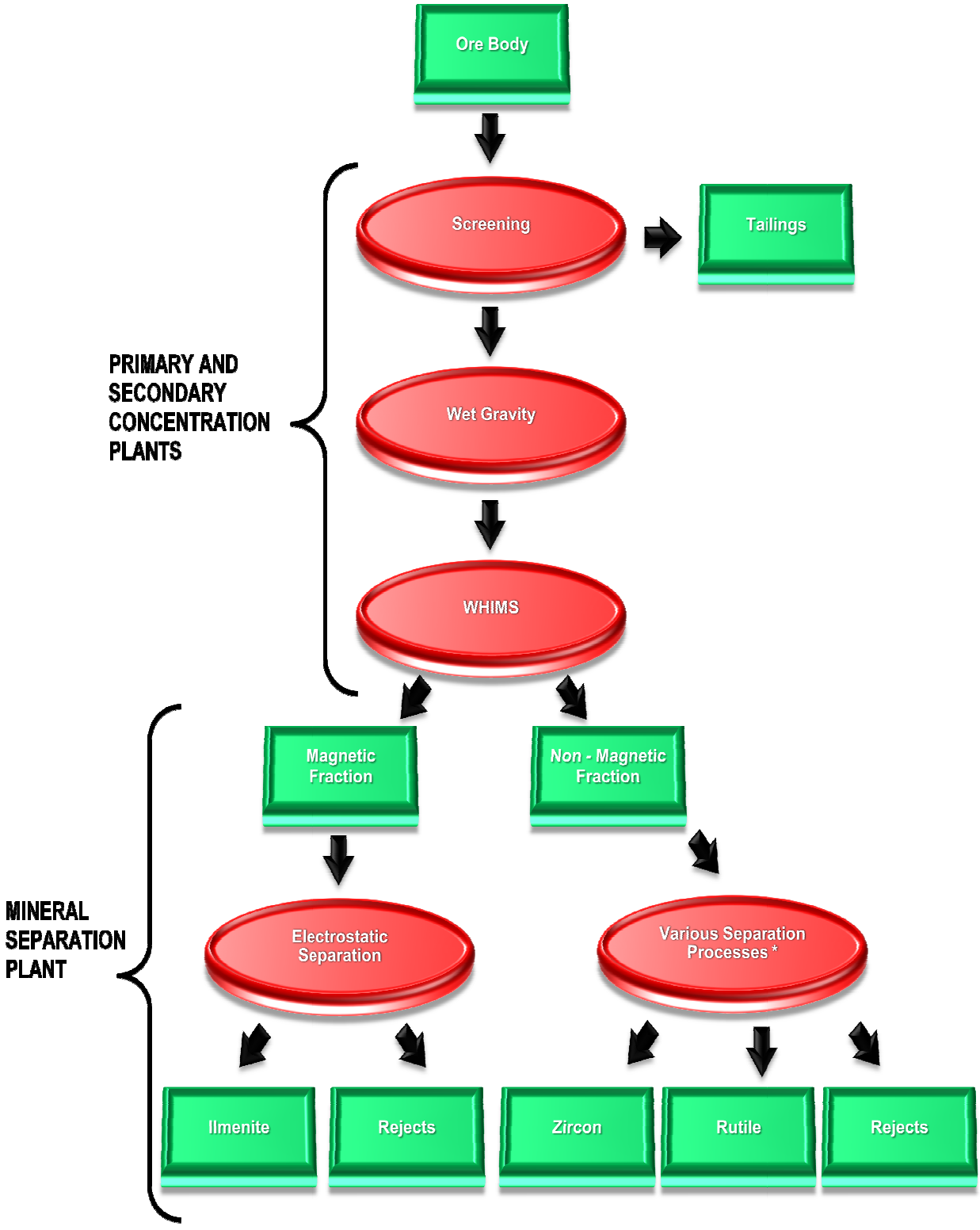

Figure 33. ***Block representation of the heavy mineral feeds, products and separation processes at Exxaro Namakwa Sands.***

The green blocks represent either feed to a process or a product. The red ovals represent a separation process. The various separation processes (indicated by asterisk) and products are illustrated in more detail in the next figure.

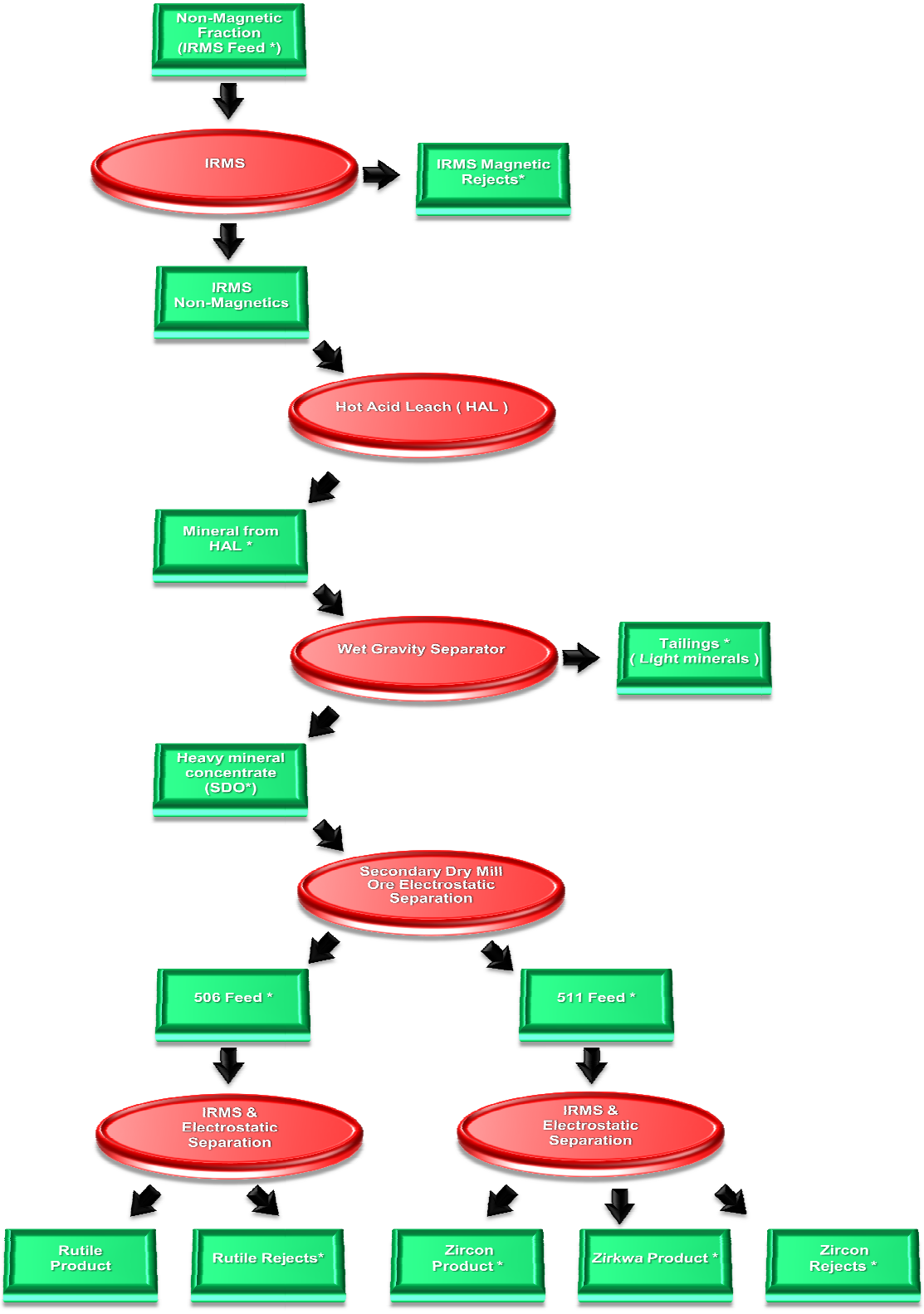

Figure 34. ***Block representation relating more detail of the various separation processes in the Mineral Separation Plant at Exxaro Namakwa Sands that lead to the prime zircon, zirkwa and rutile products.***

The green blocks represent either feed to a process or a product. The red ovals represent a separation process.

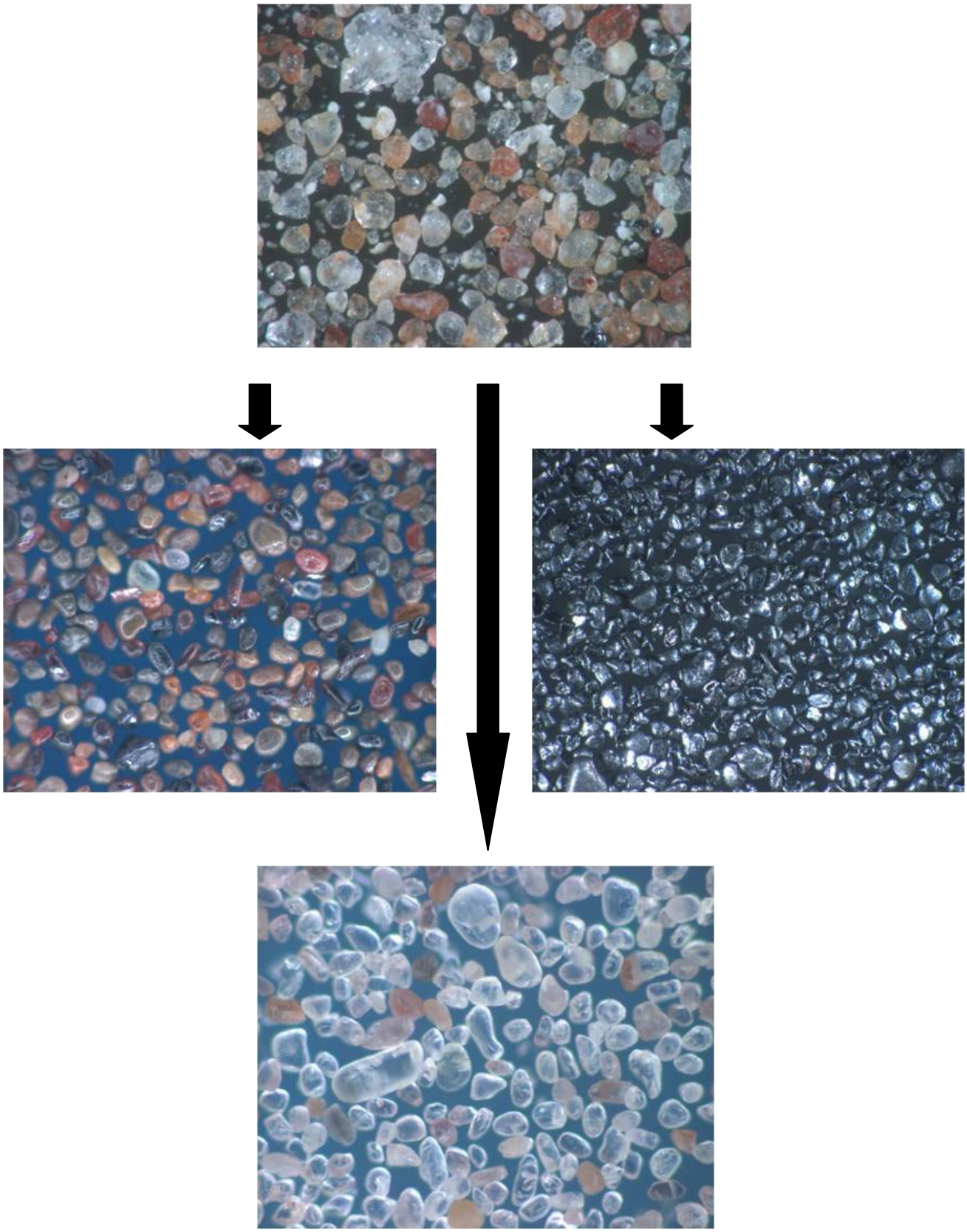

Figure 35. Photos of the ore body (top), as the starting point of the heavy mineral separation process and rutile (left), ilmenite (right) and zircon (bottom) as the end products.

5.3 RESULTS AND DISCUSSIONS

5.3.1 Radiometry and XRF Results

The amounts of rare earth elements and iron associated with zircon can be correlated with the total radioactivity concentration of zircon (Figure 36) (Rozendaal and Philander (2008)). A similar approach was taken by radiometric characterisation of the feeds and products of the heavy mineral separation process, in order to indicate their radiological differences in relation to their separation process. The findings will be used in the implementation phase of grade control.

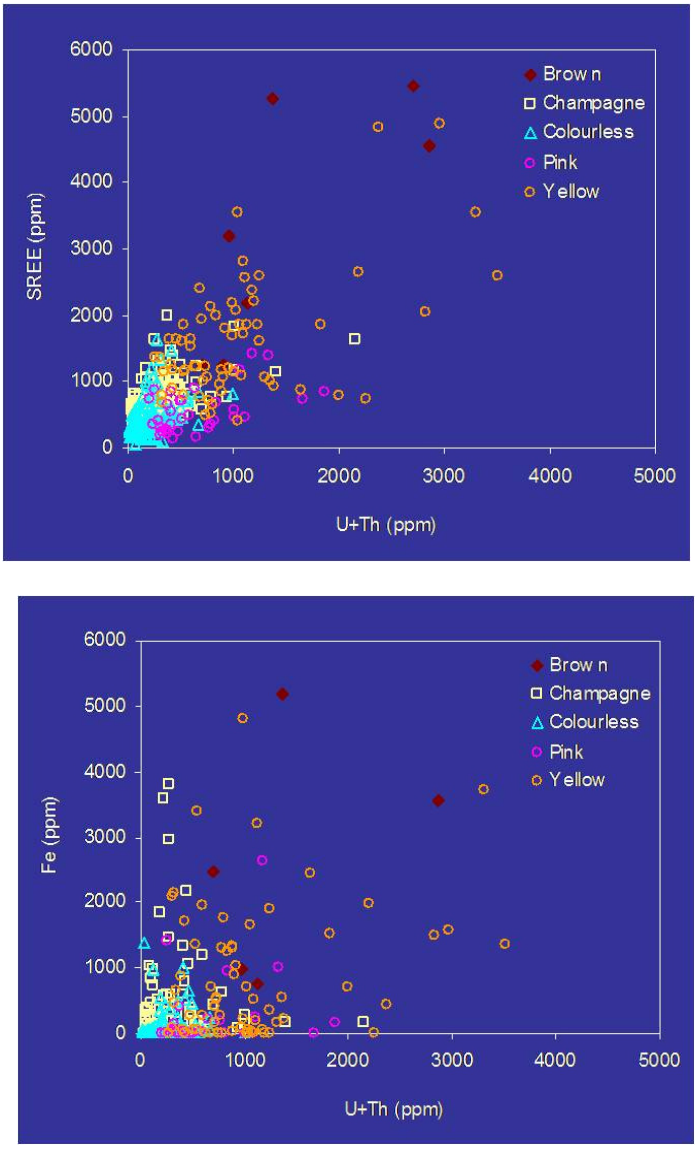

Figure 36. Iron and the Sum of Rare Earth Elements associated with zircon as a function of the total radioactivity concentration.

The radioisotope concentrations and elemental concentrations of the samples are grouped according to their separation process and summarised in Table 24 and Table 25 for radiometry and XRF respectively. The error presented with a result is the total error (i.e. combination of the systematic and statistical errors according to the error propagation rule). The individual ^{238}U and ^{232}Th concentrations against sample number for all the separation processes are depicted in Figure 37 and Figure 38 respectively. The total concentration is depicted in Figure 39, while Figure 40 depicts the ^{238}U concentration against the ^{232}Th concentration.

5.3.2 Discussion of IRMS Feed Results

The ^{238}U concentrations formed a grouping where all the concentrations were within 1 standard deviation. The second and third ^{232}Th concentrations grouped together with the first concentration far lower than the others but still within the 99 % confidence interval. This indicates that the sources of the feed may have mineralogical differences that influence the ^{232}Th concentration much more than the ^{238}U concentrations. The ^{238}U to ^{232}Th ratios for the three concentrations were 0.48, 0.37 and 0.37 with an average of 0.41. The total concentration of the entry feed is in-between 500 ppm and 1000 ppm.

5.3.3 Discussion of IRMS Magnetic Rejects Results

The ^{238}U concentrations of these samples were of the lowest in the whole process. They were almost ten times less than the ^{232}Th concentrations which were of the highest (only one of the zircon reject concentrations was higher) of all the products/feeds. The ^{238}U : ^{232}Th ratios were 0.12, 0.10 and 0.10 with an average of 0.11. This were the lowest ^{238}U : ^{232}Th and is due to the presence of the monazite, a magnetic mineral which is known to contain thorium, in the tailings. Due to the high ^{232}Th concentration, the magnetic rejects were one of the two products that were above the 1000 ppm total concentration and formed a grouping of concentrations that were clearly separate from the rest.

5.3.4 Discussion of IRMS Magnetic Rejects Results

The ^{238}U concentration is close to that of the IRMS feed and one of the rutile rejects. The ^{232}Th concentration is higher than the ^{238}U. This product has the second highest thorium concentration due to the presence of the mineral monazite. The ^{238}U : ^{232}Th was 0.52. The total concentration of the entry feed was in-between 500 ppm and 1000 ppm.

Table 24 ***Concentrations of the heavy mineral sand samples obtained with radiometry for ^{238}U, ^{232}Th and the total concentration for a counting time of 3600 s.***

Sample ID		Concentration (ppm)					
		^{238}U	σ	^{232}Th	σ	Total	σ
IRMS-Feed	1	190	10	394	18	584	20
	2	192	10	512	23	704	25
	3	193	10	522	24	715	25
IRMS-Magnetic Rejects	1	120	6	1022	46	1142	46
	2	114	6	1128	51	1242	51
	3	99	5	984	44	1083	45
IRMS-Non Magnetic	1	215	11	413	19	627	22
Hot Acid Leach Recycle	1	408	21	368	17	777	27
	2	390	20	364	16	755	26
	3	388	20	454	20	842	28
Wet Gravity Tailings	1	160	8	139	6	299	10
	2	40	2	69	3	109	4
	3	87	4	135	6	222	8
SDO	1	278	14	239	11	517	18
	2	276	14	327	15	603	20
	3	289	15	467	21	756	26
	4	283	14	485	22	768	26
506-Feed	1	123	6	161	7	285	10
	2	122	6	183	8	305	10
	3	128	7	235	11	364	12
Rutile Rejects	1	132	7	262	12	394	14
	2	192	10	587	26	779	28
	3	270	14	502	23	772	26
	4	234	12	648	29	882	32
511-Feed	1	308	16	564	25	872	30
	2	313	16	576	26	889	30
Zircon Product	1	249	13	118	5	367	14
	2	264	13	116	5	380	14
	3	272	14	120	5	392	15
Zirkwa Product	1	362	18	228	10	590	21
	2	324	17	302	14	626	21
Zircon Reject	1	362	18	1073	48	1435	52
	2	386	20	1646	74	2032	77

Table 25 ***Concentrations of the heavy mineral sand samples obtained with XRF.***

Sample ID		Concentration (ppm)					
		U	σ	Th	σ	Total	σ
IRMS-Feed	1	183	49	378	7	562	49
	2	186	50	517	10	703	51
	3	188	50	510	10	698	51
IRMS-Magnetic Rejects	1	121	32	1012	19	1133	38
	2	101	27	1142	22	1243	35
	3	99	26	964	18	1063	32
IRMS-Non Magnetic	1	212	57	415	8	626	57
Hot Acid Leach Recycle	1	377	101	370	7	748	101
	2	374	100	348	7	722	100
	3	373	100	464	9	837	100
Wet Gravity Tailings	1	160	43	139	3	298	43
	2	40	11	70	1	110	11
	3	86	23	137	3	223	23
SDO	1	280	75	240	5	519	75
	2	288	77	329	6	618	77
	3	290	77	478	9	767	78
	4	276	74	490	9	767	74
506-Feed	1	121	32	162	3	283	32
	2	124	33	183	3	307	33
	3	129	34	243	5	372	35
Rutile Rejects	1	134	36	261	5	395	36
	2	199	53	556	11	755	54
	3	265	71	516	10	780	71
	4	242	65	680	13	922	66
511-Feed	1	314	84	565	11	879	84
	2	323	86	513	10	836	87
Zircon Product	1	247	66	122	2	369	66
	2	263	70	122	2	385	70
	3	281	75	123	2	404	75
Zirkwa Product	1	358	96	231	4	589	96
	2	316	84	298	6	614	84
Zircon Reject	1	344	92	1060	20	1403	94
	2	362	97	1629	31	1991	101

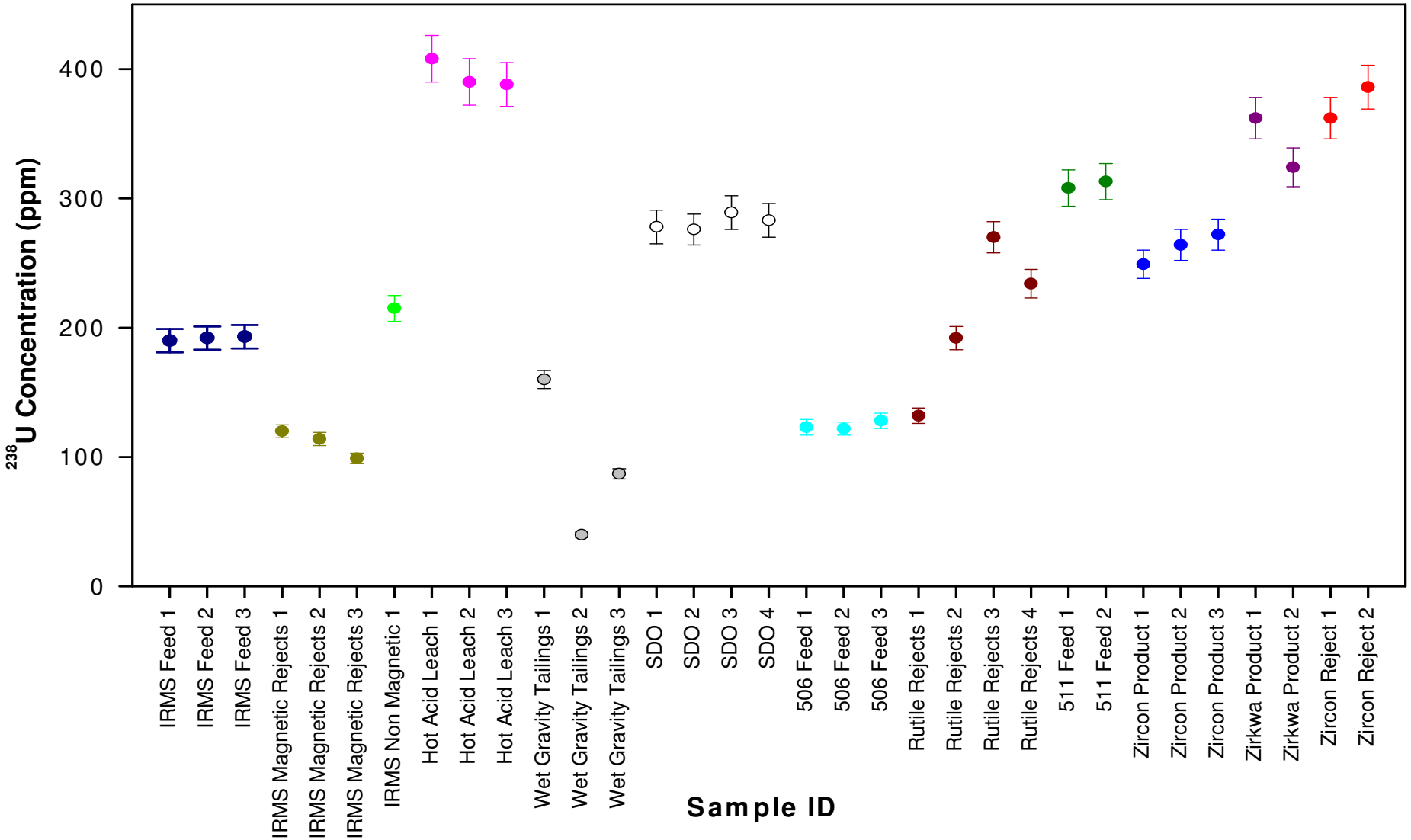

Figure 37. ***The ^{238}U concentration for samples collected at different locations in the Mineral Separation Plant***

The error bars depict the total error (i.e. statistical and systematic).

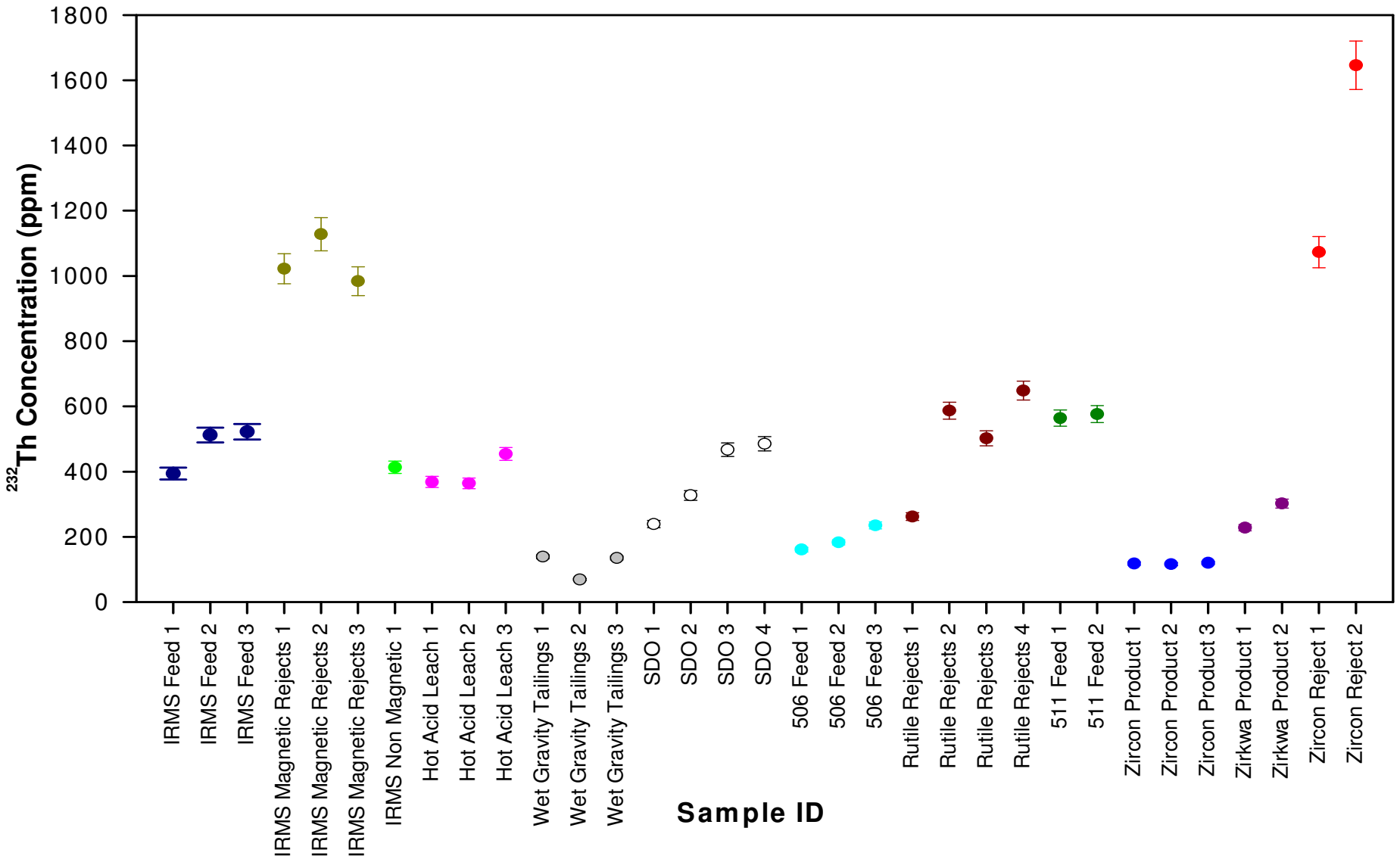

Figure 38. ***The ^{232}Th concentration for samples collected at different locations in the Mineral Separation Plant The error bars depict the total error (i.e. statistical and systematic).***

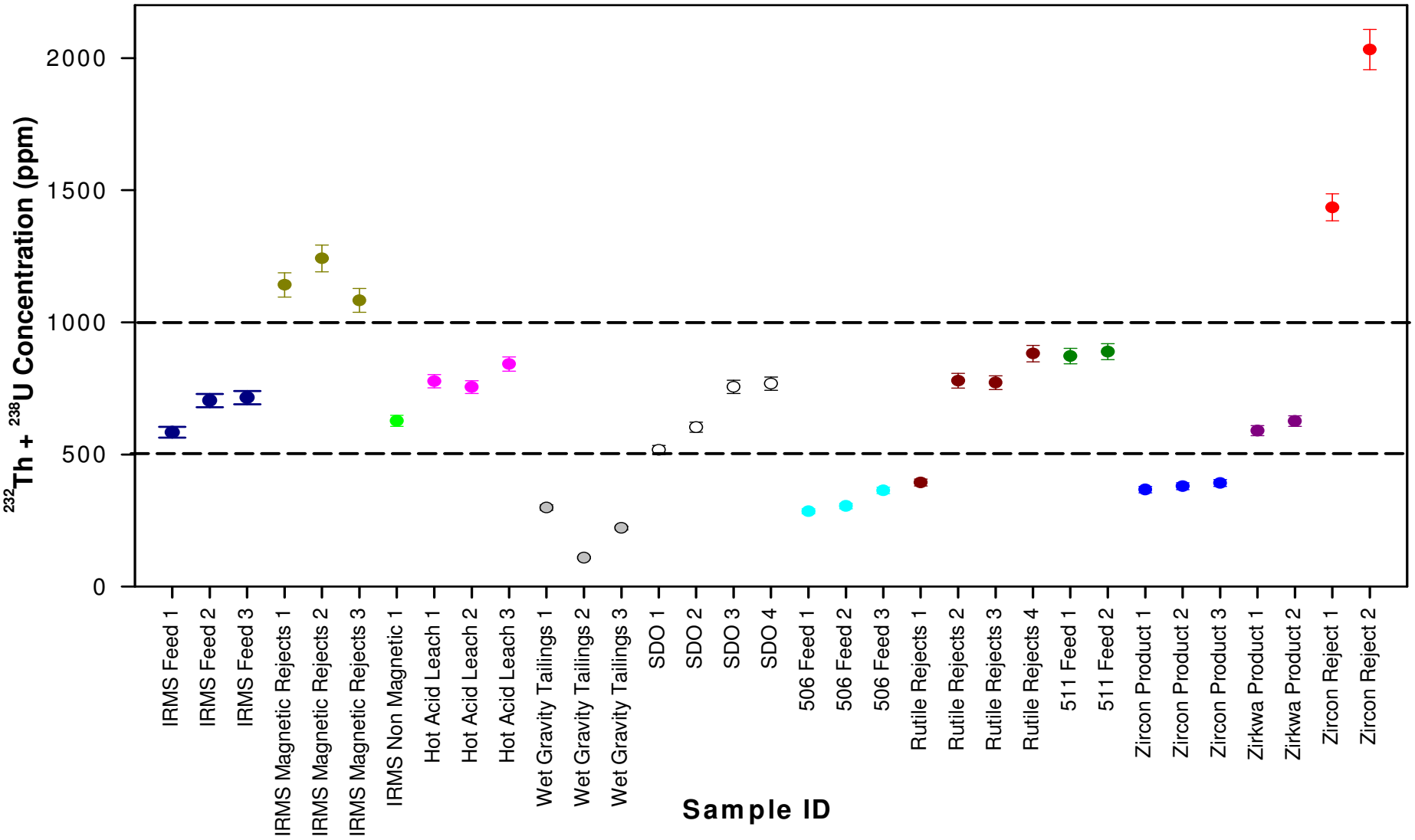

Figure 39. ***The total (^{238}U +^{232}Th) concentration for samples collected at different locations in the Mineral Separation Plant The dashed lines indicate the total concentrations of 500 ppm and 1000 ppm. The error bars depict the total error (i.e. statistical and systematic).***

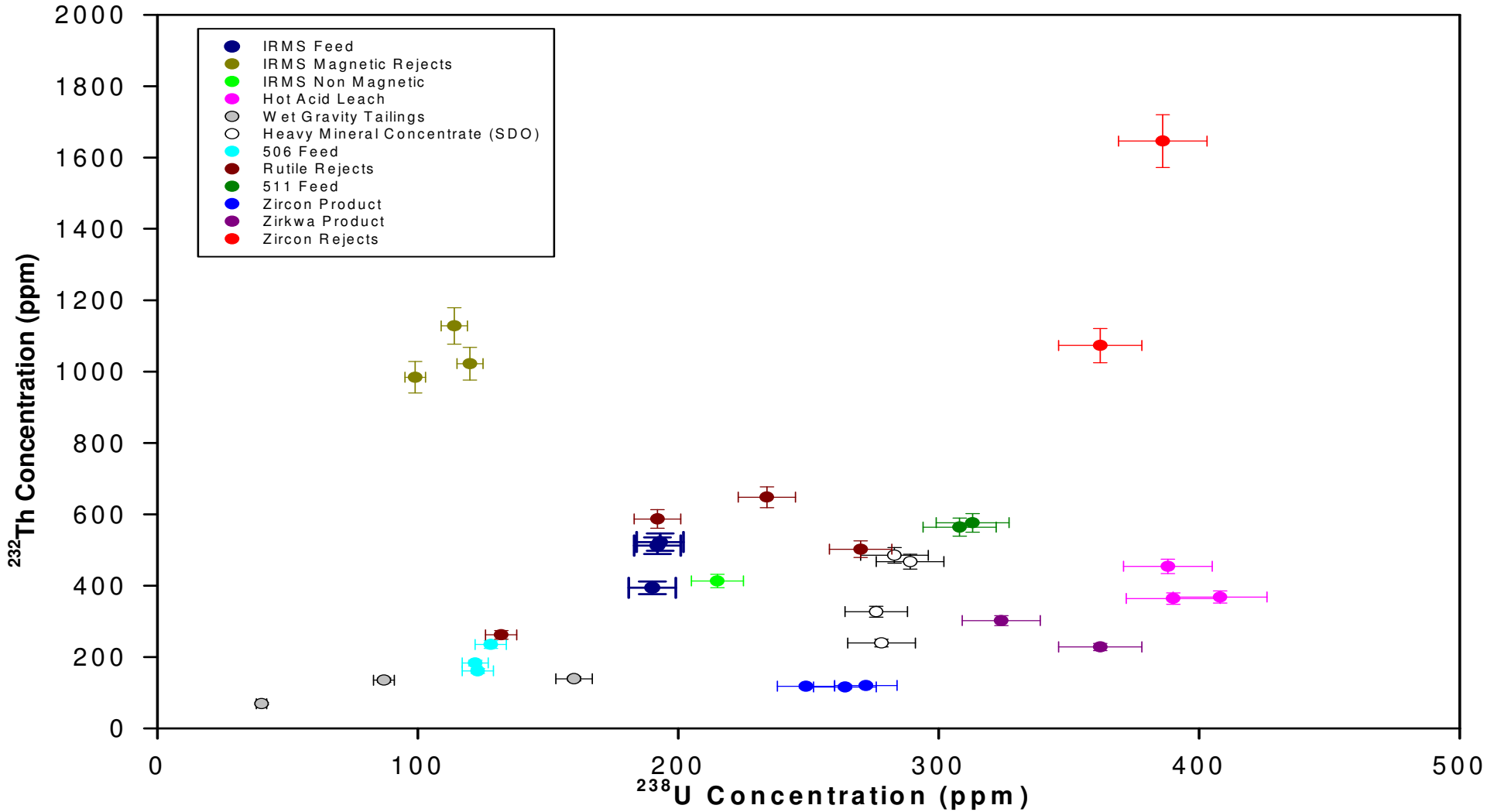

Figure 40. ***The ^{238}U concentration compared to the ^{232}Th concentration of all the samples collected at different locations in the Mineral Separation Plant.***

The error bars depict the total error (i.e. statistical and systematic).

5.3.5 Discussion of Hot Acid Leach Results

In the hot acid leach process surface contamination is removed. These contaminants have a shielding effect which once removed resulted in the highest ^{238}U concentrations of all the processes. For most of the ^{232}Th concentrations the opposite were observed, the concentrations were lower than that of the previous process. The ^{238}U : ^{232}Th ratio for the hot acid leach process were 1.1, 1.1 and 0.86 with an average of 1.0. The total concentrations were higher than the previous process but still below 1000 ppm.

5.3.6 Discussion of Wet Gravity Tailings Results

The ^{238}U concentrations have a very large variation. Only one of the ^{232}Th concentrations is more than 3 standard deviations from the rest of the group. Since these tailings are mostly light minerals it is possible that some heavy minerals are included. This would explain the non-uniform character of the concentrations. Only in one case was the ^{238}U concentration more than the ^{232}Th concentration (^{238}U : ^{232}Th equal to 1.2). For the other cases the ratios were less with values of 0.57 and 0.65. The average ratio is 0.79. For the first time in the process the total concentrations were below 500 ppm.

5.3.7 Discussion of SDO Results

The ^{238}U concentrations formed a grouping with values around 1 standard deviation from each other. The ^{232}Th concentrations have a larger spread in values. The ^{238}U : ^{232}Th ratios were 1.2, 0.85, 0.62 and 0.58 with an average of 0.80. The total concentrations were in between 500 ppm and 1000 ppm.

5.3.8 Discussion of 506 Feed Results

The ^{238}U concentrations of this feed were low compared to most of the other products/feeds. The concentrations were comparable to the IRMS Magnetic Rejects. It was also the case for the ^{232}Th concentrations, laying in between the Wet Gravity Tailings and the second SDO concentration. The ^{238}U concentrations were lower than the ^{232}Th

concentrations with ratios of 0.77, 0.66 and 0.55, with an average of 0.66. The total concentrations were below 500 ppm.

5.3.9 Discussion of Rutile Rejects Results

The Rutile Rejects have a large spread in the ^{238}U concentration. Rutile Reject-1 uranium concentration was within 1 standard deviation of the 506 Feed while the others were within 2 standard deviations of the IRMS Feed, SDO and Zircon Products. A similar behaviour was observed with the ^{232}Th concentrations which were spread between 506 Feed, 511 Feed, SDO and IRMS Feed. The uranium-238-to thorium-232 ratios were 0.50, 0.33, 0.54 and 0.36. The average ^{238}U : ^{232}Th was equal to 0.43. The total concentration of Rutile Reject-1 was below 500 ppm. The other total concentrations were in between 500 ppm and 1000 ppm. It is possible that Rutile Reject-1 was incorrectly labelled and was an example of a pure rutile product or a SDO sample. This could explain its different radiometric character to that of the other samples. However, rutile is not classified according to radioactivity but to its impurities (Van Zyl, 2009). Since these data were not available it cannot be ascertained if this was indeed the case.

5.3.10 Discussion of 511 Feed Results

The ^{238}U concentrations were grouped within 1 standard deviation. The ^{232}Th concentrations were also grouped within 1 standard deviation. The concentrations were higher than most of the previous products and feeds with the exception of the IRMS Magnetic Rejects and Rutile Rejects-4. The ^{238}U concentrations were lower than the ^{232}Th concentrations with ratios of 0.55 and 0.54, with an average of 0.54. The total concentrations of this non-conductive feed were in contrast to the conductive 506 Feed with total concentrations below 1000 ppm whereas the 511 Feeds were below 500 ppm.

5.3.11 Discussion of Zircon Product Results

The ^{238}U concentrations were within 1 standard deviation around the value of 260 ppm. For the first time in the process the ^{238}U concentrations were more than twice the ^{232}Th concentrations with ^{238}U : ^{232}Th equal to 2.1, 2.3 and 2.3. The average ^{238}U : ^{232}Th was 2.2.

This characteristic of the zircon product was unique to any of the products/feeds of the separation process. The ^{232}Th concentrations were the lowest of all the products except Wet Gravity Tailings-2. The total concentrations were below 500 ppm and agreed with the pure zircon classification.

5.3.12 Discussion of Zirkwa Product Results

The ^{238}U concentrations were the second highest together with the zircon rejects. The second concentration was within 1 standard deviation of the 511 Feed. The ^{232}Th concentrations were within 1 standard deviation to some of the 506 Feed and SDO concentrations. The total concentrations were between 500 ppm and 1000 ppm and agreed with the zirkwa classification. Although many of the previous products/feeds lay in this region its average ^{238}U : ^{232}Th, equal to 1.3, was different compared to the other products/feeds. The individual ^{238}U : ^{232}Th were 1.6 and 1.1. The only other products that had a similar ratio were two Hot Acid Leach feeds. Despite the same ratio their characteristics are not the same.

5.3.13 Discussion of Zircon Rejects Results

The ^{238}U concentrations are the second highest together with the zirkwa products. The ^{232}Th concentrations are of the highest with Zircon Reject-1 in the range of the IRMS Magnetic Rejects and Zircon Reject-2 in the order of 1600 ppm. The ^{238}U : ^{232}Th for the two samples were 0.34 and 0.23 with an average of 0.29. With total concentrations of more than 1380 ppm these products were clearly unsuitable for the market.

5.3.14 Comparison to XRF

The radiometry and XRF concentrations for each of the separation processes were compared in order to confirm that radiometry can be a feasible alternative to XRF for grade control. All the uranium and thorium concentrations determined by radiometry are within 1 standard deviation of the respective XRF determined concentrations. Individual comparisons are depicted in Figure 41 to Figure 52.

All the concentrations of uranium and thorium respectively were used to quantify the degree of relationship between radiometry and XRF by means of a correlation. The ideal correlation is a straight line from zero to the maximum concentration. It means that a concentration determined with radiometry yields an identical result with XRF. Concentration errors are taken into account in this determination.

Figure 53 depicts the comparison of the uranium concentrations together with the ideal correlation line. All 33 concentrations are positioned on the correlation line. (It is observed that at the higher end the XRF concentrations are consistently lower than those of radiometry. This is due to the XRF analysis that needed extrapolation to higher concentrations since its standards were below the concentrations measured.) The correlation coefficient is 0.992 and the correlation for uranium can therefore be described as excellent.

The comparison of the thorium concentrations together with the ideal correlation line are depicted in Figure 54. Of the 33 concentrations only one was not on the ideal correlation line. The correlation coefficient is 0.998 and the correlation for thorium can therefore be described as excellent.

Figure 55 depicts the comparison of the total concentrations together with the ideal correlation line. All the measurements are positioned on the correlation line. The correlation coefficient is 0.998 and the correlation for the total concentration can therefore be described as excellent.

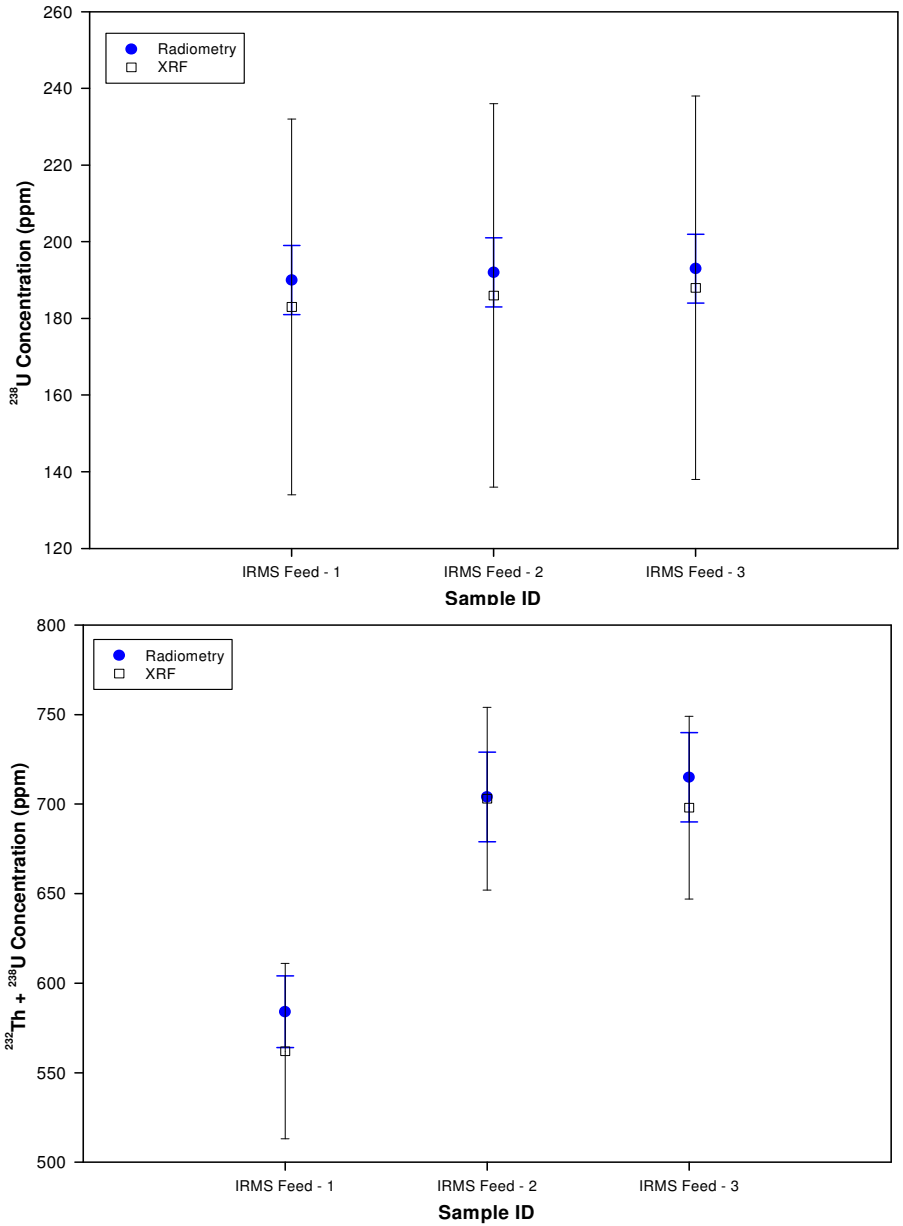

Figure 41. ***Radiometric and XRF sample concentrations for samples labelled IRMS Feed.***

Samples were taken from the IRMS Feed after it entered the Mineral Separation Plant. Top left is the ^{238}U concentration (ppm), top right the ^{232}Th concentration (ppm) and bottom left is total concentration. The error bars depict the total error (i.e. statistical and systematic).

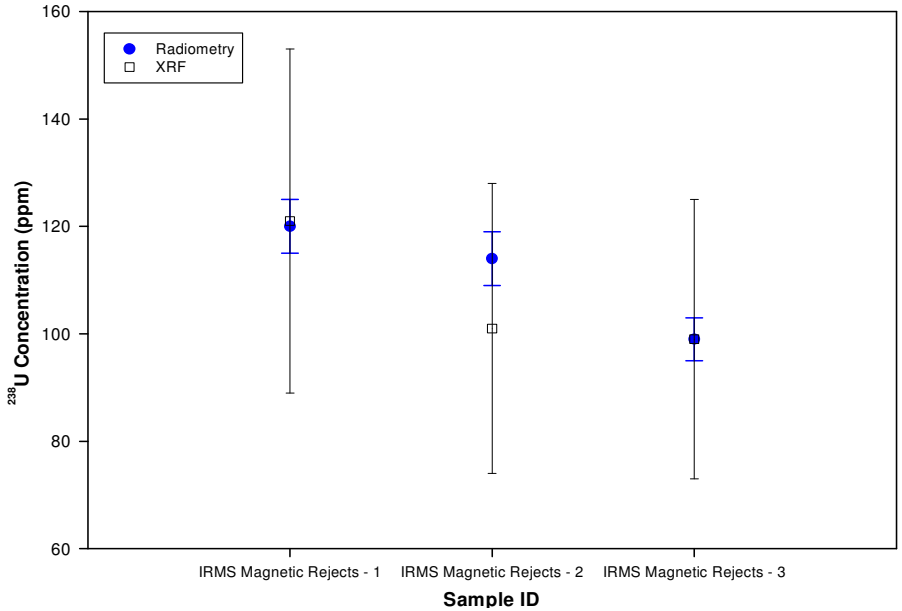

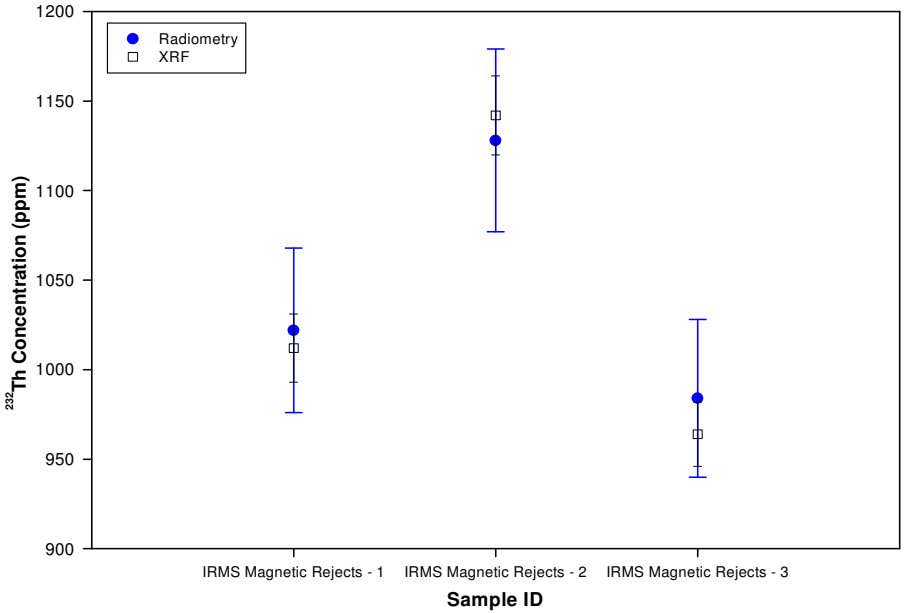

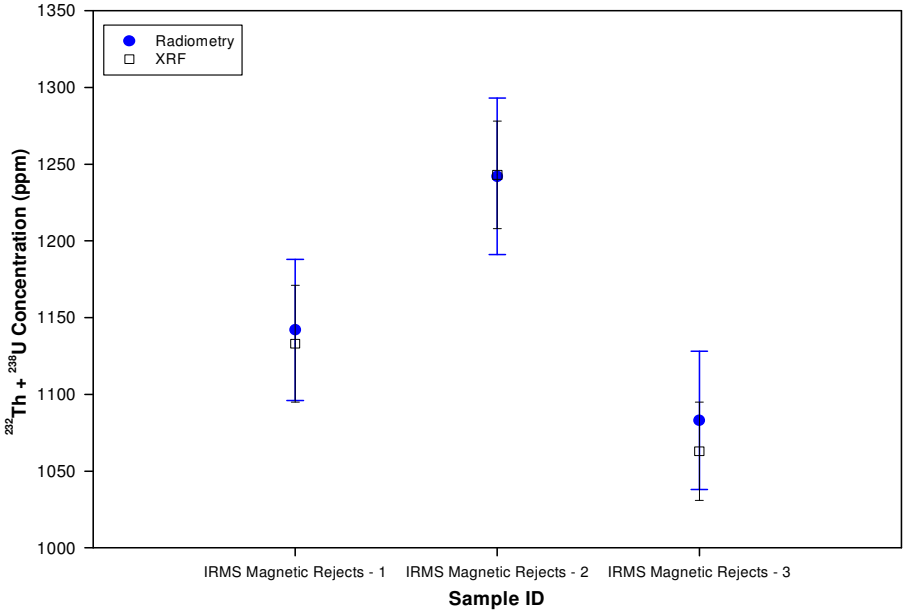

Figure 42. ***Radiometric and XRF sample concentrations for samples labelled IRMS Magnetic Rejects 1, 2 and 3.***

Samples were taken from the IRMS Magnetic Rejects tailings created after the initial magnetic separation process. Top left is the ^{238}U concentration (ppm), top right the ^{232}Th concentration (ppm) and bottom left is total concentration. The error bars depict the total error (i.e. statistical and systematic).

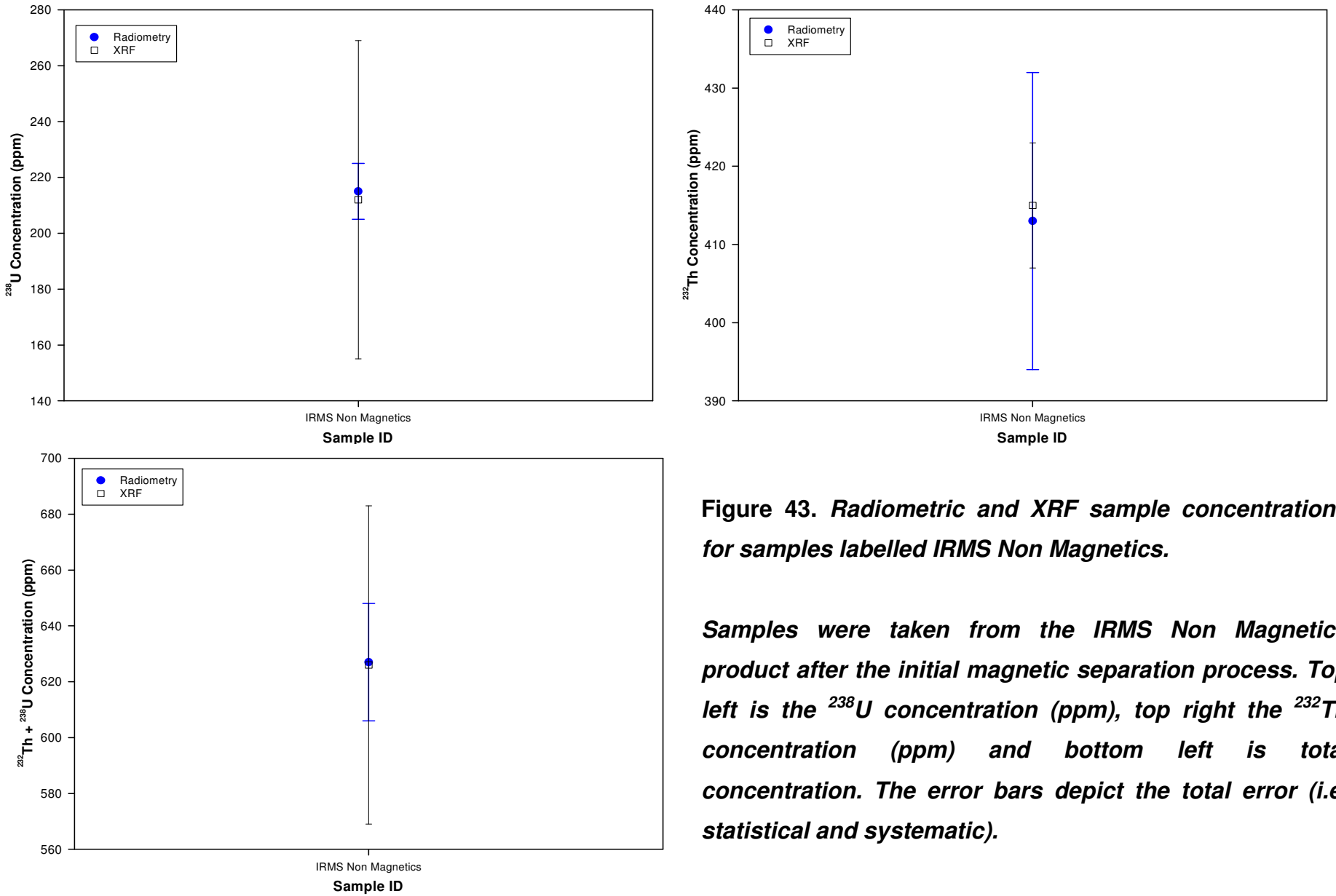

Figure 43. ***Radiometric and XRF sample concentrations for samples labelled IRMS Non Magnetics.***

Samples were taken from the IRMS Non Magnetics product after the initial magnetic separation process. Top left is the ^{238}U concentration (ppm), top right the ^{232}Th concentration (ppm) and bottom left is total concentration. The error bars depict the total error (i.e. statistical and systematic).

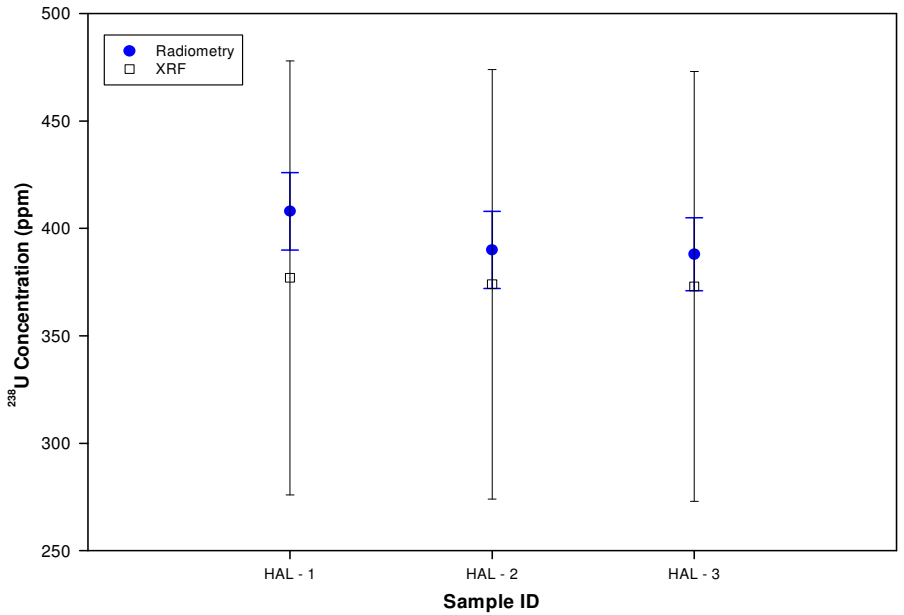

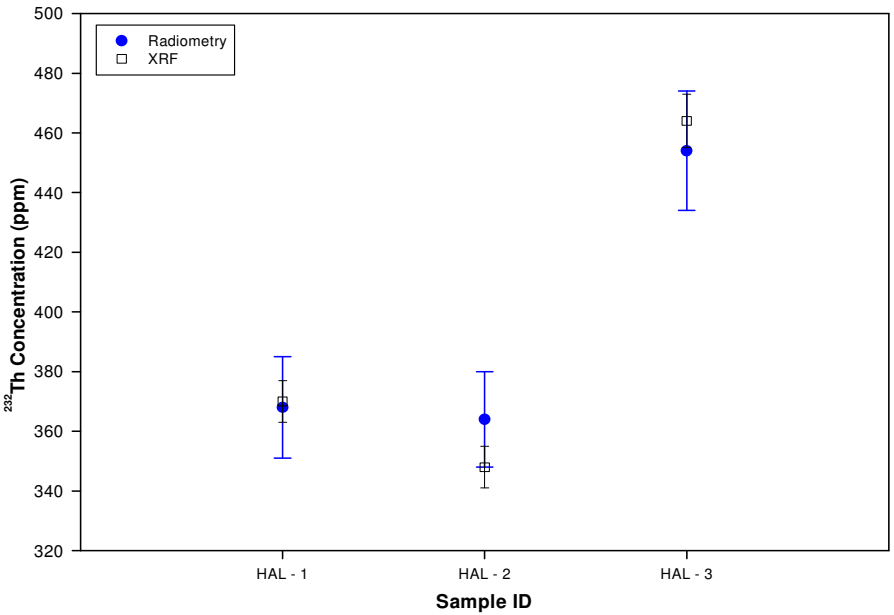

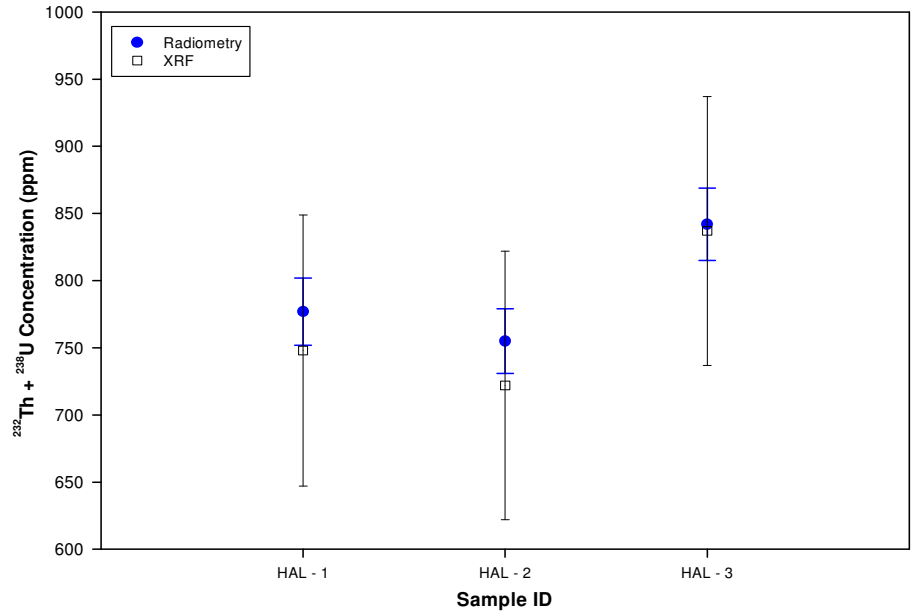

Figure 44. ***Radiometric and XRF sample concentrations for samples labelled HAL 1, 2 and 3.***

Samples were taken after the minerals left the Hot Acid Leach process. Top left is the ^{238}U concentration (ppm), top right the ^{232}Th concentration (ppm) and bottom left is total concentration. The error bars depict the total error (i.e. statistical and systematic).

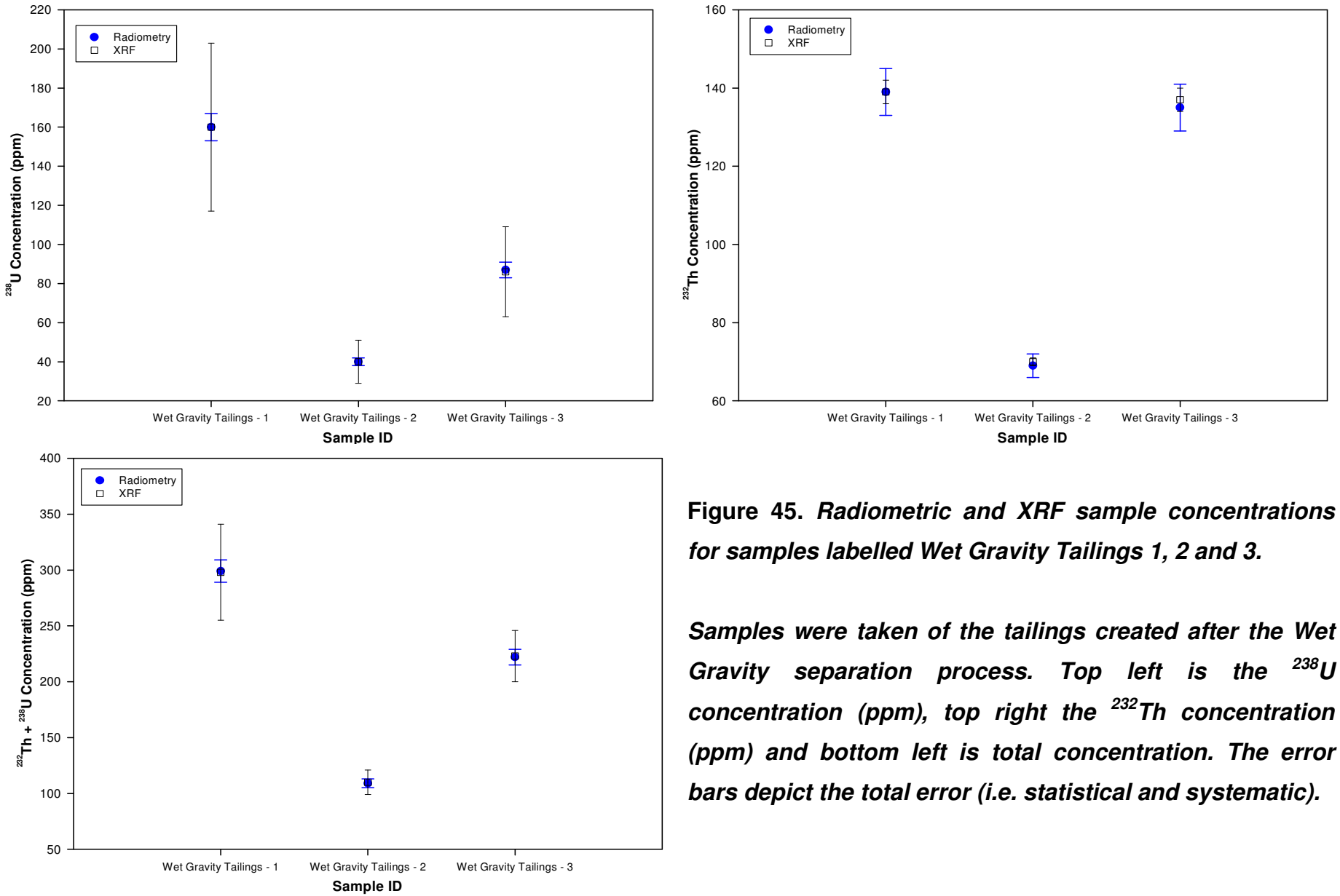

Figure 45. ***Radiometric and XRF sample concentrations for samples labelled Wet Gravity Tailings 1, 2 and 3.***

Samples were taken of the tailings created after the Wet Gravity separation process. Top left is the ^{238}U concentration (ppm), top right the ^{232}Th concentration (ppm) and bottom left is total concentration. The error bars depict the total error (i.e. statistical and systematic).

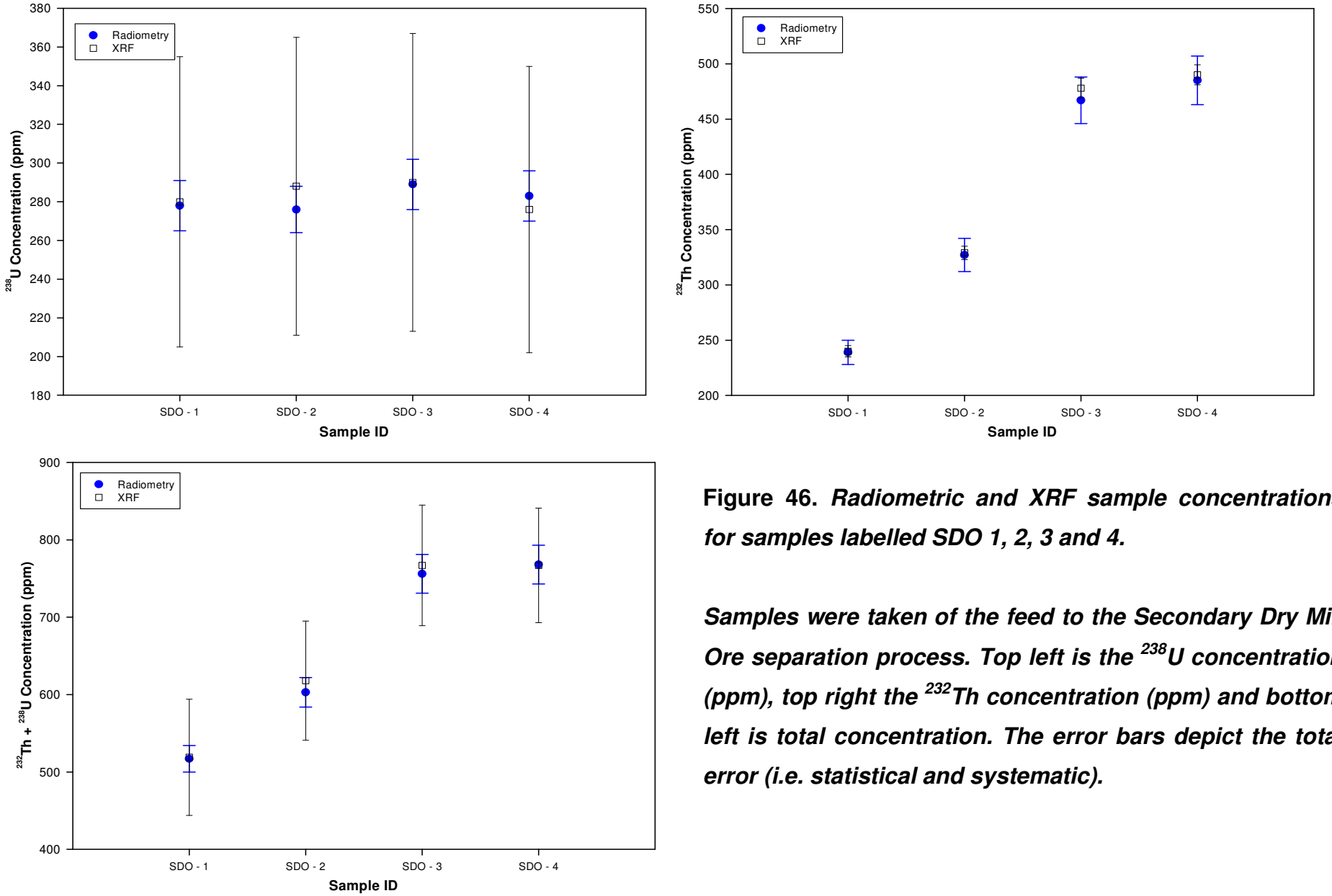

Figure 46. ***Radiometric and XRF sample concentrations for samples labelled SDO 1, 2, 3 and 4.***

Samples were taken of the feed to the Secondary Dry Mill Ore separation process. Top left is the ^{238}U concentration (ppm), top right the ^{232}Th concentration (ppm) and bottom left is total concentration. The error bars depict the total error (i.e. statistical and systematic).

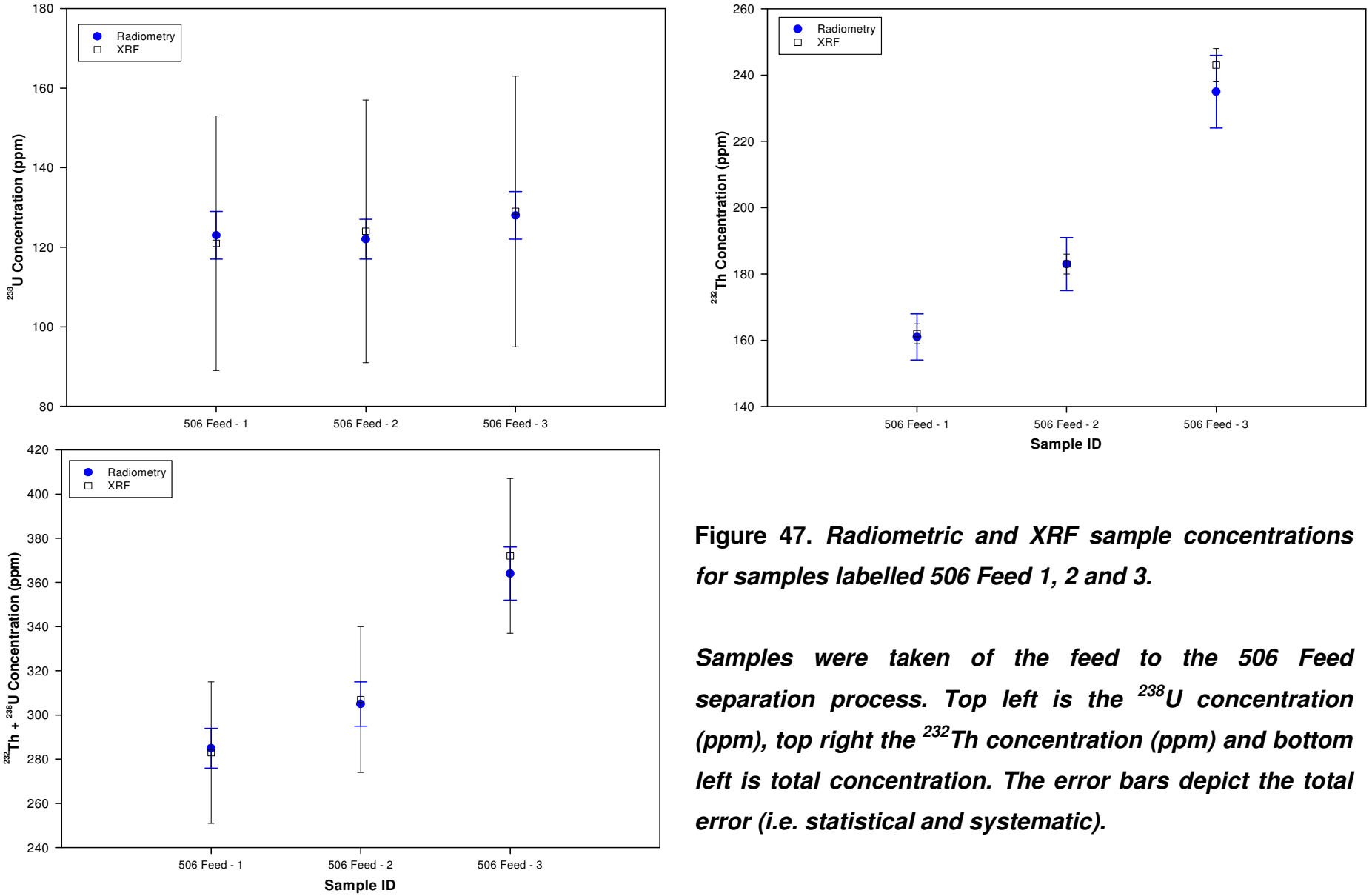

Figure 47. ***Radiometric and XRF sample concentrations for samples labelled 506 Feed 1, 2 and 3.***

Samples were taken of the feed to the 506 Feed separation process. Top left is the ^{238}U concentration (ppm), top right the ^{232}Th concentration (ppm) and bottom left is total concentration. The error bars depict the total error (i.e. statistical and systematic).

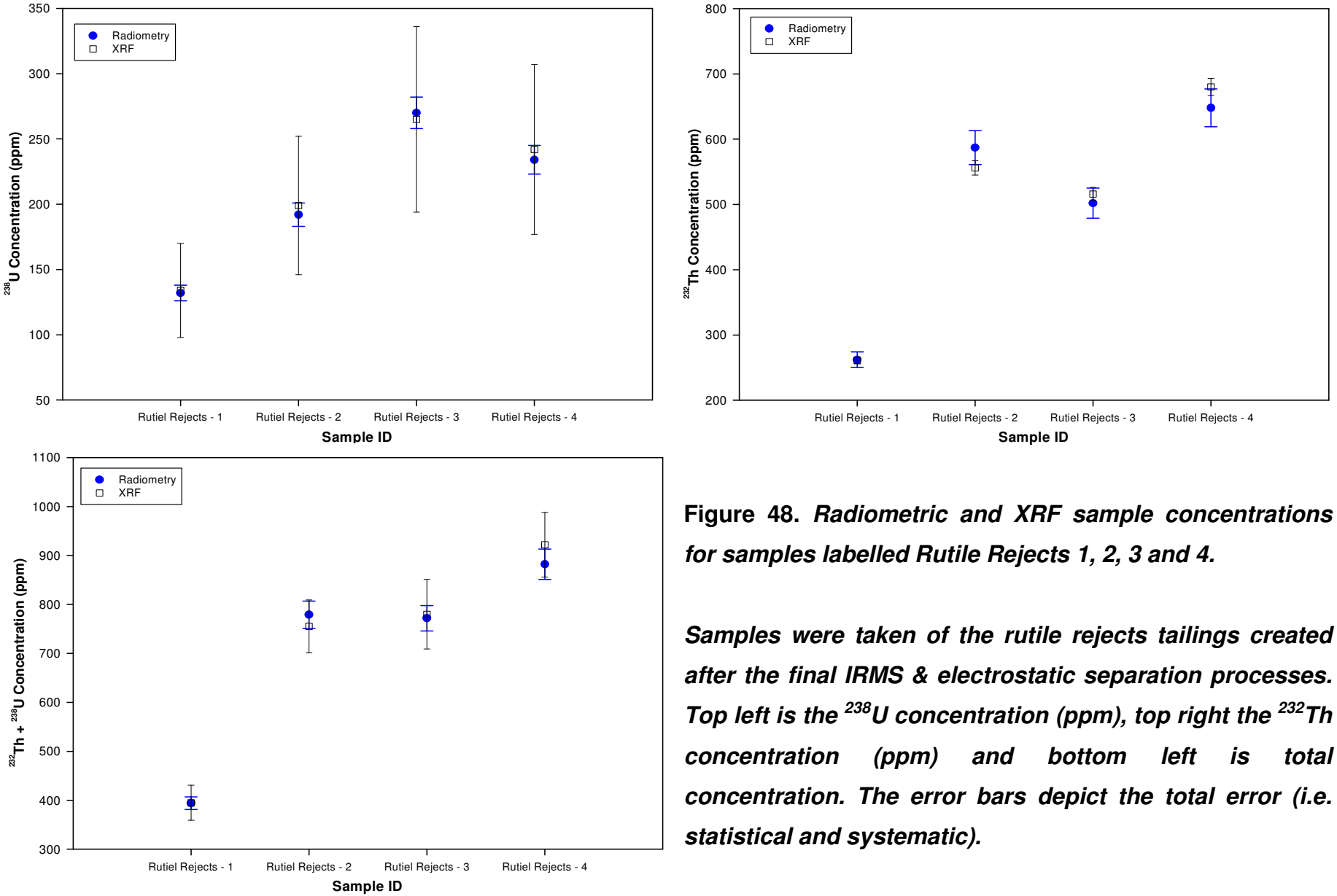

Figure 48. ***Radiometric and XRF sample concentrations for samples labelled Rutile Rejects 1, 2, 3 and 4.***

Samples were taken of the rutile rejects tailings created after the final IRMS & electrostatic separation processes. Top left is the ^{238}U concentration (ppm), top right the ^{232}Th concentration (ppm) and bottom left is total concentration. The error bars depict the total error (i.e. statistical and systematic).

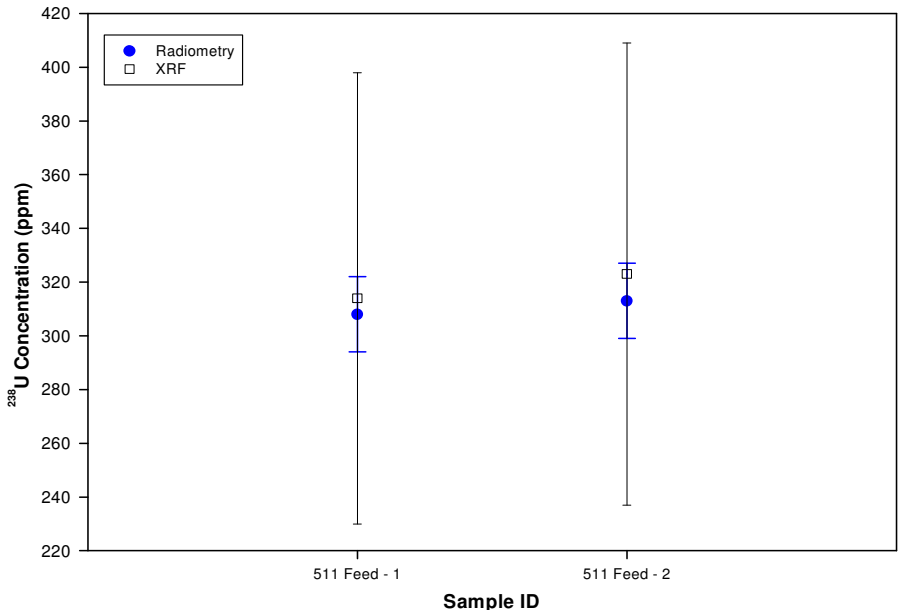

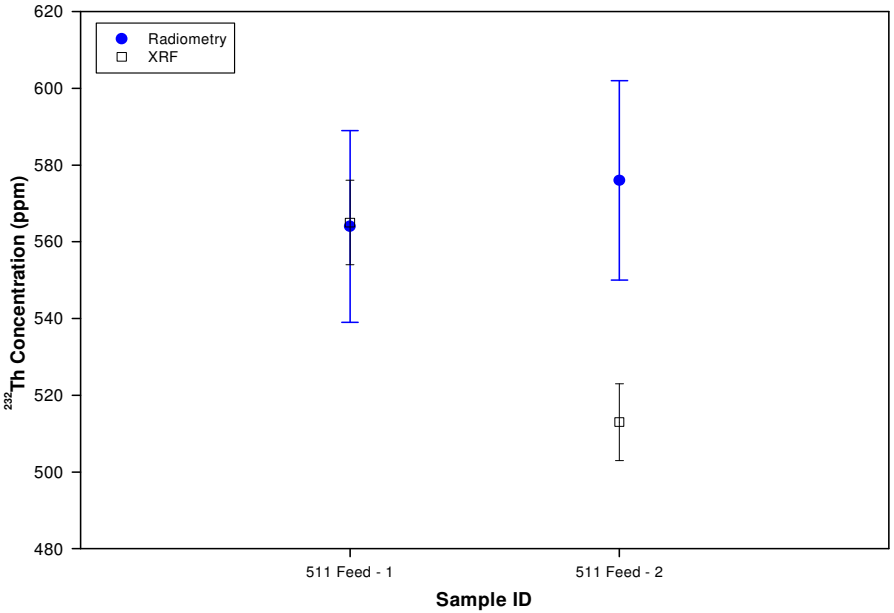

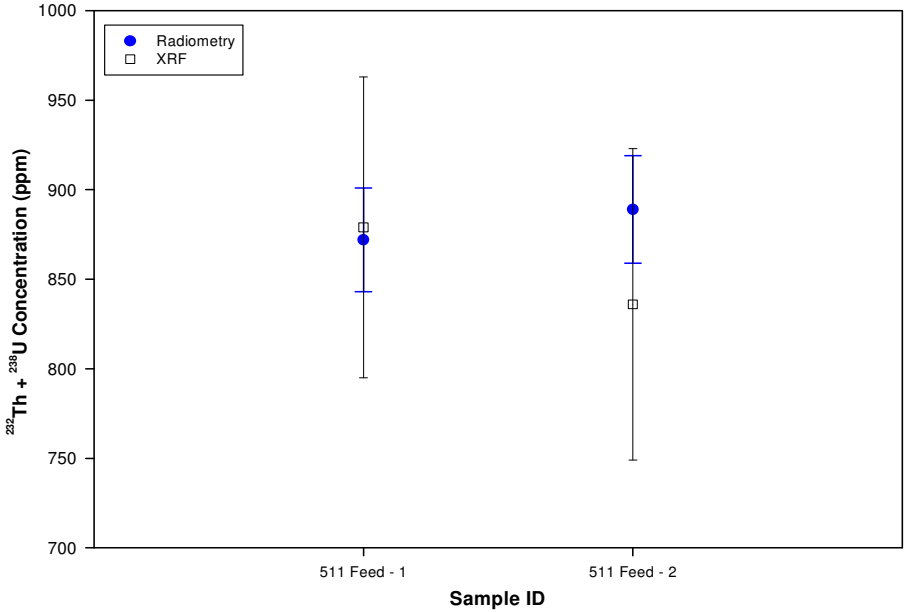

Figure 49. ***Radiometric and XRF sample concentrations for samples labelled 511 Feed 1 and 2.***

Samples were taken of the feed to the 511 Feed separation process. Top left is the ^{238}U concentration (ppm), top right the ^{232}Th concentration (ppm) and bottom left is total concentration. The error bars depict the total error (i.e. statistical and systematic).

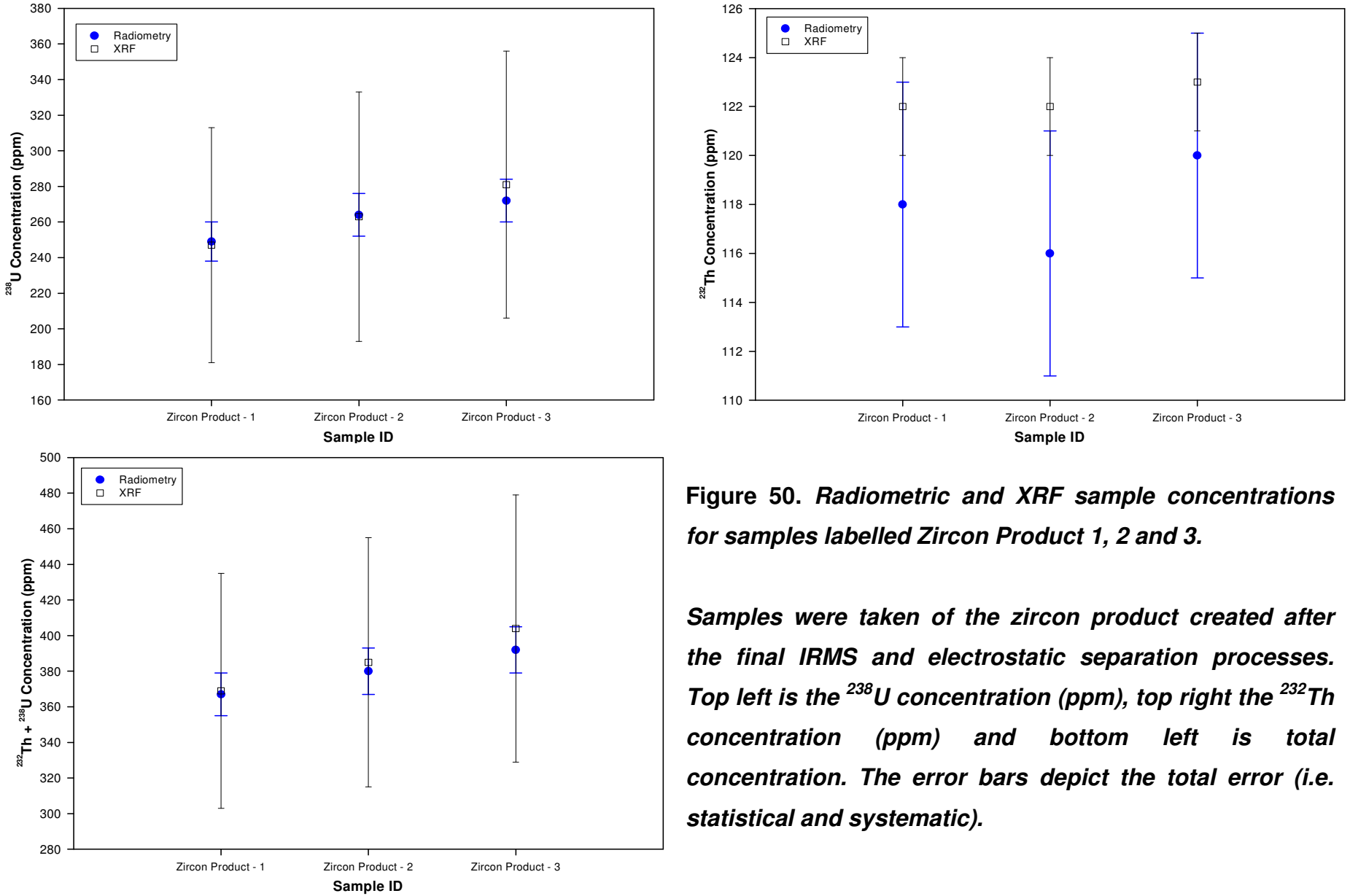

Figure 50. ***Radiometric and XRF sample concentrations for samples labelled Zircon Product 1, 2 and 3.***

Samples were taken of the zircon product created after the final IRMS and electrostatic separation processes. Top left is the ^{238}U concentration (ppm), top right the ^{232}Th concentration (ppm) and bottom left is total concentration. The error bars depict the total error (i.e. statistical and systematic).

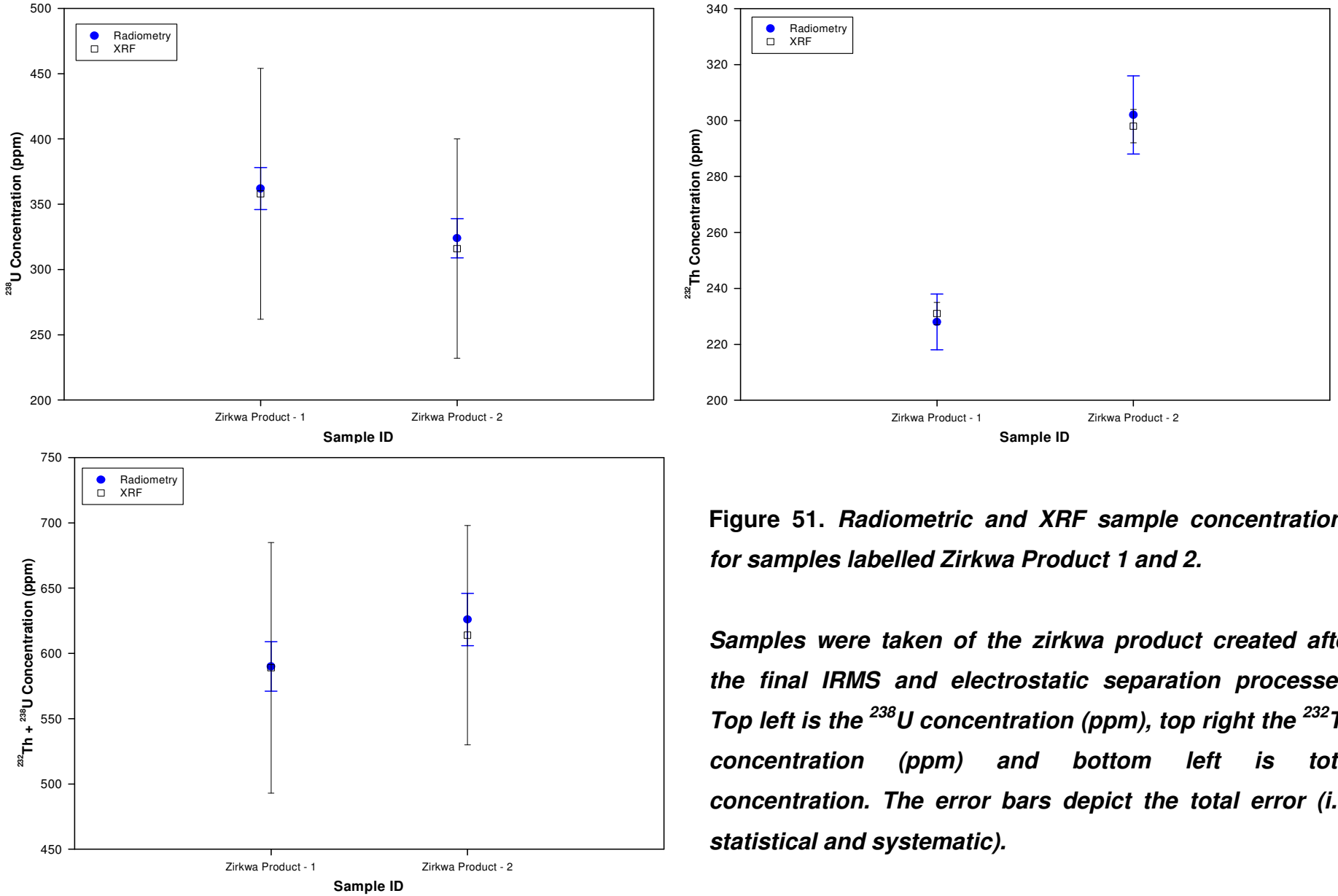

Figure 51. ***Radiometric and XRF sample concentrations for samples labelled Zirkwa Product 1 and 2.***

Samples were taken of the zirkwa product created after the final IRMS and electrostatic separation processes. Top left is the ^{238}U concentration (ppm), top right the ^{232}Th concentration (ppm) and bottom left is total concentration. The error bars depict the total error (i.e. statistical and systematic).

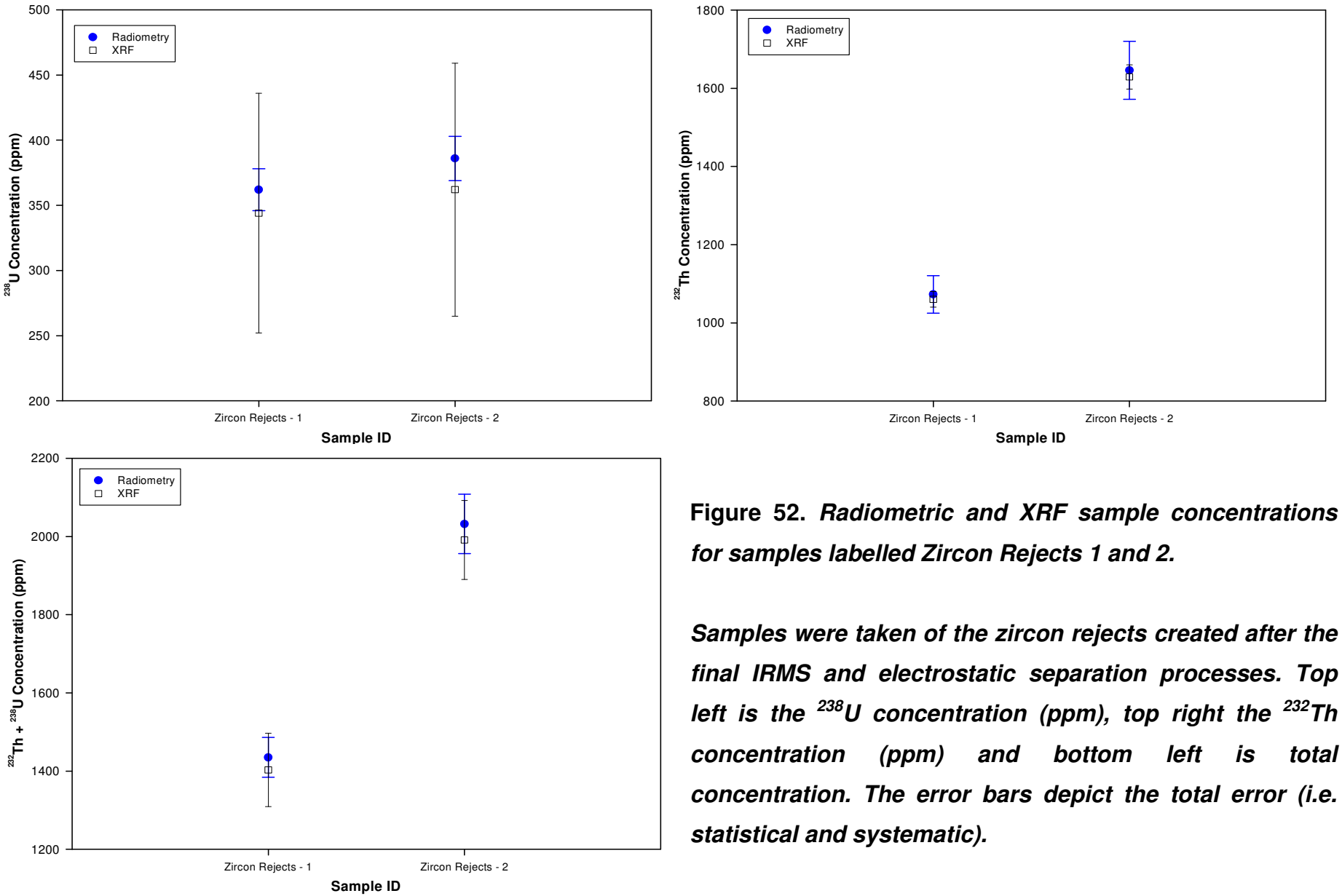

Figure 52. ***Radiometric and XRF sample concentrations for samples labelled Zircon Rejects 1 and 2.***

Samples were taken of the zircon rejects created after the final IRMS and electrostatic separation processes. Top left is the ^{238}U concentration (ppm), top right the ^{232}Th concentration (ppm) and bottom left is total concentration. The error bars depict the total error (i.e. statistical and systematic).

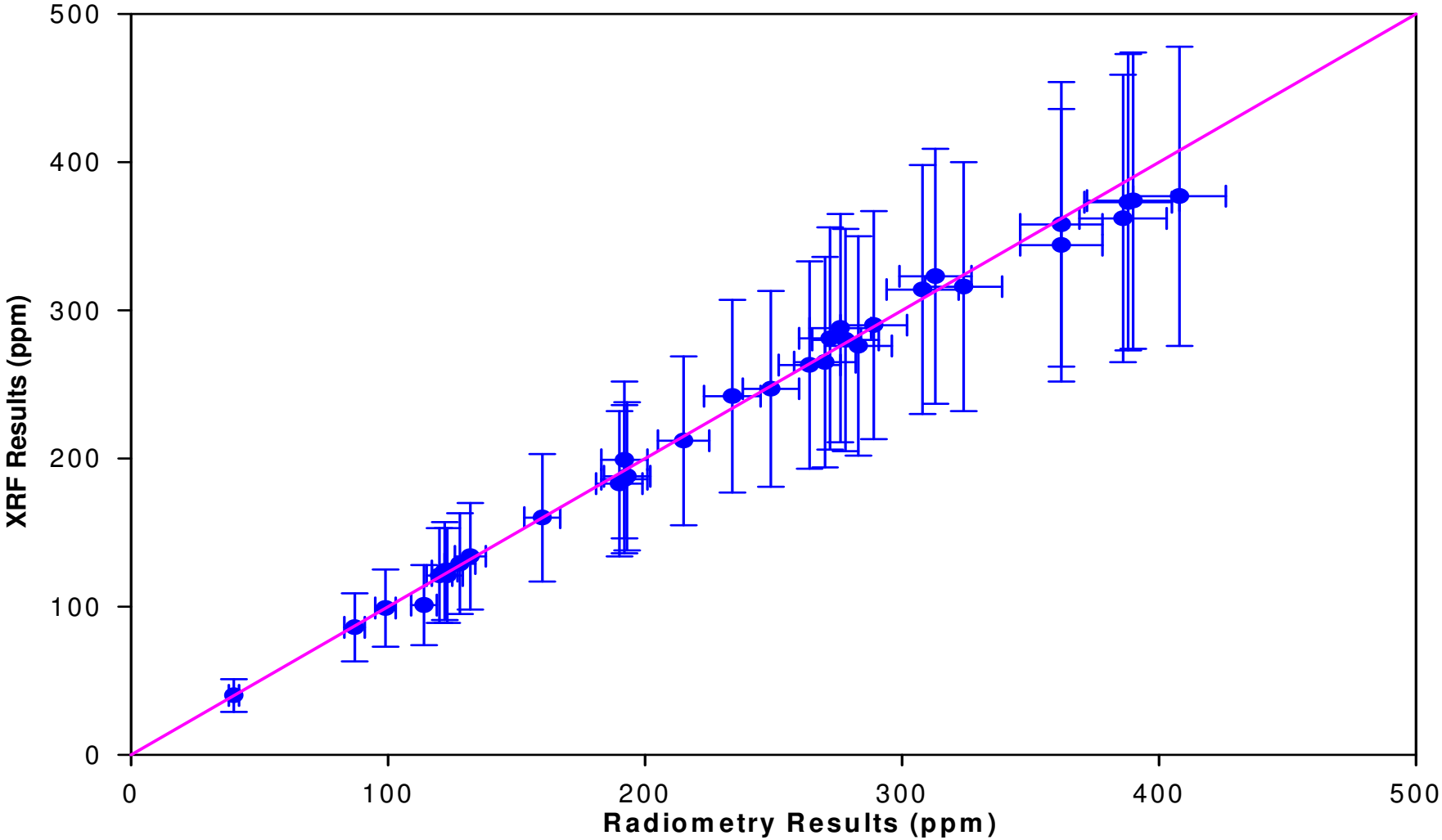

Figure 53. ***Comparison between the uranium sample concentrations of the mineral sands as obtained by radiometry and XRF. The solid line indicates the ideal correlation where the concentrations of radiometry and XRF are identical. The horizontal line of sample concentrations depicts the samples that were below the XRF detection limit. The error bars indicate the total error (i.e. statistical and systematic).***

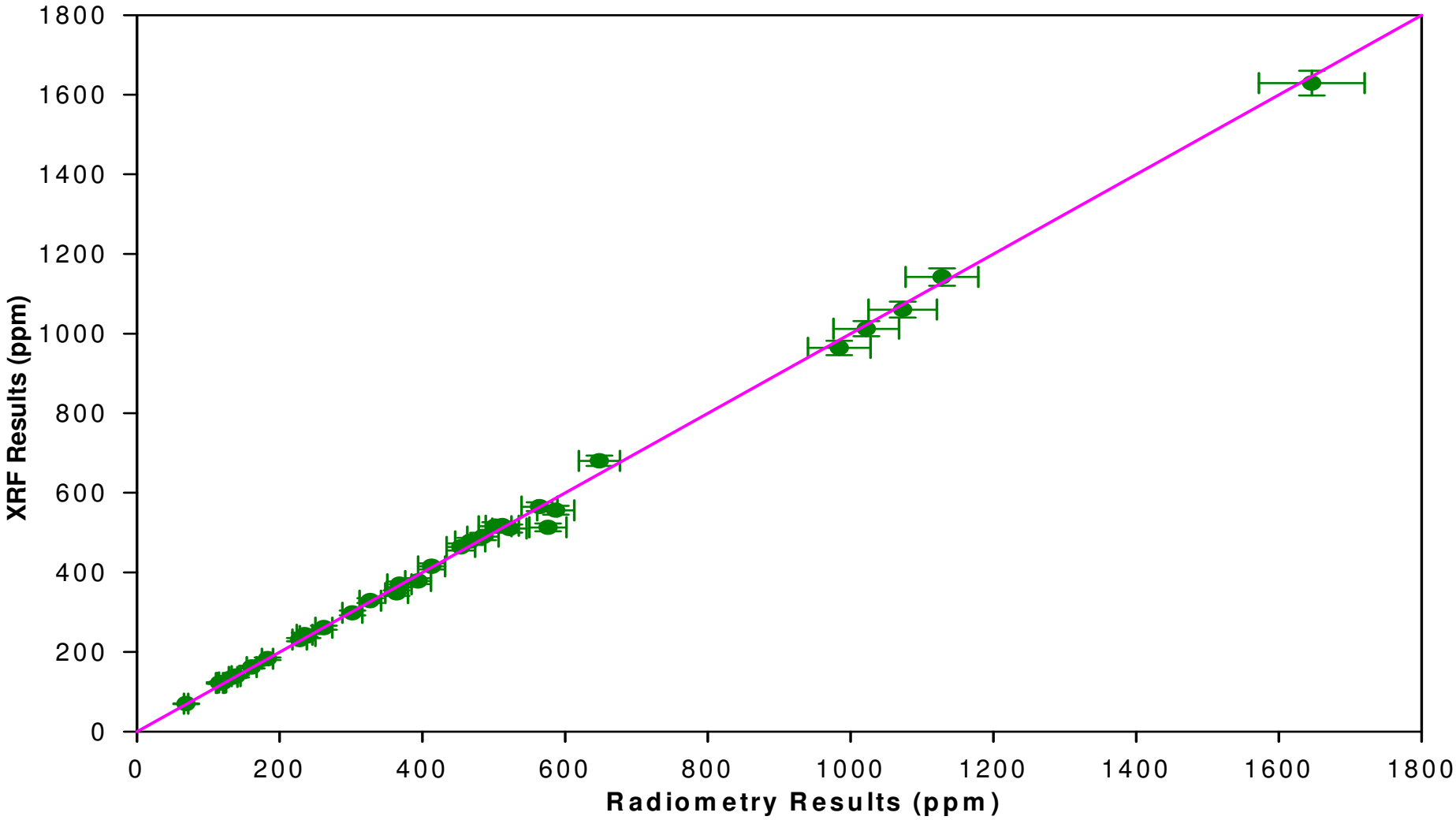

Figure 54. ***Comparison between the thorium sample concentrations of the mineral sands as obtained by radiometry and XRF. The solid line indicates the ideal correlation where the concentrations of radiometry and XRF are identical. The error bars indicate the total error (i.e. statistical and systematic).***

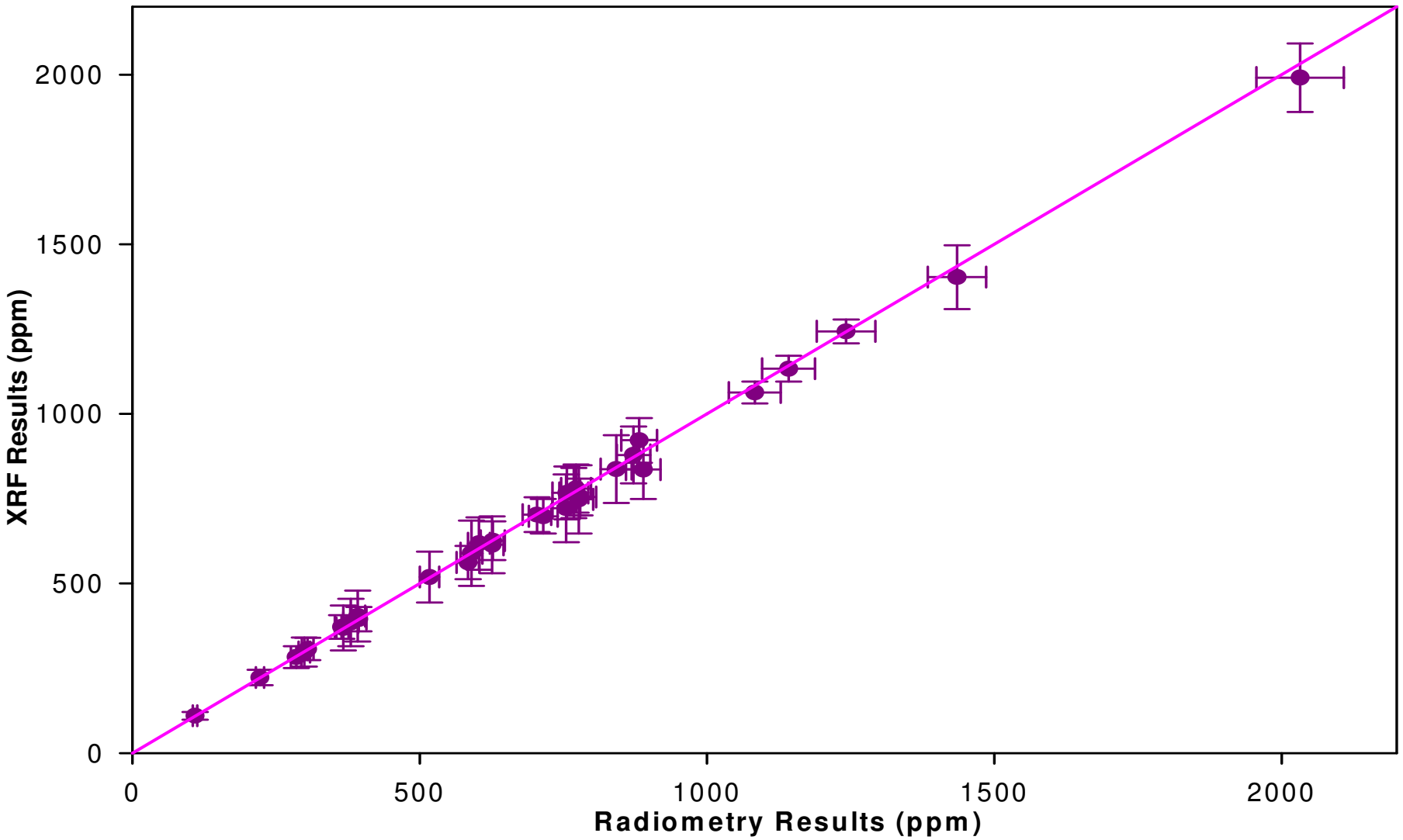

Figure 55. ***Comparison between the total sample concentrations of the mineral sands as obtained by radiometry and XRF. The solid line indicates the ideal correlation where the concentrations of radiometry and XRF are identical. The error bars indicate the total error (i.e. statistical and systematic).***

5.3.15 Counting time comparison

An effective on-line radiometry system should be able to count samples in less time than the 3600 s used in this study. Notwithstanding the fact that in plant conditions a scintillation detector would be better suited, the effect of a reduction in counting time on the sample concentration, while all other parameters were kept constant, was investigated. All the samples were measured using counting times of 3600 s, 900 s, 300 s, 60 s, 15 s, 5 s and 1 s. The concentrations of the different counting times and their correlation with the concentrations obtained with 3600 s are important as it indicates the accuracy of the measurement. Correlations were therefore determined for all the data sets.

The derived concentrations for the counting times 900 s, 300 s and 60 s were within 1 standard deviation of those obtained with 3600 s (Table 26 to Table 28). The concentrations resulting from counting times of 15 s, 5 s and 1 s were in the worst cases within 2 standard deviations of the 3600 s concentrations (Table 29 to Table 31). An example of the results obtained with different counting times is depicted in Figure 56. (Figure 56 is an example of a case where the higher branching ratios of the 352 keV and 609 keV gamma rays of uranium benefitted the determination of the concentration as more counts (and therefore better counting statistics) were obtained in these photopeaks compared to the other photopeaks. For this reason the uranium concentrations show less variation in the error than the thorium concentrations.)

All the correlations can be described as excellent to good. The correlation for the ^{238}U concentrations ranged from 0.999 (900 s) to 0.853 (1 s). For the ^{232}Th the correlation ranged from 0.999 (900 s) to 0.894 (5 s) – the 1 s correlation was better than the 5 s one with a value of 0.904. The correlation for the total concentrations were between a value of 0.999 (900 s) and 0.896 (5 s) – again with the 1 s correlation of 0.901 better than the 5 s value. As an example are the correlations for 900 s and 5 s against 3600 s depicted in Figure 57, Figure 58 and Figure 59 for the concentrations of the three radioisotopes. The correlations for all the counting times are tabulated in Table 32.

The results of this investigation demonstrated that accurate results can be obtained even with short counting times, taking into account that the statistical error will increase as the counting time is reduced.

Table 26 ***Concentrations of the heavy mineral sand samples obtained with radiometry for ^{238}U, ^{232}Th and the total concentration for a counting time of 900 s.***

Sample ID		Concentration (ppm)					
		^{238}U	σ	^{232}Th	σ	Total	σ
IRMS-Feed	1	191	10	401	18	592	21
	2	191	10	522	24	713	26
	3	192	10	529	24	721	26
IRMS-Magnetic Rejects	1	119	6	1010	46	1129	46
	2	113	6	1134	51	1247	51
	3	102	5	999	45	1101	45
IRMS-Non Magnetic	1	214	11	411	19	625	22
Hot Acid Leach Recycle	1	413	21	365	17	778	27
	2	388	20	372	17	760	26
	3	391	20	459	21	850	29
Wet Gravity Tailings	1	153	8	152	7	305	10
	2	40	2	70	3	110	4
	3	86	4	134	6	220	8
SDO	1	277	14	241	11	519	18
	2	273	14	326	15	599	20
	3	289	15	470	21	759	26
	4	280	14	482	22	762	26
506-Feed	1	123	6	163	7	287	10
	2	120	6	185	8	305	10
	3	130	7	237	11	367	13
Rutile Rejects	1	127	7	253	11	381	13
	2	189	10	587	26	776	28
	3	266	14	496	22	762	26
	4	241	12	667	30	908	33
511-Feed	1	309	16	563	25	871	30
	2	314	16	587	27	901	31
Zircon Product	1	252	13	113	5	366	14
	2	268	14	125	6	393	15
	3	268	14	125	6	393	15
Zirkwa Product	1	366	19	239	11	604	22
	2	327	17	298	13	625	21
Zircon Reject	1	356	18	1024	46	1380	50
	2	384	20	1631	73	2016	76

Table 27 ***Concentrations of the heavy mineral sand samples obtained with radiometry for ^{238}U, ^{232}Th and the total concentration for a counting time of 300 s.***

Sample ID		Concentration (ppm)					
		^{238}U	σ	^{232}Th	σ	Total	σ
IRMS-Feed	1	193	10	399	18	591	21
	2	193	10	527	24	719	26
	3	192	10	531	24	724	26
IRMS-Magnetic Rejects	1	120	6	1002	45	1121	46
	2	113	6	1108	50	1221	50
	3	99	5	1002	45	1101	46
IRMS-Non Magnetic	1	217	11	412	19	630	22
Hot Acid Leach Recycle	1	415	21	388	18	802	28
	2	387	20	364	17	751	26
	3	391	20	463	21	854	29
Wet Gravity Tailings	1	158	8	154	7	312	11
	2	39	2	63	3	102	4
	3	89	5	142	7	231	8
SDO	1	275	14	233	11	509	18
	2	277	14	321	15	599	20
	3	291	15	461	21	752	26
	4	281	14	486	22	767	26
506-Feed	1	133	7	239	11	371	13
	2	121	6	175	8	296	10
	3	131	7	235	11	366	13
Rutile Rejects	1	128	7	248	11	376	13
	2	189	10	601	27	790	29
	3	267	14	507	23	774	27
	4	238	12	654	30	892	32
511-Feed	1	311	16	577	26	888	31
	2	317	16	605	27	922	32
Zircon Product	1	247	13	112	5	360	14
	2	267	14	115	5	382	15
	3	267	14	97	5	364	14
Zirkwa Product	1	372	19	239	11	611	22
	2	326	17	290	13	617	21
Zircon Reject	1	367	19	1061	48	1428	52
	2	383	20	1644	74	2027	77

Table 28 ***Concentrations of the heavy mineral sand samples obtained with radiometry for ^{238}U, ^{232}Th and the total concentration for a counting time of 60 s.***

Sample ID		Concentration (ppm)					
		^{238}U	σ	^{232}Th	σ	Total	σ
IRMS-Feed	1	186	10	401	19	587	21
	2	190	10	517	24	706	26
	3	198	10	505	24	702	26
IRMS-Magnetic Rejects	1	119	6	1073	49	1192	50
	2	120	6	1144	53	1264	53
	3	111	6	979	45	1090	46
IRMS-Non Magnetic	1	221	12	431	21	653	24
Hot Acid Leach Recycle	1	404	21	349	17	753	27
	2	389	20	357	17	746	26
	3	393	20	394	19	787	28
Wet Gravity Tailings	1	152	8	132	7	284	11
	2	38	2	78	5	115	5
	3	81	5	103	6	183	8
SDO	1	277	14	231	11	507	18
	2	271	14	317	15	588	21
	3	284	15	453	21	737	26
	4	233	12	424	20	657	24
506-Feed	1	123	6	140	7	263	10
	2	121	6	209	10	330	12
	3	124	7	204	10	329	12
Rutile Rejects	1	134	7	165	8	299	11
	2	190	10	628	29	818	31
	3	262	14	501	24	763	27
	4	238	12	688	32	927	34
511-Feed	1	312	16	516	24	828	29
	2	318	16	604	28	922	33
Zircon Product	1	249	13	107	6	356	14
	2	259	13	99	5	358	14
	3	263	14	112	6	375	15
Zirkwa Product	1	362	19	202	10	563	21
	2	322	17	278	14	600	21
Zircon Reject	1	363	19	1073	49	1437	53
	2	373	19	1644	75	2017	78

Table 29 ***Concentrations of the heavy mineral sand samples obtained with radiometry for ^{238}U, ^{232}Th and the total concentration for a counting time of 15 s.***

Sample ID		Concentration (ppm)					
		^{238}U	σ	^{232}Th	σ	Total	σ
IRMS-Feed	1	190	11	376	21	566	23
	2	185	10	463	25	649	27
	3	170	10	452	25	622	26
IRMS-Magnetic Rejects	1	129	8	1059	52	1188	53
	2	107	6	1073	53	1180	53
	3	112	7	978	48	1090	49
IRMS-Non Magnetic	1	199	11	419	23	618	26
Hot Acid Leach Recycle	1	396	21	156	10	552	24
	2	389	21	410	22	799	31
	3	423	23	345	20	768	30
Wet Gravity Tailings	1	130	8	149	10	279	13
	2	32	3	73	7	105	8
	3	97	7	117	11	214	13
SDO	1	166	9	280	16	446	19
	2	282	15	316	18	597	24
	3	280	15	399	22	679	27
	4	264	14	372	21	636	25
506-Feed	1	124	7	112	8	236	11
	2	106	6	161	11	267	12
	3	126	7	217	13	343	15
Rutile Rejects	1	108	6	245	15	352	16
	2	194	11	569	30	763	32
	3	242	13	326	19	568	23
	4	246	14	577	30	823	33
511-Feed	1	330	18	480	25	810	31
	2	328	18	541	28	869	33
Zircon Product	1	231	13	122	9	353	15
	2	264	14	136	10	399	17
	3	264	14	102	8	366	16
Zirkwa Product	1	355	19	166	11	520	22
	2	332	18	292	17	625	25
Zircon Reject	1	345	19	1064	52	1409	55
	2	361	20	1653	79	2015	82

Table 30 ***Concentrations of the heavy mineral sand samples obtained with radiometry for ^{238}U, ^{232}Th and the total concentration for a counting time of 5s.***

Sample ID		Concentration (ppm)					
		^{238}U	σ	^{232}Th	σ	Total	σ
IRMS-Feed	1	176	12	370	27	545	29
	2	217	14	505	34	722	36
	3	180	12	559	37	740	39
IRMS-Magnetic Rejects	1	114	9	475	33	588	34
	2	117	9	1047	60	1164	60
	3	114	9	943	55	1057	55
IRMS-Non Magnetic	1	221	14	416	29	636	33
Hot Acid Leach Recycle	1	310	19	69	10	379	21
	2	431	25	290	23	722	34
	3	403	23	413	30	816	38
Wet Gravity Tailings	1	146	10	136	16	282	19
	2	32	4	92	14	123	15
	3	86	8	121	18	207	20
SDO	1	266	16	191	17	456	24
	2	279	17	241	20	520	26
	3	244	15	466	32	711	35
	4	290	18	395	28	685	33
506-Feed	1	131	9	64	9	194	13
	2	145	10	191	17	336	20
	3	138	10	207	18	346	21
Rutile Rejects	1	122	9	209	19	331	21
	2	189	12	444	30	633	33
	3	240	15	396	29	635	32
	4	235	15	529	35	764	38
511-Feed	1	297	18	332	25	628	30
	2	284	17	594	38	878	42
Zircon Product	1	241	15	136	14	378	21
	2	272	16	148	15	420	22
	3	276	17	100	13	375	21
Zirkwa Product	1	356	21	193	18	549	27
	2	312	19	314	25	627	31
Zircon Reject	1	400	23	1125	63	1526	67
	2	387	23	1734	92	2120	94

Table 31 Concentrations of the heavy mineral sand samples obtained with radiometry for ^{238}U, ^{232}Th and the total concentration for a counting time of 1s.

Sample ID		Concentration (ppm)					
		^{238}U	σ	^{232}Th	σ	Total	σ
IRMS-Feed	1	159	18	283	43	442	47
	2	154	18	557	65	711	67
	3	200	21	647	70	847	73
IRMS-Magnetic Rejects	1	167	19	1060	96	1228	98
	2	85	13	1035	95	1120	96
	3	138	20	828	84	966	86
IRMS-Non Magnetic	1	230	23	383	52	612	57
Hot Acid Leach Recycle	1	324	28	453	61	777	67
	2	341	29	354	51	694	59
	3	361	30	821	90	1182	95
Wet Gravity Tailings	1	196	21	251	42	447	47
	2	24	7	129	35	153	36
	3	72	15	217	50	289	52
SDO	1	269	24	328	45	596	51
	2	314	27	469	61	783	66
	3	224	22	410	53	634	57
	4	175	19	551	65	725	67
506-Feed	1	52	9	296	45	349	46
	2	121	15	97	25	218	29
	3	121	15	340	51	461	53
Rutile Rejects	1	99	13	207	39	306	41
	2	165	18	713	73	879	75
	3	242	23	271	44	513	50
	4	286	27	646	70	932	75
511-Feed	1	286	25	588	65	874	70
	2	327	28	589	66	916	72
Zircon Product	1	249	23	72	25	320	34
	2	241	22	93	24	334	33
	3	295	26	74	23	369	34
Zirkwa Product	1	319	28	89	24	408	37
	2	290	26	388	52	678	58
Zircon Reject	1	341	29	1075	97	1416	102
	2	302	28	1633	130	1934	133

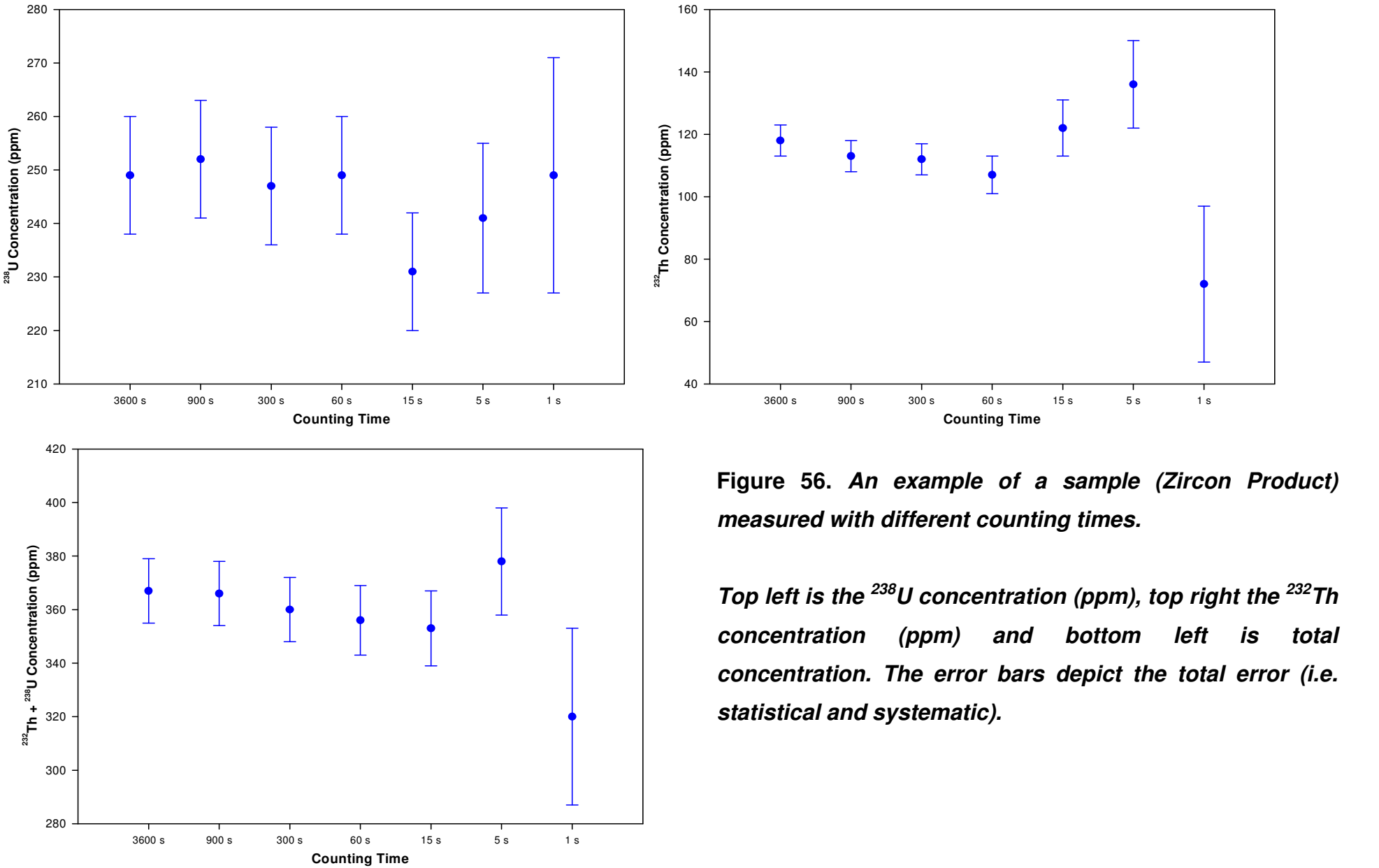

Figure 56. ***An example of a sample (Zircon Product) measured with different counting times.***

Top left is the ^{238}U concentration (ppm), top right the ^{232}Th concentration (ppm) and bottom left is total concentration. The error bars depict the total error (i.e. statistical and systematic).

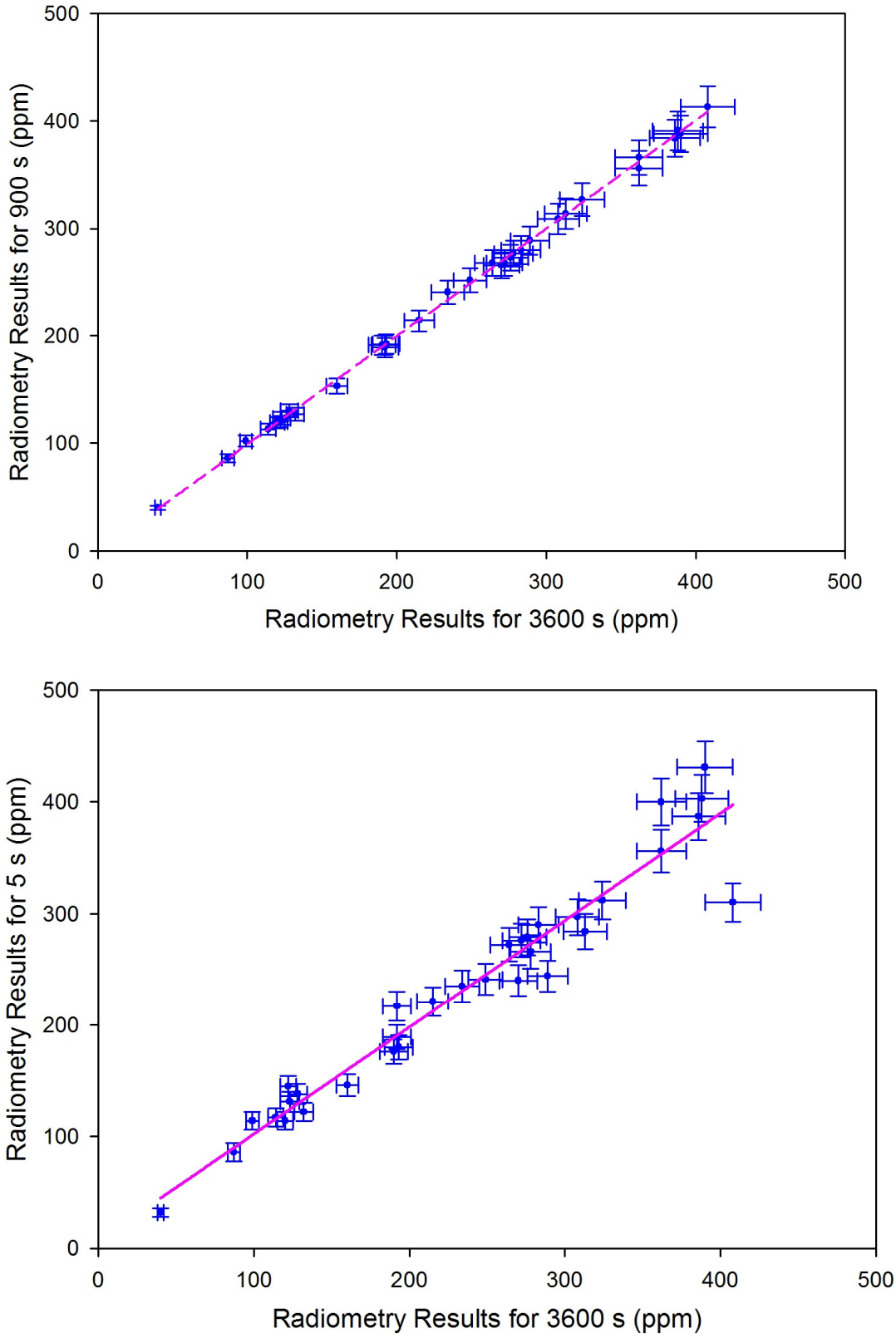

Figure 57. ***The correlations between the counting times of 3600 s and 900 s (top) and 3600 s and 5 s (bottom) for the determination of the ^{238}U concentrations.***

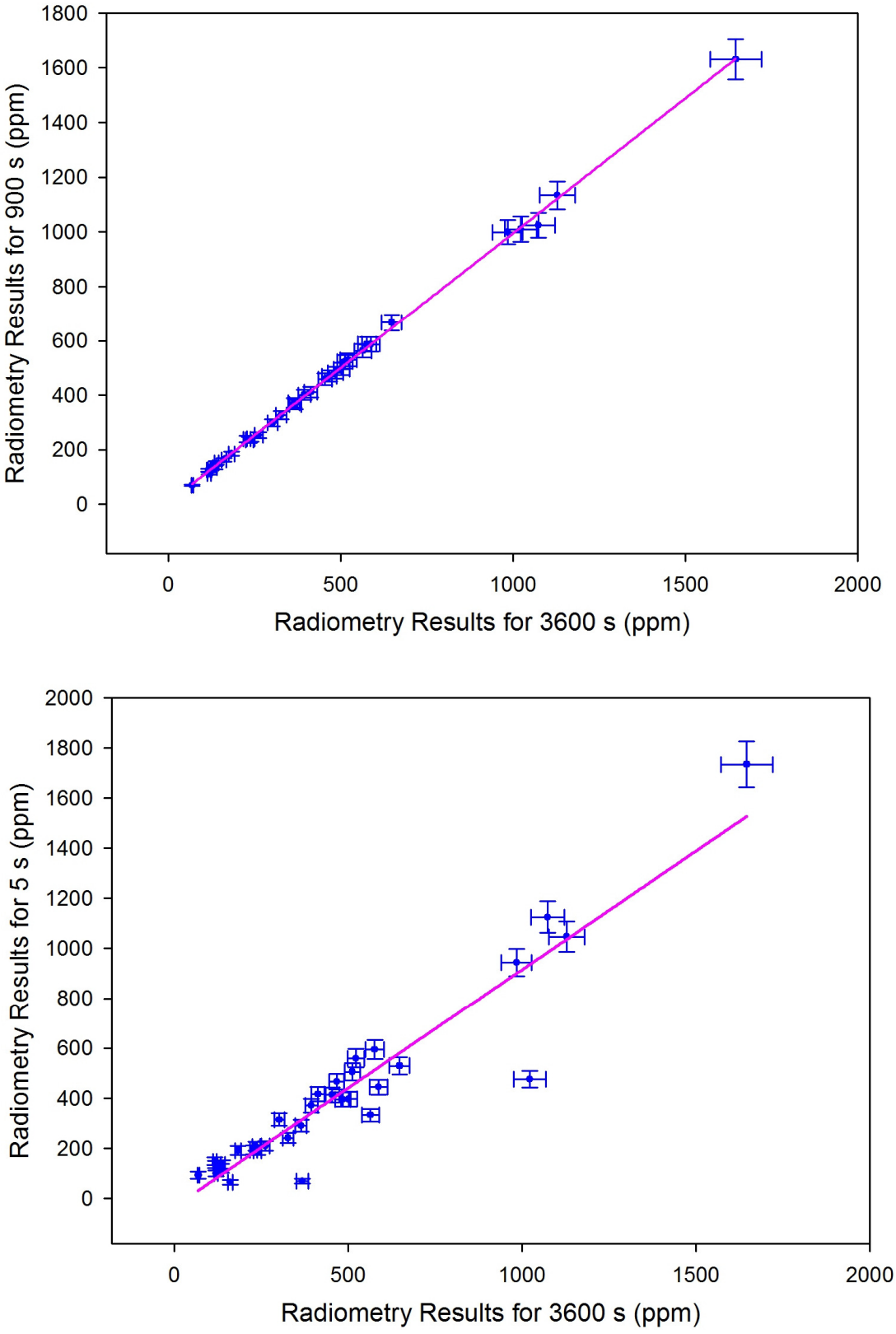

Figure 58. ***The correlations between the counting times of 3600 s and 900 s (top) and 3600 s and 5 s (bottom) for the determination of the ^{232}Th concentrations.***

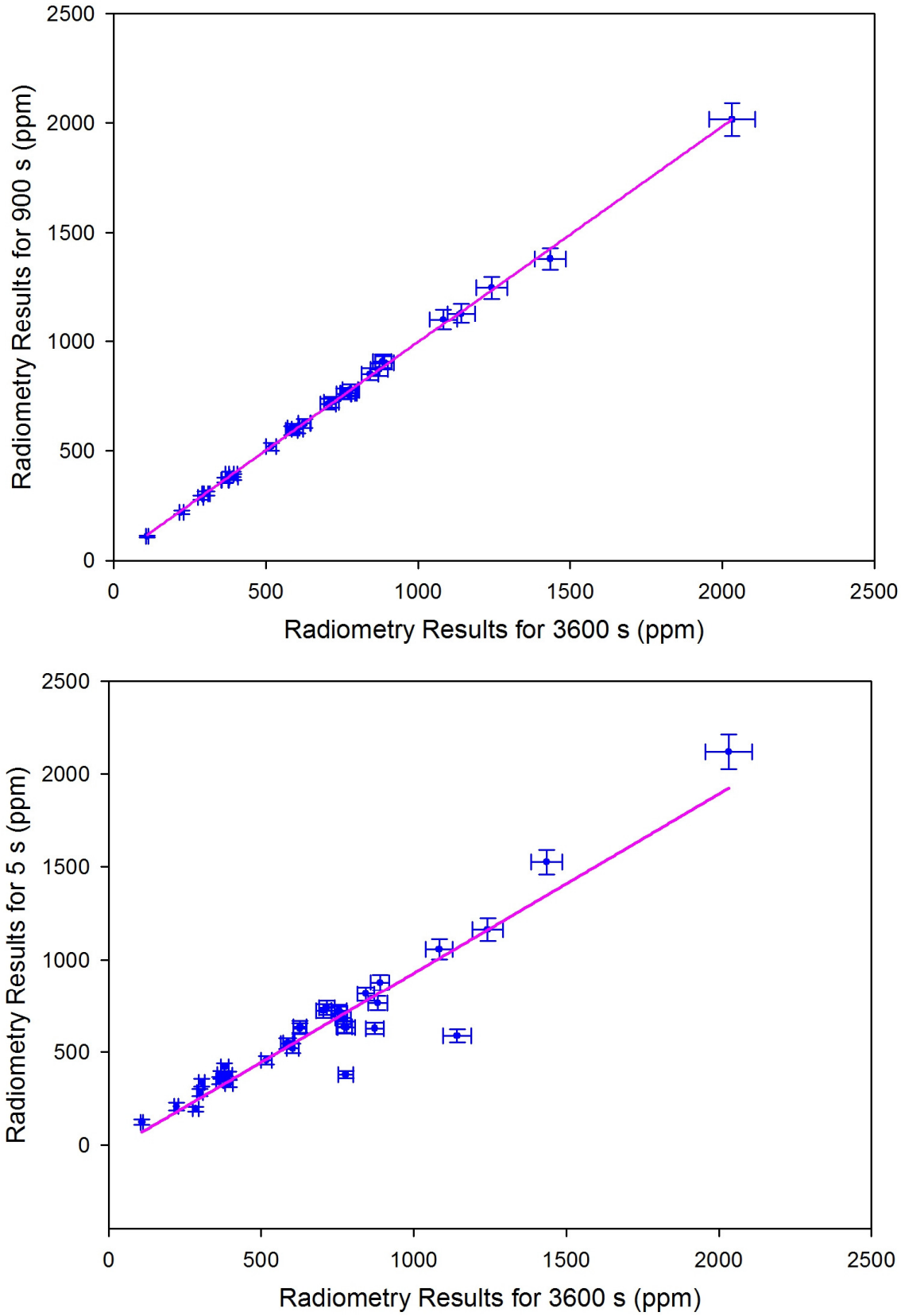

Figure 59. ***The correlations between the counting times of 3600 s and 900 s (top) and 3600 s and 5 s (bottom) for the determination of the total concentrations.***

Table 32 ***Correlation factors for determination of ^{238}U, ^{232}Th and total concentrations using different counting times compared to 3600 s***

	Counting Time (s)						
	3600	**900**	**300**	**60**	**15**	**5**	**1**
^{238}U	1.000	0.999	0.999	0.990	0.947	0.942	0.853
^{232}Th	1.000	0.999	0.997	0.994	0.975	0.894	0.904
Total	1.000	0.999	0.997	0.993	0.978	0.896	0.901

5.4 IMPLEMENTATION OF RADIOMETRY

It is observed from the characterisation of the different feeds/products that the input feed to a particular separation process is radiometrically different from the output feed/product. This difference can either be described by the total radioactivity concentrations or the uranium to thorium ratios. It was also demonstrated that radiometry can be a feasible alternative to XRF analysis when it comes to the measurement of radioactivity in heavy mineral sands. While laboratory-based radiometry cannot provide any real time control over separation processes it can be adapted for use as an online measurement method. As such is it suggested that radiometry be implemented in a Mineral Separation Plant in the following ways:

1) *Verify that the zircon and zirkwa meet the specifications*. In this application the total activity of the zircon and zirkwa need to be measured and the results compared to the specification criteria of less than 500 ppm and less than 1000 ppm total concentration respectively. A crude way of accomplishing this is by the use of a portable radiation detector. The active part of the detector is placed inside the final shipment of sand and a number of measurements are performed to obtain an average concentration. A far more effective method would be to do the analysis while the final product is on its way to the loading bin. A detector, which is mounted on top of the conveyor belt, can consistently verify the total concentration (Figure 60). This will result in improved quality assurance (over the portable option or XRF grab sample analysis) and material that is outside specification can be diverted quickly to another bin for either waste management or reclassification.

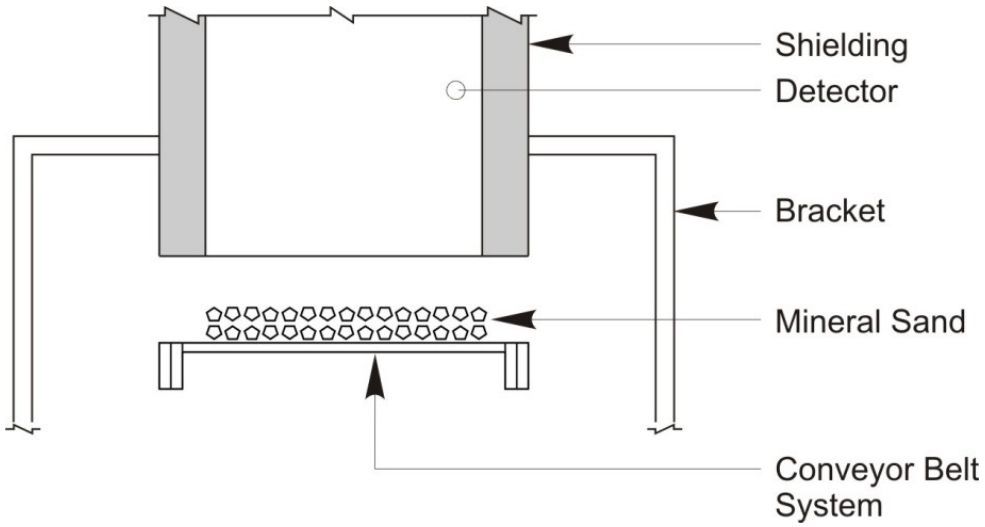

Figure 60. ***An illustration of a radiometry setup installed above a portion of a moving conveyor belt that transport heavy mineral sand.***

2) *Optimisation of the entrance feed.* The concentrations of the entry feed (IRMS Feed) were more or less constant. It is assumed that this is a result of the mining that occurred at the same heavy mineral placer during the time of sample gathering (with the analysis of more samples one can verify if this hold true). If the mineralogy of the ore body remains the same, it means that an individual set of metallurgical separation parameters can be chosen to optimise the first separation process for the feed from a particular ore body. With a similar radiometric setup as describe in 1), the feed can be screened. In this way the feeds from different ore bodies or mineralogical different feeds can be handled before the process starts without trying to fix the problem at a later separation stage which may entail more time, effort and cost.

3) *Optimisation of the separation processes.* The aim of a separation process is to separate different mineral species from one another. Similarly to the entrance feed was it observed that the concentrations of the products that enter or leave a separation process are fairly constant. By determining what the radiometric concentrations of a specific feed/product should be before and after a process it would be possible to verify the effectiveness of the separation process to extract the entire usable product. With a radiation detector set-up on both sides of the separation process (Figure 61) the product can be monitored. In real time. The

effect of changing metalluagical parameters can also be seen in real time, thus saving time and prevent a usable product from being diverted to the tailings stream.

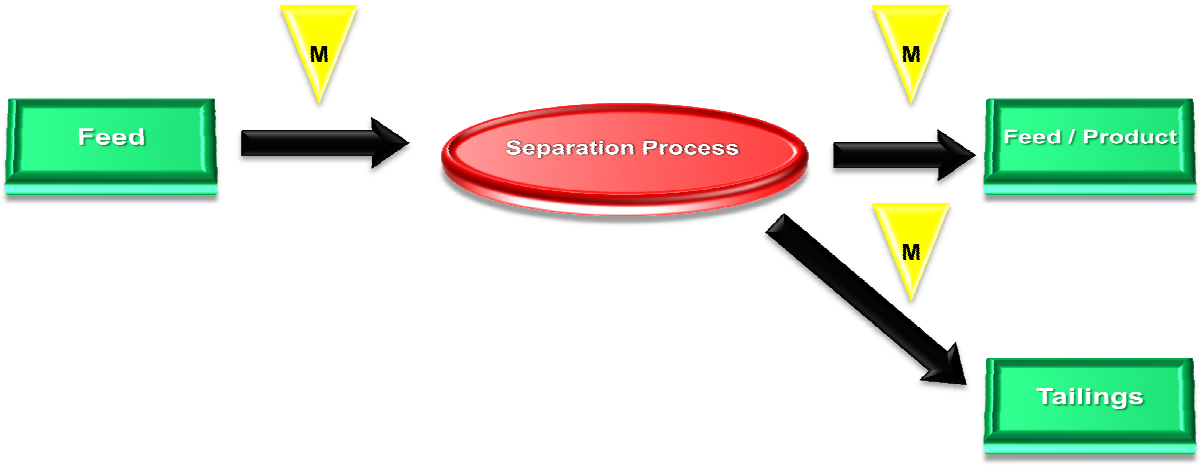

Figure 61. The basic locations for radiometric measurements with respect to a separation process. The yellow triangles indicate where radiometric measurements should be taken in order to optimise a separation process.

4) *Monitoring of tailings streams.* Radiometry can also be used to quickly characterise the tailings that are generated through different processes. In this way an inventory of products and concentrations can be created which will be useful for environmental monitoring purposes to assess the environmental liability of a process or the whole plant. The characterisation will also make it possible to make informed choices on were the tailings can be discarded e.g. either buried or safe to use for rehabilitation purposes on top of a waste dump. In the case of the monazite tailings (which are high in thorium) will the characterisation be helpful in the estimation of the ore grade since its demand is worldwide on the increase (Mining Weekly, 2010) and the possibility exists that sooner or later it will become a profitable product.

The basic locations for radiometric measurements, as set out in the above-mentioned paragraphs, are before and after a separation process (3.1.1). With this in mind will the measurement process entail, in brief, the following:

- the sample, on a conveyer belt, passes the detector,
- the grade and radioisotope ratio of the sample are determined,

- the sample undergoes the separation process,
- the sample, on a conveyer belt, passes another detector,
- the grade and radioisotope ratio of the sample are determined again,
- a decision is made on the type of sample based on its correlation with known parameters and
- a decision is made where the sample needs to go; either back to previous process for reprocessing or onwards to new process, product bin or tailings stream.

The implementation of radiometry, based on the above seems to be relatively easy to accomplish. There are however, a number of practicalities that need to be addressed before it can be successfully utilised. The first is the placement of the detectors within the plant. The placement could change the layout of the plant but more importantly it will affect the shielding of the detectors. A detector with no shielding is not advisable since large amounts of dust are normally generated in a mineral separation plant. This dust can settle on the detector and increase the background, thus interfering with the measurements. The concentration of the feed/product also influences the amount of shielding as a high concentration product will be easier to distinguish from the background (less shielding) than a lower concentration product (more shielding). As a result must a background be determined after an energy and resolution calibration was performed. This background must include the background due to radioactivity but also any possible effects that the magnetic or electrostatic processes have on the working of the detector. From the obtained information can suitable shielding be chosen so that the background effect is minimised. The type of detector that will be used is the next question to be answered. The harsh conditions of the plant will make the use of a nitrogen cooled germanium detector impractical. Scintillator detectors, such as the NaI, BGO or $LaBr_3$ are robust to withstand these conditions. The NaI is the cheapest of the three, but don't have the best efficiency. In recent years an advancement in scintillator material led to the development of $LaBr_3$(Ce) detectors. This kind of detector provides a resolution that is approximately 2 times better and an efficiency that is 1.3 times better than the NaI(Tl) detector (Ortec, 2011) of the same volume. It also has improved temperature stability. It is in this decision that the interplay between detector parameters becomes very important.

A higher efficiency would mean that the counting time of a sample can be reduced, but it also determines how close to the sample the detector can be placed and how fast the conveyor belt can move underneath the detector in order to obtain a statistical significant

measurement. A decision has to be made whether the conveyor belt must move continuously or if a start-stop system must be employed. The start-stop system will provide more time for a measurement but in a high throughput plant it may not be a viable option. Once the choice of detector is narrowed down one has to decide on the method of peak area calculation that will result in a statistical significant measurement. Generally a window is set around the areas of concern in a gamma spectrum e.g. 1.37 – 1.57 MeV for potassium, 1.66 – 1.86 MeV for uranium and 2.41 – 2.81 MeV for thorium (IAEA, 1991) and the number of counts determined. Nowadays the full-spectrum analysis method (Hendricks et al., 2001) receives more attention due to the use of the whole spectrum resulting in smaller counting times. Contrary to the window method can this method not be used without first determining the necessary fitting parameters for the material in which it is going to be applied. This means that it has to be done for every separation process. The radiometry system also needs to address dead time of the detector. Non-paralysable electronics do exist and must be incorporated into the online system to prevent an off-specification load of sand that passes the detector while it is still busy working on the previous load. Another parameter that needs to be addressed is the density of the material and its effect on the measurement. In later stages of processing the density of the feed/product may be relatively constant as the product contains only one type of mineral but this is not the case for example the entrance feed. The thickness of the sample is also information that is needed as variations can be just as detrimental to the measurement as wrong densities. Radon loss must also be considered. In laboratory conditions the uranium concentrations in the mineral sand were underestimated by as much as 1.92 %. However the samples were not open to the environment, so the effect needs to be investigated to quantify the possible underestimation.

In addition, engineering and metallurgical aspects also need to be investigated. This includes amongst others the integration of the radiometry set-up with the existing software, the setup of a splitter system at each process for rerouting of off-specification feeds/products to respective locations, the effect of the metallurgical parameters on the radioactivity concentrations. This is of importance when a specific separation process needs to be optimised or changed to fit another type of feed.

Finally, all these aspects have an influence on the results, but also on the uncertainty of the measurement. As part of the result the uncertainty will determine the action level under which the system will identify the sample and where the sample needs to go. Its

determination is therefore crucial to ensure that the radiometry system will be able to distinguish between samples that lie very close to a specification border line. Many of the above-mentioned aspects are interlinked and a suitable solution may require much iteration before the optimal solution is found. However, the final system would provide a easy and cost effective method that can provide an online method of optimising and real-time control over the heavy mineral separation processes.

From this discussion it is obvious that this study is the first step towards the application of radiometry in the heavy mineral sand industry. While all of the above-mentioned aspects cannot be solved overnight the best solution is to start with the zircon/zirkwa verification method. The criteria level makes it easy to verify and the results can be confirmed with laboratory based radiometry. Thereafter one can move to the tailings stream characterisation and the optimisation of the entrance feed. Since many of the above mentioned aspects will be solved by then the optimisation of a separation process will follow easier.

5.5 CONCLUSIONS

Heavy mineral sands were characterised according to the criteria of separate uranium and thorium concentrations, the total concentration and the uranium-to-thorium ratio. Based on this approach radiometric differences were observed between the various samples and representative processes. For many of the processes the concentrations of its samples were within 1 to 3 standard deviations from each other. This is an indication that the particular separation process produces products that are radiometrically fairly constant. It was also observed that when all the results were viewed collectively, it was difficult to distinguish among the different processes, like SDO and Zirkwa Product. This is not problematic as the one process is not a feed to the other and results will therefore not interfere or complicate the separation process. The other criterion, that of the uranium-to-thorium ratio, proved to be a better method to differentiate between separation processes – especially when concentrations were nearly indistinguishable.

To demonstrate that radiometry and XRF can produce equivalent results, the sample concentrations were also determined with XRF and the two sets of results compared. The correlation between the data was excellent for both radioisotopes. This indicated that radiometry can be used as alternative to XRF for determination of concentrations. With the

prospects of performing online radiometric analysis this means that radiometry is a faster method than XRF, but with the same accuracy. The applicability of radiometry as an online measurement technique was also investigated by the successive determination of concentration by reducing the counting time while keeping all other parameters constant. The comparison between results was in most cases very good due to the increase in the statistical error.

Grade control (from entry feed to final product) and the efficiency of separation processes and the monitoring of tailings streams can therefore be monitored with the use of radiometry, but it has a shortcoming. Radiometry measures only the radioactivity concentration of the heavy mineral sands and not the concentrations of other elements or impurities that also forms part of the specification criteria (Chapter 1). If it can be demonstrated that zircon with a radioactivity concentration of less than 500 ppm are always in specification regarding the other impurities then radiometry would be regarded as the replacement of XRF in all aspects. This needs to be investigated as for now XRF is still needed in grade control. For radiometry to be applied online certain site specific criteria need to be investigated. This means that the setup time for radiometry is longer than XRF, but the cost benefit lies in the fact that processing decisions can then be implemented quickly in order to optimise the final product and therefore increasing revenue.

CHAPTER 6 THE VINEYARD SOIL APPLICATION

In this chapter radiometry is applied with the aim to demonstrate its applicability as a possible useful tool in soil classification by defining some terroir characteristics of three Pinotage producing vineyards from a radiometric viewpoint. The chapter starts with brief descriptions of terroir and the geological setting of the three vineyards. Thereafter the measured ^{238}U, ^{232}Th and ^{40}K concentrations of soil and rock samples are presented and discussed. Next the results of the comparison exercise with XRF are presented. This is followed by a brief overview of a follow-up in-situ radiometric study at one of the vineyards and finally the conclusions, of radiometry as a vineyard soil application, are given.

6.1 INTRODUCTION TO TERROIR

South Africa has 110 200 hectares (or 1.5 % of the total world wine producing surface area) under vines (Bargmann, 2003). This area accounts for 3.1 % of the international wine production, placing South Africa in 7th position with France (20.9 %), Italy (18.7 %) and Spain (15.1 %) at the top three positions.

One of South Africa's most favourable areas for wine producing is the Stellenbosch region of the Western Cape. It is internationally known for producing top quality white and red wines. Although a diversity of cultivars is grown in the area, quality comparisons both locally and on national scale have shown that probably the best Pinotage wine produced in South Africa comes from a localised area north of Stellenbosch. Some of the parameters that are used in quality comparisons are: flavour, colour, pH of the wine, and chemical composition. All these factors are influenced by the "terroir" of the area.

Wine experts don't agree on the precise definition of the term "terroir" (Wikipedia, 2006) but a large contribution to this encompassing term is the geography of the area (Wooldridge, 2003). Some of the components are climate, topography and soil type (Robinson, 2006). Topography refers to the natural landscape features such as valleys, mountains, outcrops, rivers and dams. All of which influence the way the climate interacts with the area. Soil type refers to aspects such as intrinsic nature of the soil (e.g. drainage, fertility and heat retaining ability (Robinson, 2006), particle size range and soil mineralogy (Wooldridge, 2003). An important aspect of soil mineralogy is the clay fraction

(Wooldridge, 2003) which relates to the amount of potassium in the soil and is one of the factors that influence the pH of the wine (Koegelenberg, 2003).

6.2 GEOLOGICAL SETTING

Three Pinotage producing wine estates in the Stellenbosch region, Kanonkop (4-star), Simonsig (2-star) and Spier (Platter, 2002) were selected (Figure 62). All three have different wine quality, soil profiles and bedrock characteristics (Figure 63).

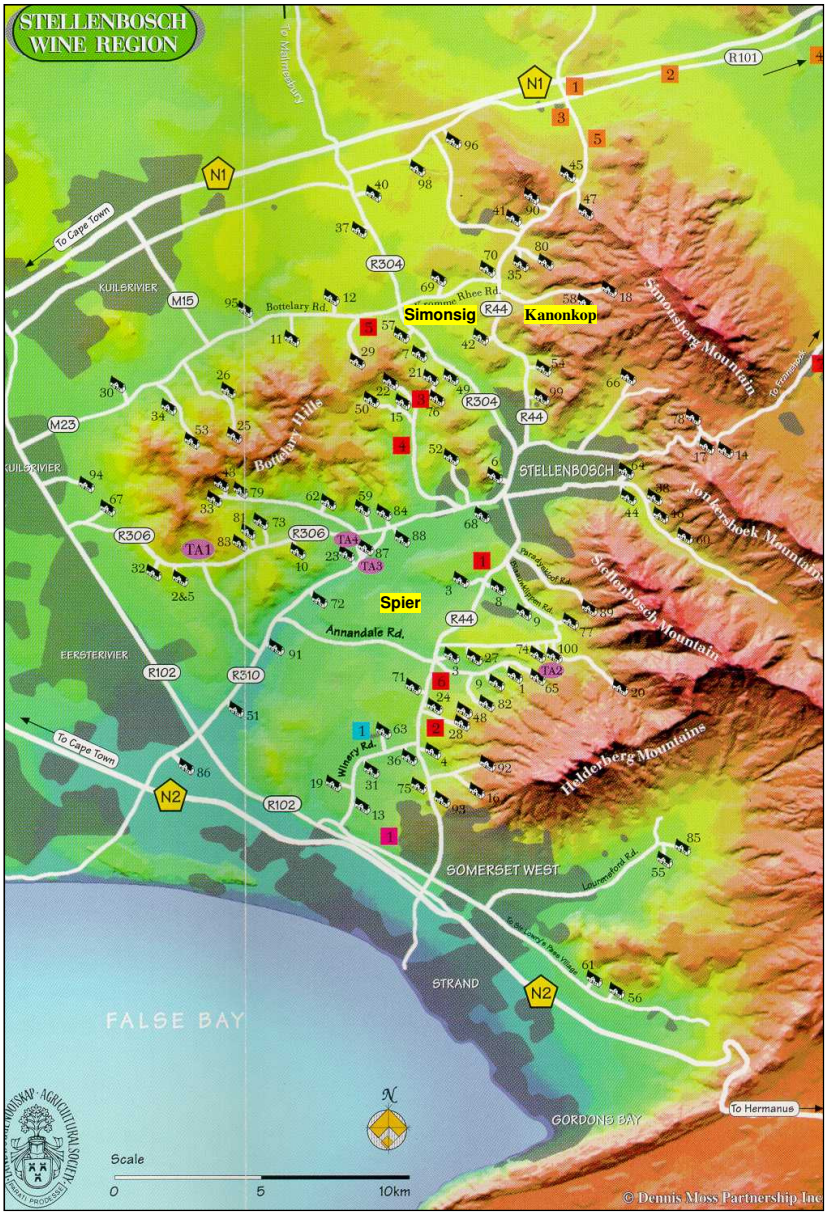

Figure 62: Geomorphology and location of the three wine estates, Kanonkop, Simonsig and Spier.

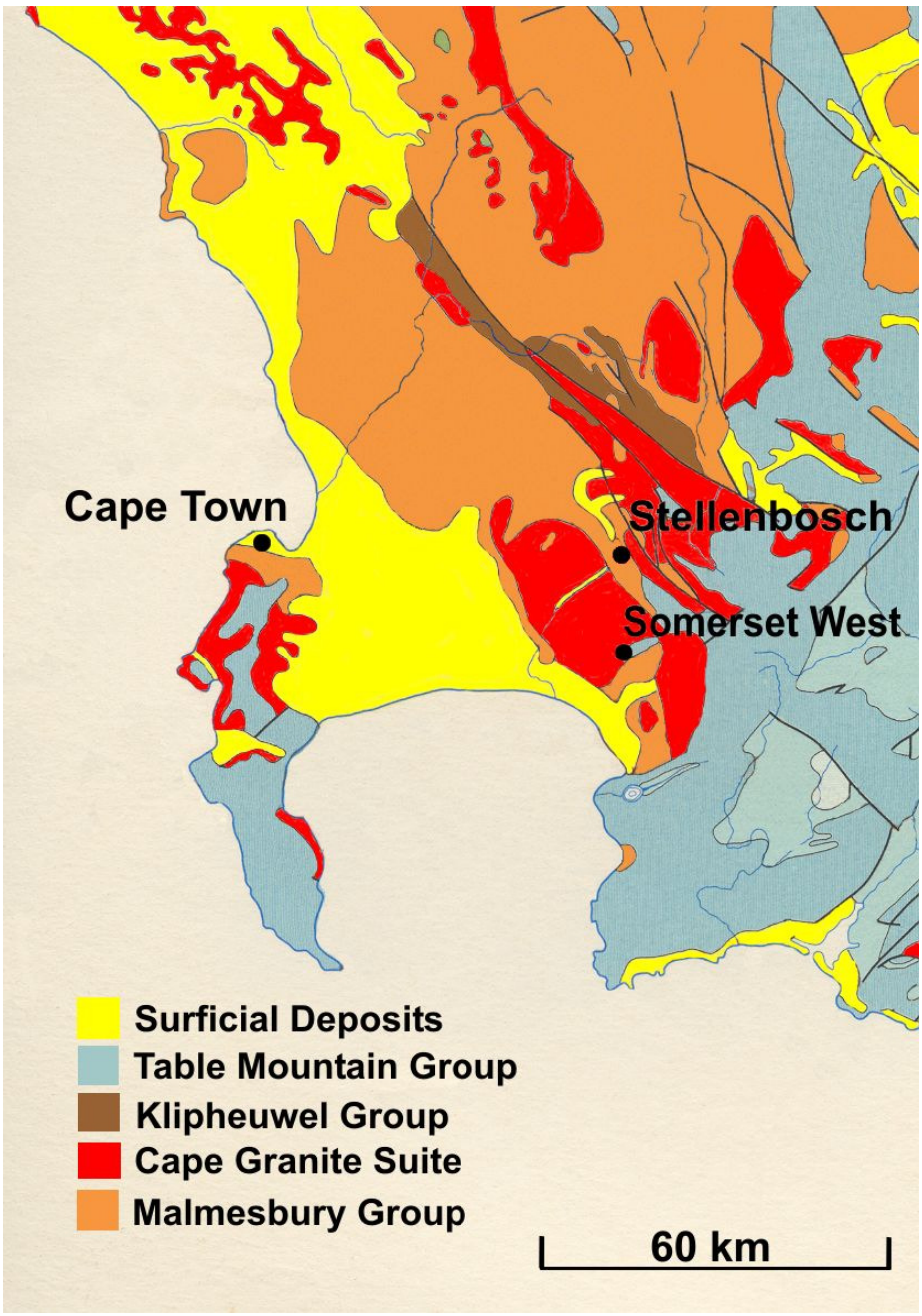

Figure 63: ***A map of the Western Cape, illustrating the different geologies of the region.***

The Stellenbosch region forms the basis for a diversity of lithologies. The oldest rocks form part of the Neoproterozoic Malmesbury Group (~700Ma) and consist of a complex sedimentary sequence of deformed meta-volcanic rocks dominated by phyllites, schists and minor greenstones. These soft and friable rocks are deeply weathered and produce a dense clay-rich soil. These lithologies have been intruded by the Cape Granite Suite (515-565Ma), which consists mainly of coarse-grained, porphyritic S-type granites. Outcrops

weather positively and the soils generated by the granites are sandy with visible feldspar grains and often transported. Locally, structurally controlled deep kaolinization of the granites occurs producing an in situ, clay-rich soil profile. Thick sequence coarse clastic sediments of the Ordovician-Silurian Table Mountain Group unconformly overlie the Precambrian lithologies. These, mainly orthoquartzites, are responsible for the spectacular mountain scenery that typifies the Stellenbosch region. It produces extensive scree fans on the slopes and a transported barren sandy soil cover in the valleys.

Kanonkop is in the Stellenbosch Pluton area with parts underlain by the Franschoek Formation of the Swartland Subgroup. As this is part of the Malmesbury Group, the geology is dominated by sandstones and clays (with clay minerals, quartz, feldspar and chlorite-sericite). Two areas on this farm were chosen; one against a mountain slope (Top Block) and the other more on the lower ground (Bottom Block). The latter has no rock outcrop while only poor outcrop is visible on the Top Block. The soils are classified Hutton to Glovelly (Van der Merwe, 2001) with the colour of the Top Block gravely orange to brown with many shale pebbles and sandstone. The Bottom Block soil is more a rich red brown colour, with fewer pebbles and more fine-grained than the Top Block.

The same Malmesbury group sediments are seen in the Simonsig rocks with soils classified as Glenrosa (Van der Merwe, 2001). Here again two blocks were identified. The first Kriekbult is flat-lying and considered part of the Simonsberg with a rich red, clayey, fine-grained igneous soil consisting of weathered products of granite, shale and Table Mountain Group sandstone derivatives. The other block is Simonsig, which is on a high lying part of the Devon Valley. Soils are orange-brown in colour, clayey and contain minerals such as biotite and feldspars.

Although Spier is also in the Stellenbosch Pluton, the geology primarily consists of Cape Granite with alkali feldspar phenocrysts and porphyritic biotite (Sa1 type) granites. At Spier the soils are sandy, coarse-grained, light brown in colour and classified as Fernwood (Van der Merwe, 2001).

6.3 RESULTS AND DISCUSSIONS

6.3.1 Radiometry and XRF Results

Radiometry was used to define some terroir characteristics of the three vineyards by the determination of the uranium, thorium and potassium concentrations in their soils and rocks. The uranium and thorium concentrations are indicators of whether the mineralogy of the soil is the same as the underlying bedrock (Rozendaal, 2001) as well as the soil maturity (meaning the extent of transport and reworking) (Rozendaal et al., 2004). Koomans (2000) demonstrated that soils with high ^{40}K concentration reflect a fine grain size and is a function of clay content. The proviso being that the clays is illite or kaolinite with adsorbed potassium. The potassium concentration will therefore be related to differences in the clay content of the soils.

This investigation assumes that the observed characteristics are due to the geology and soil type that are naturally found in the area and not from artificial means like fertilisers. Fertilisers can contain 0.2 ppm uranium per bag (IAEA, 2006), but also potassium that can be in the order of 70 g/kg. The presence of fertilisers can therefore influence the radiometric character of an area.

The radioisotope concentrations and elemental concentrations of the samples are grouped according to their location and summarised in Table 33 and Table 34 for radiometry and XRF respectively. The error presented with a result is the total error (i.e. combination of the systematic and statistical errors according to the error propagation rule). Also note that many of the uranium concentrations of XRF have the value of 1.0 ± 0.3 ppm that relates to a concentration that was below the XRF detection limit. The individual concentrations against sample number for all the areas are depicted in Figure 64, Figure 65 and Figure 66 respectively.

Table 33 ***Radioisotope concentrations of the vineyard soil samples determined with radiometry.***

Sample ID		Concentration					
		^{238}U (ppm)	Σ	^{232}Th (ppm)	σ	^{40}K (%)	σ
Kanonkop Bottom Block – Surface	1A	2.8	1.0	15	1	0.42	0.03
	1B	3.5	1.3	18	1	0.36	0.02
	1C	2.9	1.0	13	1	0.41	0.03
	1D	3.0	1.1	15	1	1.6	0.1
	1E	3.1	1.1	17	1	0.46	0.03
Kanonkop Top Block - 1m	2A	3.2	1.2	20	1	1.9	0.1
	2B	4.8	1.7	24	1	0.86	0.06
	2C	3.2	1.1	16	1	0.92	0.05
	2D	4.2	1.5	23	1	0.91	0.05
	2E	4.0	1.4	23	1	1.4	0.1
Kanonkop Top Block – Surface	3A	3.7	1.3	21	1	2.0	0.1
	3B	4.5	1.6	21	1	0.88	0.05
	3C	3.0	1.1	18	1	0.98	0.05
	3D	6.8	2.5	24	1	0.98	0.05
	3E	1.9	0.7	25	1	1.4	0.1
Kanonkop Top Block – Crushed	4 (1)	6.3	2.3	42	2	5.3	0.3
Rock	4 (2)	6.3	2.3	42	2	5.3	0.3
Spier – 1m	5-1m	1.4	0.5	7.0	0.3	0.29	0.02
Spier – Surface	5A	1.1	0.4	5.5	0.3	0.16	0.01
	5B	1.5	0.5	10	1	0.10	0.01
	5C	2.0	0.7	7.9	0.4	0.17	0.01
	5D	1.7	0.6	6.9	0.3	0.14	0.01
	5E	2.1	0.8	10	1	0.35	0.02
Spier - Crushed Rock	6	4.3	1.6	19	1	5.4	0.3
Simonsig Kriekbult – 1m / 2m	7-1m	2.3	0.8	14	1	0.60	0.04
	7-2m	2.9	1.1	23	1	0.53	0.05
Simonsig Kriekbult – Surface	8A	2.3	0.8	11	1	0.51	0.03
	8B	1.8	0.7	5.0	0.2	0.43	0.03
	8C	1.7	0.6	11	1	0.38	0.03
	8D	2.4	0.9	9.4	0.4	0.53	0.04
	8E	2.2	0.8	11	1	0.57	0.03
Simonsig – Surface	9A	3.9	1.4	15	1	1.5	0.1
	9B	3.7	1.3	16	1	1.6	0.1
	9C	2.4	0.9	10	1	0.80	0.06
	9D	1.4	0.5	5.6	0.3	0.53	0.04
	9E	2.6	0.9	7.5	0.4	1.1	0.1
Simonsig – 1m	9-1m(1)	6.7	2.4	15	1	1.3	0.1
	9-1m(2)	6.7	2.4	15	1	1.3	0.1
Simonsig Dam - Crushed Rock	10(1)	4.5	1.6	19	1	3.4	0.2
	10(2)	4.5	1.6	19	1	3.4	0.2
Simonsig - Crushed Rock	11(1)	4.0	1.5	17	1	4.5	0.2
	11(2)	4.0	1.5	17	1	4.5	0.2

Table 34 ***Radioisotope concentrations of the vineyard soil samples determined with XRF.***

Sample ID		Concentration					
		U (ppm)	σ	Th (ppm)	σ	K (%)	σ
Kanonkop Bottom Block – Surface	1A	1.0	0.3	15	0.3	0.42	0.04
	1B	1.0	0.3	18	0.3	0.37	0.03
	1C	1.0	0.3	14	0.3	0.42	0.04
	1D	1.0	0.3	15	0.3	1.6	0.1
	1E	1.0	0.3	17	0.3	0.47	0.04
Kanonkop Top Block - A 1m	2A	1.0	0.3	19	0.4	1.9	0.2
	2B	5.9	2	24	1	0.85	0.07
	2C	1.0	0.3	17	0.3	0.91	0.08
	2D	1.0	0.3	23	0.4	0.91	0.08
	2E	4.9	1	24	1	1.4	0.1
Kanonkop Top Block – Surface	3A	5.2	1	21	0.4	1.9	0.2
	3B	3.8	1	21	0.4	0.89	0.07
	3C	4.3	1	19	0.4	0.99	0.08
	3D	5.4	1	24	1	0.98	0.08
	3E	6.5	2	25	1	1.4	0.1
Kanonkop Top Block - Crushed Rock	4 (1)	10	3	44	1	5.3	0.4
	4 (2)	5.9	2	38	1	5.3	0.4
Spier – 1m	5-1m	1.0	0.3	6.8	0.1	0.30	0.02
Spier – Surface	5A	1.0	0.3	5.5	0.1	0.16	0.01
	5B	1.0	0.3	10	0.2	0.10	0.01
	5C	1.0	0.3	7.6	0.1	0.18	0.01
	5D	1.0	0.3	7.3	0.1	0.14	0.01
	5E	1.0	0.3	10	0.2	0.36	0.03
Spier - Crushed Rock	6	4.1	1	19	0.4	5.4	0.4
Simonsig Kriekbult – A	7-1m	1.0	0.3	14	0.3	0.59	0.05
	7-2m	1.0	0.3	22	0.4	0.54	0.04
Simonsig Kriekbult – Surface	8A	1.0	0.3	10	0.2	0.50	0.04
	8B	1.0	0.3	5.9	0.1	0.43	0.04
	8C	1.0	0.3	11	0.2	0.38	0.03
	8D	1.0	0.3	10	0.2	0.53	0.04
	8E	1.0	0.3	10	0.2	0.57	0.05
Simonsig – Surface	9A	1.0	0.3	15	0.3	1.5	0.1
	9B	5.0	1	16	0.3	1.6	0.1
	9C	3.8	1	10	0.2	0.81	0.06
	9D	1.0	0.3	5.3	0.1	0.53	0.04
	9E	1.0	0.3	8.5	0.2	1.1	0.1
Simonsig – E 1m	9-1m (1)	1.0	0.3	14	0.3	1.3	0.1
	9-1m (2)	4.2	1	13	0.3	1.3	0.1
Simonsig Dam - Crushed Rock	10 (1)	1.0	0.3	20	0.4	3.4	0.3
	10 (2)	4.1	1	18	0.3	3.4	0.3
Simonsig - Crushed Rock	11 (1)	1.0	0.3	17	0.3	4.5	0.4
	11 (2)	4.3	1	19	0.4	4.5	0.4

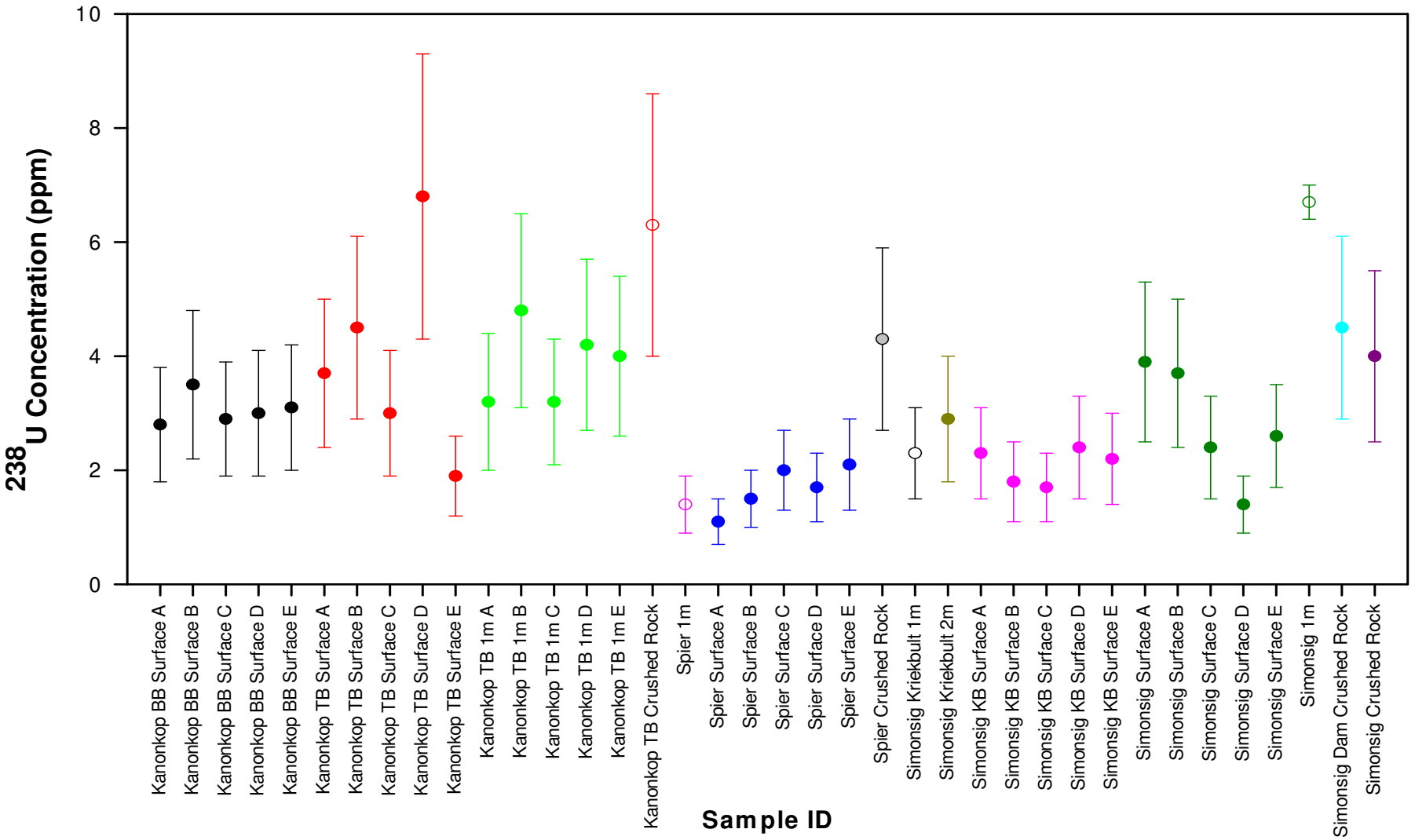

Figure 64. ***The ^{238}U concentration for samples collected from different locations at the three different vineyards.. The error bars depict the total error (i.e. statistical and systematic).***

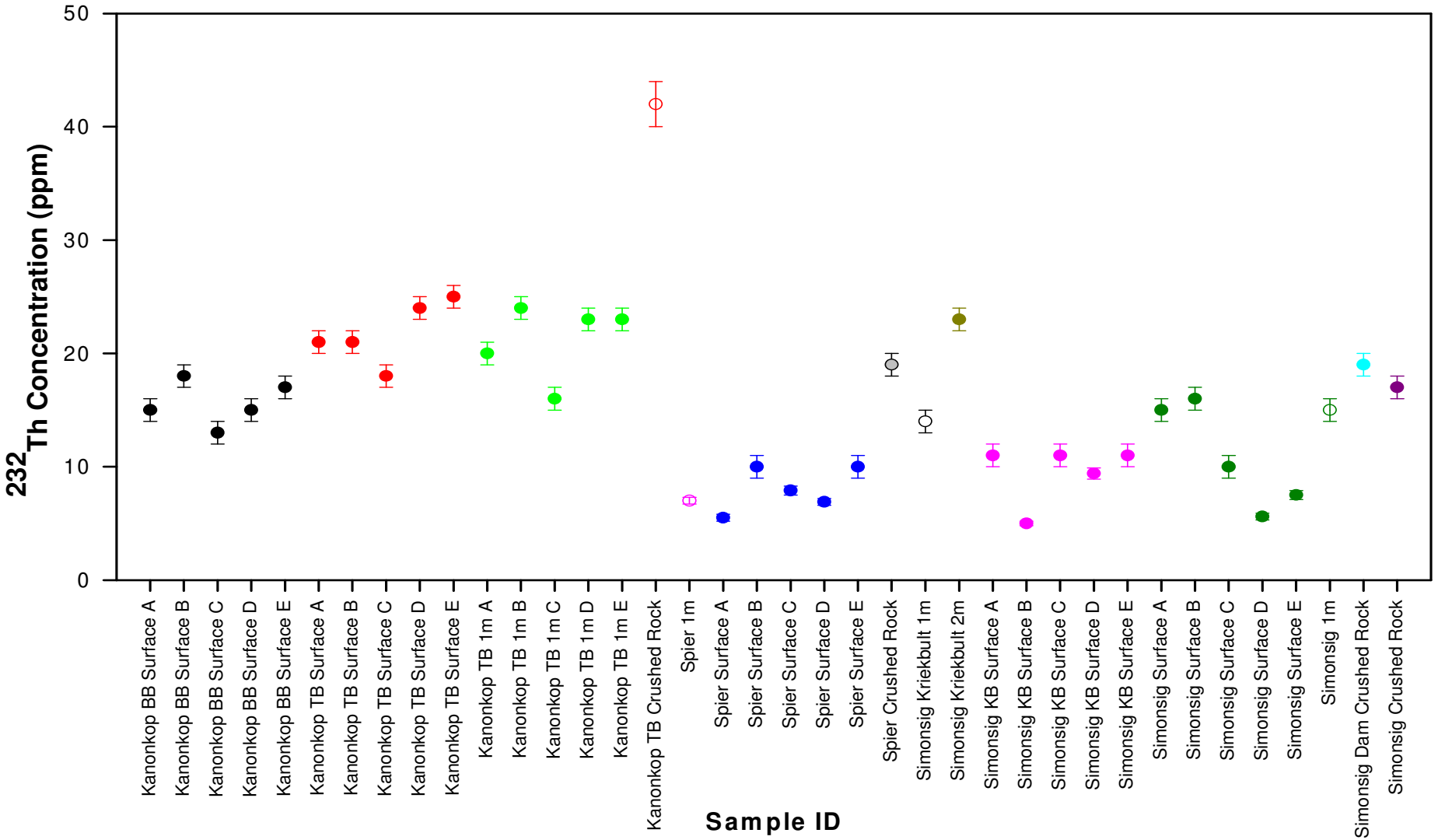

Figure 65. ***The ^{232}Th concentration for samples collected from different locations at the three different vineyards. The error bars depict the total error (i.e. statistical and systematic).***

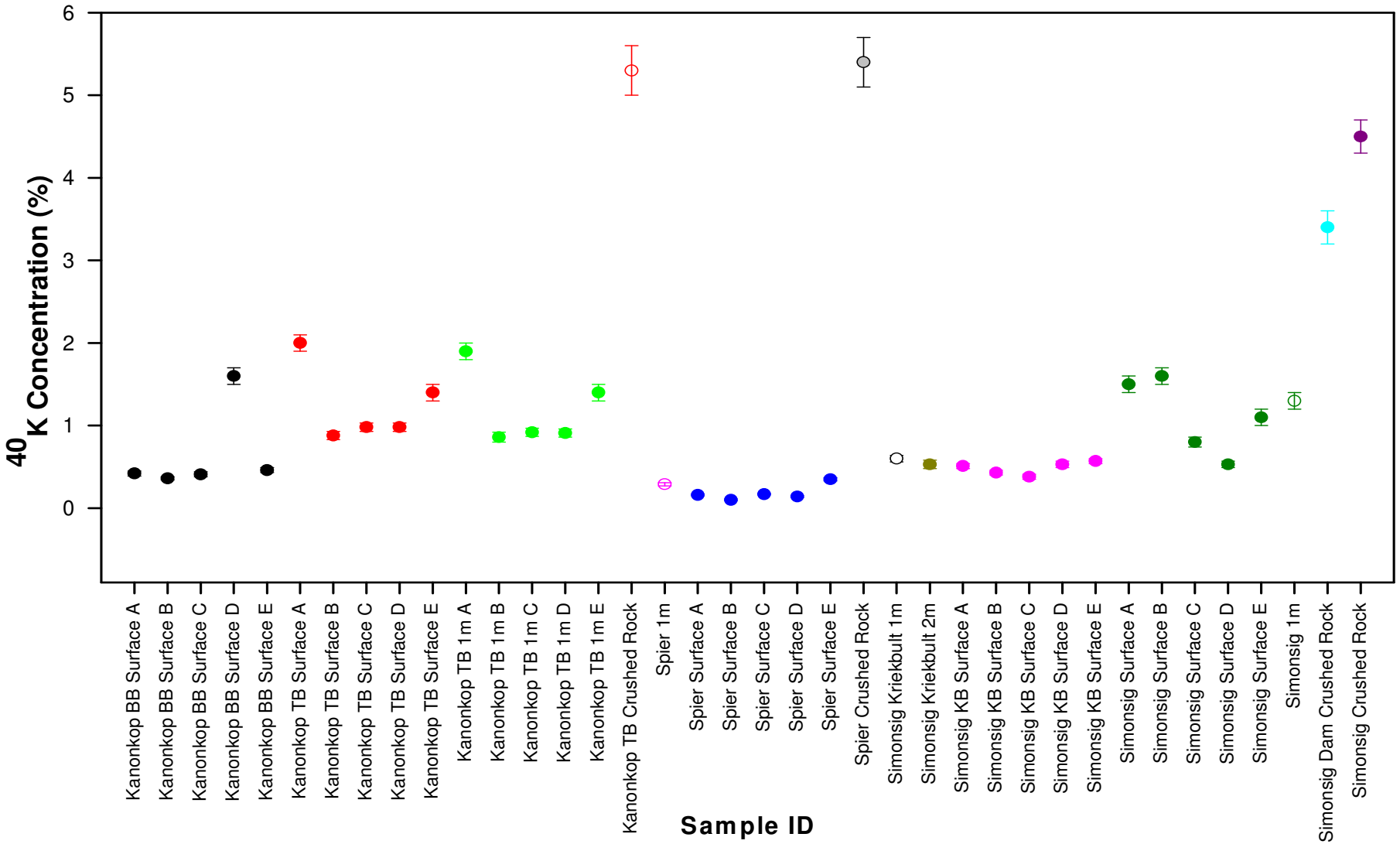

Figure 66. ***The ^{40}K concentration for samples collected from different locations at the three different vineyards. The error bars depict the total error (i.e. statistical and systematic).***

6.3.2 Discussion of Kanonkop Results

Uranium:

The Bottom Block surface concentrations are approximately equal over the sampling area with 1 standard deviation between the highest and lowest value, whereas the Top Block surface concentrations have a variation of 2 standard deviations. The uranium distribution in the soils is different and therefore not from the same origin or the leaching process is different for the different parts of the vineyard.

At the Top Block the 1m depth concentrations has a higher average (3.7 ± 0.6 ppm) than the surface concentrations (2.8 ± 0.5 ppm). The concentrations are however still within 1 standard deviation, meaning that the uranium content is fairly constant over the 1m depth. The concentration of the crushed rock is higher than the average surface concentration. This can indicate that the uranium is not from the bedrock or that substantial leaching took place within the soil. In relation to the other areas Kanonkop has the highest average concentration of uranium in the surface soils.

Thorium:

The surface concentrations at Bottom Block lay within 3 standard deviations around an average value of 16 ± 0.4 ppm. The surface concentrations at Top Block are higher than Bottom Block and have an average of 22 ± 0.4 ppm. This indicates a difference in mineralogy of the two soils.

The Top Block surface concentrations are within a maximum of 2 standard deviations of those of the 1 m depth, indicating a similar thorium distribution in the soils. The crushed rock is two times higher and indicates (together with the uranium) that the soils are perhaps not from the bedrock. In relation to the other areas Kanonkop has the highest average concentration of thorium in the surface soils.

Potassium:

Both the surface concentrations at Bottom Block and Top Block are well grouped together, laying at averages of 0.42 ± 0.01 % and 1.1 ± 0.03 %. In the Bottom Block there is one outlier concentration that is within 10 standard deviations from the average. Still the concentrations indicate a fairly homogeneous distribution of potassium in the soils. In the

Top Block there are two outlier concentrations that are within 8 standard deviations from the average. The Top Block surface concentrations are higher than the surface concentrations of the Bottom Block.

The surface concentrations of Top Block are nearly identical to the 1 m depth concentrations, indicating a similar potassium distribution in the soils. The crushed rock concentration is more than five times higher, indicating the leaching and absorption of potassium by the vegetation or a difference in origin. In relation to the other areas Kanonkop has the highest average concentration of potassium in the surface soils.

The soils of Kanonkop were classified in section 6.2. as Hutton to Glovelly, which indicates that the clay content is not constant over the area. This agrees with the observation that the Bottom Block was finer grained than the Top Block, meaning that the Bottom Block may have higher clay content than the Top Block. According to Koomans (2000) this can be deduced by comparing the ^{40}K concentrations in the different soils, with the higher concentration linked to the higher clay content. However, the ^{40}K concentrations of the Bottom Block were lower than those of the Top Block. This discrepancy could be attributed to various reasons for example the vines in the Bottom Block consumed more of the potassium in the soil, the soils have different leaching properties or that (more) fertiliser was added to the Top Block.

6.3.3 Discussion of Spier Results

Uranium:

At the surface a variation of 1 standard deviation is observed. The average surface concentration and the 1 m depth concentration are also within 1 standard deviation. The uranium distribution is therefore very similar in the 1 m depth. The crushed rock is higher in concentration than the surfaces. The soil could be not from the bedrock or uranium leaching from the soil could have taken place. In relation to the other areas Spier has the lowest average concentration of uranium in the surface soils.

Thorium:

The variation in the surface concentrations is at most 4 standard deviations from one another. The average surface concentration is within 1 standard deviation from the 1 m depth concentration. This could relate to a similar thorium distribution in the soil. The crushed rock is higher in concentration than the surfaces, pointing towards soils that did

not originate from the bedrock. In relation to the other areas Spier has the lowest average concentration of thorium in the surface soils.

Potassium:

The surface concentrations are grouped around an average value of 0.15 ± 0.01 %. Only one clear outlier is found amongst the concentrations. Still the concentrations indicate a fairly homogeneous distribution of potassium in the soils. The Fernwood soil of Spier is derived from Cape Granite and has lower clay content than the Malmesburgy soils (i.e. Simonsig and Kanonkop). The ^{40}K concentrations of the soils are lower than for the other soils and therefore agrees to Koomans's (2000) statement. The 1 m depth concentration is within 5 standard deviations higher than the surface concentrations. The crushed rock concentration is also higher and within 1 standard deviation of the crushed rock of Kanonkop. It can indicate that leaching is much more pronounced with granite derived soils.

6.3.4 Discussion of Simonsig Results

Uranium:

The surface concentrations at Kriekbult are grouped around an average of 2.00 ± 0.3 ppm with values that differ within 1 standard deviation. The surface concentrations of Simonsig show more variation - higher and lower values compared to Kriekbult (similar to Kanonkop). Although Simonsig's average of 2.1 ± 0.4 ppm is within 1 standard deviation to that of Kriekbult it seems that the uranium distribution in the two soils is not much alike, perhaps due to a difference in mineralogy or reworking of the soil. The 1 m depth and 2 m depth concentrations are within 1 standard deviation of the surface concentrations. This indicates a fairly constant uranium distribution throughout the soil to a level of 2 m. At Simonsig the average surface concentrations are lower than the 1 m depth concentration but individual surfaces do have a 1 standard deviation agreement. The Simonsig Dam crushed rock and Simonsig crushed rock are both within 1 standard deviation of all the samples except Surface D, which is within 2 standard deviations. The uranium may therefore originate in the bedrock found at Simonsig.

Thorium:

At Simonsig and Kriekbult the thorium concentration increases with depth. The surface concentrations are very different whereas the surface concentrations at Kriekbult are grouped together. Those at Simonsig show more variation (similar to Kanonkop). It seems

that the thorium distribution in the two soils is not much alike, perhaps due to a difference in mineralogy. The concentration of thorium in the crushed rock is similar to each other but also to that of Spier.

The 1 m depth concentrations of Kriekbult and Simonsig are within 1 standard deviation. In the case of Kriekbult the 1 m depth concentration is higher than the surface concentrations whereas at Simonsig the 1 m depth concentration is within 1-2 standard deviations from two of the surface concentrations. The maturity of the soils is therefore different.

The Simonsig Dam crushed rock and Simonsig crushed rock concentrations are within two standard deviations of each other. They are also comparable to the 1m depth and some of the surface concentrations. This could indicate the same origin. Some of the surface concentrations of both areas are lower in concentration than the bedrock. This shows a different origin emphasising that Simonsig has two mineralogical different soil types. This is also indicated by the Kriekbult 2 m depth concentration that is higher than both the Kriekbult 1 m depth concentration and the crushed rock concentrations.

Potassium:
The surface concentrations at Kriekbult are grouped around the average value of 0.48 ± 0.01 % with between 1 and 3 standard deviation difference between values. The 1m depth and 2 m depth concentrations are within 1 standard deviation but also higher than the surface concentrations, an indicator of possible leaching or absorption from the top soil.

The surface concentrations at Simonsig have a larger variation between values ranging from 3 to 5 standard deviations between values. This variation indicates local differences in the amount of leaching or absorption of potassium in the soil. The Simonsig concentrations are in general higher than those of Kriekbult.

This difference in the potassium distribution indicates that the clay content of Simonsig and Kriekbult is not the same. However, the soils of Simonsig show a discrepancy similar to those of Kanonkop. The Glenrosa soil at Kriekbult is finer than the other Simonsig Glenrosa soil, but the Simonsig soil contains higher concentrations of ^{40}K than the Kriekbult soil. Reasons for this may be similar to those given for Kanonkop. Furthermore, the rock concentration is higher than the surface concentrations, indicating the leaching and absorption of potassium by the vegetation or a difference in origin.

6.3.5 Correlation between Radiometry and XRF

The radiometry and XRF concentrations for each of the locations were compared in order to confirm that radiometry can be used as an alternative to XRF. Individual comparisons are depicted in Figure 67 to Figure 79. Many of the XRF uranium concentrations are below the detection limit. From the remainder most are within 1 standard deviation, with only a few concentrations that are within 2 or 3 standard deviations from each other. Most of the thorium concentrations are within 1 standard deviation with only 8 concentrations that are within 2-3 standard deviations from each other. All the potassium concentrations determined by radiometry are within 1 standard deviation of the respective XRF determined concentrations.

To quantify the degree of relationship between radiometry and XRF all the concentrations (for a specific radioisotope) were used to determine a correlation. The ideal correlation is a straight line from zero to the maximum concentration. It means that a concentration determined with radiometry yields an identical result with XRF. Concentration errors are taken into account in this determination.

Figure 80 depicts the comparison of the uranium concentrations together with the ideal correlation line. From the 42 concentrations, more than 50 % (27) were below the XRF detection limit (seen as a row of measurements along the XRF value of 1.0 ppm). With these included only 26 % (11) were positioned on the ideal correlation line. The correlation coefficient is 0.314 and the correlation for uranium can therefore be described as poor. This is mainly due to the many samples that are very low in uranium concentration. With a refinement to the detection limits of XRF, perhaps by means of using a low concentration standard a more acceptable correlation between the two methods is expected. The comparison of the thorium concentrations together with the ideal correlation line are depicted in Figure 81. Of the 42 concentrations 37 were positioned on the ideal correlation line. The correlation coefficient is 0.985 and the correlation for thorium can therefore be described as excellent. Figure 82 depicts the comparison of the potassium concentrations together with the ideal correlation line. All 42 concentrations are positioned on the correlation line. The correlation coefficient is 0.999 and the correlation for potassium can therefore be described as excellent.

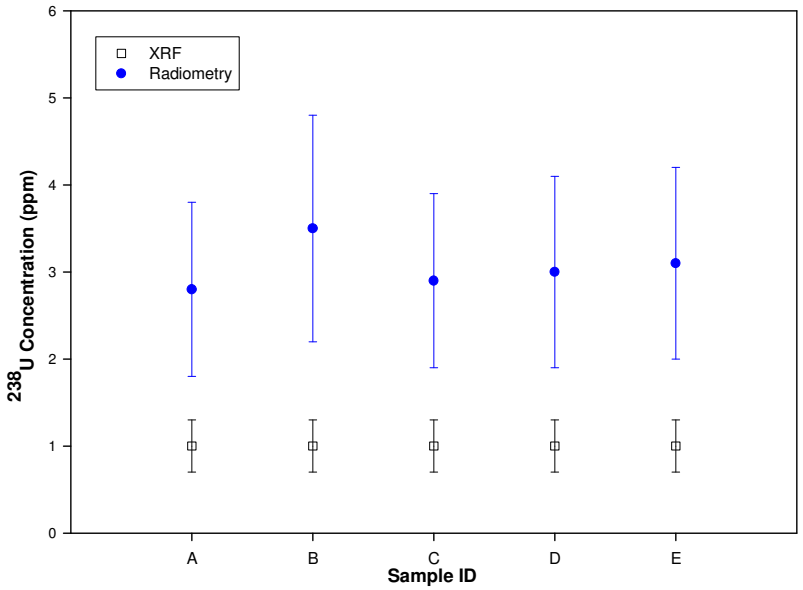

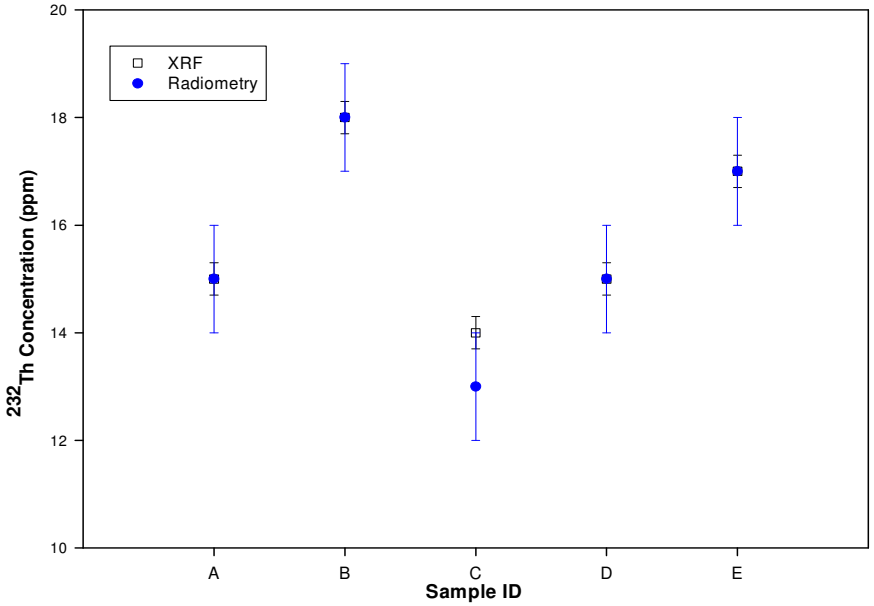

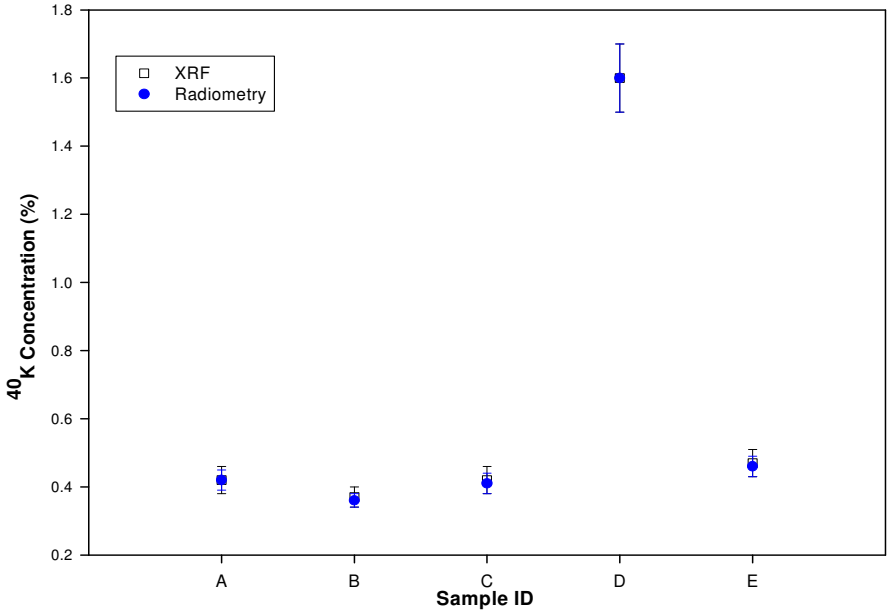

Figure 67. ***Radiometric and XRF sample concentrations for samples labelled Kanonkop Bottom Block Surface A, B, C, D and E.***

Samples were taken from the surface of the Kanonkop Bottom Block area. Top left is the ^{238}U concentration (ppm), top right the ^{232}Th concentration (ppm) and bottom left is the ^{40}K concentration (%). An XRF measurement of 1 ppm depicts a concentration value that was below the detection limit. The error bars indicate the total error (i.e. statistical and systematic).

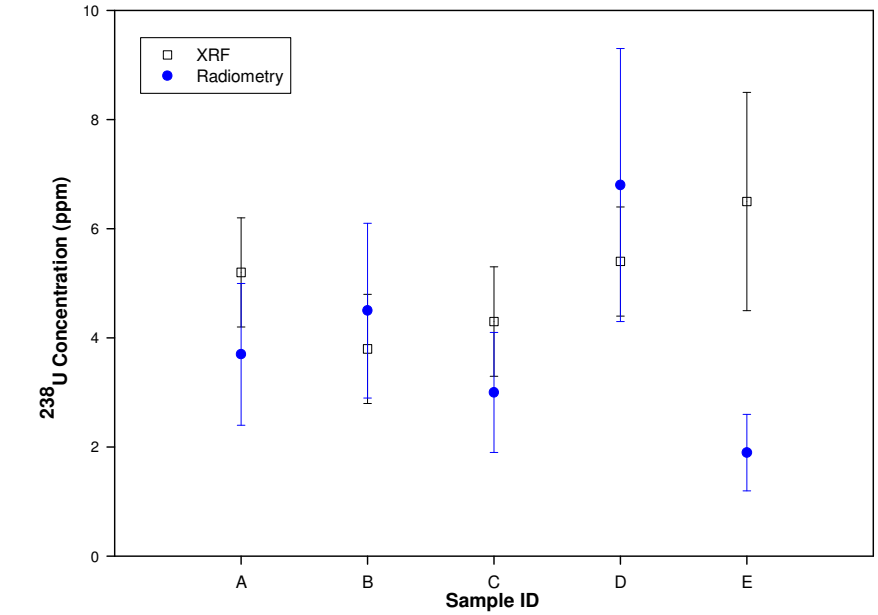

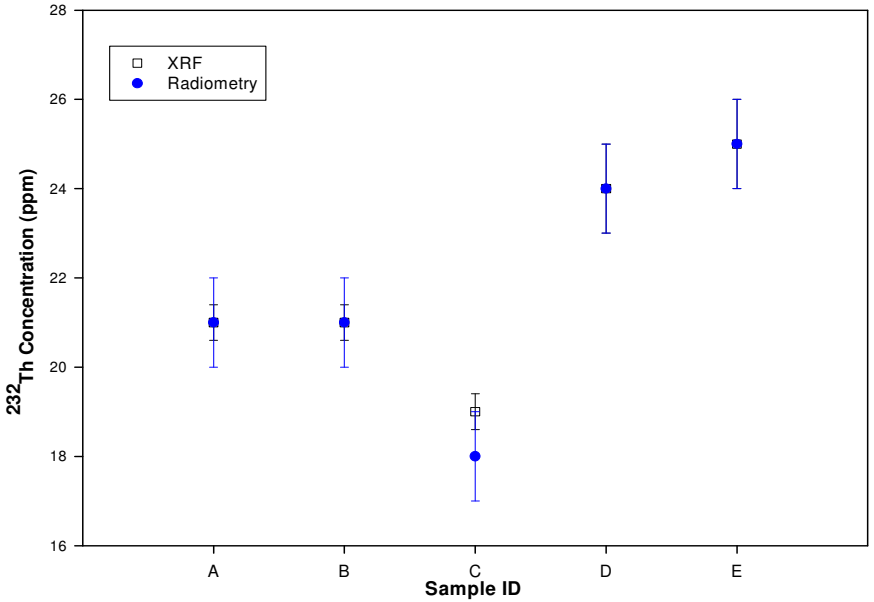

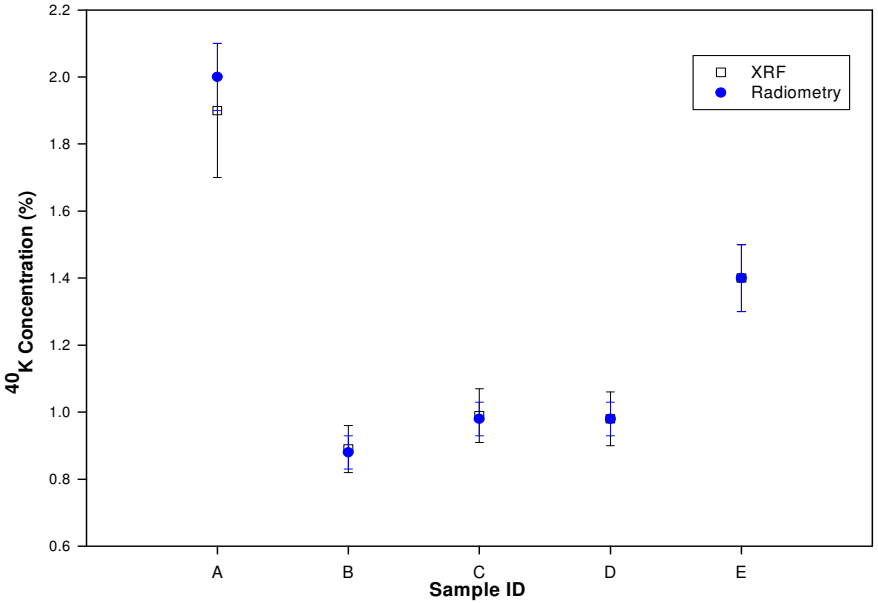

Figure 68. ***Radiometric and XRF sample concentrations for samples labelled Kanonkop Top Block Surface A, B, C, D and E.***

Samples were taken from the surface of the Kanonkop Top Block area. Top left is the ^{238}U concentration (ppm), top right the ^{232}Th concentration (ppm) and bottom left is the ^{40}K concentration (%). The error bars indicate the total error (i.e. statistical and systematic).

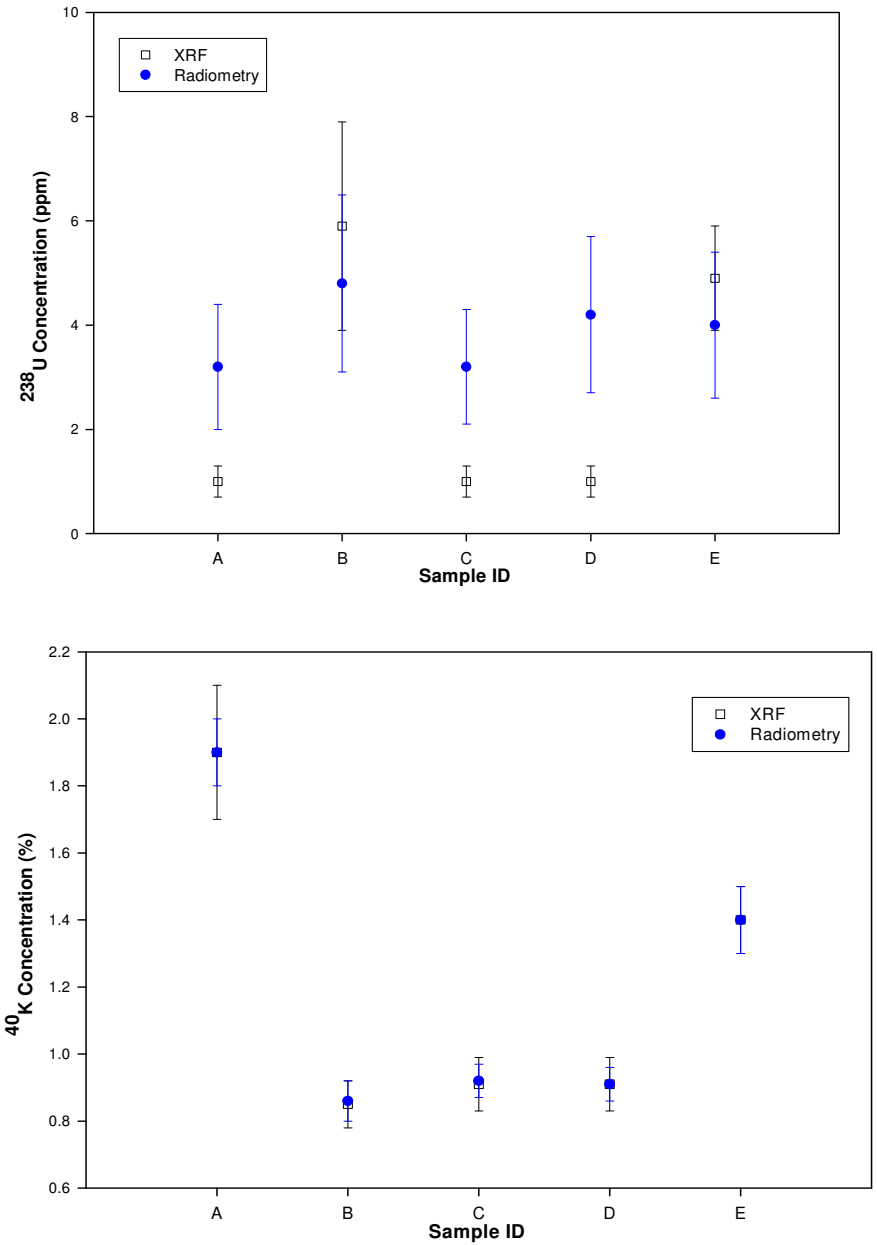

Figure 69. ***Radiometric and XRF sample concentrations for samples labelled Kanonkop Top Block 1m.***

Samples were taken at a depth of 1 metre below the surface of the Kanonkop Top Block area. Top left is the ^{238}U concentration (ppm), top right the ^{232}Th concentration (ppm) and bottom left is the ^{40}K concentration (%). An XRF measurement of 1 ppm depicts a concentration value that was below the detection limit. The error bars indicate the total error (i.e. statistical and systematic).

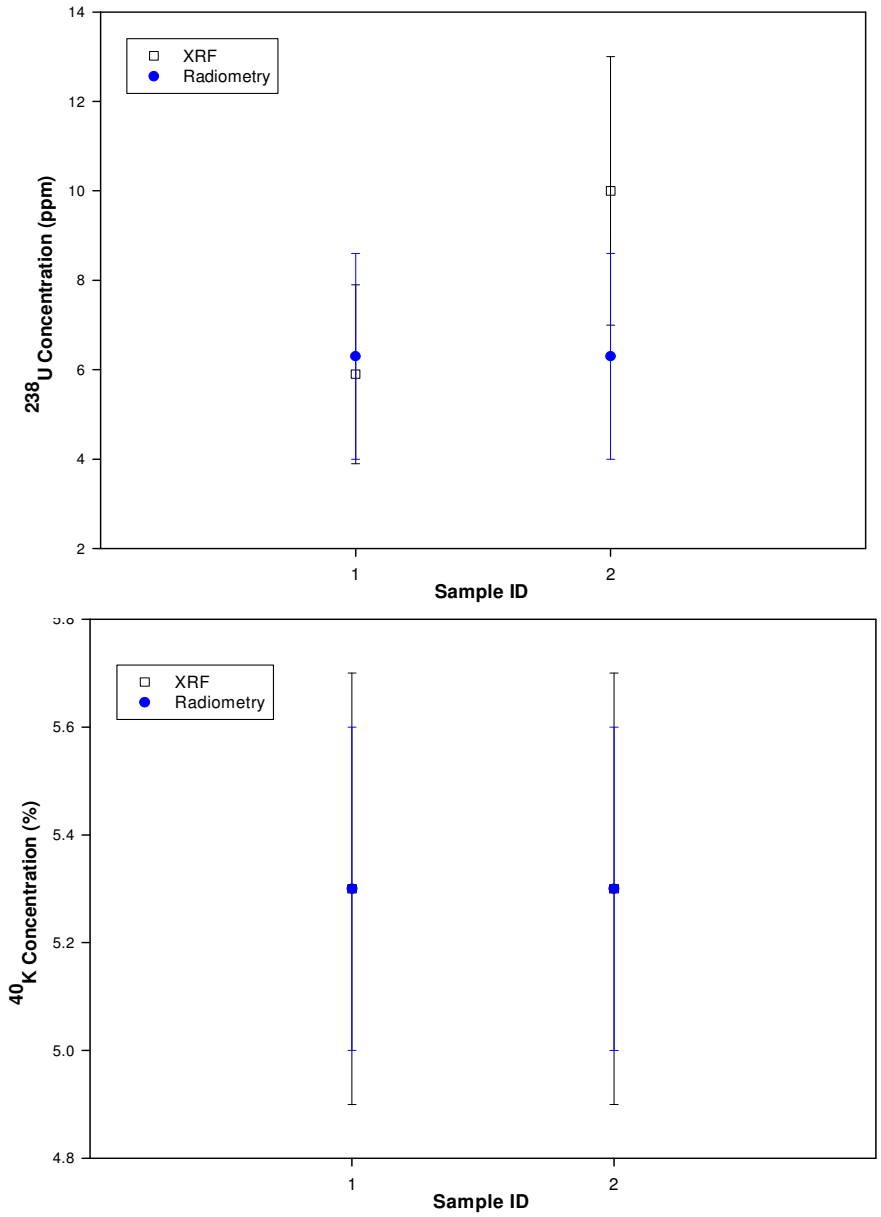

Figure 70. ***Radiometric and XRF sample concentrations for samples labelled Kanonkop Top Block Crushed Rock 1 and 2.***

Samples were taken from the outlying rock on the Kanonkop Top Block area and crushed. Top left is the ^{238}U concentration (ppm), top right the ^{232}Th concentration (ppm) and bottom left is the ^{40}K concentration (%).. The error bars indicate the total error (i.e. statistical and systematic).

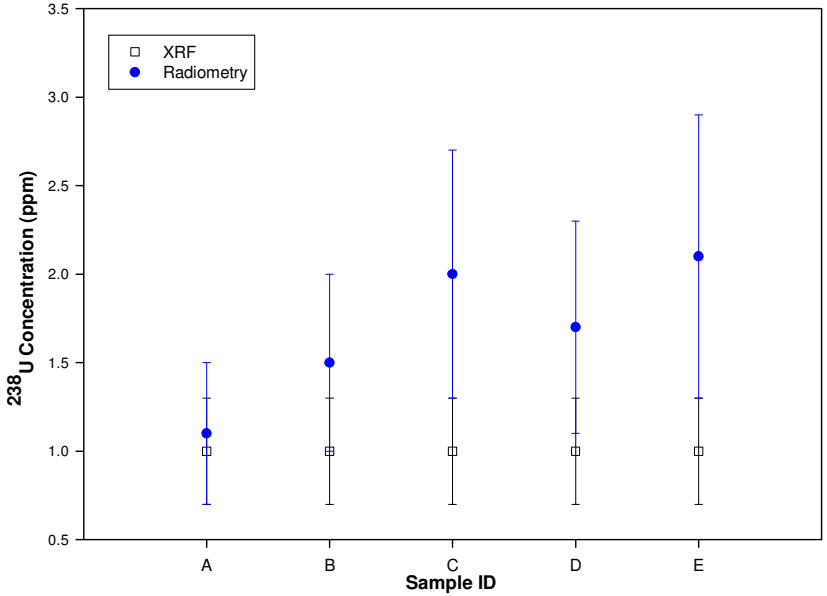

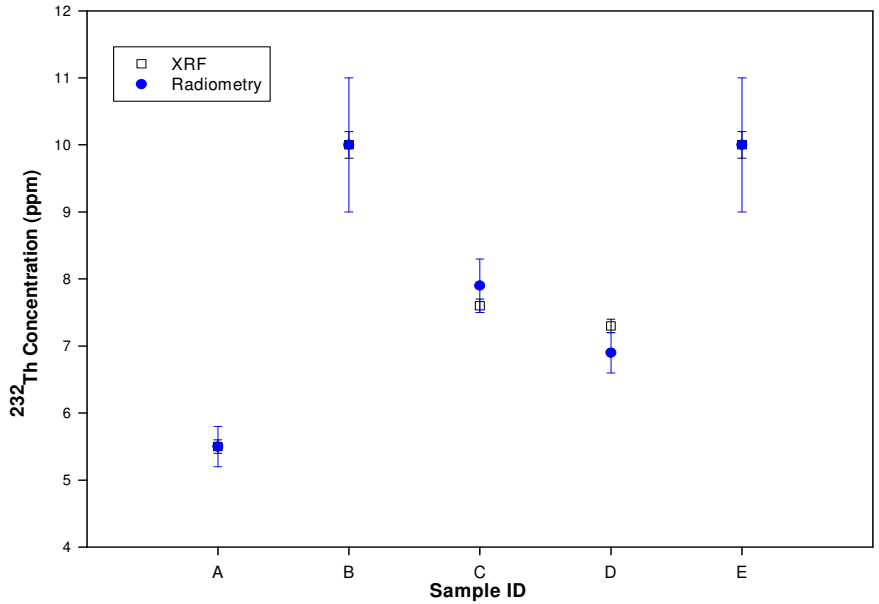

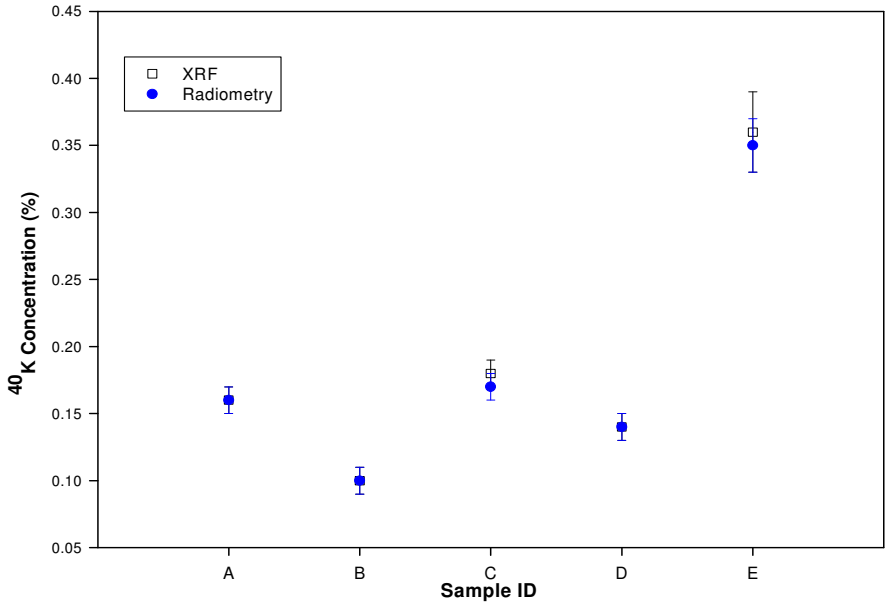

Figure 71. ***Radiometric and XRF sample concentrations for samples labelled Spier Surface A, B, C, D and E.***

Samples were taken from the surface of the Spier area. Top left is the ^{238}U concentration (ppm), top right the ^{232}Th concentration (ppm) and bottom left is the ^{40}K concentration (%). An XRF measurement of 1 ppm depicts a concentration value that was below the detection limit. The error bars indicate the total error (i.e. statistical and systematic).

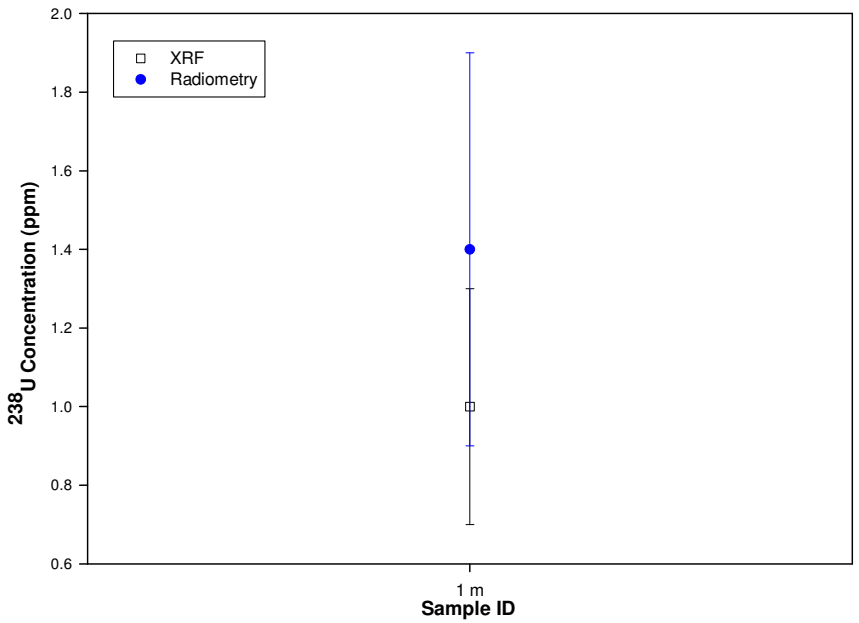

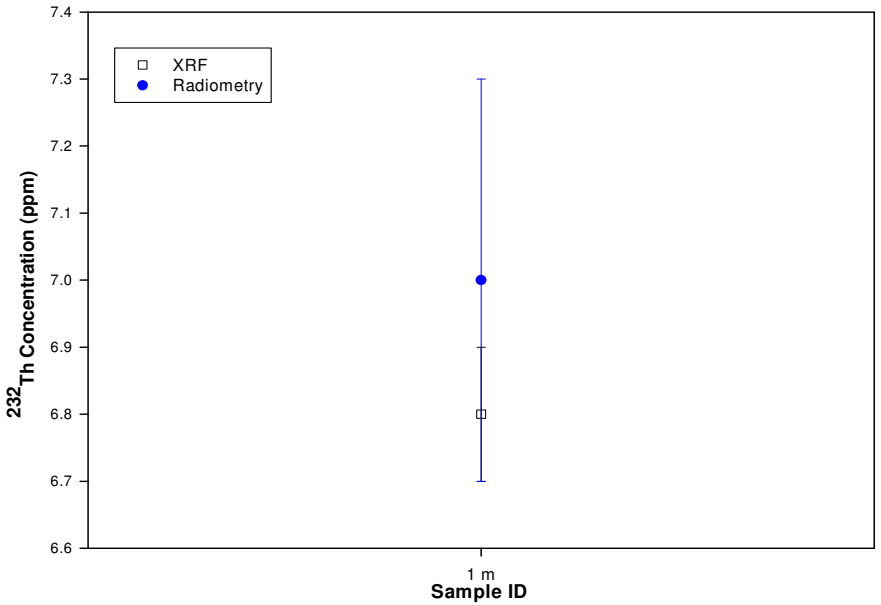

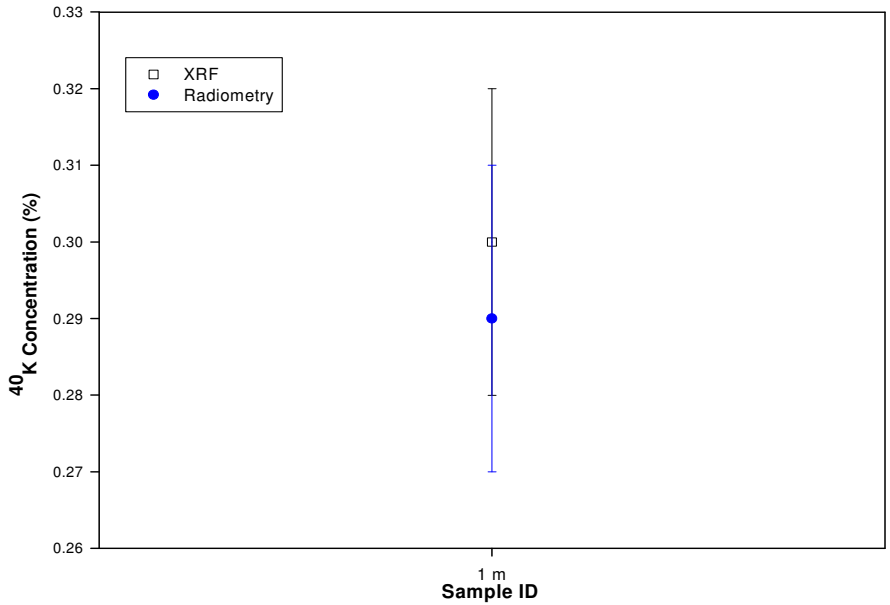

Figure 72. ***Radiometric and XRF sample concentrations for samples labelled Spier 1m.***

Samples were taken at a depth of 1 metre below the surface of Spier area. Top left is the ^{238}U concentration (ppm), top right the ^{232}Th concentration (ppm) and bottom left is the ^{40}K concentration (%). The error bars indicate the total error (i.e. statistical and systematic).

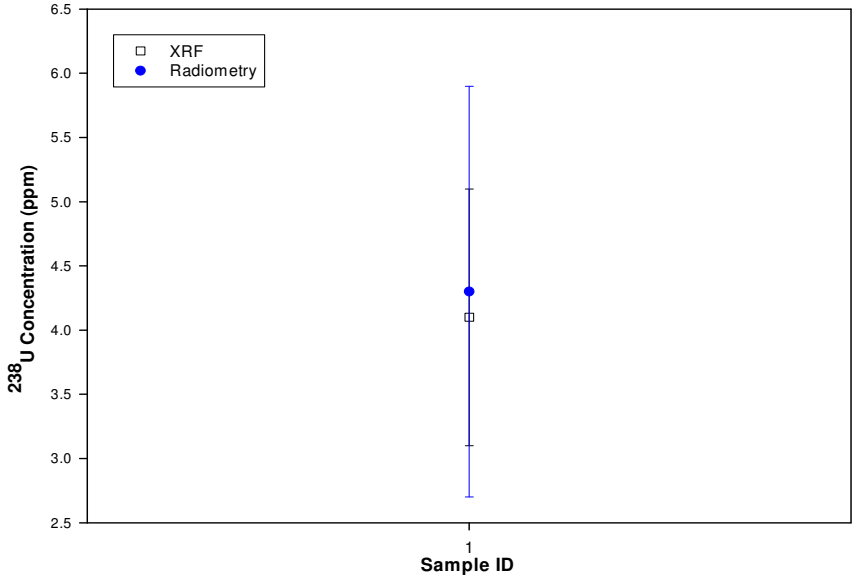

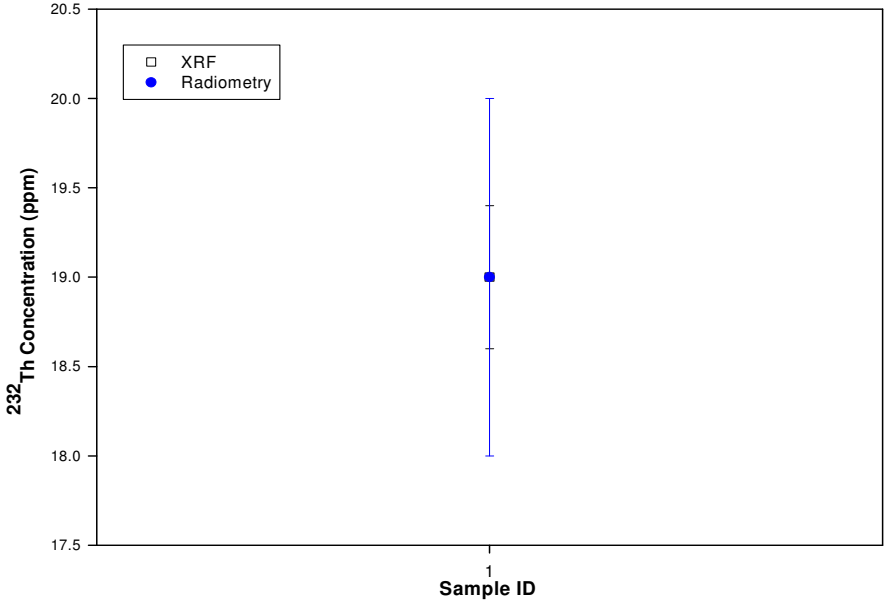

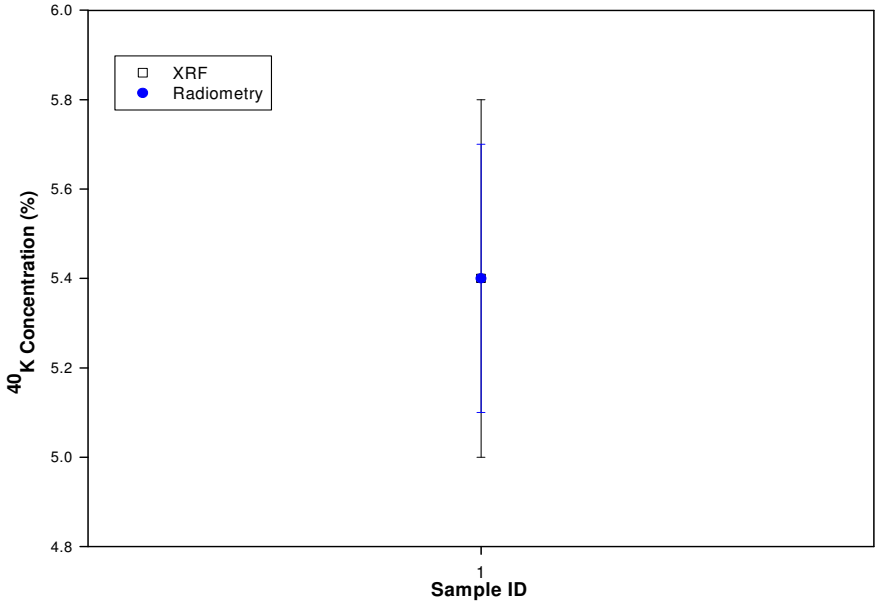

Figure 73. ***Radiometric and XRF sample concentrations for the one sample labelled Spier Crushed Rock.***

Samples were taken from the outlying rock on the Spier area and crushed. Top left is the ^{238}U concentration (ppm), top right the ^{232}Th concentration (ppm) and bottom left is the ^{40}K concentration (%). The error bars indicate the total error (i.e. statistical and systematic).

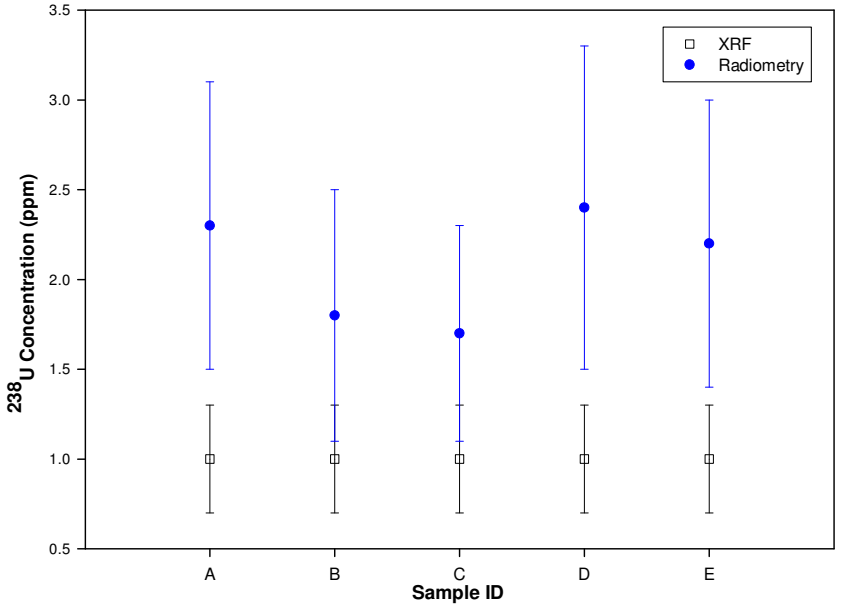

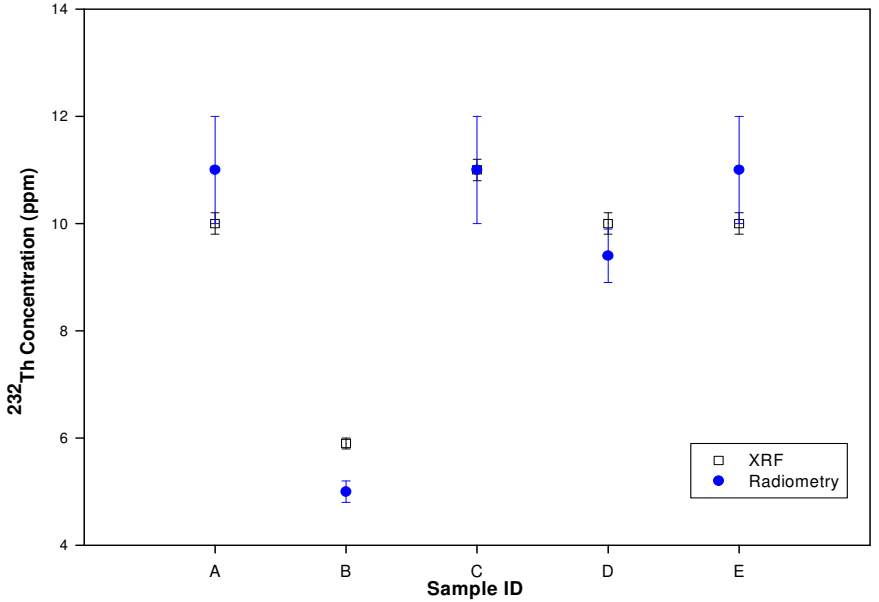

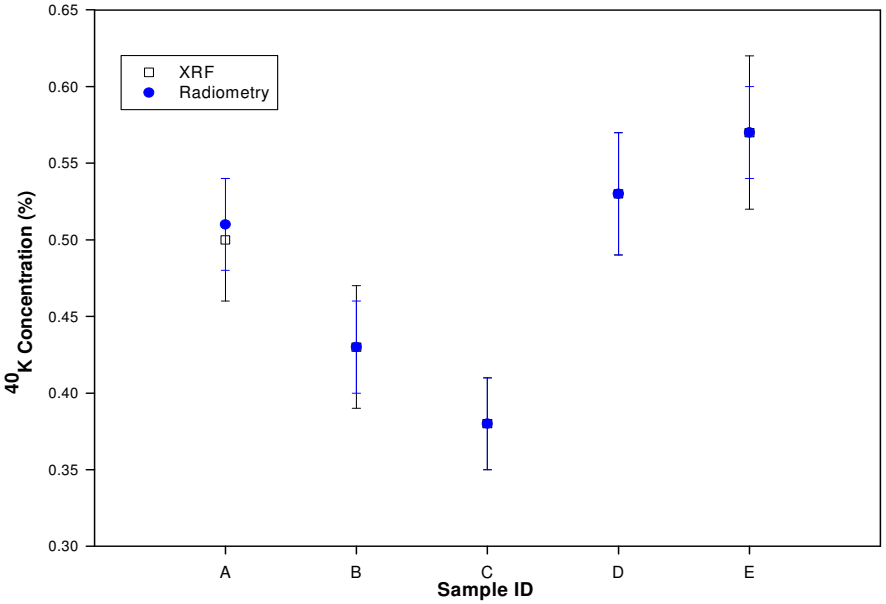

Figure 74. ***Radiometric and XRF sample concentrations for samples labelled Simonsig Kriekbult Surface A, B, C, D and E.***

Samples were taken from the surface of the Simonsig Kriekbult. Top left is the ^{238}U concentration (ppm), top right the ^{232}Th concentration (ppm) and bottom left is the ^{40}K concentration (%). An XRF measurement of 1 ppm depicts a concentration value that was below the detection limit. The error bars indicate the total error (i.e. statistical and systematic).

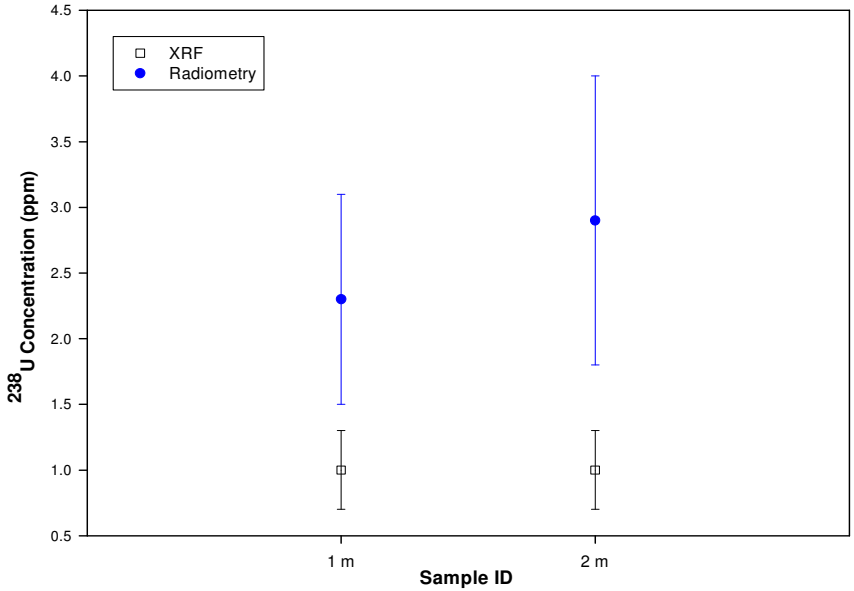

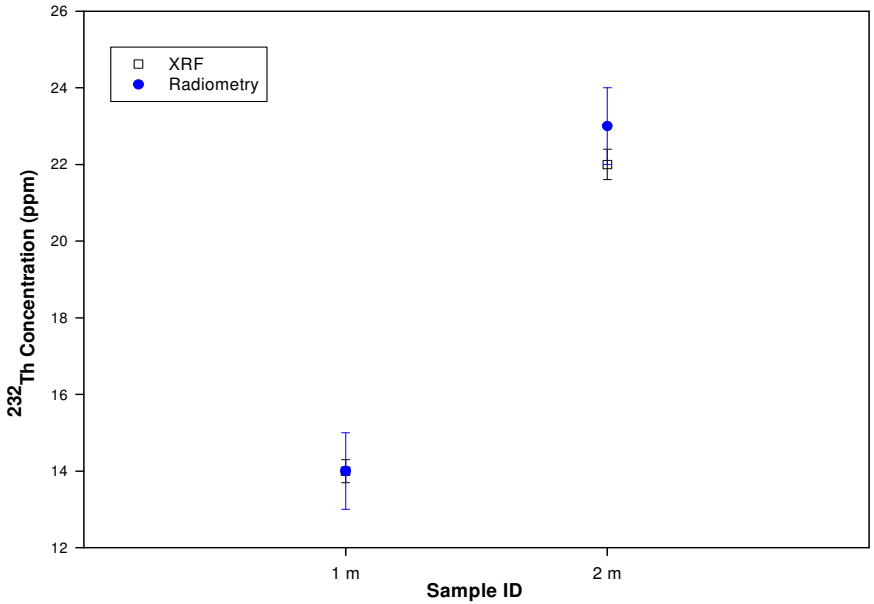

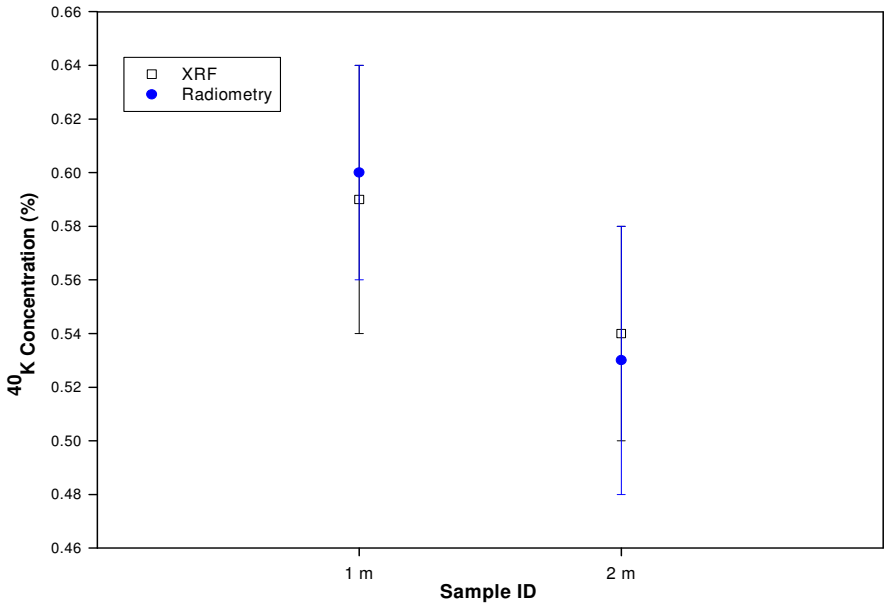

Figure 75. ***Radiometric and XRF sample concentrations for samples labelled Simonsig Kriekbult 1 m and 2 m.***

Samples were taken at a depth of 1 metre and 2 metre below the surface of the Simonsig Kriekbult area. Top left is the ^{238}U concentration (ppm), top right the ^{232}Th concentration (ppm) and bottom left is the ^{40}K concentration (%). An XRF measurement of 1 ppm depicts a concentration value that was below the detection limit. The error bars indicate the total error (i.e. statistical and systematic).

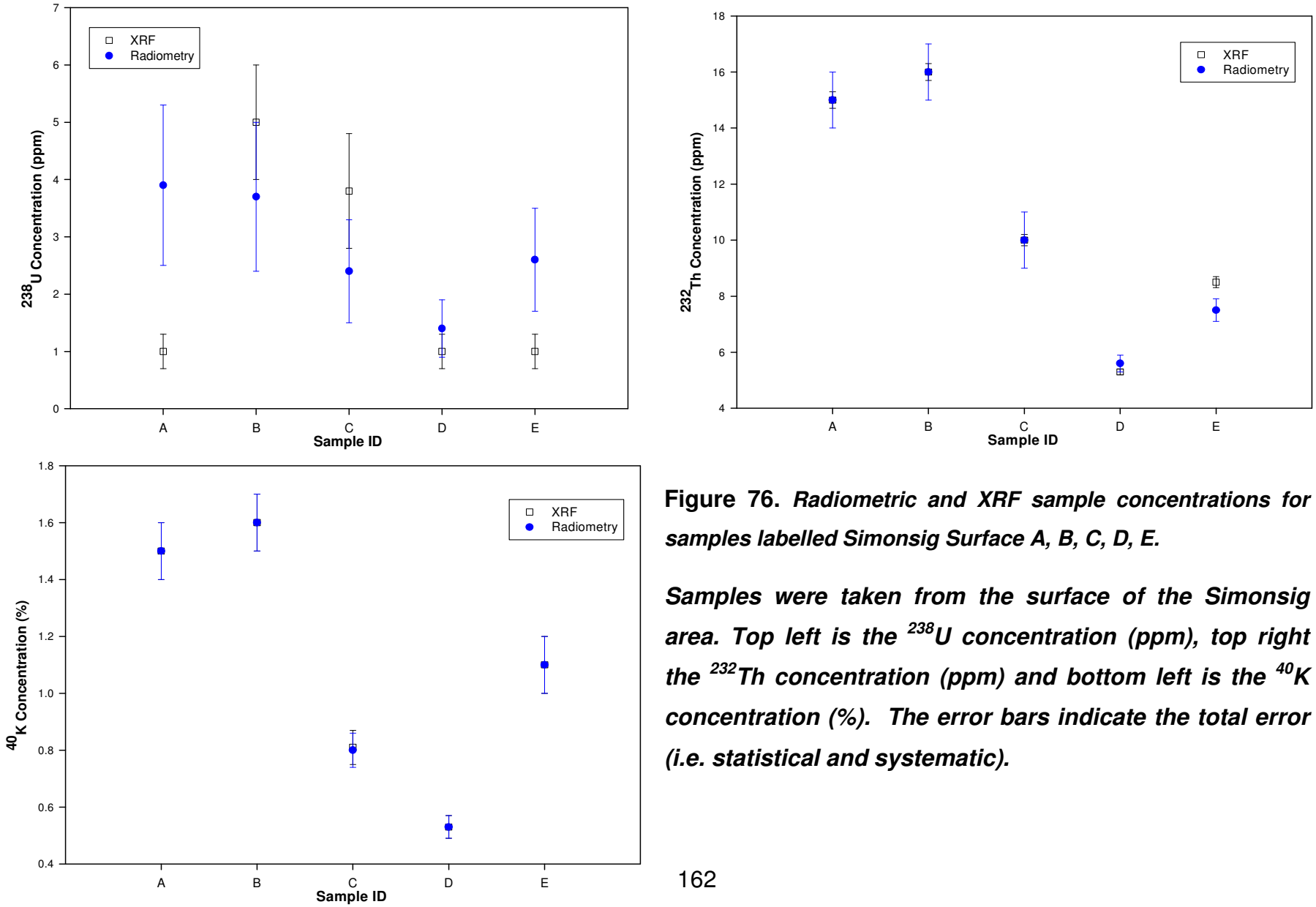

Figure 76. ***Radiometric and XRF sample concentrations for samples labelled Simonsig Surface A, B, C, D, E.***

Samples were taken from the surface of the Simonsig area. Top left is the ^{238}U concentration (ppm), top right the ^{232}Th concentration (ppm) and bottom left is the ^{40}K concentration (%). The error bars indicate the total error (i.e. statistical and systematic).

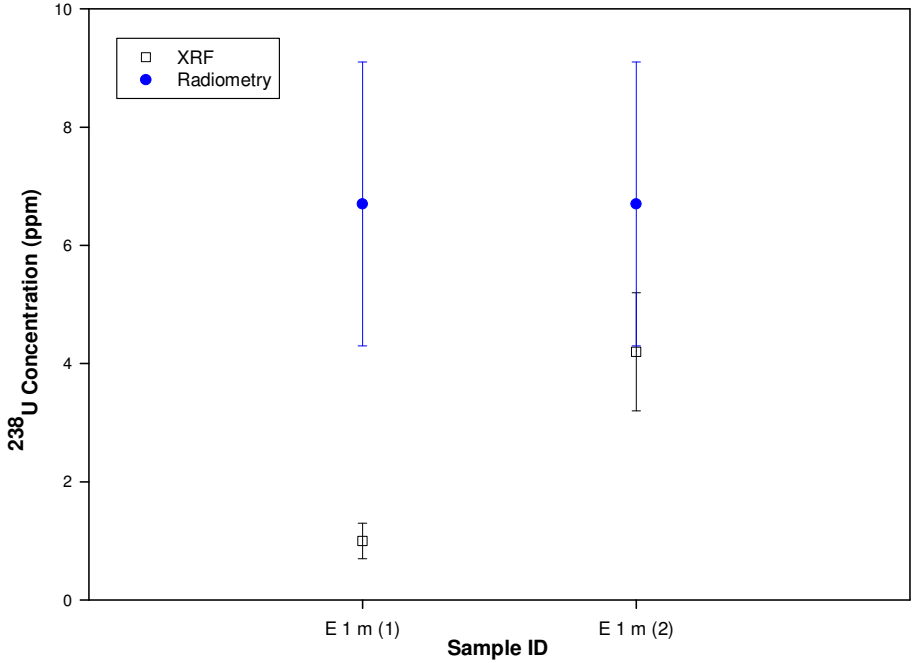

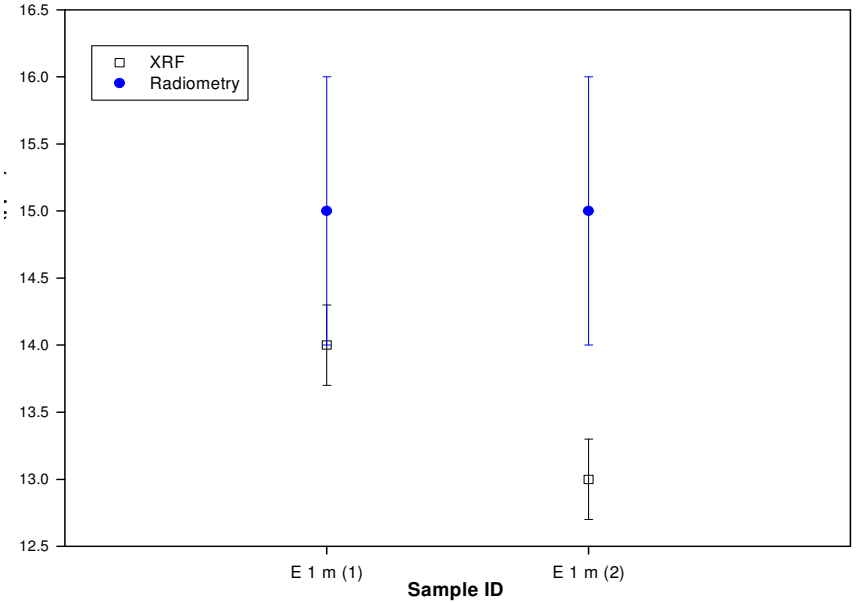

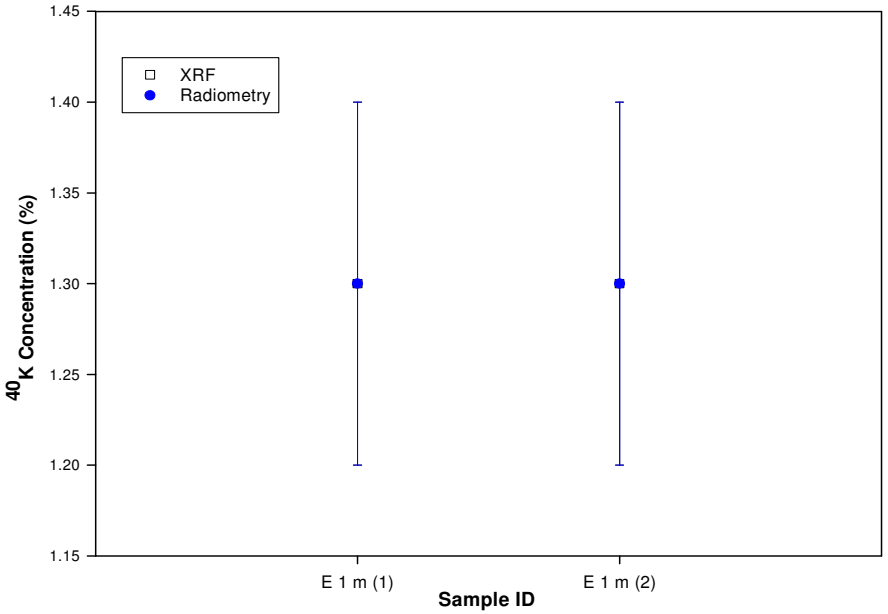

Figure 77. ***Radiometric and XRF sample concentrations for samples labelled Simonsig E 1m(1) and E 1m(2).***

Samples were taken at a depth of 1m of the Simonsig area. Top left is the ^{238}U concentration (ppm), top right the ^{232}Th concentration (ppm) and bottom left is the ^{40}K concentration (%). An XRF measurement of 1 ppm depicts a concentration value that was below the detection limit. The error bars indicate the total error (i.e. statistical and systematic).

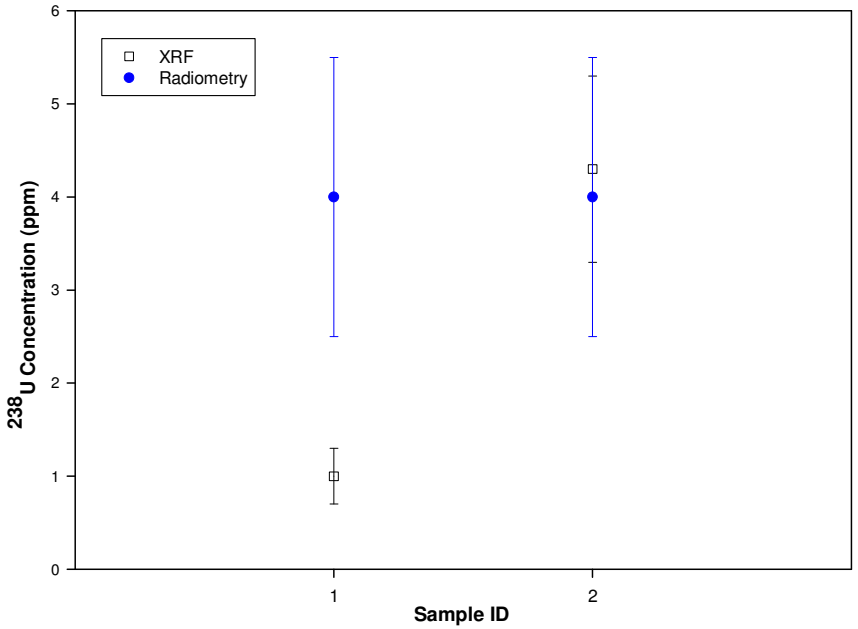

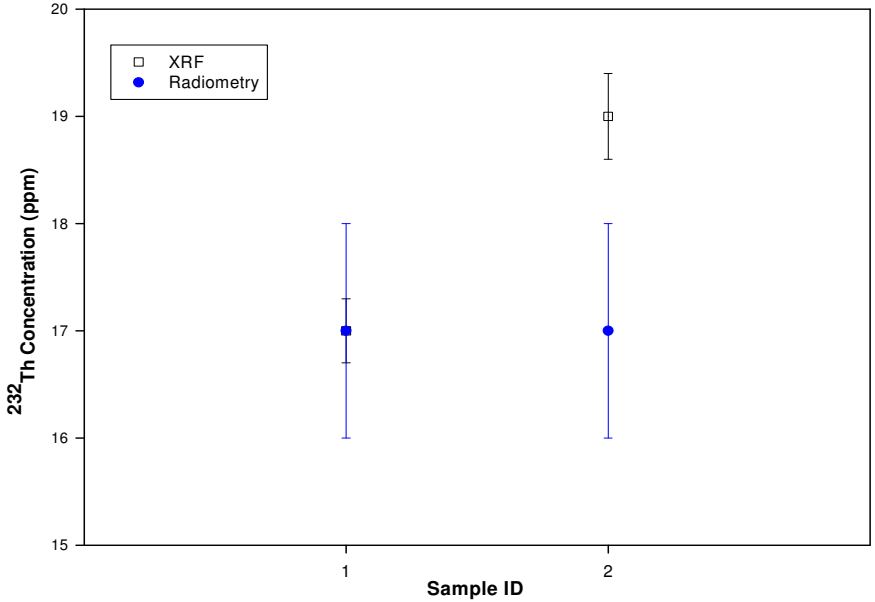

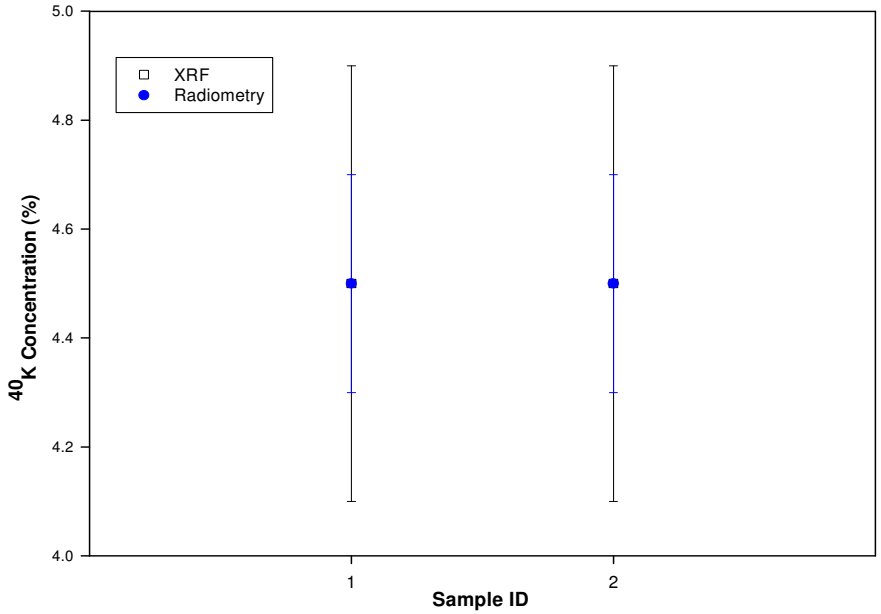

Figure 78. ***Radiometric and XRF sample concentrations for samples labelled Simonsig Crushed Rock 1 and 2.***

Samples were taken from the outlying rock near the Simonsig area and crushed. Top left is the ^{238}U concentration (ppm), top right the ^{232}Th concentration (ppm) and bottom left is the ^{40}K concentration (%). An XRF measurement of 1 ppm depicts a concentration value that was below the detection limit. The error bars indicate the total error (i.e. statistical and systematic).

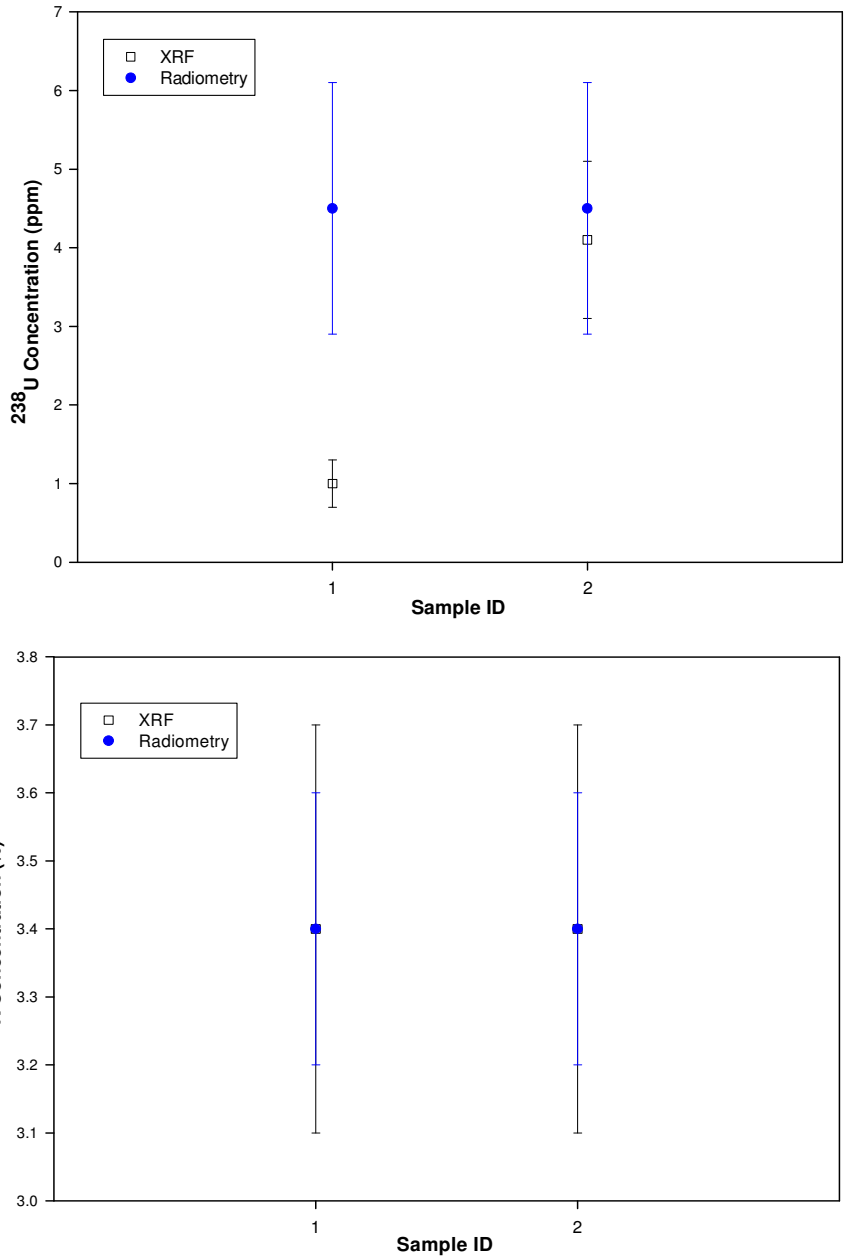

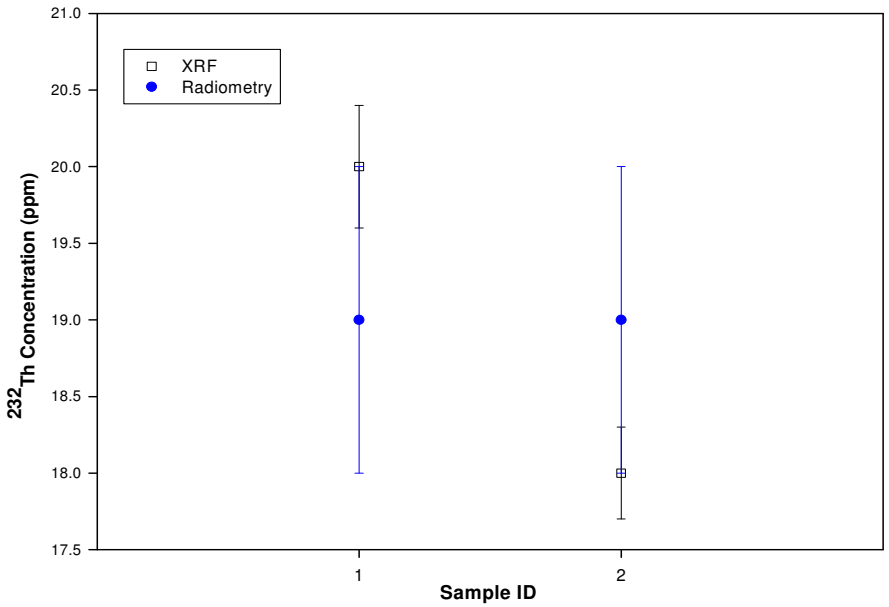

Figure 79. ***Radiometric and XRF sample concentrations for samples labelled Simonsig Dam Crushed Rock 1 and 2.***

Samples were taken from the outlying rock near the Simonsig Dam area and crushed. Top left is the ^{238}U concentration (ppm), top right the ^{232}Th concentration (ppm) and bottom left is the ^{40}K concentration (%). An XRF measurement of 1 ppm depicts a concentration value that was below the detection limit. The error bars indicate the total error (i.e. statistical and systematic).

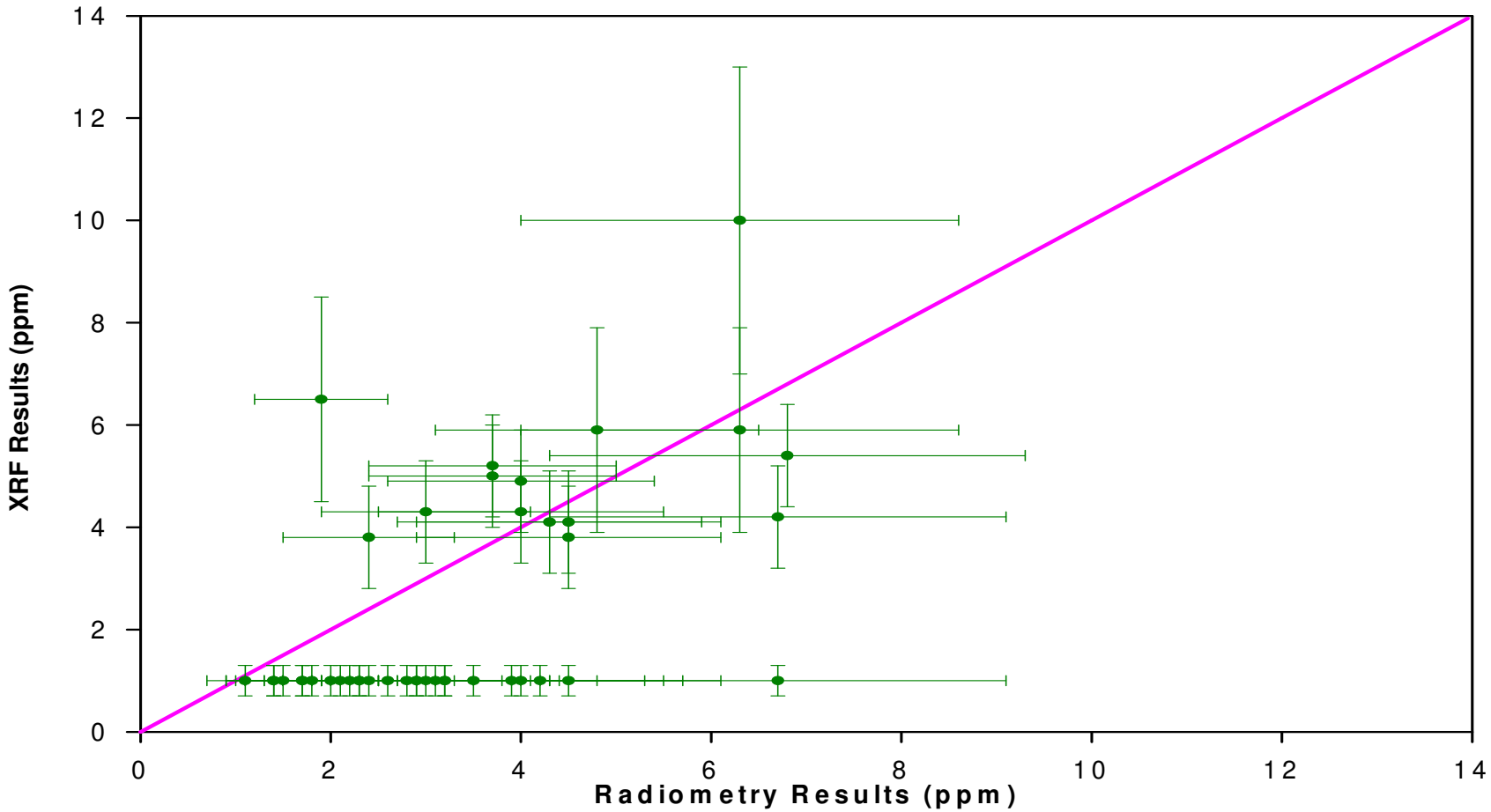

Figure 80. ***Comparison between the uranium sample concentrations of the vineyard soils as obtained by radiometry and XRF. The solid line indicates the ideal correlation where the concentrations of radiometry and XRF are identical. The horizontal line of sample concentrations depicts the samples that were below the XRF detection limit. The error bars indicate the total error (i.e. statistical and systematic).***

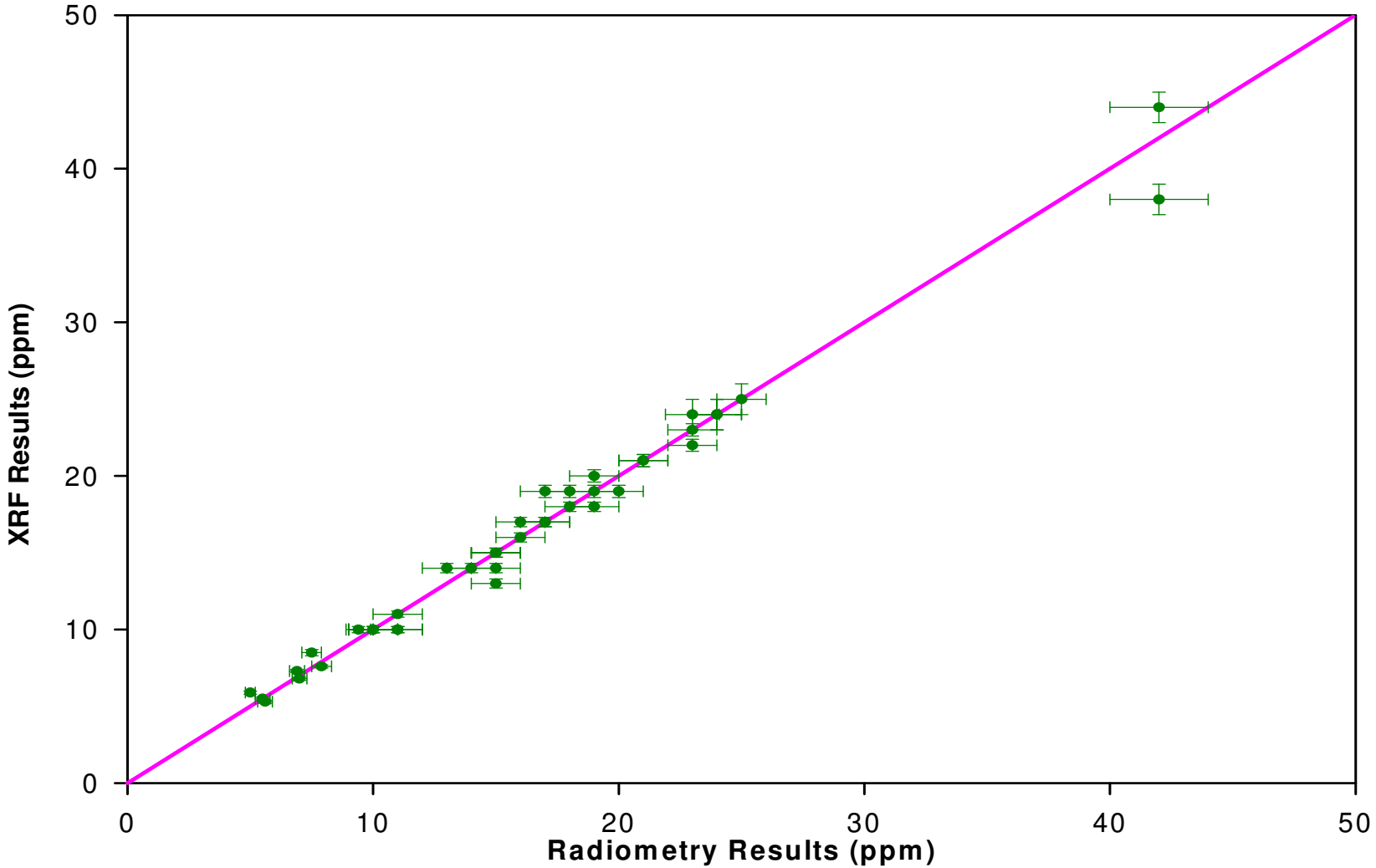

Figure 81. ***Comparison between the thorium sample concentrations of the vineyard soils as obtained by radiometry and XRF. The solid line indicates the ideal correlation where the concentrations of radiometry and XRF are identical. The error bars indicate the total error (i.e. statistical and systematic).***

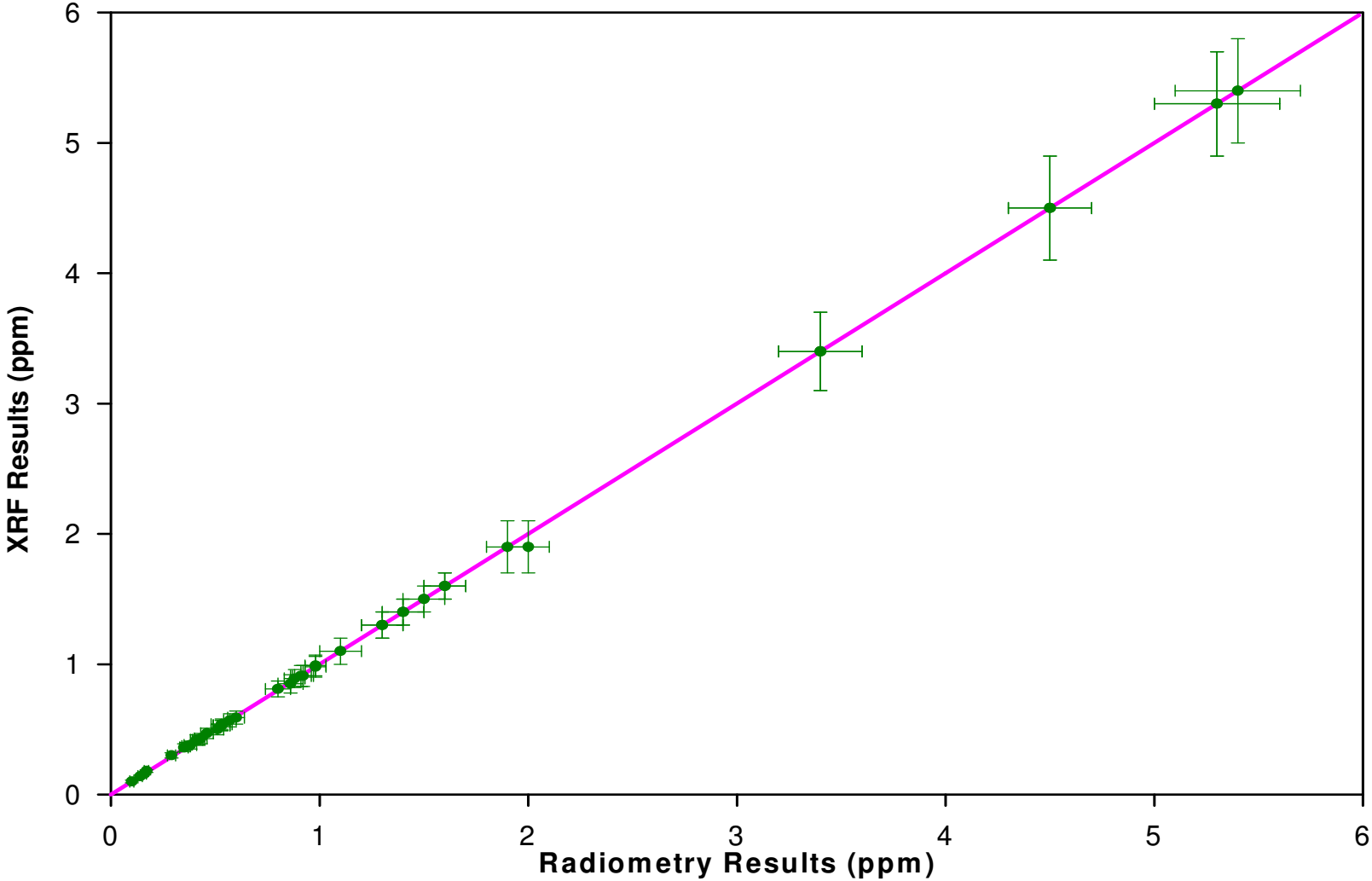

Figure 82. ***Comparison between the potassium sample concentrations of the vineyard soils as obtained by radiometry and XRF. The solid line indicates the ideal correlation where the concentrations of radiometry and XRF are identical. The error bars indicate the total error (i.e. statistical and systematic).***

6.3.6 In-situ Radiometry Studies

The investigation into terroir characteristics and the radiometric properties of soil, as discussed in this dissertation, was the pilot study for the application of radiometry in the agriculture. With the initial results in hand, it became apparent that radiometry could be a possible alternative technique for use in soil classification. To investigate whether the success of the laboratory-based method can be extended to in-situ measurements, a follow-up study, using the mobile MEDUSA detector (De Meijer, 1996) was conducted at Simonsig (Newman et al. 2003; Rozendaal et al., 2004).

The MEDUSA gamma ray detector system consists of a highly sensitive CsI(Na) gamma-ray detector, a GPS device, an ALADIN control unit and a laptop. The detector collects data from an area of about 5 m^2 around the detector. The detector view of depth at the centre of this area is 30-50 cm, but decreases towards the edge of the area. The system was mounted off the ground on the front of an off-road vehicle (Figure 83 from Newman et al. 2003; Rozendaal et al., 2004)) and trailed between the vineyards of Simonsig At a speed of ~2 m/s and an integration time of two seconds the detector averages the concentration of the radioisotopes over about 10 m^2. Mapping the area along lines spaced 10 m apart, resulted in a map of 500-600 points per hectare at a speed of six hectares per hour. Measurements were calibrated by taking surface samples which were analysed on the laboratory-based radiometry system. Afterward maps of the ^{40}K, ^{232}Th and ^{238}U concentration distributions were generated from the collected concentrations in conjunction with the GPS data. These maps are depicted in Figure 84 (Newman et al. 2003; Rozendaal et al., 2004) and indicate variations in the radioisotope concentrations over the surveyed area. In-situ measurements could therefore be used as a fast method to acquire radiometric information on surface soil.

Similar in-situ (MEDUSA) and ex-situ studies were later done to further the application of radiometry in viticulture. The first study investigated the correlations between the natural radioisotope concentrations in soils and the vine-growth potential (Modisane, 2005), another studies the systematic effects that are of importance during the activity concentration determination of vineyard soil samples (Joseph, 2007). Recently a study that investigated the feasibility of using radiometry as a method to determine the physic-chemical parameters of vineyard soil (Mlwilo, 2010) was also completed. Relevant findings of these studies will be discussed next.

Figure 83. ***The MEDUSA detector mounted in front of an off-road vehicle*** **(Newman et al. 2003; Rozendaal et al., 2004).**

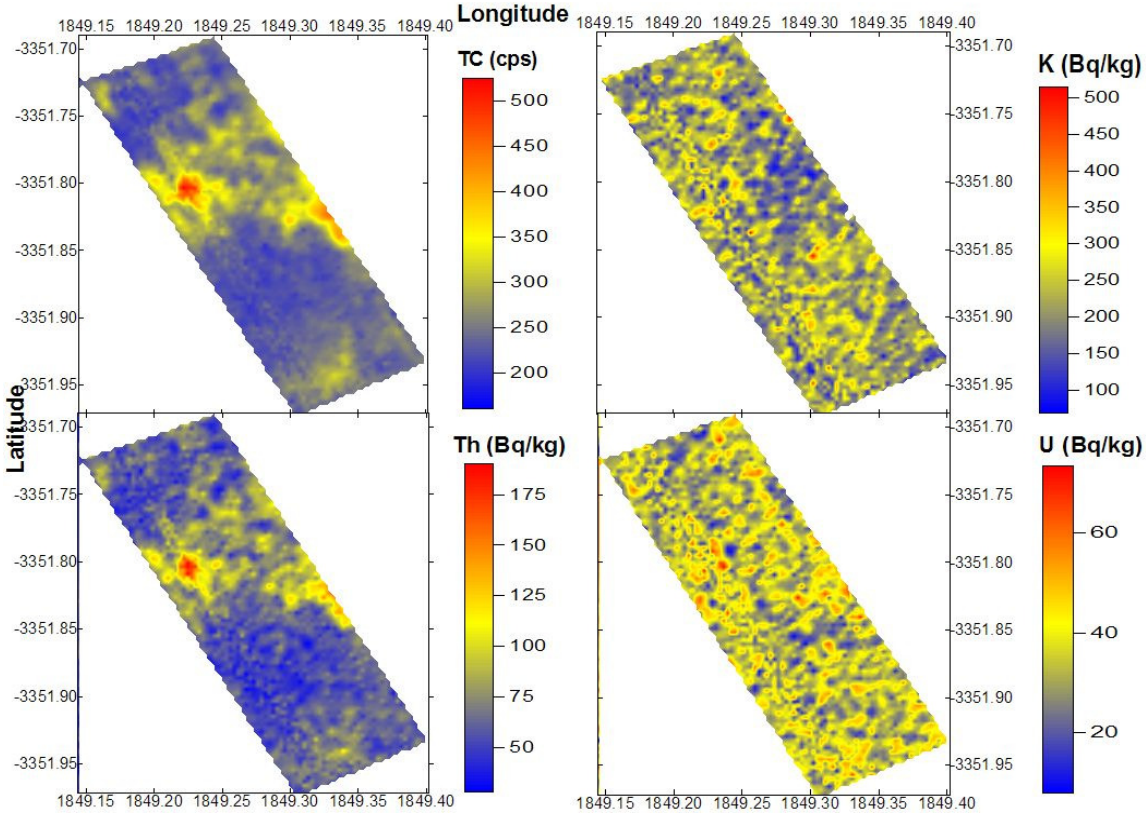

Figure 84. ***The radioisotope distributions of a section of the Simonsig vineyard obtained with the MEDUSA gamma ray detector system*** **(Newman et al. 2003; Rozendaal et al., 2004).**

Modisane (2005) studied two areas on Simonsig namely Nuweland and Pomphuis to determine if a link exists between the soil chemical properties that infer growth potential and the natural radioactivity found in the soil. He acquired in-situ and ex-situ data from these areas that revealed that the areas are statistically different, mainly due to the contribution of ^{232}Th. The concentration ranges for Nuweland were: 0.86 – 1.9 %, 10 - 17 ppm and 3.5 - 4.5 ppm for ^{40}K, ^{232}Th and ^{238}U respectively. For Pomphuis the ranges were: 0.21 – 1.6 %, 4.9 – 15 ppm and 1.6 – 4.1 ppm for ^{40}K, ^{232}Th and ^{238}U respectively. In order to link the radiometric data with vine-growth potential he correlated chemical data, obtained using traditional soil analyses, with the radioisotope concentrations. For the Nuweland soil he found significant correlations between ^{40}K and citric acid and soil resistance and between ^{238}U and carbon. The Pomphuis soil revealed correlations between ^{232}Th and citric acid and ^{238}U and potassium, calcium and magnesium. From the correlations Modisane concluded that firstly as the depth of the soil increases, the correlation between chemical parameters decreases and secondly as the concentration increases, the relationship between chemical parameters decreases. Finally he concluded that the different soils forms found in these areas are associated with different degrees of vine-growth potential and since radiometry can measure these differences, radiometry can be useful to predict vine-growth potential.

Joseph (2007) studied Block 2 on Simonsig. He obtained in-situ and ex-situ data but with the focus to study the systematic effects encountered during a determination of the three radioisotope concentrations. His method of determining the efficiency (and also Modisane and Mlwilo) is different from the one used in this study. The end result of this internal standard method (Felsmann, and Denk, 1992) should not differ very much from the approach taken in this study. Joseph did not make a conclusion on the terroir link with the soil concentrations.

Mlwilo (2010) investigated in detail the feasibility of using radiometry as an alternative to traditional methods for the determination of the physico-chemical parameters of soil. All three Simonsig areas already mentioned was revisited namely Nuweland, Pomphuis and Block 2 and in-situ and ex-situ data collected. The concentration ranges for Nuweland were: 0.25 – 1.3 %, 3.4 - 14 ppm and 1.4 – 3.8 ppm for ^{40}K, ^{232}Th and ^{238}U respectively. For Pomphuis the ranges were: 0.12 – 1.2 %, 2.7 – 13 ppm and 0.89 – 5.5 ppm for ^{40}K, ^{232}Th and ^{238}U respectively. For Block 2 the ranges were: 0.51 – 0.90 %, 6.8 – 27 ppm and 2.3 – 5.5 ppm for ^{40}K, ^{232}Th and ^{238}U respectively. He compared the soil physic-chemcical

parameters of three areas and showed large variations exist between the area (which is also observed in the radiometry results). From this observation he concluded that two types of soil are present at Simonsig. Mlwilo also correlated the radiometry data with the physico-chemical parameters of the soil. He found that the radiometric data were significantly correlated with major elements MgO, TiO and K_2O and trace elements Li, K, Se and exchangeable cations Na and Mg. He also indicated that the radiometric data correlated positively with clay and negatively with sand. His results also indicated that there were no significant variations between the results for soil depths 0 - 30 cm and 30 – 60 cm. He concluded that radiometry can be used to derive physico-chemical parameters of soil.

Comparing the work of Modisane (2005) and Mlwilo (2010) with the present study one observes that each study had a different focus; all investigating different aspects of terroir while proposing the suggestion that radiometry can be used as an alternative method for soil classification. Mlwilo's conclusion that Simonsig has two types of soil agrees with the findings of this study. While he only investigated Simonsig his conclusion on the correlation between clay and radiometric data also agrees with that of Koomans (2000) and this study. Neither of the two authors indicated that fertilisers can have an effect on their results. Contrary to this study, where geology and radiometric parameters are linked, is it not a problem as they focused on the elements in the soil irrespective where it came from.

The range of concentrations that were calculated for each of the study areas are summarised in Table 35. Although the placing of Nuweland and Pomphuis is unknown in relation to this study area Kriekbult and Simonsig Area, good agreement between the radioisotope data sets are found. From this agreement one can assume that Kriekbult is similar to Block 2 while Simonsig is similar to Nuweland/Pomphuis area. This again agrees with the previously stated finding of two soil types found at Simonsig vine estate.

Table 35 ***Summary of the range of radioisotope concentrations determined by Modisane (2005), Mlwilo (2010) and this study for the of the vineyard soil samples of Simonsig.***

Author	Area	^{40}K (%)	^{232}Th (ppm)	^{238}U (ppm)
De Villiers	Simonsig	0.53 – 1.6	5.6 – 16	1.4 – 6.7
De Villiers	Kriekbult	0.38 – 0.6	5.0 – 23	1.7 – 2.9
Modisane	Nuweland	0.86 – 1.9	10 - 17	3.5 – 4.5
Mlwilo	Nuweland	0.25 – 1.3	3.4 - 14	1.4 – 3.8
Mlwilo	Pomphuis	0.12 – 1.2	2.7 - 13	0.89 – 5.5
Modisane	Pomphuis	0.21 – 1.6	4.9 - 15	1.6 – 4.1
Mlwilo	Block 2	0.51 – 0.90	6.8 - 27	2.3 – 5.5

6.4 CONCLUSIONS

The terroir of a region consists of various components that have an influence on the quality of wine. In this application of radiometry, some terroir characteristics based on soil type, of the three Pinotage producing vineyards were derived according to their respective radioisotope concentrations. The ^{40}K concentrations demonstrated that the Kanonkop and Simonsig soils are fine-grained and clay-rich (Malmesbury Group derived) compared to the sandy coarse-grained soils of Spier (Cape Granite Suite and Table Mountain Group derived). This could be a significant contributing factor to the contrast between the quality of Pinotage from the various areas, i.e. Pinotage vines producing good quality wine prefer clay-rich soil (Saayman, 1992). The variation of ^{232}Th activity is a function of the presence of S-type granites. Thorium is hosted by stable minerals such as zircon, apatite and monazite and anomalous activity in soils indicate derivation from proximal granites. Spier soils are granite derived and are apparently not conducive to the production of quality Pinotage wine. ^{238}U variation also shows that Spier soil is low on uranium. This is attributed to the high solubility of uranium minerals hosted essentially by granites and resultant dispersion by surface transport agents. From the combination of the information obtained it seems that two types of soil are present at both Kanonkop and Simonsig. The radioisotope concentrations of the investigated areas are depicted in Figure 85 as a ternary plot, which indicates the different radiometric characteristics of Kanonkop, Spier and Simonsig.

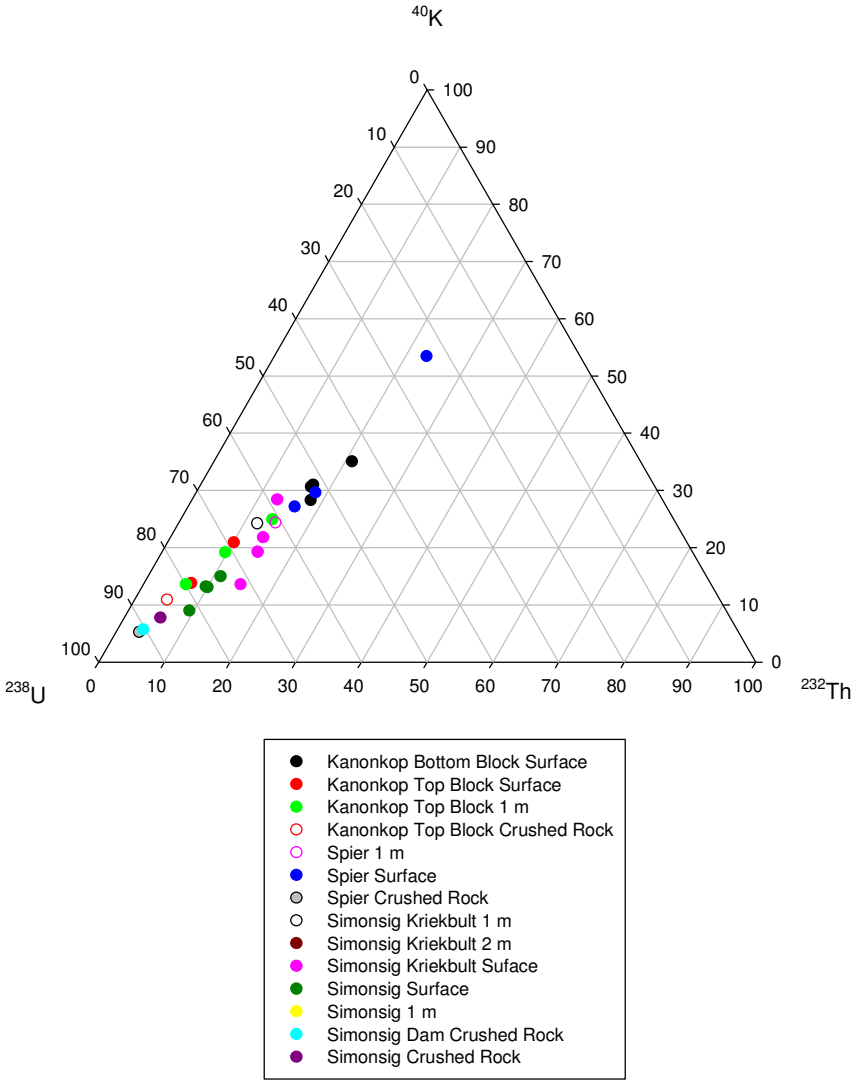

Figure 85. ***Ternary plot of the ^{238}U, ^{232}Th and ^{40}K concentrations (expressed as a percentage obtained by the ratio of the concentration to the sum of the concentrations) for Kanonkop, Spier and Simonsig.***

A positive correlation between radiometry and XRF were found and confirmed that radiometry can be used as alternative to determine the uranium, thorium and potassium concentrations in soil. The correlation between these two methods was very good for thorium and excellent for potassium. The uranium correlation was poor but only because the soil samples were very low in uranium concentration (based on the radiometry results lower than XRF detection limits). The use of a low concentration standard may result in a more acceptable correlation between the two methods, but as the XRF detection limit also depends on other factors, such as the properties of the instrument, it might not be worthwhile to implement. The advantage of radiometry in this regard is that if lower limits of detection are needed, the sample counting time, as a first step, can just be increased without added expenditure. The correlations conclude that radiometry can be used to

reflect potassium (clay) content of soils and on the nature of the bedrock and maturity of the soils. When only these elements are of concern, radiometry offers to be a feasible alternative to conventional methods. A drawback of the laboratory-based radiometry is that a 30 day waiting period is required for the sample to reach secular equilibrium before a measurement result can be obtained. This requirement is needed to increase the accuracy of the method, but estimations of the concentrations or a larger error can be introduced if faster turnaround times are needed.

It was shown that with the use of in-situ radiometry, subtle differences in radioisotope concentrations in soils could be detected within a relatively short period. In-situ radiometry is therefore favourable for the determination of soil type for large areas. Area classification is especially useful in areas where loosening of soils (before planting of vines) or improvement of the soil through use of chemicals over several years, might have changed the properties of the soil in such a way that the original characteristics of the soil are no longer noticeable. Radioisotope distribution maps may therefore be a valuable tool in the decision making process relating to cultivars and rootstocks for specific regions.

In-situ radiometry has the disadvantage that the obtained results are only applicable to the top 30-50 cm of the soil. This may not be sufficient in areas where information of the deeper soil is needed, for example most of the vine roots are found in the top 1 m or as much as 6 m (Stepke, 2010), but alternatives are sampling, depth profiling using a commercially available radiometric logger system and auger drilling. Another shortcoming of the in-situ method is that concentrations are averaged over a 10 m^2 area. While subtle differences in concentrations are rarely needed for in-situ measurements, it can be complemented with sampling and laboratory-based radiometry if this kind of information is needed.

It was assumed that the areas under investigation did not use fertilisers in order to make conclusions regarding the relationship between geology and soil. In the case of the uranium and thorium it may have been a reasonable assumption but for the potassium concentrations this may not be valid since fertilisers can contain a large amount of potassium which may explain the inconsistencies observed in some of the results. While the presence of fertilisers may have influenced the results and conclusions, it does provide an additional application of radiometry. With radiometry the present distribution of fertilisers (or baseline situation in case of virgin soil) can be mapped as well as the successive use of added potassium and the uptake thereof by the vines monitored with regular sampling or surveying.

CHAPTER 7 CONCLUSIONS

In this chapter the important aspects of the application of radiometry as a laboratory measurement technique and the application of radiometry in heavy mineral sand separation and soil classification are reviewed. Suggestions are also made for future work in this field of study.

7.1 CONCLUSIONS

In this study radiometry was used to characterise heavy mineral sand and vineyard soil samples according to their ^{238}U, ^{232}Th and ^{40}K concentrations for application in firstly heavy mineral separation and secondly soil classification.

The first objective was to set-up and calibrate radiometry as a laboratory-based method with a measurement error of less than 10%. The objective for the first application was, as it was never been done before, to demonstrate that radiometry can be used as an alternative for grade control of heavy mineral sands to improve the cost benefit of the separation process. The objective of the second application was to demonstrate, as a pilot study, that radiometry can be used as a possible tool in soil classification in order to contribute to the optimisation of land use with respect to vine cultivar, wine quality and possibly production.

Through the use of various calibration procedures and correction factors was the high purity germanium detection system able of a systematic error of 5.1 % in a uranium measurement for the heavy mineral sand samples and 36.3 % for the vineyard soil samples, 4.5 % in a thorium measurement and 4.7 % in a potassium measurement. Counting times were chosen as such to produce a statistical error of less than 2%. The first objective was reached for the heavy mineral sand samples, but due to the assumed high loss of radon in the soil samples, not for the vineyard soil samples.

Samples obtained from the various heavy mineral separation processes were characterised. Based on their total concentration and uranium-to-thorium ratios it were possible to differentiate between the different processes. In the other investigations, that of XRF comparison and counting time reduction, it was demonstrated that radiometry have excellent correlation with XRF. Grade control (from entry feed to final product), the

efficiency of separation processes, the optimisation of the processes and the monitoring of tailings streams can be done with the use of radiometry, but it has a shortcoming in that can only measure radioactivity concentrations and not other impurities. Therefore radiometry does not replace XRF in all aspects. The practical implementation of radiometry as an online technique was also discussed. While the set-up time would be longer than for XRF due to various site specific data that are needed, the cost benefit lies in the fact that processing decisions can then be implemented quickly in order to optimise the final product and therefore increasing revenue.

Characterisation of vineyard soil samples indicated that soil type can be determined based on variations in the radioisotopes, especially ^{40}K that was linked to the clay content of soil. It was also demonstrated that the correlation between radiometry and XRF was excellent for thorium and potassium. The uranium concentrations of the soils were below the detection limit of XRF, as a result the correlation between radiometry and XRF was poor. It is expected that this correlation will be better when a lower standard is used for comparison. The main concern of this part of the study was the unknown factor of the use of fertilisers. The application is better suited for application on virgin soil or as a comparative technique between fertiliser sessions or reworking of the soil. The results of this study together with the In-situ studies performed by Newman et al. (2003), Modisane (2005) and Mlwilo (2010) indicated that radiometry has merit as a method that can be used in soil classification and optimisation of land use in the viticulture.

7.2 FUTURE WORK

It is suggested that the entry feed to the heavy mineral separation plant is investigated to confirm whether the same mining site relate to similar mineralogies and hence similar radiometric properties. It is also suggested to study the correlation between the magnetic and electrostatic properties of the minerals to the radiometric properties for further separation or recovery processes. The application of the full spectrum analysis method to each of the separation processes can also add value to the future use of radiometry in this field. Furthermore, it is suggested that a study is undertaken to demonstrate that zircon with a radioactivity concentration of less than 500 ppm is always in specification regarding the other impurities.

The vineyard soil application was done under the assumption that no fertilizer was used in the vineyards. This is in most cases not true. While the comparison between unfertilized soil and its relationship to the geology is very difficult to investigate in a production vineyard, it is possible in a virgin vineyard. Another suggestion is the investigation in the use and uptake of fertilizer in a vineyard by comparing results before and after fertilisation. The impact of geology on the vineyard can be extended to more areas of the three vineyards.

REFERENCES

Abbas M.I. (2001) *HPGe detector photopeak efficiency calculation including self-absorption and coincidence corrections for Marinelli beaker sources using compact analytical expressions.* Int. J. Appl. Radiat. Isot. **54**, 761.

Amrani D., Tahtat M. (2001) *Natural radioactivity in Algerian building materials.* Int. J. Appl. Radiat. Isot. **54**, 687.

Álvarez C.A., Vivero T.D. (2002) *Application of natural gamma radiometric equipment in an underground mine in Spain,* International Journal of Mineral Processing, 65(1), 1.

Ay□ik G.A. (1992) *Efficiency Calibration of Ge(Li) Detectors, and the Effects of Geometry and Physical Properties of Samples on the Efficiency of Detectors,* Journal of Radioanalytical and Nuclear Chemistry 157(1), 115.

Bargmann C.J. (2003) *Geology and wine production in the coastal region, Western Cape province, South Africa.* Geoscience Canada 30(4), 161.

Bateman H. (1910) *The solution of a system of differential equations, occurring in the theory of radioactive decay*. Proc. Camb. Philos. Soc. 15, 423.

Berger M.J., Hubbell J.H. (1999) *Photon cross sections database*. National Institute of Standards and Technology.

Boshkova T., Minev L. (2001). *Corrections for self-attenuation in gamma-ray spectrometry of bulk samples*. Int. J. Appl. Radiat. Isot. 54, 777.

Brodzinski R.L., Miley H.S., Reeves J.H., Avignone F.T. (1995) *Low background germanium spectrometry- the bottom line three years later.* Journal of Radioanalytical and Nuclear Chemistry Articles, 193, 61.

Brown T.L., LeMay H.E., Bursten B.E. (1991) In: *Chemistry, the central science.* 5th Ed, Prentice-Hall International, New Yersey.

Castrup H. (2004) *Estimating and Combining Uncertainties,* Proceedings of the 8th Annual ITEA Instrumentation Workshop, Lancaster Ca, 5 May.

Chanturiya V.A. (2001) *Modern problems of mineral processing in Russia,* The European Journal of Mineral Processing and Environmental Protection, Volume 1, 25.

Clayton C.G., (Editor) (1983) In: *Applications of Nuclear techniques in Mineral exploration mining and process control.* Int. J. Appl. Radiat. Isot. 34, 1.

CSIR (2000) In: *National Land-cover 2000*, publication of the Council for Scientific and Industrial Research and Agricultural Research Council, South Africa.

Currie L,H. (1968) *Limits for qualitative detection and quantitative determination*. Analytical Chemistry, 40, 586.

Debertin K., Helmer R.G. (1988) In: *Gamma- and x-ray spectrometry with semiconductor detectors.* Elsevier Science Publishers B.V., Amsterdam.

Debertin K., Ren, J. (1989) *Measurement of the activity of radioactive samples in Marinelli beakers.* Nucl. Instr. and Meth. A278, 541.

De Felice P., Angelini P., Fazio A., Capogni M. (2002) *A national campaign for coincidence-summing correction in γ-ray spectrometry.* Appl. Radiat. Isot. 56, pp 117-123.

De Meijer, R.J., Lesscher, H.M.E., Schuiling, R.D., Elburg, M.E. (1990) *Estimate of the heavy mineral content in sand and its provenance by radiometric methods.* Nucl. Geophys. 4, 455.

De Meijer, R.J., Donoghue J.F. (1995) *Radiometric fingerprinting of sediments on the Dutch, German and Danish coasts.* Quaternary International 26, 43.

De Meijer R.J., Tanczos I.C., Stapel C. (1996) *Radiometry as a technique for use in coastal research.* Geological Society Special Publication, **117**, 289.

De Meijer, R.J., Stapel, C., Jones, D.G., Roberts, P.D., Rozendaal, A., Macdonald, W.G. (1997a) *Improved and new uses of natural radioactivity in mineral exploration and processing.* Explor. Min. Geol. 6, 105.

De Meijer R.J., Stapel C., Rozendaal A., Macdonald W.G., Donoghue J.F. (1997b) *New approaches to radiometry in heavy mineral exploration and processing.* Heavy Minerals 1997, 187.

De Meijer, R.J., Put L.W., Schuiling R.D., de Reus J.H., Wiersma J. (1998) *Provenance of coastal sediments using natural radioactivity of heavy mineral sands.* Rad. Prot. Dosimety. 24, 55.

Department of Minerals and Energy, Republic of South Africa. (2008) In: *MB Bulletin*, Directorate: Mineral Economics.

Department of Minerals and Energy, Republic of South Africa (2009) In: *MB Bulletin*, Directorate: Mineral Economics.

Dryák P., Kovář P., Plchová L, Šuráň J. (1989) *Correction for the marinelli geometry.* J. Radioanal. Nucl. Chem., Letters 135 281.

Dryák P., Kovář P., Šuráň J. (2002) *Determination of corrections to true summantions of photons for measurements in Marinelli beakers.* Int. J. Appl. Radiat. Isot. 56, 111.

Ďurčík, M., Havlík. F. (1996) *Experimental study of radon and thoron diffusion through barriers.* J. Radioanal. Nucl. Chem., Articles, 209 (2), 307.

Durrance E.M. (1986) In: *Radioactivity in Geology -Principles and Applications.* Ellis Horwood Limited, Great Britain.

Esterhuyse J.L (1996) *The geology of the Graauwduinen heavy mineral sand deposit*. Restricted Radiological Report, Namakwa Sands Limited.

Evans R.D. In: *The atomic nucleus*, McGraw-Hill, New York (1955).

Felsmann M., Denk H.J. (1992) *Efficiency calibration of germanium detectors with internal standards.* J. Radioanal. Nucl. Chem., Articles, 157 (1), 47.

Firestone R.B. (1996) *Table of Radioactive Isotopes* (Ed. Shirley, V.S.). John Wiley & Sons, New York.

Garcia-Talavera M. (2001) *Coincidence summing corrections for the natural decay series in γ-ray spectrometry*, Journal of Radiation and Isotopes 54, 769.

Genet M. (1995) *The discovery of uranic rays: A short step for Henri Becquerel but a giant leap for science.* Radiochim. Acta. 70-71, 3.

Gilmore G., Hemingway J.D. (1995) In: *Practical Gamma-Ray Spectrometry*. John Wiley & Sons, New York.

Glosup J.G., Axelrod M.C. (1996) *Systematic Error Revisited,* Proceedings of the Section for Physical and Engineering Sciences of the American Statistical Association, 1996 Joint Statistical Meeting, Chicago, Illinois, 4-8 August.

Greenfield M.B., De Meijer R.J., Put L.W., Wiersma J., Donoghue J.F. (1989) *Monitoring beach sand transport by use of radiogenic heavy minerals.* Nucl Geophys, 3, 231.

Haase G., Tait D., Wiechen A. (1993) *Application of a new Monte Carlo method for determination of summation and self-attenuation corrections in gamma spectroscopy.* Nucl. Instr and Methods in Physics Research A, 336, 206.

Hasan M., Bódizs D., Czifrus Sz. (2002). *A simplified technique to determine the self-absorption correction for sediment samples.* Int. J. Appl. Radiat. Isot. 57, 915.

Hendricks P.H.G.M., Limburg J., de Meijer R.J. (2001) *Full spectrum analysis of natural gamma ray spectra.* Journal of Environmental Radioactivity, 53**,** 365**.**

Hubbell J.H (1999) *Compilation of photon cross sections: some historical remarks and current status*. X-Ray Spectrometry 28, 215.

Human C. (2005) *Private communication*, Anglo Vaalriver Operations.

International Atomic Energy Agency (IAEA) (1976a) In: *Exploration for uranium ore deposits.* Symposium Proceedings 29 March - 2 April, Vienna.

International Atomic Energy Agency (IAEA) (1976b) In: *Nuclear techniques in geochemistry and geophysics.* Symposium Proceedings 25 – 29 November, Vienna.

International Atomic Energy Agency (IAEA) (1987) In: *Report on the Preparation and Certification of IAEA Gamma Spectroscopy Reference Materials*. IAEA, Vienna.

International Atomic Energy Agency (IAEA) (1991) In: *Airborne Gamma Ray Spectrometer Surveying.* Technical Report Series No 323, IAEA, Vienna.

International Atomic Energy Agency (IAEA) (2000) In: *Generic Procedures for Assessment and Response during a Radiological Emergency*. IAEA TECDOC Series Number 1162, Vienna.

International Atomic Energy Agency (IAEA) (2006) In: *Assessing the need for radiation protection measures in work involving minerals and raw materials.* Vienna.

Jabbar A., Arshed W., Bhatti A.S., Ahmad S.S., Rehman S., Dilband M. (2009) *Measurement of soil radioactivity levels and radiation hazard assessment in mid Rechna interfluvial region, Pakistan.* Journal of Radioanalytical and Nuclear Chemistry, 283 (2), 371.

Jones D.G. (2001) *Development and application of marine gamma-ray measurements: a review.* Journal of Environmental Radioactivity, 53, 313.

Joseph A.D. (2007) *Radiometric Study of Soil: The Systematic Effects,* M.Sc. thesis, unpublished, University of Western Cape.

Khan K., Khan H.M. (2001) *Natural gamma-emitting radionuclides in Pakistani Portland cement.* Int. J. Appl. Radiat. Isot. 54, 861.

Killeen P.G.(1997) *Nuclear Techniques for Ore Grade Estimation.* Proceedings of the 4th Decennial International Conference on Mineral Exploration edited by Gubins, p. 677.

Klusoň J. (2001) *Environmental monitoring and in situ gamma spectrometry*, Radiation Physics and Chemistry 61, 209.

Knoll G. F. (1979) In: *Radiation detection and measurement*. 1st Edition, John Wiley & Sons, New York.

Koegelenberg D. (2003) *pH – a manageable quality parameter*. Wynboer.

Koomans R.L. (2000) *Sand in motion*, Ph.D. thesis, unpublished, University of Groningen.

Korun M., Martinčič R. (1993) *The determination of the optimal shape of the samples in gamma-ray spectroscopy.* Proceedings of the Austrian-Italian-Hungarian Radiation Protection Symposium, Obergurgl, Vol 2, 276.

Lindsay R., de Mejier R.J., Maleka P.P., Newman R.T., Motlhabane T.G.K., de Villiers D. (2004) *Monitoring the radon flux from gold-mine dumps by gamma ray mapping*. Nucl. Instr. Methods in Physics Research B 213, 775.

Macdonald W.G. (1996) *The Geelwal Karoo heavy mineral deposit: A modern day beach placer*. M.Sc. thesis, unpublished, University of Stellenbosch.

Macdonald W.G., Rozendaal, A., de Meijer R.J. (1997) *Radiometric characteristics of heavy mineral deposits along the west coast of South Africa.* Mineralium Deposita, 32, 171.

Mange M.A., Maurer H. (1991) In: *Heavy Minerals in Colour*, Springer.

McGraw-Hill (1982) In: *McGraw-Hill Encyclopaedia of Science and Technology*. 5th Edition, McGraw-Hill, New York.

Mining Weekly (2010) *Great Western initiates BFS for South African monazite project,* 9 June.

Mlwilo N.A. (2010) *Radiometric characterisation of vineyard soils, Western Cape, South Africa,* Ph.D. thesis, unpublished, University of Western Cape.

Modisane T.J.D. (2005) *Correlations between natural radionuclide concentrations in soils and vine-growth potential.* M.Sc thesis, unpublished, University of North-West.

Nada A. (2003) *Evaluation of natural radionuclides at Um-Greifat area, eastern desert of Egypt.* Int. J. Appl. Radiat. Isot. 58, 275.

Nations Encyclopedia (2010) *South Africa Agriculture, Information about Agriculture in South Africa,* http://www.nationencyclopedia.com/economies/Africa/South-Africa-Agriculture.html, site visited December.

Newman R.T. (1996) *Single proton transfer on ^{55}Mn,* Ph.D. thesis, unpublished, University of Cape Town.

Newman R.T., Lindsay R., Joseph A.D., de Meijer R.J. (2003) *Radiometric Assesment of Terroir – A First Exploration at Simonsig, South Africa.* Draft NGD/KVI Report.

Nunez-Lagos R., Vitro A.(1996) *Shielding and background reduction.* Int. J. Appl. Radiat. Isot. 47, 1011.

Örgün Y., Altinsoy N., Gültekin A.H., Karahan G., Celebi N. (2005) *Natural radioactivity levels in granitic plutons and groundwaters in Southwest part of Eskisehir, Turkey.* Int. J. Appl. Radiat. Isot. 63, 267.

Oyedele J.A. (2006) *Assessment of the natural radioactivity in the soils of Windhoek city, Nambia, Southern Africa.* Rad. Prot. Dosimetry **121(3)**, 337.

Park T.S., Jeon W.J. (1995) *Measurement of Radioactive Samples in Marinelli Beakers by Gamma-ray Spectroscopy.* J. Rad Anal and Nuclear Chemisry 193, 133.

Philander C., Rozendaal A., de Meijer R.J. (1999) *Characteristics of zircon in placer deposits along the west coast of South Africa.* South African Journal of Science 95, 381.

Philander C. (2001) *Private Communication.* Namakwa Sands Limited.

Platter J. (2002) In: *South African Wines*. Creda Press, South Africa.

Robinson J. (ed) (2006) In: *The Oxford Companion to Wine.* 3rd Edition, Oxford University Press, 2006

Rozendaal A. (2001) *Private Communication*, Department of Geology, University of Stellenbosch.

Rozendaal A., de Villiers D., van der Merwe O. (2004) *The use of radiometry as an indicator of terroir characteristics in the winelands of the Stellenbosch region, South Africa.* Proceedings of the 32nd International Geological Congress, Florence.

Rozendaal A., Philander C. (2007) *Recovery of duricrust sterilized heavy mineral resources at the Namakwa Sands Mine South Africa: a geometallurgical challenge.* Proceedings of the 6th International Heavy Minerals Conference "Back to Basics", The South African Institute of Mining and Metallurgy.

Rozendaal A., Philander C. (2008) *Heavy mineral placer deposits along the West Coast of South Africa – a world class resource of zircon, ilmenite and rutile.* Proceedings of the 9th Annual Conference for Applied Mineralogy, Brisbane, Australia, September.

Saayman D. (1992) *Natural influences and wine quality. Part 2: The role of soil*, Wynboer, **8**, 49.

SAInfo (2010) http://www.southafrica.info/business/economy/wine-160210.htm, *SA wine industry "driving jobs, GDP",* visited site in December.

Sánchez F., Navarro E., Ferrero J.L., Moreno A., Roldán C. (1991) *A Monte Carlo based method of including gamma self-absorption for the analysis of environmental samples.* Nuclear Instruments and Methods in Physics Research, B61, 535.

Sbarato V.M., Sánchez H.J. (2001) *Analysis of arsenic pollution in groundwater aquifers by X-ray fluorescence.* Int. J. Appl. Radiat. Isot. 54, 737.

Sima O. (1991) *On the method of Dryák et al. for self-absorption correction calculations*. J. Radioanal. Nucl. Chem. Letters 155 (2), 75.

Sima O. (1996) *Applications of Monte Carlo calculations to gamma-spectrometric measurements of environmental samples.* Int. J. Appl. Radiat. Isot. 47, 919.

Sima O., Dovlete C. (1997) *Matrix effects in the activity measurement of environmental samples – implementation of specific corrections in a gamma-ray spectrometry analysis program.* Int. J. Appl. Radiat. Isot. 48, 59.

Sima O., Arnold D. (2000) *Accurate computation of coincidence summing corrections in low level gamma-ray spectroscopy.* Int. J. Appl. Radiat. Isot. 53, 51.

Spicer E. (2003) *Personal communication*. Department of Geology, Stellenbosch University, South Africa.

Singh J., Singh H., Singh S., Bajwa B.S., Sonkawade R.G. (2009) *Comparative study of natural radioactivity levels in soil samples from the Upper Siwaliks and Punjab, India using gamma-ray spectroscopy.* Journal of Environmental Radioactivity, 100(1), 94.

Spiegel M.R., Stephens L.J. (1998) In: *Schaum's outline of theory and problems of statistics*. 3rd Edition, McGraw-Hill, New York.

Stepke I.M.S (2010). *Effect of soil parameters and canopy structure on root growth and distribution*, M.Sc (Agric) thesis, unpublished, University of Stellenbosch, South Africa.

Strom D.J., Stansbury P.S. (1992) *Minimum detectable activity when background is counted longer than the sample*. Health Physics 63, 360.

Strydom J. (2009) *Private communication*, Restricted information, Richards Bay Minerals, South Africa.

Tsoulfandis N. (1983) In: *Measurement and detection of radiation*. McGraw-Hill, New York.

TZ Minerals International (2003a) *The global zircon industry 2002-2008 – the challenge of supply deficits*. TZMI, Perth, Australia.

TZ Minerals International (2003b) *Mineral sands report.* Issue 87, TZMI, Perth, Australia.

United States Geological Survey. (2007) *The mineral industry of South Africa*, 2007 Minerals Yearbook.

United States Geological Survey (2009) *The mineral industry of South Africa*, 2009 Minerals Yearbook.

Van der Merwe O. (2001) *The relationship between geology, soil and winestyle at three sites near Stellenbosch, South Africa*, B.Sc. (Hons) thesis, unpublished, University of Stellenbosch, South Africa.

Van der Walt, C. (2001) *Private communication*, Richards Bay Minerals.

Van Rooyen T.J. (2000) *Private communication*, iThemba LABS.

Van Wijngaarden L.B., Venema R.J., De Meijer R.J., Zwasman J.J.G., Van Os G., Gieske J.M.J. (2002) *Radiometric Sand-mud characterization in the Rhine-Meuse estuary part A: Fingerprinting*. Geomorphology 43, 87.

Van Zyl L. (2009) *Private communication*, Restricted information, Exxaro Namakwa Sands, South Africa.

Vargas M.J., Fernández T., Díaz N.C., Sánchez D.P. (2002) *Monte Carlo simulation of the self-absorption corrections for natural samples in gamma-ray spectrometry.* Int. J. Appl. Radiat. Isot. 57, 893.

Venema L.B., de Meijer R.J. (2000) *Natural radionuclides as tracers of the dispersal of dredge soil dumped at sea.* Journal of Environmental Radioactivity, 0, 1.

Verplancke J. (1992) *Low level gamma spectroscopy: low, lower, lowest.* Nucl. Instr. Meth. A312, 174.

Wikipedia (2006) http://en.wikipedia.org/wiki/terroir, *Terroir,* visited site in May.

Wikipedia (2010) http://en.wikipedia.org/wiki/South_African_wine, *South African Wine,* visited site in December.

Wooldridge J. (2003) *Geology and terroir in the Western Cape winelands*. Wynboer, **12**.

Yücel H., Çetiner M.A.., Demirel H. (1998) *Use of the 1001 keV peak of 234mPa daughter of 238U in measurement of uranium concentration by HPGe gamma-ray spectrometry.* Nuclear Instruments and Methods in Physics Research A, 413, 74.

APPENDIX A MEASUREMENT UNITS

The relationship between the unit for the specific activity, Bq/kg and the units for the concentration, which are parts per million (ppm) and percentage (%), can be derived in the following manner.

Firstly, calculate the activity of 1 g uranium. Using the natural abundance of ^{238}U, 1 g of uranium consists of 0.9927 g ^{238}U. It is also true that 1 g of uranium is 1/238 mole ^{238}U. According to Brown et al. (1991) the number of atoms per 1 g uranium is

$$N = \frac{0.9927 \times 10^{-6}}{238} \times 6.022 \times 10^{23}. \quad \text{A.1}$$

By substituting ^{238}U half-life of 1.41 × 10^{17}s (Firestone, 1996) and the above value for *N* in the activity equation (i.e. Equation 2.7), the activity of 1 g uranium is calculated as

$$A_{1g} = 12347 \text{ Bq}. \quad \text{A.2}$$

Secondly, express 1 ppm in weight units, which is

$$1 ppm = \frac{1g}{1000000\,g} = \frac{1g}{1000 kg}. \quad \text{A.3}$$

Finally combine Equations A.2 and A.3 and then it follows that

$$1\ ppm = 12.35 \text{ Bq/kg } ^{238}\text{U}. \quad \text{A.4}$$

Using the appropriate values, the above-mentioned derivation can be done for ^{232}Th and ^{40}K as well. The relationships for these two radioisotopes are

$$1\ ppm\ \text{Th} = 4.10 \text{ Bq/kg } ^{232}\text{Th} \quad \text{A.5}$$

and

$$1\%\ K = 302\ Bq/kg\ ^{40}K \text{ in KCl} \quad \text{A.6}$$

or

$$1\%\ K = 251\ Bq/kg\ ^{40}K \text{ in } K_2O \quad \text{A.7}$$

with

$$1\ \% = 10\ 000 \text{ ppm} \quad \text{A.8}$$

APPENDIX B STATISTICS

B.1 INTRODUCTION

Radioactive decay is a random process on the nuclear level, in that it is impossible to predict when a specific nucleus will decay. The results of a repeated measurement of a quantity associated with a radioactive sample e.g. number of counts in a photopeak will therefore show fluctuations. To account for these fluctuations, an error is associated with a measurement. The error can also be used to describe the repeatability (also called precision) of a measurement or classify sample populations. If a measurement is repeated a few times and the results are consistent with each other, taking the errors into account, it is said that the precision is good. Similarly, when several samples are measured and their results are consistent, again taking their errors into account, one can deduce that they represent, within certain limits, the same population.

The error is expressed by the standard deviation, which is explained in the following section with a few statistics definitions. Also included in this section are weighting factors and error propagation.

B.2 STATISTICAL CONCEPTS

B.2.1 Arithmetic Mean Value

In a data set, a certain value x_i can appear many times in the set. When the number of occurrences is divided by the number of measurements N the frequency distribution $F(x_i)$ is obtained. Plotting these values will show that there exists a fluctuation around a certain value. This value is called the arithmetic mean value and is defined as

$$\mu_a = \frac{1}{N}\sum x_i. \qquad \text{B.1}$$

B.2.2 Sample and Predicted Variance

The mean value is not necessarily representative of the whole sample set. When a measurement is repeated a large number of times many of the repetitions will be close to the mean, while a few tend to either of the extremes. This fluctuation between the different

values is quantified by the sample (or observed) variance s^2. It is defined (Spiegel and Stephens, 1998) as

$$s^2 = \frac{1}{N-1}\sum \varepsilon_i^2, \qquad \text{B.2}$$

with the variation ε_i,

$$\varepsilon_i = x_i - \mu_a, \qquad \text{B.3}$$

as the amount by which a particular value differs from the arithmetic mean.

The frequency distribution of a set of measurements can be predicted based on the detector probability to absorb a gamma ray (p) and the number of gamma rays incident on the detector (n). The product of these two values

$$pn = \mu \qquad \text{B.4}$$

is defined as the mean value. In the case where p is small and n very large a choice of distributions exists. If μ is larger than 20 a Gaussian distribution is formed, while smaller mean values will result in a Poisson distribution. For both these approximations a predicted variance, σ^2 is defined as

$$\sigma^2 = \mu. \qquad \text{B.5}$$

B.2.3 Standard Deviation

The sample variance gives an indication of how a value will change to another if a specific measurement is repeated a number of times. Still, it would be better to have a value that is a measure of how much a measurement will deviate from the true mean value. In other words, what is the error associated with a single measurement? The answer to this question lies in the definition of the standard deviation.

When only one measurement is done, one has to assume that the value obtained, x, is equal to the mean. A further assumption would be that the sample variance fits the predicted distribution model. Therefore, from Equations B.2 and B.5 it follows that

$$x = \mu = \sigma^2 = s^2. \qquad \text{B.6}$$

Based on Equation B.6 the standard deviation of individual observations is defined as

$$\sigma = \sqrt{s^2} = \sqrt{x}. \qquad \text{B.7}$$

(An individual observation is typically the photopeak counts from the measurement of a single gamma energy.)

Using the standard deviation in conjunction with the measured value, $x_i \pm \sigma$, an interval in a data set is made. If this set was normally distributed and the number of measurements was large it would include 68.29 % of the possible measurements. (If one expands this region to $\pm 2\sigma$, 95.45 % of the values are included, while 99.73 % applies when $\pm 3\sigma$ is used.) The percentage value is called the confidence level, while the end values of the $\pm k\sigma$ interval are called the k^{th} confidence limits.

B.2.4 Weighting Factors

When more than one measurement, each with its own error is used to determine the mean value and its standard deviation the calculation is different from what was discussed so far. In these cases a weighting factor w_i, defined as (Debertin and Helmer, 1988)

$$w_i = \frac{1}{\sigma_{x_i}^2}\left(\sum \frac{1}{\sigma_{x_j}^2}\right)^{-1}, \qquad \text{B.8}$$

is assigned to each measurement. All the weighting factors normalise to 1, i.e.

$$\sum w_i = 1. \qquad \text{B.9}$$

As a result, the mean value and its standard deviation are calculated by the expressions

$$\mu = \frac{\sum w_i x_i}{\sum w_i} \qquad \text{B.10}$$

and

$$\sigma_\mu = \sqrt{\left(\sum \frac{1}{\sigma_{x_i}^2}\right)^{-1}}. \qquad \text{B.11}$$

B.2.5 Error Propagation

More than often the original measurement is used in a calculation to determine another quantity. For example, the number of counts in a peak is measured, but through a calculation it is converted to an activity value. Just as the original value propagates through the calculation to a final value, so must the associated error be propagated through the calculation. The propagation of errors is based on the equation of Tsoulfandis (1983)

$$\sigma_\mu = \sqrt{\sum\left(\frac{\partial u}{\partial x_i}\right)^2 \sigma_i^2 + 2\sum\sum\left(\frac{\partial u}{\partial x_i}\right)\left(\frac{\partial u}{\partial x_j}\right)\rho_{ij}\sigma_i^2\sigma_j^2}. \qquad \text{B.12}$$

Normally the variables are uncorrelated so that $\rho_{ij} = 0$ and Equation B.12 simplifies to

$$\sigma_\mu = \sqrt{\sum \left(\frac{\partial u}{\partial x_i} \right)^2 \sigma_i^2}. \qquad \text{B.13}$$

The expressions for the total error for four types of calculations, derived from Equation B.13, are given below.

- If $u = x \pm y$ then

$$\sigma_\mu = \sqrt{\sigma_x^2 + \sigma_y^2}. \qquad \text{B.14}$$

- If $u = xy$ then

$$\sigma_\mu = u \sqrt{\left(\frac{\sigma_x}{x} \right)^2 + \left(\frac{\sigma_y}{y} \right)^2}. \qquad \text{B.15}$$

- If $u = Ax$ then

$$\sigma_\mu = A\sigma_x. \qquad \text{B.16}$$

- If $u = \frac{x}{B}$ then

$$\sigma_\mu = \frac{\sigma_x}{B}. \qquad \text{B.17}$$

APPENDIX C MINIMUM DETECTABLE ACTIVITY

The expression to calculate the minimum detectable activity (MDA) was chosen based on the information discussed below.

The calculation of the MDA depends on the experimental circumstances under which the measurements were done. With the assumption that the variance in the background photopeak is numerically identical to the background, Currie (1968) derived an expression for the MDA. It is based on the number of counts present in a background photopeak (*B*) (at a 95 % confidence level) as

$$MDA'' = \frac{2.71 + 3.29\sqrt{2B}}{T_s \times \varepsilon \times I}, \qquad \text{C.1}$$

with T_S the counting time, ε the photopeak efficiency at the energy of interest and I the photon intensity of the gamma ray.

The assumption Currie used is often not true as the total number of channels used to identify the background photopeak (*n*) differs from the number of channels in the background photopeak (*m*). For such cases Gilmore and Hemingway (1995) proposed an alternative expression for the MDA

$$MDA' = \frac{2.71 + 3.29\sqrt{B\left(1 + \frac{n}{2m}\right)}}{T_s \times \varepsilon \times I}, \qquad \text{C.2}$$

assuming that the sample and the background have the same counting times.

However, in a typical measurement situation the sample and background counting times are different. To correct for this discrepancy, Strom and Stansbury (1992) estimated the background photopeak area using the background counting time T_B, the background count rate R_B ($=B/T_B$) and the sample counting time T_S. The MDA is then expressed by

$$MDA = \frac{2.71 + 3.29\sqrt{\frac{R_B}{T_s} + \frac{R_B}{T_B}}}{T_s \times \varepsilon \times I}. \qquad \text{C.3}$$

In this study the sample and background counting times were different so Equation C.3 was used to calculate MDA values.

APPENDIX D SPECIFIC ACTIVITY OF REFERENCE SAMPLES

D.1 RGU-1

The uranium content of the IAEA reference sample, RGU-1, is specified as 400 ± 1.1 µg/g (IAEA, 1987) and the volume and mass were 400.0 ml and 487.37 g respectively. The uranium mass of the sample is therefore

$$m' = 400\ \mu g/g\ \times 487.37\ g = 0.195\ g. \qquad \text{D.1}$$

Using Equations A.2 and D.1, the number of ^{238}U atoms (N) was calculated as 4.90 x 10^{20}. By substituting ^{238}U half-life of 1.41 × 10^{17}s (Firestone, 1996) and the value for N in the specific activity equation (i.e. Equations 2.10 and 2.7), the specific activity of RGU-1 was calculated as

$$SA = \frac{A}{m} = \frac{\lambda N}{m} = \frac{(\ln 2)N}{mT_{1/2}} = \frac{\ln 2 \times 4.90 \times 10^{20}}{0.48737 \times 1.410 \times 10^{17}} \qquad \text{D.2}$$

= 4940 ± 14 Bq/kg.

D.2 RGTh-1

The thorium content of the IAEA reference sample, RGTh-1, is specified as 800 ± 8 µg/g (IAEA, 1987) and the volume and mass were 400.0 ml and 515.73 g respectively. Using a similar derivation as the one in D.1, and the values of *m'*= 0.413g, *A* = 232, % = 1 and ^{232}Th half-life of 4..434 × 10^{17}s (Firestone, 1996) the specific activity of ^{232}Th was calculated as **3250 ± 33 Bq/kg**.

D.3 KCl

The specific activity of potassium chloride was calculated as **16252 ± 81.3 Bq/kg** using a similar derivation as the one in D.1, and the values of *m'*= 1000g, *A* = 40, % = 1.172 × 10^{-4} , molar mass of 74.55 g/mol and ^{40}K half-life of 4.0377 × 10^{16}s (Firestone, 1996).